Frontier Materials & Technologies

Founded in 2008
№ 1
2024
16+
Quarterly
Scientific Journal

The Founder is
Togliatti State University

Until December 2021,
the journal was published under
the title
**"Science Vector
of Togliatti State University".**

Indexed in Scopus.
Included in the List of HAC,
RSCI core, DOAJ,
"White List".
Available in Crossref,
Google Scholar.

Registered by the Federal
Service for Supervision
of Communications,
Information Technology
and Mass Media
(Registration Certificate
ПИ No. ФС77-83040
dated March 31, 2022).

Desktop publishing:
Natalya A. Nikitenko

*Responsible/technical
editor:*
Natalya A. Nikitenko

Mailing Address:
14, Belorusskaya St.,
Togliatti,
Russia, 445020
Phone: **(8482) 44-91-74**
E-mail:
vektornaukitgu@yandex.ru

Website:
https://vektornaukitech.ru

Passed for printing
29.03.2024.
Published 17.06.2024.
Format 60×84 1/8.
Digital printing.
Conventional printed sheets 14.2.
Circulation is 30 copies.
Order 3-482-23
The price is free.

Togliatti State University
Publishing
14, Belorusskaya St.,
Togliatti, Russia, 445020

EDITORIAL BOARD INFORMATION

СВЕДЕНИЯ О ЧЛЕНАХ РЕДКОЛЛЕГИИ

Карпов Михаил Иванович, член-корреспондент РАН, доктор технических наук, профессор, заведующий лабораторией материаловедения (Институт физики твердого тела Российской академии наук, Черноголовка, Россия).
Scopus AuthorID: 7004130343
ResearcherID: Q-9288-2016
Кацман Александр Владимирович, кандидат физико-математических наук, PhD, старший научный сотрудник (Технион – Израильский технологический институт, Хайфа, Израиль).
Scopus AuthorID: 7004225554
Кудря Александр Викторович, доктор технических наук, профессор, заместитель заведующего кафедрой металловедения и физики прочности (Национальный исследовательский технологический университет «МИСиС», Москва, Россия).
Scopus AuthorID: 6603628218
Кузьмин Сергей Викторович, член-корреспондент РАН, доктор технических наук, профессор, первый проректор, профессор кафедры «Оборудование и технология сварочного производства» (Волгоградский государственный технический университет, Волгоград, Россия).
Scopus AuthorID: 57217278342
ResearcherID: I-7424-2012
ORCID: https://orcid.org/0000-0003-2802-8497
Макаров Алексей Викторович, член-корреспондент РАН, доктор технических наук, главный научный сотрудник, заведующий отделом материаловедения и лабораторией механических свойств (Институт физики металлов имени М.Н. Михеева Уральского отделения Российской академии наук, Екатеринбург, Россия).
Scopus AuthorID: 36889178900
Scopus AuthorID: 57195590138
ResearcherID: D-5663-2016
ORCID: https://orcid.org/0000-0002-2228-0643
Мулюков Радик Рафикович, член-корреспондент РАН, доктор физико-математических наук, профессор, директор (Институт проблем сверхпластичности металлов Российской академии наук, Уфа, Россия).
Scopus AuthorID: 7003520439
ResearcherID: B-3800-2016
ORCID: https://orcid.org/0000-0002-0452-3816
Наймарк Олег Борисович, доктор физико-математических наук, профессор, заведующий лабораторией «Физические основы прочности» (Институт механики сплошных сред Уральского отделения Российской академии наук, Пермь, Россия).
Scopus AuthorID: 6701720806
Носов Николай Васильевич, доктор технических наук, профессор, профессор кафедры «Технология машиностроения, станки и инструменты» (Самарский государственный технический университет, Самара, Россия).
Scopus AuthorID: 6602506825
Пилинский Александр Вениаминович, кандидат технических наук, доцент, MSME (Master of Science in Mechanical Engineering), менеджер («Реймер Металс Корпорейшн», Лос-Анджелес, США).
Романов Алексей Евгеньевич, доктор физико-математических наук, профессор Института перспективных систем передачи данных, руководитель научно-исследовательского центра перспективных функциональных материалов и лазерных коммуникационных систем (Национальный исследовательский университет ИТМО, Санкт-Петербург, Россия).
Scopus AuthorID: 7202768874
Рубаник Василий Васильевич, член-корреспондент Национальной академии наук Беларуси, доктор технических наук, заведующий лабораторией физики металлов (Институт технической акустики Национальной академии наук Беларуси, Витебск, Республика Беларусь).
Scopus AuthorID: 57215218253
Старобинский Рудольф Натанович, доктор технических наук, профессор, научный консультант (консалтинг-бюро “Prof. Starobinski. Silencers. Consulting and Engineering”, Гамбург, Германия).
Scopus AuthorID: 6602638504
Сундер Рамасуббу, член Индийской академии наук, кандидат технических наук, директор (“BISS (P) Ltd”, Бангалор, Индия).
Scopus AuthorID: 7003530245
ResearcherID: H-6740-2016
ORCID: https://orcid.org/0000-0001-6143-0723
Табаков Владимир Петрович, доктор технических наук, профессор, заведующий кафедрой «Инновационные технологии в машиностроении» (Ульяновский государственный технический университет, Ульяновск, Россия).
Scopus AuthorID: 6701501345
ResearcherID: E-1832-2017
ORCID: https://orcid.org/0000-0002-2568-9401
Шишков Владимир Александрович, доктор технических наук, начальник технического отдела (ООО «Палладио», Тольятти, Россия).
Эстрин Юрий Захарович, доктор физико-математических наук, профессор, профессор кафедры инженерных материалов (Университет им. Монаша, Мельбурн, Австралия).
Scopus AuthorID: 7005031984

CONTENT

СОДЕРЖАНИЕ

doi: 10.18323/2782-4039-2024-1-67-1

Changes in the structure, mechanical and corrosion properties of the Mg–Zn–Zr system alloy subjected to equal channel angular pressing

Denis A. Aksenov*[1,2,3], junior researcher
Elvira I. Fakhretdinova[1,2], PhD (Engineering), researcher
Rashid N. Asfandiyarov[1,2,4], PhD (Engineering), researcher
Arseniy G. Raab[2,5], PhD (Engineering), researcher
Arseniy E. Sharipov[2], graduate student
Mariya A. Shishkunova[2], postgraduate student
Yuliya R. Sementeeva[2], graduate student

[1]*Institute of Physics of Molecules and Crystals of Ufa Federal Research Center of RAS, Ufa (Russia)*
[2]*Ufa University of Science and Technology, Ufa (Russia)*

***E-mail: aksyonovda@mail.ru**

[3]ORCID: https://orcid.org/0000-0002-2652-2646
[4]ORCID: https://orcid.org/0000-0002-5522-4314
[5]ORCID: https://orcid.org/0000-0003-1993-413X

Received 05.06.2023 *Accepted 25.08.2023*

Abstract: Magnesium alloys are considered promising materials for the production of bioresorbable implants. Their main disadvantages are low strength and corrosion resistance in biological environment. In the work, the authors studied the effect of severe plastic deformation using the equal channel angular pressing (ECAP) method on the structure, mechanical properties, and corrosion resistance of the Mg–8.6Zn–1.2Zr magnesium alloy. It was identified that one ECAP cycle at 400 °C leads to a substantial hardening of the Mg–8.6Zn–1.2Zr alloy by ~10 %, up to 330 MPa. Structural studies showed that dynamic recrystallisation plays a significant role in the structure transformation. ECAP leads to the formation of a bimodal structure with large deformed grains with an average transverse size of 20±4 μm and recrystallised grains with an average transverse size of 6±2 μm. It was found that with a decrease in the strain temperature up to 250 °C, the process of deformation-induced decay of the supersaturated solid solution takes place. Electrical conductivity of a sample after ECAP at 400 °C amounted 29±2 % according to the International Annealed Copper Standard (IACS), while second ECAP cycles lead to an increase in the electrical conductivity up to 32±2 % IACS. Using the electrochemical corrosion method, the authors found that one ECAP cycle at 400 °C leads to a slight decrease in the corrosion resistance of the alloy under study compared to the initial state. The study showed that the corrosion current increases from 24 to 32 μA/cm^2, while the subsequent ECAP cycle at 250 °C increases the corrosion current more than twice (up to 57 μA/cm^2).

Keywords: Mg–Zn–Zr system alloys; Mg–8.6Zn–1.2Zr; magnesium alloys; high strength of magnesium alloys; ECAP; corrosion resistance; electrical conductivity; dynamic recrystallisation during ECAP.

Acknowledgments: The work was supported by the Russian Science Foundation (grant No. 22-79-10325, https://www.rscf.ru/project/22-79-10325/).

The paper was written on the reports of the participants of the XI International School of Physical Materials Science (SPM-2023), Togliatti, September 11–15, 2023.

For citation: Aksenov D.A., Fakhretdinova E.I., Asfandiyarov R.N., Raab A.G., Sharipov A.E., Shishkunova M.A., Sementeeva Yu.R. Changes in the structure, mechanical and corrosion properties of the Mg–Zn–Zr system alloy subjected to equal channel angular pressing. *Frontier Materials & Technologies*, 2024, no. 1, pp. 9–17. DOI: 10.18323/2782-4039-2024-1-67-1.

INTRODUCTION

Currently, magnesium alloys are considered as promising materials for the development and production of biodegradable implants, to use in traumatology and surgery [1–3]. The attention was paid to these alloys for a good reason: magnesium has an elastic modulus close to human bone; it is non-toxic and biocompatible with the human body [4]. However, for the full use of these materials, it is necessary to eliminate a number of their demerits, first, to increase the strength characteristics. Alloying is one of the ways to solve this problem. Magnesium itself has a low capacity for strain hardening, but alloying can increase the hardening effect during thermomechanical processing. In particular, widespread magnesium systems with zinc and zirconium can be selected. Due to solid solution strengthening in Mg–Zn systems, the strength increases, and additional alloying with zirconium allows increasing ductility [5–7]. For magnesium alloys, processes of multi-cycle rolling with decreasing temperature are widespread [8]. As a result of this processing, products with high strength are produced due to the formation of a lineage and partially recrystallised structure. One should, note that the high extent of the boundaries of deformed grains, and the high dislocation density in this case can negatively affect the corrosion resistance of magnesium alloys [9–11].

Researchers have also drawn attention to methods based on the principles of severe plastic deformation. It is shown in [12–14] that high-pressure torsion can lead to

more efficient refinement of the structure of magnesium materials compared to rolling, however, this deformation method is not scalable. Another approach is equal channel angular pressing (ECAP). As a rule, to achieve strength above 300 MPa, from 2 to 4 deformation treatment cycles are carried out [15–17]. In this case, the effect of sliding along the main base plane has been identified, which reduces the ECAP effectiveness, and in some cases even leads to softening of the material with an increase in the number of deformation cycles [18–20]. However, thermomechanical processing, including ECAP and carried out according to special technological modes, can achieve the required set of properties.

The purpose of this work is to determine the influence of the deformation mode during equal channel angular pressing (ECAP) on the features of the structural state formation, corrosion resistance and mechanical characteristics of the Mg–Zn–Zr system alloy.

METHODS

The magnesium Mg–8.6Zn–1.2Zr (wt. %) alloy was chosen as the research material. Chemical analysis was carried out on a Thermo Scientific ARL Optim'X X-ray fluorescence spectrometer. The material as-delivered is a strip 20 mm thick, from which samples with a diameter of 20 mm, and a length of 100 mm were cut along the rolling direction on an ARTA-120 spark-cutting mill.

The initial state was taken to be after prolonged annealing at 400 °C for 24 h. The mode was chosen based on literature data [21–23] and state diagrams of the Mg–Zn and Mg–Zr systems. Annealing was carried out in air in a Snol 8.2/1000 furnace with air cooling.

Deformation processing using the ECAP method was carried out in 2 regimes.

1. Initial temperature of equipment and blanks is 400 °C, channel intersection angle is 120°, and deformation rate is 1 mm /s, 1 cycle.

2. Processing according to mode 1, then 1 ECAP cycle according to *Bc* route (the blank was turned around 90° relative to the longitudinal axis), at an initial temperature of the equipment and blanks of 250 °C, the channel intersection angle of 90°, the deformation rate of 1 mm/s, in copper shell 1.5 mm thick.

Structural studies were performed using an Olympus GX51 light microscope and a JSM6490 scanning electron microscope.

Mechanical tests were carried out in accordance with GOST 1497-84. For tensile tests, proportional cylindrical samples with a working part diameter of 3 mm and an initial gauge length of 15 mm were used. Tests were performed on an Instron 5982 electromechanical static test system, at room temperature, at a rate of 1 mm/min.

Electrical conductivity was determined using a VE-27NTs eddy-current meter, converting the obtained values into IACS (International Annealed Copper Standard).

Electrochemical corrosion tests were carried out using an Elins R-5X potentiostat-galvanostat-impedancemeter in Ringer's solution with pH=7.4 in a three-electrode 80 ml cell with a silver chloride reference electrode and a platinum counter electrode. The tests were carried out at a temperature of 37 °C for 12 h, while during the first 2 h the electrode free corrosion potential was measured until a steady state was established on the surface of the sample. To obtain polarisation curves after establishing a steady state, a potential sweep was performed in the range from −300 to +300 mV relative to the steady-state value of the electrode potential with a scanning velocity of 0.25 mV/s. The current and corrosion potential were calculated from polarisation curves using Tafel sections [24].

RESULTS

In the initial heat-treated state, the Mg–8.6Zn–1.2Zr alloy sample has a coarse-grained state with a bimodal grain size distribution (Fig. 1). Large grains with an average transverse size of 30±10 μm and small recrystallised grains with an average transverse size of 4±2 μm are observed. The initial state can be additionally characterised by such a structure-sensitive parameter as electrical conductivity, which helps to assess indirectly, the change in the solid solution concentration in the alloy during further deformation processing. In the initial state, the electrical conductivity was 29±2 % IACS.

As a result of deformation processing carried out in regimes 1 and 2, it was identified that the structure bimodal appearance was preserved in the samples (Fig. 2). After 1 ECAP cycle, the deformation texture is clearly pronounced, coarse grains are turned in the direction of shear action in the ECAP focus, their average transverse size decreased to 20±4 μm, recrystallised grains have an average transverse size of 6±2 μm and are located mainly along the boundaries of large deformed grains. This indicates the implementation of processes of both grain transformation and dynamic recrystallisation. The second cycle in regime 2 does not make significant changes to the nature of the structure. Coarse deformed grains with an average transverse size of 18±4 μm and recrystallised grains with an average transverse size of 5±2 μm are observed.

After deformation in regime 1, the electrical conductivity remained at the level of 29±2 % IACS. After deformation in regime 2, it was 32±2 % IACS. This change is most likely explained by temperature conditions.

The results of mechanical tensile tests indicate an increase in the Mg–8.6Zn–1.2Zr alloy strength after ECAP (Fig. 3). After the 1st ECAP cycle, the tensile strength increased from 300±7 to 330±5 MPa; the 2nd cycle did not lead to an increase in strength.

The next important characteristic of the material for the production of implants is its corrosion resistance. From the analysis of the obtained results of corrosion tests presented in the form of polarisation curves, the values of the corrosion current (i_{corr}) and free corrosion potential (E_{corr}) were obtained (Table 1). Fig. 4 shows that Tafel regions are observed on the cathode branches of the samples. As a result of ECAP treatment in regimes 1 and 2, the surfaces of the samples are passivated, as evidenced by the lower value of the free corrosion potential E_{corr}. Based on the results presented in Table 1, the initial sample with the minimum corrosion current i_{corr} has the best corrosion properties. The displacement of the cathodic branches indicates a change in the surface area available for the cathodic reaction.

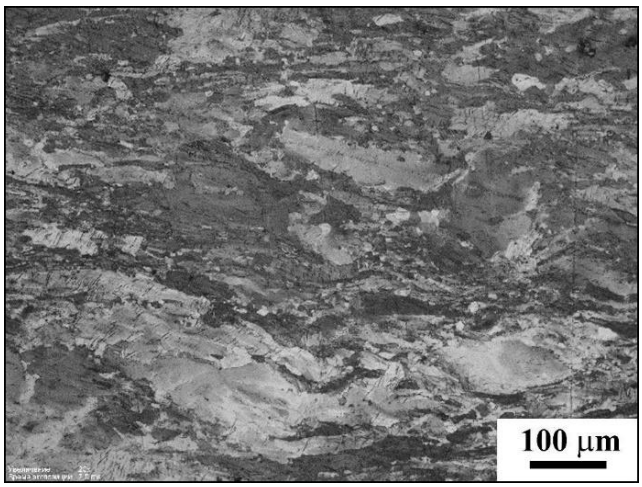

Fig. 1. *The structure of the Mg–Zn–Zr system alloy after annealing at 400 °C for 24 h. Light microscopy*
Рис. 1. *Структура сплава системы Mg–Zn–Zr после отжига при 400 °С в течение 24 ч. Световая микроскопия*

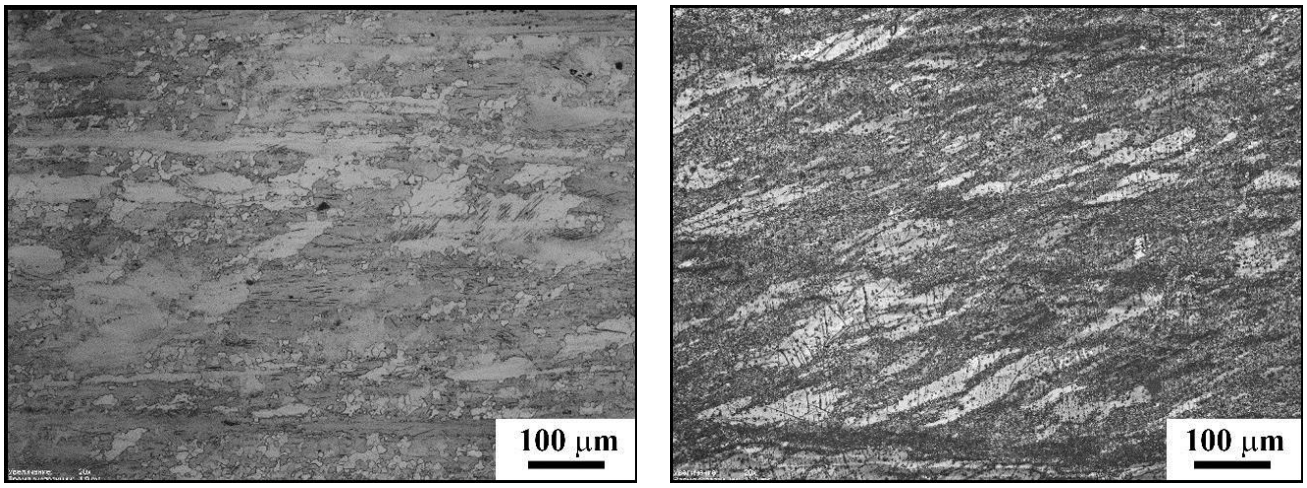

a ***b***

Fig. 2. *The structure of the Mg–Zn–Zr system alloy after ECAP according to regimes 1 (**a**) and 2 (**b**)*
Рис. 2. *Структура сплава системы Mg–Zn–Zr после РКУП по режиму 1 (**а**) и 2 (**b**)*

DISCUSSION

The strength properties, and corrosion resistance of a magnesium alloy are closely related to its structural state. Structure refinement can have a dual effect on the corrosion resistance of magnesium alloys. With the Mg–Al system, grinding will lead to an increase in corrosion resistance [25], while for a Mg–Zn–Zr system alloy, the nature of the corrosion behaviour may be different, due to the type and distribution of the second phase dispersed particles along the grain boundaries, and therefore an increase in the corrosion rate is possible [26]. The results of measuring electrical conductivity can indirectly prove the change in the solid solution concentration and the process of precipitation of the second phase particles. It is known that at temperatures above 300 °C, the solubility of both Zn and Zr increases. Thus, ECAP at 250 °C leads to the decomposition of the solid solution of alloying elements. It was found that in regime 1, when the temperature was 400 °C, the electrical conductivity corresponded to the value of the annealed state of 29 % IACS. Regime 2 at a temperature of 250 °C leads to an increase in the material electrical conductivity up to 32 % IACS. Thus, lowering the deformation processing temperature to 250 °C will lead to deformation-stimulated decomposition of the solid solution.

Electrochemical tests for corrosion resistance indicate that the magnesium alloy sample in the annealed state is of greatest importance, which is caused by the equilibrium state of the grain boundaries [27]. A decrease in the average transverse size of coarse and recrystallised grains, texturing, and the possible increase in the number of crystal lattice defects, as well as a change in the solid solution state, lead to an increase in corrosion currents. Moreover, after high-temperature deformation processing in regime 1,

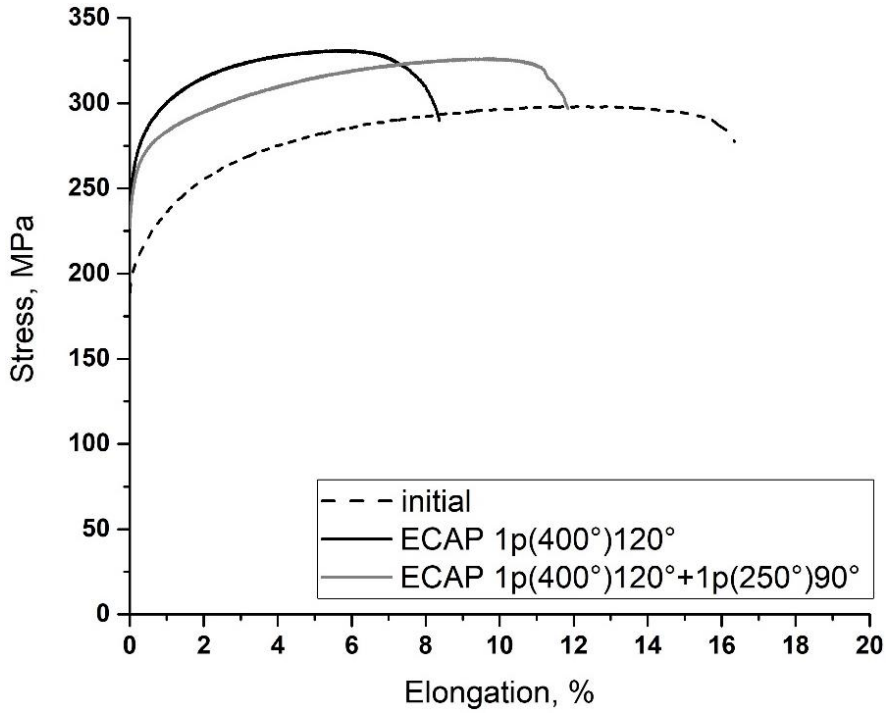

Fig. 3. *Curves of mechanical tests of the Mg–Zn–Zr system alloy after annealing at 400 °C, ECAP according to regimes 1 and 2*
Рис. 3. *Кривые механических испытаний сплава системы Mg–Zn–Zr после отжига при 400 °C, РКУП по режимам 1 и 2*

Table 1. *Values of corrosion current and free corrosion potential*
Таблица 1. *Значения тока коррозии и потенциала свободной коррозии*

State	I_{corr}, μA /cm^2	E_{corr}, V
Initial state (400 °C, 24 h)	24.05±5.46	−1.428±0.013
ECAP, regime 1	32.06±16.20	−1.382±0.030
ECAP, regime 2	57.00±6.22	−1.391±0.085

the increase is ~25 %, and after the 2nd cycle of deformation at a lower temperature (250 °C) in accordance with regime 2, the corrosion current increases by more than 2 times relative to the initial state.One should note that on the Mg–8.6Zn–1.2Zr alloy, it was possible to achieve high values of ultimate strength and offset yield strength within just one ECAP cycle. Table 2 presents a comparison of the achieved strength characteristics with the results of other studies on the alloys of similar chemical composition.

CONCLUSIONS

It was identified that during ECAP deformation processing of the Mg–8.6Zn–1.2Zr alloy, temperature plays a significant role. Thus, at 400 °C, the main mechanism of structure formation during deformation is dynamic recrystallisation, while the solid solution state is maintained.

Deformation processing of the Mg–8.6Zn–1.2Zr alloy by ECAP, 1 cycle, channel intersection angle 120°, 400 °C (mode 1), leads to the formation of a structure with recrystallised grains with an average transverse size of 6±2 μm, and larger deformed grains directed along the shear direction, with an average transverse size of 20±4 μm. Such structural state provides an increase in tensile strength relative to the initial one annealed by ~10 %, up to 330 MPa.

Electrical conductivity measurements, indirectly indicate that lowering the temperature of ECAP deformation processing to 250 °C leads to deformation-induced decomposition of the supersaturated solid solution. The electrical conductivity after deformation in regime 1 was 29±2 % IACS, while the final electrical conductivity after deformation of the Mg–8.6Zn–1.2Zr alloy in regime 2 differs from the initial state by 3 % and amounts to 32±2 % IACS.

Table 2. *Mechanical characteristics of the Mg–Zn–Zr system alloy after ECAP*
Таблица 2. *Механические характеристики сплава системы Mg–Zn–Zr после РКУП*

Work	Mode	UTS, MPa	YTS, MPa	Percentage elongation, %
Current work	ECAP, regime 1	330	267	8
	ECAP, regime 2	325	245	12
[16]	4 ECAP cycles, *Bc* route, 220 °C, channel intersection angle 90°	290	231	27
[28]	2 ECAP cycles, *Bc* route, channel intersection angle 90°	341	264	23
	4 ECAP cycles, *Bc* route, 220 °C, channel intersection angle 90°	334	277	21
[29]	2 ECAP cycles, 250 °C, channel intersection angle 90°	326	175	25

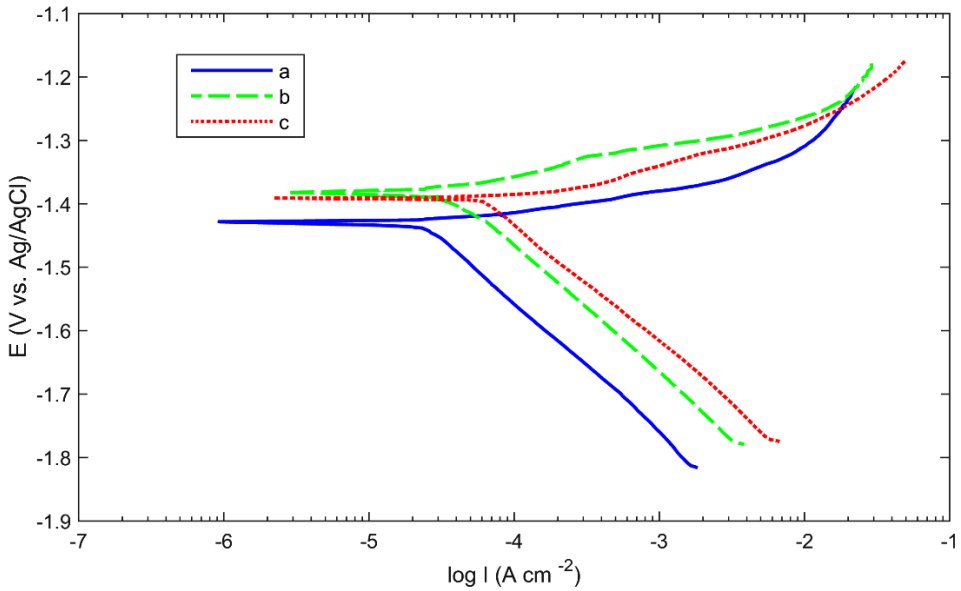

Fig. 4. *Polarisation curves: a – initial state; b – regime 1; c – regime 2*
Рис. 4. *Поляризационные кривые: a – исходное состояние; b – режим 1; c – режим 2*

The results of electrochemical corrosion tests indicate that the magnesium alloy sample in the initial annealed state, has the greatest resistance to corrosion. 1 ECAP cycle at 400 °C leads to an increase in the corrosion current by 25 % (32.06±16.20 μA/cm^2), while subsequent deformation at 250 °C leads to an increase in the corrosion current by more than 2 times (57.00± ±6.22 μA/cm^2).

REFERENCES

1. Li N., Zheng Y. Novel Magnesium Alloys Developed for Biomedical Application: A Review. *Journal of Materials Science and Technology*, 2013, vol. 29, no. 6, pp. 489–502. DOI: 10.1016/j.jmst.2013.02.005.
2. Chen Y., Xu Z., Smith C., Sankar J. Recent advances on the development of magnesium alloys for biodegradable implants. *Acta Biomaterialia*, 2014, vol. 10, no. 11, pp. 4561–4573. DOI: 10.1016/j.actbio.2014.07.005.
3. Gu X.-N., Zheng Y.-F. A review on magnesium alloys as biodegradable materials. *Frontiers of Materials Science in China*, 2010, vol. 4, pp. 111–115. DOI: 10.1007/s11706-010-0024-1.
4. Saris N.-E.L., Mervaala E., Karppanen H., Khawaja J.A., Lewenstam A. Magnesium: An update on physiological,

clinical and analytical aspects. *Clinica Chimica Acta*, 2000, vol. 294, no. 1-2, pp. 1–26. DOI: 10.1016/S0009-8981(99)00258-2.
5. Yin D., Zhang E., Zeng S. Effect of Zn on mechanical property and corrosion property of extruded Mg-Zn-Mn alloy. *Transactions of Nonferrous Metals Society of China*, 2008, vol. 18, no. 4, pp. 763–768. DOI: 10.1016/S1003-6326(08)60131-4.
6. Cai S., Lei T., Li N., Feng F. Effects of Zn on microstructure, mechanical properties and corrosion behavior of Mg–Zn alloys. *Materials Science and Engineering: C*, 2012, vol. 32, no. 8, pp. 2570–2577. DOI: 10.1016/j.msec.2012.07.042.
7. Zhao T., Hu Y., Pan F., He B., Guan M., Yuan Y., Tang A. Effect of Zn Content on the Microstructure and Mechanical Properties of Mg–Al–Sn–Mn Alloys. *Materials*, 2019, vol. 12, no. 19, article number 3102. DOI: 10.3390/ma12193102.
8. Bohlen J., Kurz G., Yi S., Letzig D. Rolling of magnesium alloys. *Advances in Wrought Magnesium Alloys*. Sawston, Woodhead Publishing Limited, 2012, pp. 346–375.
9. Xin R., Li B., Li L., Liu Q. Influence of texture on corrosion rate of AZ31 Mg alloy in 3.5wt.% NaCl. *Materials & Design*, 2011, vol. 32, no. 8-9, pp. 4548–4552.
10. Zheng F., Chen H., Zhang Y., Wang W., Nie H. Microstructure evolution and corrosion resistance of AZ31 magnesium alloy tube by stagger spinning. *International Journal of Minerals, Metallurgy and Materials*, 2022, vol. 29, pp. 1361–1372. DOI: 10.1007/s12613-021-2396-x.
11. Sun J., Zhao W., Yan P., Chen K., Jiao L., Qiu T., Wang X. Effect of Corrosive Medium and Surface Defect-Energy on Corrosion Behavior of Rolled ZK61M Alloy. *Materials*, 2022, vol. 15, no. 12, article number 4091. DOI: 10.3390/ma15124091.
12. Li W., Liu X., Zheng Y. et al. In vitro and in vivo studies on ultrafine-grained biodegradable pure Mg, Mg-Ca alloy and Mg-Sr alloy processed by high-pressure torsion. *Biomaterials Science*, 2020, no. 18, pp. 5071–5078. DOI: 10.1039/D0BM00805B.
13. Medeiros M.P., Carvalho A.P., Isaac A., Afonso C.R.M., Janeček M., Minárik P., Celis M.M., Figueiredo R.B. Using high pressure torsion to process magnesium alloys for biological applications. *Journal of Materials Research and Technology*, 2023, vol. 22, pp. 3075–3084. DOI: 10.1016/j.jmrt.2022.12.127.
14. Yan Z., Zhu J., Zhang Z., Wang Q., Xue Y. The microstructural, textural, and mechanical effects of high-pressure torsion processing on Mg alloys: A review. *Frontiers in Materials*, 2022, vol. 9, article number 964992. DOI: 10.3389/fmats.2022.964992.
15. Merson D., Brilevsky A., Myagkikh P., Tarkova A., Prokhorikhin A., Kretov E., Frolova T., Vinogradov A. The Functional Properties of Mg–Zn–X Biodegradable Magnesium Alloys. *Materials*, 2020, vol. 13, no. 3, article number 544. DOI: 10.3390/ma13030544.
16. Yin D.L., Cui H.L., Qiao J., Zhang J.F. Enhancement of mechanical properties in a Mg–Zn–Zr alloy by equal channel angular pressing at warm temperature. *Materials Research Innovations*, 2015, vol. 19, no. 9, pp. 9–28. DOI: 10.1179/1432891715Z.0000000001912.
17. Vinogradov A., Vasilev E., Kopylov V.I., Linderov M., Brilevesky A., Merson D. High Performance Fine-Grained Biodegradable Mg-Zn-Ca Alloys Processed by Severe Plastic Deformation. *Metals*, 2019, vol. 9, no. 2, article number 186. DOI: 10.3390/met9020186.
18. Jahadi R., Sedighi M., Jahed H. ECAP effect on the micro-structure and mechanical properties of AM30 magnesium alloy. *Materials Science and Engineering: A*, 2014, vol. 593, pp. 178–184. DOI: 10.1016/j.msea.2013.11.042.
19. Straumal B., Martynenko N., Temralieva D. et al. The Effect of Equal-Channel Angular Pressing on Microstructure, Mechanical Properties, and Biodegradation Behavior of Magnesium Alloyed with Silver and Gadolinium. *Crystals*, 2020, vol. 10, no. 10, article number 918. DOI: 10.3390/cryst10100918.
20. Gopi K.R., Shivananda Nayaka H. Microstructure and mechanical properties of magnesium alloy processed by equal channel angular pressing (ECAP). *Materials Today: Proceedings*, 2017, vol. 4, no. 9, pp. 10288–10292. DOI: 10.1016/j.matpr.2017.06.366.
21. Chen M., Ma C., Liu Q., Cheng M., Wang H., Hu X. Plastic Deformation Mechanism of High Strength and Toughness ZK61 Magnesium Alloy Plate by Multipass Horizontal Continuous Rolling. *Materials*, 2023, vol. 16, no. 3, article number 1320. DOI: 10.3390/ma16031320.
22. Alawad M.O., Alateyah A.I., El-Garaihy W.H., BaQais A., Elkatatny S., Kouta H., Kamel M., El-Sanabary S. Optimizing the ECAP Parameters of Biodegradable Mg–Zn–Zr Alloy Based on Experimental, Mathematical Empirical, and Response Surface Methodology. *Materials*, 2022, vol. 15, no. 21, article number 7719. DOI: 10.3390/ma15217719.
23. Choi H.Y., Kim W.J. Effect of thermal treatment on the bio-corrosion and mechanical properties of ultrafine-grained ZK60 magnesium alloy. *Journal of the Mechanical Behavior of Biomedical Materials*, 2015, vol. 51, pp. 291–301. DOI: 10.1016/j.jmbbm.2015.07.019.
24. Scully J.R. Polarization resistance method for determination of instantaneous corrosion rates. *Corrosion*, 2000, vol. 56, no. 2, pp. 199–218. DOI: 10.5006/1.3280536.
25. Aung N.N., Zhou W. Effect of grain size and twins on corrosion behaviour of AZ31B magnesium alloy. *Corrosion Science*, 2010, vol. 52, no. 2, pp. 589–594. DOI: 10.1016/j.corsci.2009.10.018.
26. Zeng R., Kainer K.U., Blawert C., Dietzel W. Corrosion of an extruded magnesium alloy ZK60 component–The role of microstructural features. *Journal of Alloys and Compounds*, 2011, vol. 509, no. 13, pp. 4462–4469. DOI: 10.1016/j.jallcom.2011.01.116.
27. Shang B., Lei L., Wang X., He P., Yuan X., Dai W., Li J., Jiang Y., Sun Y. Effects of grain boundary characteristics changing with cold rolling deformation on intergranular corrosion resistance of 443 ultra-pure ferritic stainless steel. *Corrosion Communications*,

2022, vol. 8, pp. 27–39. DOI: 10.1016/j.corcom.2022.07.002.
28. Yan J., Qin Z., Yan K. Mechanical properties and microstructure evolution of Mg-6 wt%Zn alloy during equal-channel angular pressing. *Metals*, 2018, vol. 8, no. 10, article number 841. DOI: 10.3390/met8100841.
29. Dumitru F.-D., Higuera-Cobos O.F., Cabrera J.M. ZK60 alloy processed by ECAP: Microstructural, physical and mechanical characterization. *Materials Science and Engineering: A*, 2014, vol. 594, pp. 32–39. DOI: 10.1016/j.msea.2013.11.050.

СПИСОК ЛИТЕРАТУРЫ

1. Li N., Zheng Y. Novel Magnesium Alloys Developed for Biomedical Application: A Review // Journal of Materials Science and Technology. 2013. Vol. 29. № 6. P. 489–502. DOI: 10.1016/j.jmst.2013.02.005.
2. Chen Y., Xu Z., Smith C., Sankar J. Recent advances on the development of magnesium alloys for biodegradable implants // Acta Biomaterialia. 2014. Vol. 10. № 11. P. 4561–4573. DOI: 10.1016/j.actbio.2014.07.005.
3. Gu X.-N., Zheng Y.-F. A review on magnesium alloys as biodegradable materials // Frontiers of Materials Science in China. 2010. Vol. 4. P. 111–115. DOI: 10.1007/s11706-010-0024-1.
4. Saris N.-E.L., Mervaala E., Karppanen H., Khawaja J.A., Lewenstam A. Magnesium: An update on physiological, clinical and analytical aspects // Clinica Chimica Acta. 2000. Vol. 294. № 1-2. P. 1–26. DOI: 10.1016/S0009-8981(99)00258-2.
5. Yin D., Zhang E., Zeng S. Effect of Zn on mechanical property and corrosion property of extruded Mg-Zn-Mn alloy // Transactions of Nonferrous Metals Society of China. 2008. Vol. 18. № 4. P. 763–768. DOI: 10.1016/S1003-6326(08)60131-4.
6. Cai S., Lei T., Li N., Feng F. Effects of Zn on microstructure, mechanical properties and corrosion behavior of Mg–Zn alloys // Materials Science and Engineering: C. 2012. Vol. 32. № 8. P. 2570–2577. DOI: 10.1016/j.msec.2012.07.042.
7. Zhao T., Hu Y., Pan F., He B., Guan M., Yuan Y., Tang A. Effect of Zn Content on the Microstructure and Mechanical Properties of Mg–Al–Sn–Mn Alloys // Materials. 2019. Vol. 12. № 19. Article number 3102. DOI: 10.3390/ma12193102.
8. Bohlen J., Kurz G., Yi S., Letzig D. Rolling of magnesium alloys // Advances in Wrought Magnesium Alloys. Sawston: Woodhead Publishing Limited, 2012. P. 346–375.
9. Xin R., Li B., Li L., Liu Q. Influence of texture on corrosion rate of AZ31 Mg alloy in 3.5wt.% NaCl // Materials & Design. 2011. Vol. 32. № 8-9. P. 4548–4552.
10. Zheng F., Chen H., Zhang Y., Wang W., Nie H. Microstructure evolution and corrosion resistance of AZ31 magnesium alloy tube by stagger spinning // International Journal of Minerals, Metallurgy and Materials. 2022. Vol. 29. P. 1361–1372. DOI: 10.1007/s12613-021-2396-x.
11. Sun J., Zhao W., Yan P., Chen K., Jiao L., Qiu T., Wang X. Effect of Corrosive Medium and Surface Defect-Energy on Corrosion Behavior of Rolled ZK61M Alloy // Materials. 2022. Vol. 15. № 12. Article number 4091. DOI: 10.3390/ma15124091.
12. Li W., Liu X., Zheng Y. et al. In vitro and in vivo studies on ultrafine-grained biodegradable pure Mg, Mg-Ca alloy and Mg-Sr alloy processed by high-pressure torsion // Biomaterials Science. 2020. № 18. P. 5071–5078. DOI: 10.1039/D0BM00805B.
13. Medeiros M.P., Carvalho A.P., Isaac A., Afonso C.R.M., Janeček M., Minárik P., Celis M.M., Figueiredo R.B. Using high pressure torsion to process magnesium alloys for biological applications // Journal of Materials Research and Technology. 2023. Vol. 22. P. 3075–3084. DOI: 10.1016/j.jmrt.2022.12.127.
14. Yan Z., Zhu J., Zhang Z., Wang Q., Xue Y. The microstructural, textural, and mechanical effects of high-pressure torsion processing on Mg alloys: A review // Frontiers in Materials. 2022. Vol. 9. Article number 964992. DOI: 10.3389/fmats.2022.964992.
15. Merson D., Brilevsky A., Myagkikh P., Tarkova A., Prokhorikhin A., Kretov E., Frolova T., Vinogradov A. The Functional Properties of Mg–Zn–X Biodegradable Magnesium Alloys // Materials. 2020. Vol. 13. № 3. Article number 544. DOI: 10.3390/ma13030544.
16. Yin D.L., Cui H.L., Qiao J., Zhang J.F. Enhancement of mechanical properties in a Mg–Zn–Zr alloy by equal channel angular pressing at warm temperature // Materials Research Innovations. 2015. Vol. 19. № 9. P. 9–28. DOI: 10.1179/1432891715Z.0000000001912.
17. Vinogradov A., Vasilev E., Kopylov V.I., Linderov M., Brilevesky A., Merson D. High Performance Fine-Grained Biodegradable Mg-Zn-Ca Alloys Processed by Severe Plastic Deformation // Metals. 2019. Vol. 9. № 2. Article number 186. DOI: 10.3390/met9020186.
18. Jahadi R., Sedighi M., Jahed H. ECAP effect on the micro-structure and mechanical properties of AM30 magnesium alloy // Materials Science and Engineering: A. 2014. Vol. 593. P. 178–184. DOI: 10.1016/j.msea.2013.11.042.
19. Straumal B., Martynenko N., Temralieva D. et al. The Effect of Equal-Channel Angular Pressing on Microstructure, Mechanical Properties, and Biodegradation Behavior of Magnesium Alloyed with Silver and Gadolinium // Crystals. 2020. Vol. 10. № 10. Article number 918. DOI: 10.3390/cryst10100918.
20. Gopi K.R., Shivananda Nayaka H. Microstructure and mechanical properties of magnesium alloy processed by equal channel angular pressing (ECAP) // Materials Today: Proceedings. 2017. Vol. 4. № 9. P. 10288–10292. DOI: 10.1016/j.matpr.2017.06.366.
21. Chen M., Ma C., Liu Q., Cheng M., Wang H., Hu X. Plastic Deformation Mechanism of High Strength and Toughness ZK61 Magnesium Alloy Plate by Multipass Horizontal Continuous Rolling // Materials. 2023. Vol. 16. № 3. Article number 1320. DOI: 10.3390/ma16031320.
22. Alawad M.O., Alateyah A.I., El-Garaihy W.H., BaQais A., Elkatatny S., Kouta H., Kamel M., El-Sanabary S.

Optimizing the ECAP Parameters of Biodegradable Mg–Zn–Zr Alloy Based on Experimental, Mathematical Empirical, and Response Surface Methodology // Materials. 2022. Vol. 15. № 21. Article number 7719. DOI: 10.3390/ma15217719.
23. Choi H.Y., Kim W.J. Effect of thermal treatment on the bio-corrosion and mechanical properties of ultrafine-grained ZK60 magnesium alloy // Journal of the Mechanical Behavior of Biomedical Materials. 2015. Vol. 51. P. 291–301. DOI: 10.1016/j.jmbbm.2015.07.019.
24. Scully J.R. Polarization resistance method for determination of instantaneous corrosion rates // Corrosion. 2000. Vol. 56. № 2. P. 199–218. DOI: 10.5006/1.3280536.
25. Aung N.N., Zhou W. Effect of grain size and twins on corrosion behaviour of AZ31B magnesium alloy // Corrosion Science. 2010. Vol. 52. № 2. P. 589–594. DOI: 10.1016/j.corsci.2009.10.018.
26. Zeng R., Kainer K.U., Blawert C., Dietzel W. Corrosion of an extruded magnesium alloy ZK60 component – the role of microstructural features // Journal of Alloys and Compounds. 2011. Vol. 509. № 13. P. 4462–4469. DOI: 10.1016/j.jallcom.2011.01.116.
27. Shang B., Lei L., Wang X., He P., Yuan X., Dai W., Li J., Jiang Y., Sun Y. Effects of grain boundary characteristics changing with cold rolling deformation on intergranular corrosion resistance of 443 ultra-pure ferritic stainless steel // Corrosion Communications. 2022. Vol. 8. P. 27–39. DOI: 10.1016/j.corcom.2022.07.002.
28. Yan J., Qin Z., Yan K. Mechanical properties and microstructure evolution of Mg-6 wt%Zn alloy during equal-channel angular pressing // Metals. 2018. Vol. 8. № 10. Article number 841. DOI: 10.3390/met8100841.
29. Dumitru F.-D., Higuera-Cobos O.F., Cabrera J.M. ZK60 alloy processed by ECAP: Microstructural, physical and mechanical characterization // Materials Science and Engineering: A. 2014. Vol. 594. P. 32–39. DOI: 10.1016/j.msea.2013.11.050.

Изменение структуры, механических и коррозионных свойств сплава системы Mg–Zn–Zr, подвергнутого равноканальному угловому прессованию

Аксенов Денис Алексеевич*[1,2,3], младший научный сотрудник
Фахретдинова Эльвира Илдаровна[1,2], кандидат технических наук, научный сотрудник
Асфандияров Рашид Наилевич[1,2,4], кандидат технических наук, научный сотрудник
Рааб Арсений Георгиевич[2,5], кандидат технических наук, научный сотрудник
Шарипов Арсений Елисеевич[2], магистрант
Шишкунова Мария Андреевна[2], аспирант
Сементеева Юлия Рамилевна[2], магистрант

[1]*Институт физики молекул и кристаллов Уфимского федерального исследовательского центра РАН, Уфа (Россия)*
[2]*Уфимский университет науки и технологий, Уфа (Россия)*

***E-mail: aksyonovda@mail.ru**

[3]ORCID: https://orcid.org/0000-0002-2652-2646
[4]ORCID: https://orcid.org/0000-0002-5522-4314
[5]ORCID: https://orcid.org/0000-0003-1993-413X

Поступила в редакцию 05.06.2023 *Принята к публикации 25.08.2023*

Аннотация: Магниевые сплавы считаются перспективными материалами для изготовления биорезорбируемых имплантатов. Их основные недостатки – низкая прочность и коррозионная стойкость в биологических средах. В работе изучалось влияние интенсивной пластической деформации методом равноканального углового прессования (РКУП) на структуру, механические свойства и коррозионную стойкость магниевого сплава Mg–8,6Zn–1,2Zr. Установлено, что 1 цикл РКУП при 400 °C ведет к заметному упрочнению сплава Mg–8,6Zn–1,2Zr на ~10 %, до 330 МПа. Структурные исследования показали, что в трансформации структуры существенную роль играет динамическая рекристаллизация. РКУП ведет к формированию структуры бимодального вида с крупными деформированными зернами со средним поперечным размером 20±4 мкм и рекристаллизованными зернами со средним поперечным размером 6±2 мкм. Установлено, что с понижением температуры деформации до 250 °C происходит процесс деформационно-индуцированного распада пересыщенного твердого раствора. Электропроводность образца после РКУП при 400 °C составляла 29±2 % согласно International Annealed Copper Standard (IACS), в то время как 2 цикла РКУП при 250 °C ведут к повышению электропроводности до 32±2 % IACS. Методом электрохимической коррозии установлено, что 1 цикл РКУП при 400 °C приводит к незначительному снижению коррозионной стойкости исследуемого сплава по сравнению с исходным состоянием. Показано, что ток коррозии увеличивается с 24 до 32 мкА/см^2, в то время как последующий цикл РКУП при 250 °C увеличивает ток коррозии более чем в 2 раза (до 57 мкА/см^2).

Ключевые слова: сплавы системы Mg–Zn–Zr; Mg–8,6Zn–1,2Zr; магниевые сплавы; высокая прочность магниевых сплавов; РКУП; коррозионная стойкость; электропроводность; динамическая рекристаллизация при РКУП.

Благодарности: Работа выполнена при поддержке Российского научного фонда (грант № 22-79-10325, https://www.rscf.ru/project/22-79-10325/).

Статья подготовлена по материалам докладов участников XI Международной школы «Физическое материаловедение» (ШФМ-2023), Тольятти, 11–15 сентября 2023 года.

Для цитирования: Аксенов Д.А., Фахретдинова Э.И., Асфандияров Р.Н., Рааб А.Г., Шарипов А.Е., Шишкунова М.А., Сементеева Ю.Р. Изменение структуры, механических и коррозионных свойств сплава системы Mg–Zn–Zr, подвергнутого равноканальному угловому прессованию // Frontier Materials & Technologies. 2024. № 1. С. 9–17. DOI: 10.18323/2782-4039-2024-1-67-1.

doi: 10.18323/2782-4039-2024-1-67-2

Low-temperature superplastic deformation of the EK79 nickel-based superalloy with the mixed ultrafine-grained microstructure

Elvina V. Galieva*[1], PhD (Engineering), researcher
Ekaterina Yu. Klassman[2], postgraduate student, engineer
Vener A. Valitov[3], Doctor of Sciences (Engineering), leading researcher
Institute for Metals Superplasticity Problems of RAS, Ufa (Russia)

***E-mail: galieva_elvina_v@mail.ru**

[1]ORCID: https://orcid.org/0000-0002-1074-6274
[2]ORCID: https://orcid.org/0000-0003-1984-5137
[3]ORCID: https://orcid.org/0000-0002-1349-6047

Received 22.09.2023 *Accepted 03.11.2023*

Abstract: One of the most effective ways to increase the processing plasticity of advanced superalloys (heat-resistant nickel-based alloys) is the formation of an ultrafine-grained (UFG) microstructure in bulk semi-finished products. Such a microstructure is a necessary condition for the manifestation of the structural superplasticity effect in the technological processes of manufacturing products from such superalloys. One of the most promising methods for producing UFG microstructures is thermomechanical treatment (TMT) according to the multiple isothermal forging scheme. It has been shown that the EK79 superalloy after TMT, with a gradual decrease in the processing temperature from 0.88 to 0.62 Ts (where Ts is the strengthening phase dissolution temperature) leads to the transformation of the initial microduplex fine-grained microstructure into a mixed UFG microstructure. Such a mixed UFG microstructure consists of: 1) relatively coarse (inherited from the fine-grain microstructure) particles – γ'-phase with a size of 3.0±0.8 μm; 2) γ-grains, and incoherent γ'-phase particles with a size of 0.3–0.5 μm; 3) strengthening coherent intragranular γ'-phase particles with a size of 0.05–0.1 μm, released upon cooling from the TMT temperature to room temperature. During uniaxial compression tests, the EK79 superalloy with such microstructure, demonstrates low-temperature superplasticity in the temperature range of 800–1000 °C. It has been found that an increase in the deformation temperature up to 1000 °C, leads to the increase of γ-phase grains to micron size. The maintenance of superplastic properties in the presence of relatively coarse incoherent particles in the microstructure of the second phase (γ'-phase) is apparently related to the fact that the deformation is localised in the UFG component.

Keywords: heat-resistant nickel-based superalloy; EK79; strengthening phase; microduplex microstructure; ultrafine-grained microstructure; low-temperature superplasticity; thermomechanical treatment; uniaxial compression.

Acknowledgements: The work was financially supported by the Russian Science Foundation grant No. 22-79-00271, https://www.rscf.ru/project/22-79-00271/.

Electron microscopic study and mechanical tests were carried out on the base of Collaborative Access Center "Structural and Physical-Mechanical Study of Materials" of IMSP of RAS.

For citation: Galieva E.V., Klassman E.Yu., Valitov V.A. Low-temperature superplastic deformation of the EK79 nickel-based superalloy with the mixed ultrafine-grained microstructure. *Frontier Materials & Technologies*, 2024, no. 1, pp. 19–27. DOI: 10.18323/2782-4039-2024-1-67-2.

INTRODUCTION

Nickel-based superalloys are used for production of gas turbines in the aerospace and energy generating industries, due to their good mechanical properties, such as high temperature strength, creep resistance and fatigue life capability, and corrosion resistance [1–3]. Such characteristics of mechanical properties are achieved through complex alloying of modern superalloys, having a complex chemical composition, including more than 10 alloying elements [1; 3; 4]. In these alloys, the required values of performance (service) characteristics are achieved both due to effective solid-solution strengthening, with refractory alloying elements, and due to the release of a plastic matrix γ-phase of coherent particles inside the grains, for example, a strengthening γ'-phase based on the $Ni_3(Al,Ti)$ intermetallide [1; 5; 6].

The desire of the developers of superalloys to achieve maximum heat-resistant characteristics by complicating, the chemical composition and increasing the volume fraction of the strengthening γ'-phase, led to a sharp decrease in their technological plasticity, and an increase in the complexity of their deformation processing [5–7]. For example, complex alloyed superalloys such as EK79 and EP975, the volume fraction of the strengthening γ'-phase of which reaches 40 and 55 %, respectively, have low technological plasticity. This is due to the fact that in these alloys, the strengthening γ'-phase is released from the supersaturated solid solution of the matrix (γ-phase) almost instantly, in the form of nanosized coherent particles of spherical or cuboid shape [5; 7]. The release of such particles occurs both during thermal and thermomechanical treatment. In the latter case, nanosized γ'-phase particles are released primarily in the near-surface layers of a hot blank, the outer surface of which is intensively cooled during its transfer from a high-temperature furnace to a press die and then during subsequent deformation. This leads to a sharp decrease in technological plasticity, and as a consequence,

to the formation of a network of small cracks on the side surface of a deformable superalloy blank. During further hot stamping, this can lead to the growth of microcracks, up to the destruction of the deformed blank.

Superalloys such as Inconel 718, and its Russian analogue EK61 (KhN58MBYuD), in which strengthening is achieved through the release of nanosized γ"-phase (Ni_3Nb) particles, are more technologically advanced [8]. Expansion of technological capabilities when processing hard-to-deform superalloys (heat-resistant nickel alloys) is possible due to the superplasticity (SP) effect, and can be achieved as a result of the formation of an ultrafine-grained (UFG) or nanocrystalline (NC) microstructure in these materials [9–11]. The methodological approach patented in [9] consisting in carrying out thermomechanical treatment (TMT), with a step-by-step decrease in temperature, allows ensuring a step-by-step transformation of the initial coarse-grained microstructure into a fine-grained microduplex microstructure. With a subsequent decrease in the processing temperature, the microstructure is refined to the UFG state and further up to the nano-crystalline state. This methodological approach turned out to be very effective when processing other alloys, based on aluminium, magnesium, titanium, and even intermetallic compounds based on the latter [10]. It should also be noted that in the paper [10], the principles of the method of multi-axial isothermal forging (MIF) are formulated, which makes it possible to obtain homogeneous bulk nanostructured semi-finished products of metals and alloys, including heat-resistant and intermetallic ones.

One of the most promising methods for microstructure refinement in superalloy is thermomechanical treatment [11–13], during which the use of a scheme (MIF) is effective [10; 14]. Thus, in the previous work [15], using the example of the EP975 superalloy with the same type of strengthening phase, it was shown that TMT with a gradual decrease in the processing temperature, leads to the production of a mixed UFG microstructure, and during uniaxial tensile tests, an superalloy with such a microstructure demonstrates maximum superplasticity characteristics (δ=1320 %; m=0.5) achieved at a temperature of 1000 °C and a strain rate of $\dot{\varepsilon}=10^{-3}$ s^{-1}.

To evaluate the characteristics of superplastic properties, the method of isothermal deformation, according to the uniaxial tension scheme is traditionally used [16–18]. In the case of using superplastic deformation in traditional technological processes (stamping, forging), which are carried out mainly according to the scheme of uniaxial compression, when producing a complex-profile part, a complex stress-strain state will arise in it, characterised by the action of both tensile and compressive stresses [15; 19; 20]. In particular, during traditional stamping of a part, compressive stresses will predominantly act in its central zone, and tensile stresses will act on the periphery in the tangential direction [21; 22]. Therefore, when using the effect of superplasticity in practice in the technological process of manufacturing parts from a specific hard-to-deform superalloy, it is important both to determine the optimal modes for producing UFG microstructure semi-finished products from the selected material and to identify the features of microstructural changes during subsequent deformation according to the uniaxial compression scheme.

The purpose of this work is to study the influence of thermomechanical treatment on the formation of a mixed ultrafine-grained microstructure in the EK79 superalloy, as well as to evaluate the mechanical properties of such a microstructure, when tested according to a uniaxial compression scheme.

METHODS

The studies were carried out on the EK79 heat-resistant nickel superalloy. In this superalloy, strengthening is achieved due to the precipitation of intragranular coherent particles of the γ'-phase, based on the $Ni_3(Al,Ti)$ intermetallic compound. The chemical composition of the studied EK79 superalloy is presented in Table 1, and corresponds to GOST 5632-2014. For the EK79 superalloy, the well-known Utimet 520 superalloy is the closest in chemical composition.

The original material was a deformed blank with a diameter of 400 mm and a thickness of 40 mm, with a homogeneous fine-grained microduplex microstructure, from which samples measuring 40×50×70 mm^3 were cut. To obtain the UFG microstructure, TMT of the samples was carried out using the MIF scheme developed by the Institute for Metals Superplasticity Problems of the Russian Academy of Sciences [15]. TMT was carried out on a hydraulic press equipped with an isothermal stamping block, with a force of 6.3 MN, in the temperature range of (0.88–0.62) Tγ' (Tγ' is the γ'-phase dissolution temperature). The strain rate was $\dot{\varepsilon}=10^{-2}$–$10^{-3}$ s^{-1}.

The microstructure was studied using a TESCAN MIRA 3 LMH scanning electron microscope, and a JEM-2000EX transmission electron microscope. To carry out electron backscatter diffraction (EBSD) analysis at various structural levels, several EBSD maps were obtained, with a scanning step from 0.06 to 5 μm, depending on the structural state. Due to the peculiarity of the EBSD method, all low-angle grain boundaries with misorientation less than 2°

Table 1. *Chemical composition of the EK79 heat-resistant nickel-based superalloy*
Таблица 1. *Химический состав жаропрочного никелевого сплава ЭК79*

Superalloy	Component content, wt. %												
	C	Cr	Co	V	W	Mo	Nb	Al	Ti	B	Si	Mn	La
EK79	0.06	11	14	0.5	2.5	4.5	2.7	3	2.6	≤0.01	≤0.30	≤0.04	≤0.08

were excluded from consideration. Compression tests were carried out on a Schenck RMS-100 universal dynamometer. For mechanical uniaxial compression tests, cylindrical samples with a diameter of 10 mm, and a height of 15 mm were used.

RESULTS

Formation of a mixed UFG microstructure in the EK79 superalloy during TMT

The initial microstructure of the EK79 superalloy, with an average γ-phase grain size of 8–9 μm and large incoherent particles, – strengthening γ'-phase grains with a size of 3.0±0.8 μm is shown in Fig. 1. Using scanning and transmission electron microscopy, it was found that the superalloy contains dispersed (0.2–0.3 μm) coherent γ'-phase particles inside the γ-phase grains, which are usually released upon cooling from the stamping temperature to room temperature (Fig. 1 a, 1 b). According to EBSD analysis, it was found that in the initial fine-grained microstructure, all grains have different orientations in space, and the microstructure itself is homogeneous (Fig. 1 c).

Low-temperature TMT in the temperature range of (0.88–0.62) Tγ', using the MIF scheme, led to the formation of a mixed UFG microstructure from an UFG component, which is a mixture of incoherent γ'-phase particles, and γ-phase grains with a size of 0.3–0.5 μm. The volume fraction of the UFG component exceeds 80 %. Moreover, in the UFG microstructure, individual coarse particles – globular-shape γ'-phase grains with a size of 3.0±0.8 μm are relatively evenly distributed (Fig. 1 d, 1 f). These coarse particles are well identified on the results of EBSD analysis (Fig. 1 f). Probably, they were formed earlier at the high-temperature TMT stage, during which the initial fine-grained duplex microstructure was formed. The proportion of relatively large γ'-phase precipitates in the EK79 superalloy is 10 %. When cooling from the processing temperature, coherent nanosized γ'-phase particles with a size of 0.05–0.1 μm are revealed in the body of the γ-phase grains.

It should be noted that in the EK79 superalloy under study, the matrix γ-phase and the strengthening γ'-phase have the same type of crystal lattice – a face-centred cubic lattice, and the lattice mismatch parameters are very small (less than 1 %). Therefore, the applied EBSD analysis method, does not allow distinguishing between phases and perceives (represents them) on EBSD maps as one phase. Based on the results of the analysis of such maps (Fig. 1 c, 1 f), it is clear that all small γ-phase grains and incoherent γ'-phase particles-grains less than 1 μm in size are separated by high-angle grain boundaries (γ/γ), with a grain-boundary angle of more than 15°, and interphase (γ/γ') boundaries, and are also coloured in different colours indicating their different crystallographic orientations. Noteworthy is the fact that in large ("inherited" from the microduplex microstructure) γ'-phase particles, a colour gradient is revealed, i. e., the colour within one grain changes contrast, and in the place where the contrast change occurs, subboundaries exhibiting an increased proportion of low-angle boundaries (LABs) are revealed (Fig. 1 f). Apparently, during low-temperature TMT, local deformation of coarse γ'-phase particles occurs, along individual crystallographic planes, which leads to a change in the shape of coarse particles: the initial round shape takes on an irregular contour, in the form of individual protrusions. Probably, simultaneously with the recrystallisation process, which resulted in the UFG microstructure formation (EBSD maps show recrystallised small grains, many of which are free from dislocations, which is confirmed by transmission electron microscopy data), deformation of coarse incoherent γ'-phase particles-grains is observed. It has been found that the share of LABs in the EK79 superalloy, with a mixed UFG microstructure is 25 %.

In contrast to coarse γ'-phase particles, in the UFG component (0.3–0.5 μm in size), during deformation, the retention of the equiaxial shape of the γ-phase grains, and incoherent γ'-phase particles, as well as a lower fraction of LABs, is observed. This apparently indicates the partial development of superplastic deformation mechanisms at the final stage of low-temperature TMT, in particular the main mechanism – grain boundary sliding.

Superplastic deformation of EK79 superalloy with a UFG microstructure under uniaxial compression

The results of mechanical tests, for uniaxial compression, of the EK79 superalloy with a UFG microstructure are shown in Fig. 2. It can be observed that even at the initial stage of deformation (5–10 %) under conditions of relatively low temperatures, flow stress peaks are not detected. With increasing degree of deformation, a weak monotonic flow stress growth is observed. A more intense increase in the flow stress values at deformation degrees of more than 40 %, is apparently determined by an increase in contact friction on the end surfaces, between the deformed blank and the strikers.

Microstructural studies of samples after testing according to the uniaxial compression scheme

Microstructural studies of samples after testing under the uniaxial compression scheme are presented in Fig. 3.

Analysis of microstructural changes after deformation of the EK79 superalloy with a pre-prepared UFG microstructure indicates that, during low-temperature superplastic deformation, retention of the mixed UFG microstructure is observed. Deformed grains are free of dislocations, and twins are also detected in many γ-phase grains. At the same time, the equiaxial shape of the grains is retained, which indicates the development of the main mechanism of superplastic deformation – grain boundary sliding (Fig. 3).

Microstructural analysis showed that in the EK79 superalloy, as a result of deformation according to the uniaxial compression scheme at a temperature of 950 °C, the superalloy microstructure is stable. An increase in the deformation temperature to 1000 °C leads to the coarsening of the γ-phase grains, which is associated with the partial dissolution of smaller (less than 1 μm) γ'-phase particles, i. e., the microstructure is transformed into a fine-grained duplex microstructure. The EBSD maps (Fig. 3) show that the microstructure is characterised by a uniformly equiaxial grain shape. Maintaining equiaxiality is a sign that deformation occurs under superplastic conditions.

Various areas of the samples were studied: those in which intensive development of deformation occurs, and

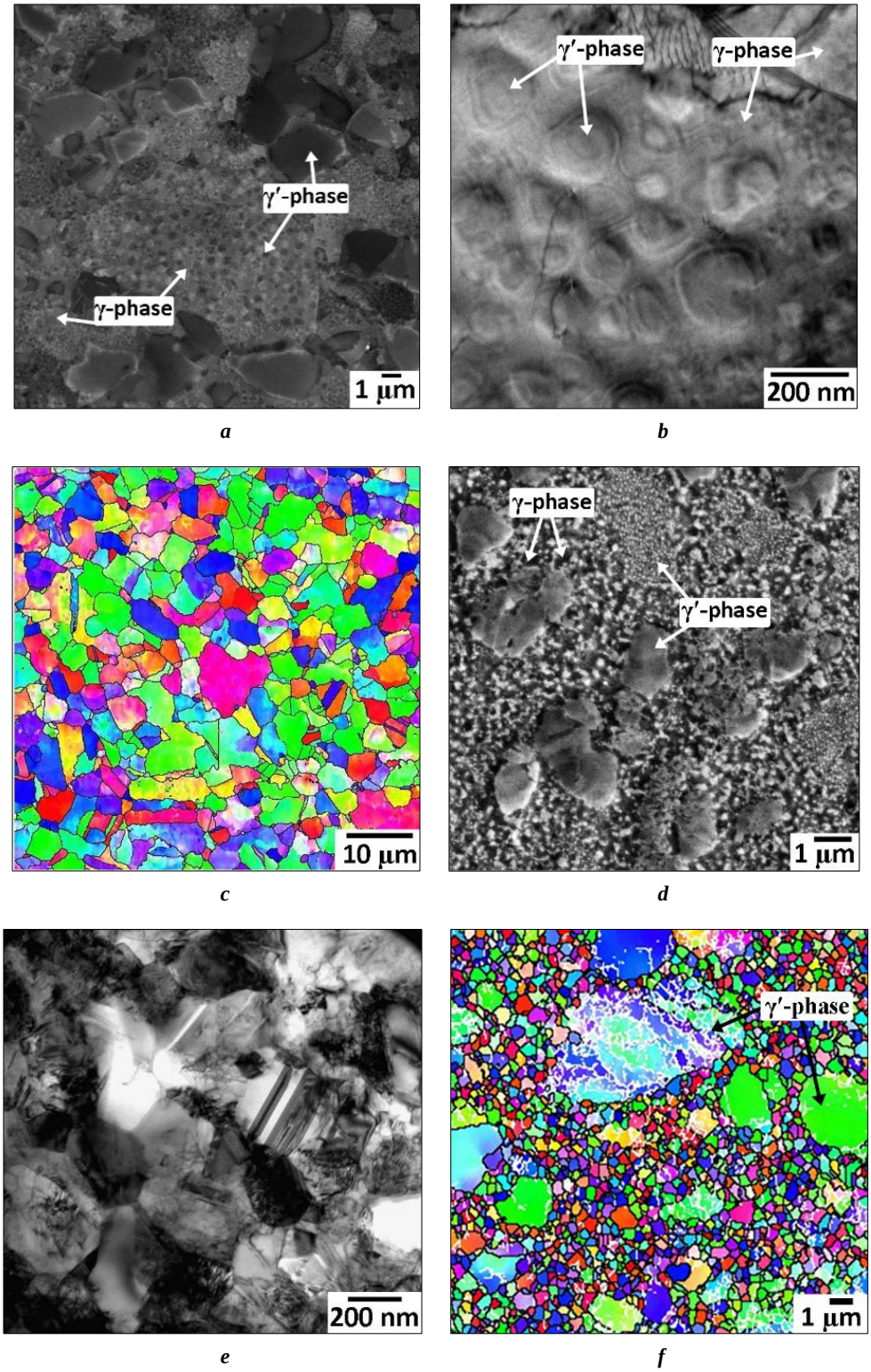

Fig. 1. *Microstructure of the EK79 superalloy:* ***a–c*** *– the initial state;* ***d–f*** *– after TMT*
Рис. 1. *Микроструктура сплава ЭК79:* ***a–c*** *– исходная;* ***d–f*** *– после ДТО*

those in which there is practically no deformation (Fig. 4). It has been found that in the zones of the samples involved in deformation (the centre of the sample), the increase in grain size is associated with both thermal influence, and stimulation by deformation, as a result of which the coarsening of grains occurs more intensively. In the stagnant zone during upset, where there is practically no deformation, grain growth is caused by the influence of high temperature, as a result of which partial γ'-phase dissolution occurs.

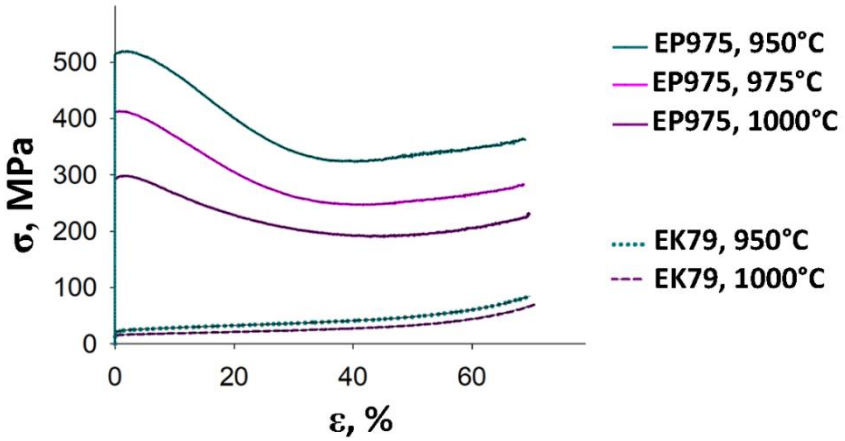

Fig. 2. *Mechanical properties of EP975 and EK79 nickel-based superalloys tested at a rate of $\dot{\varepsilon}=10^{-3}$ s^{-1} (EP975 [Repr. from: 15, p. 83])*
Рис. 2. *Механические свойства образцов из никелевых сплавов ЭП975 и ЭК79, испытанных при скорости $\dot{\varepsilon}=10^{-3}$ $с^{-1}$ (ЭП975 [Привод. по: 15, с. 83])*

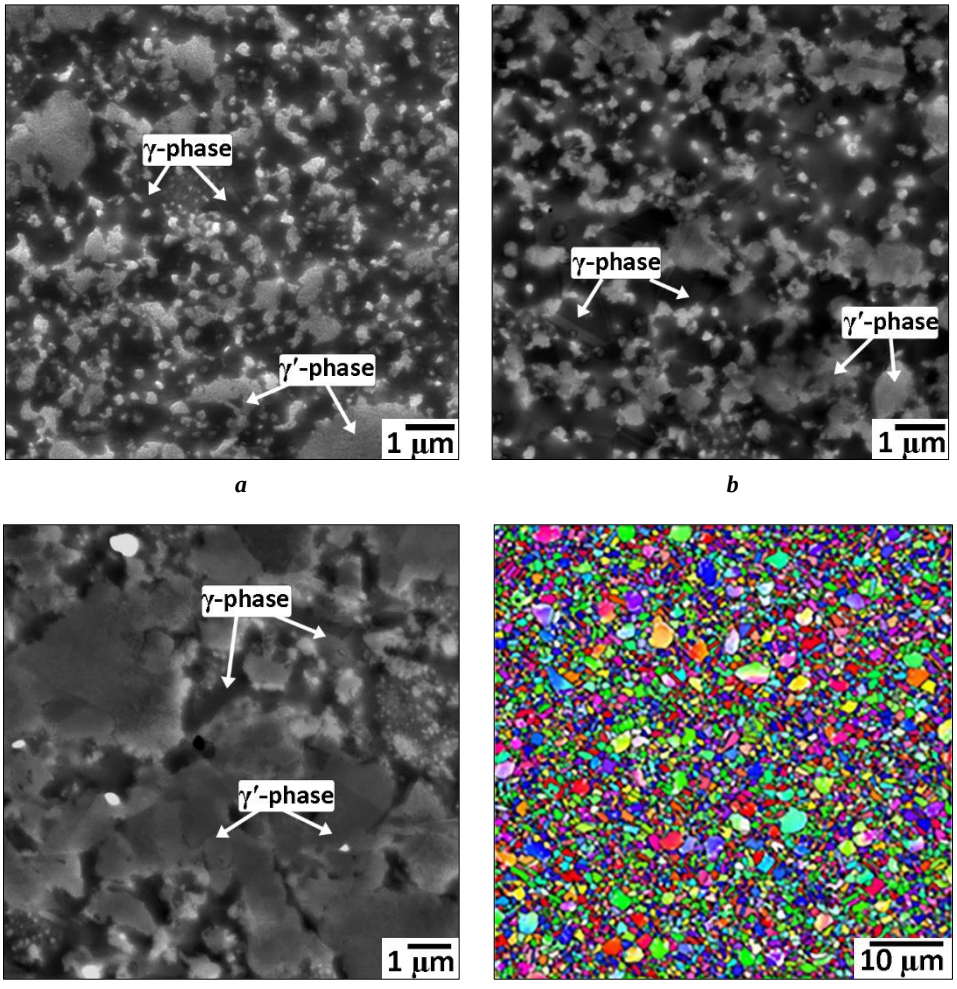

Fig. 3. *Microstructure of the EK79 superalloy with the mixed-type UFG microstructure after superplastic deformation according to the uniaxial compression scheme at $\dot{\varepsilon}=10^{-3}$ $s^{-1}$and temperatures of: **a** – 900 °C; **b** – 950 °C; **c**, **d** – 1000 °C*
Рис. 3. *Микроструктура суперсплава ЭК79 с УМЗ структурой смешанного типа после сверхпластического деформирования по схеме одноосного сжатия при $\dot{\varepsilon}=10^{-3}$ $с^{-1}$ и температуре: **a** – 900 °C; **b** – 950 °C; **c**, **d** – 1000 °C*

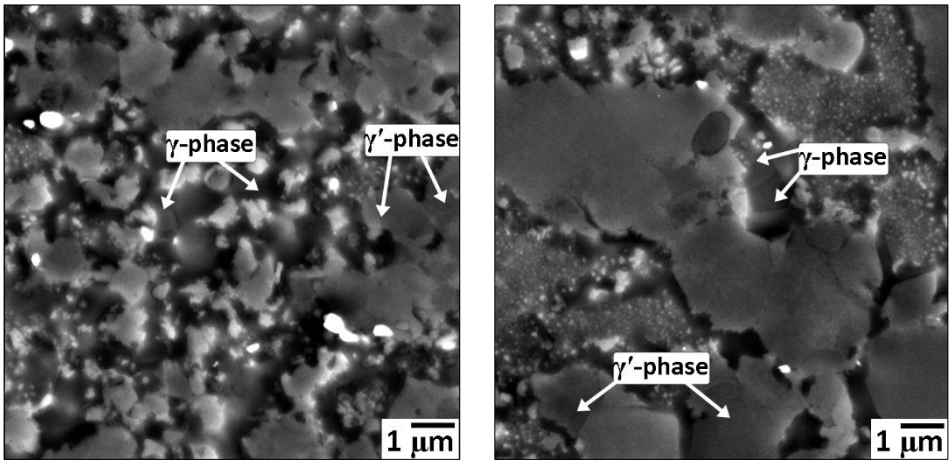

a *b*

Fig. 4. *Microstructure of the EK79 superalloy with the mixed-type UFG microstructure after superplastic deformation according to the uniaxial compression scheme at $\dot{\varepsilon}=10^{-3}$ s^{-1} and T=1000 °C:* ***a*** *– central part of the specimen;* ***b*** *– stagnant zone of the specimen*

Рис. 4. *Микроструктура сплава ЭК79 с УМЗ структурой смешанного типа после сверхпластического деформирования по схеме одноосного сжатия при $\dot{\varepsilon}=10^{-3}$ $с^{-1}$ и T=1000 °C:* ***a*** *– центральная часть образца;* ***b*** *– застойная зона образца*

DISCUSSION

Analysis of the results obtained indicates that in the process of low-temperature TMT in forgings made of EK79 superalloy, a mixed UFG microstructure is formed, in which three types of the γ'-phase particle sizes, can be distinguished: 1) relatively coarse (size of 3.0±0.8 μm) – obviously "inherited" from the original fine-grained microduplex microstructure; 2) UFG component – γ-phase grains and incoherent γ'-phase particles with a size of 0.3–0.5 μm; 3) strengthening intragranular γ'-phase particles with a size of 0.05–0.1 μm, released upon cooling, from the TMT temperature to room temperature.

The formation of a mixed UFG microstructure in the EK79 superalloy, during low-temperature TMT, is apparently determined by the following circumstances. The processing temperature is quite low, and the deformation degree, and the time during which the UFG microstructure is formed, are insufficient to ensure the development of recrystallisation in the γ'-phase particles, that are larger and stronger than the matrix γ-phase and were inherited from the duplex microstructure. Therefore, in the process of TMT according to the selected modes, the recrystallisation development occurs mainly in small grains of the plastic γ-phase, with an initial microduplex microstructure, in which coagulated γ'-phase particles were additionally distinguished.

A comparative analysis of the mechanical properties (Fig. 2) of the EP975 superalloy given in the paper [15], and the EK79 superalloy studied in this work, showed that after deformation, according to the uniaxial compression scheme, there is a significant difference in the level of flow stresses, and in the dependence of the flow stress on the degree of deformation. In the EP975 superalloy, at the initial stage of deformation (2–5 %), a peak in flow stress and a subsequent decrease are observed. This type of dependence may indicate the development of dynamic recrystallisation processes during superplastic deformation, and as a consequence, may lead to the formation of a more fine-grained microstructure. At the same time, such a peak is not observed in the EK79 superalloy in the studied temperature-rate strain range. Under the same temperature rate strain conditions, the level of flow stress in the more doped and more heat-resistant EP975 superalloy is almost an order of magnitude higher.

According to the known ideas about the UFG microstructure formation in the superalloy presented in [7; 12], at each stage, microstructure refinement is achieved step by step: by transforming the initial coarse-grained microstructure into a fine-grained duplex one at the high-temperature TMT stage, and then into an UFG microstructure at the subsequent low-temperature TMT stage. In this case, the initial fine-grained microduplex microstructure in the superalloy, under study, should have been transformed into a completely homogeneous UFG microstructure. However, in this work, as noted above, a mixed UFG microstructure was formed in the EK79 superalloy. It is obvious that during the TMT process, recrystallisation occurred predominantly in the more plastic γ-phase.

Compared to the EP975 superalloy [15], blanks made from the more plastic and less heat-resistant EK79 superalloy, were subjected to more intense TMT (the temperature range was wider than in the EP975 superalloy, and the temperature of TMT end was 150 °C lower). This fact probably determines the formation of a more fine-grained microstructure in the EK79 superalloy, since more intense TMT at lower temperatures leads to the formation of new recrystallisation centres in the form of fragments and subgrains with LABs.

A significant volume fraction of the UFG component (≥80 %), obviously plays a decisive role in the implementation of the effect of low-temperature superplasticity in the EK79 superalloy with a mixed UFG microstructure. As is known [11; 16], alloys with a UFG microstructure are characterised by a large proportion of grain boundaries, which leads to activation of the main mechanism of superplastic deformation – grain boundary sliding. Moreover, an increase in the extension of grain boundaries promotes the activation of another mechanism of superplastic

deformation – diffusion creep. Therefore, the presence in the UFG microstructure of a small amount of relatively coarse γ'-phase particles-grains, apparently, does not have a significant influence on the manifestation of the effect of low-temperature superplasticity in the material under study.

CONCLUSIONS

1. Low-temperature thermomechanical treatment of the EK79 heat-resistant nickel superalloy leads, to the transformation of a fine-grained duplex microstructure into an ultrafine-grained mixed microstructure.

2. The ultrafine-grained mixed microstructure in the EK79 superalloy consists of γ-phase grains and γ'-phase incoherent particles of 0.3–0.5 μm in size, along with which there are relatively coarse γ'-phase particles of up to 3.8 μm in size. In this case, the share of coarse particles is about 10 %, and the share of the UFG component exceeds 80 %, which plays a decisive role in the implementation of the low-temperature superplasticity effect.

3. The EK79 superalloy with a mixed UFG microstructure has thermal stability at deformation temperatures not higher than 950 °C, which provides the necessary conditions for the implementation of the low-temperature superplasticity effect in the superalloy under study even at temperatures of 800–850 °C corresponding to the ageing temperature range. The analysis of microstructural changes in the samples deformed under uniaxial compression showed that the equiaxial shape of γ-phase grains, and incoherent γ'-phase particles less than 1 μm in size is retained. The latter indicates the development of the main mechanism of superplastic deformation – grain boundary sliding.

4. An increase in the deformation temperature to 1000 °C leads to the UFG microstructure transformation into a fine-grained duplex microstructure.

REFERENCES

1. Reed R. *The Superalloys: Fundamentals and Applications*. Cambridge, Cambridge University Press Publ., 2006. 372 p.
2. Long Haibo, Mao Shengcheng, Liu Yinong, Zhang Ze, Han Xiaodong. Microstructural and compositional design of Ni-based single crystalline superalloys – A review. *Journal of Alloys and Compounds*, 2018, vol. 743, pp. 203–220. DOI: 10.1016/j.jallcom.2018.01.224.
3. Pollock T.M., Sammy Tin. Nickel-based superalloys for advanced turbine engines: Chemistry, microstructure, and properties. *Journal of Propulsion and Power*, 2006, vol. 22, no. 2, pp. 361–374. DOI: 10.2514/1.18239.
4. Satyanarayana D.V.V., Eswara P.N. Nickel-Based Superalloys. *Aerospace Materials and Material Technologies*, 2016, pp. 199–228. DOI: 10.1007/978-981-10-2134-3_9.
5. Lomberg B.S., Ovsepyan S.V., Bakradze M.M., Letnikov M.N., Mazlov I.S. The application of new wrought nickel alloys for advanced gas turbine engines. *Aviation materials and technologies*, 2017, no. S, pp. 116–129. DOI: 10.18577/2071-9140-2017-0-S-116-129.
6. Mukhtarov S., Karyagin D., Ganeev A., Zainullin R., Shakhov R., Imayev V. The Effect of Forging and Heat Treatment Variables on Microstructure and Mechanical Properties of a Re-Bearing Powder-Metallurgy Nickel Base Superalloy. *Metals*, 2023, vol. 13, no. 6, article number 1110. DOI: 10.3390/met13061110.
7. Mukhtarov S.K., Imayev V.M., Logunov A.V., Shmotin Yu.N., Mikhailov A.M., Gaisin R.A., Shakhov R.V., Ganeev A.A., Imayev R.M. Recrystallization behavior and mechanical properties of a novel Re-containing nickel-base superalloy. *Materials Science and Technology*, 2019, vol. 35, no. 13, pp. 1605–1613. DOI: 10.1080/02670836.2019.1633726.
8. Akca E., Gursel A. A Review on Superalloys and IN718 Nickel-Based INCONEL Superalloy. *Periodicals of Engineering and Natural Sciences*, 2015, vol. 3, no. 1, pp. 15–27. DOI: 10.21533/pen.v3i1.43.
9. Utyashev F.Z., Kaibyshev O.A., Valitov V.A. *Method for processing billets from multiphase alloys and the article*, patent US no. 6565683 B1, 2003. 14 p.
10. Mulyukov R.R. Development of principles for the production and study of bulk nanostructured materials at the Institute of Applied Mathematics and Mathematics of the Russian Academy of Sciences. *Nanotechnologies in Russia*, 2007, vol. 2, no. 7-8, pp. 38–53. EDN: IADHGZ.
11. Zhilyaev A.P., Pshenichnyuk A.I., Utyashev F.Z., Raab G.I. *Superplasticity and Grain Boundaries in Ultrafine-Grained Materials*. Cambridge, Woodhead Publishing, 2020. 440 p.
12. Utyashev F.Z., Sukhorukov R.Yu., Valitov V.A. Theoretical Foundations of the Use of Severe Plastic Deformation for Formation of Ultrafine Grain Structure in Superalloys. *Journal of Machinery Manufacture and Reliability*, 2021, no. 3, pp. 72–79. DOI: 10.3103/S1052618821090144.
13. Imaev V.M., Mukhtarov Sh.Kh., Logunov A.V., Ganeev A.A., Shakhov R.V., Imaev R.M. Effect of thermomechanical treatment on the microstructure and mechanical properties of a novel heavily alloyed nickel base superalloy. *Letters on Materials*, 2019, vol. 9, no. 2, pp. 249–254. DOI: 10.22226/2410-3535-2019-2-249-254.
14. Chamanfar A., Valberg H.S., Templin B., Plumeri J.E., Misiolek W.Z. Development and validation of a finite-element model for isothermal forging of a nickel-base superalloy. *Materialia*, 2019, vol. 6, article number 100319. DOI: 10.1016/j.mtla.2019.100319.
15. Galieva E.V., Klassman E.Yu., Gabbasov R.R., Stepukhov E.M., Valitov V.A. Low-temperature superplastic deformation of EK61 and EP975 wrought nickel-based superalloys with an ultrafine-grained structure. *Letters on materials*, 2023, vol. 13, no. 1, pp. 79–84. DOI: 10.22226/2410-3535-2023-1-79-84.
16. Padmanabhan K.A., Balasivanandha S.P., Mulyukov R.R., Nazarov A.A., Imayev R.M., Ghosh S.Ch. *Superplasticity. Common Basis for a Near-Ubiquitous Phenomenon*. Berlin, Springer-Verlag GmbH Publ., 2018. 526 p. DOI: 10.1007/978-3-642-31957-0.
17. Lv Shaomin, Jia Chonglin, He Xinbo, Wan Zhipeng, Li Xinxu, Qu Xuanhui. Superplastic Deformation and Dynamic Recrystallization of a Novel Disc Superalloy GH4151. *Materials*, 2022, vol. 12, no. 12, article number 3667. DOI: 10.3390/ma12223667.
18. Fedorov A.A., Bespalov A.V., Komarov R.S. Superplasticity of ZHS6-KP heat-resistant nickel alloy at high hydro-

static pressures. *Tekhnologiya legkikh splavov*, 2022, no. 1, pp. 67–75. DOI: 10.24412/0321-4664-2022-1-67-75.
19. Wen Hongning, Jin Junsong, Tang Xuefeng et al. Systematic analysis of distinct flow characteristics and underlying microstructural evolution mechanisms of a novel fine-grained P/M nickel-based superalloy during isothermal compression. *Journal of Materials Science & Technology*, 2023, vol. 162, pp. 57–73. DOI: 10.1016/j.jmst.2023.03.042.
20. Lu X.D., Zhang Y.W., Shi S.Y., Wen B., Su X., Du J.H. Hot deformation behavior of hard-to-deform Ni-based Alloy. *Journal of Physics: Conference Series*, 2021, vol. 1777, article number 012006. DOI: 10.1088/1742-6596/1777/1/012006.
21. Xu Xiao-yan, Ma Xiang-dong, Wang Hong, Ye Zhang, Chang Jian-wei, Xu Yao, Sun Guang-ai, Lu Wei-jie, Gao Yu-kui. Characterization of residual stresses and microstructural features in an Inconel 718 forged compressor disc. *Transactions of Nonferrous Metals Society of China*, 2019, vol. 29, no. 3, pp. 569–578. DOI: 10.1016/S1003-6326(19)64965-4.
22. Galieva E.V., Akhunova A.Kh., Valitov V.A., Klassman E.Yu. Computer and physical modeling of multiple isothermal forging of EK61 superalloy. *Letters on materials*, 2022, vol. 12, no. 3, pp. 243–248. DOI: 10.22226/2410-3535-2022-3-243-248.

СПИСОК ЛИТЕРАТУРЫ

1. Reed R. The Superalloys: Fundamentals and Applications. Cambridge: Cambridge University Press, 2006. 372 p.
2. Long Haibo, Mao Shengcheng, Liu Yinong, Zhang Ze, Han Xiaodong. Microstructural and compositional design of Ni-based single crystalline superalloys – A review // Journal of Alloys and Compounds. 2018. Vol. 743. P. 203–220. DOI: 10.1016/j.jallcom.2018.01.224.
3. Pollock T.M., Sammy Tin. Nickel-based superalloys for advanced turbine engines: Chemistry, microstructure, and properties // Journal of Propulsion and Power. 2006. Vol. 22. № 2. P. 361–374. DOI: 10.2514/1.18239.
4. Satyanarayana D.V.V., Eswara P.N. Nickel-Based Superalloys // Aerospace Materials and Material Technologies. 2016. P. 199–228. DOI: 10.1007/978-981-10-2134-3_9.
5. Ломберг Б.С., Овсепян С.В., Бакрадзе М.М., Летников М.Н., Мазлов И.С. Применение новых деформируемых никелевых сплавов для перспективных газотурбинных двигателей // Авиационные материалы и технологии. 2017. № S. С. 116–129. DOI: 10.18577/2071-9140-2017-0-S-116-129.
6. Mukhtarov S., Karyagin D., Ganeev A., Zainullin R., Shakhov R., Imayev V. The Effect of Forging and Heat Treatment Variables on Microstructure and Mechanical Properties of a Re-Bearing Powder-Metallurgy Nickel Base Superalloy // Metals. 2023. Vol. 13. № 6. Article number 1110. DOI: 10.3390/met13061110.
7. Mukhtarov S.K., Imayev V.M., Logunov A.V., Shmotin Yu.N., Mikhailov A.M., Gaisin R.A., Shakhov R.V., Ganeev A.A., Imayev R.M. Recrystallization behavior and mechanical properties of a novel Re-containing nickel-base superalloy // Materials Science and Technology. 2019. Vol. 35. № 13. P. 1605–1613. DOI: 10.1080/02670836.2019.1633726.
8. Akca E., Gursel A. A Review on Superalloys and IN718 Nickel-Based INCONEL Superalloy // Periodicals of Engineering and Natural Sciences. 2015. Vol. 3. № 1. P. 15–27. DOI: 10.21533/pen.v3i1.43.
9. Utyashev F.Z., Kaibyshev O.A., Valitov V.A. Method for processing billets from multiphase alloys and the article: patent US № 6565683 B1, 2003. 14 p.
10. Мулюков Р.Р. Развитие принципов получения и исследование объемных наноструктурных материалов в ИПСМ РАН // Российские нанотехнологии. 2007. Т. 2. № 7-8. С. 38–53. EDN: IADHGZ.
11. Zhilyaev A.P., Pshenichnyuk A.I., Utyashev F.Z., Raab G.I. Superplasticity and Grain Boundaries in Ultrafine-Grained Materials. Cambridge: Woodhead Publishing, 2020. 440 p.
12. Utyashev F.Z., Sukhorukov R.Yu., Valitov V.A. Theoretical Foundations of the Use of Severe Plastic Deformation for Formation of Ultrafine Grain Structure in Superalloys // Journal of Machinery Manufacture and Reliability. 2021. № 3. P. 72–79. DOI: 10.3103/S1052618821090144.
13. Имаев В.М., Мухтаров Ш.Х., Логунов А.В., Ганеев А.А., Шахов Р.В., Имаев Р.М. Влияние деформационно-термической обработки на микроструктуру и механические свойства нового высоколегированного никелевого сплава // Письма о материалах. 2019. Т. 9. № 2. С. 249–254. DOI: 10.22226/2410-3535-2019-2-249-254.
14. Chamanfar A., Valberg H.S., Templin B., Plumeri J.E., Misiolek W.Z. Development and validation of a finite-element model for isothermal forging of a nickel-base superalloy // Materialia. 2019. Vol. 6. Article number 100319. DOI: 10.1016/j.mtla.2019.100319.
15. Galieva E.V., Klassman E.Yu., Gabbasov R.R., Stepukhov E.M., Valitov V.A. Low-temperature superplastic deformation of EK61 and EP975 wrought nickel-based superalloys with an ultrafine-grained structure // Letters on materials. 2023. Vol. 13. № 1. P. 79–84. DOI: 10.22226/2410-3535-2023-1-79-84.
16. Padmanabhan K.A., Balasivanandha S.P., Mulyukov R.R., Nazarov A.A., Imayev R.M., Ghosh S.Ch. Superplasticity. Common Basis for a Near-Ubiquitous Phenomenon. Berlin: Springer-Verlag GmbH, 2018. 526 p. DOI: 10.1007/978-3-642-31957-0.
17. Lv Shaomin, Jia Chonglin, He Xinbo, Wan Zhipeng, Li Xinxu, Qu Xuanhui. Superplastic Deformation and Dynamic Recrystallization of a Novel Disc Superalloy GH4151 // Materials. 2022. Vol. 12. № 12. Article number 3667. DOI: 10.3390/ma12223667.
18. Федоров А.А., Беспалов А.В., Комаров Р.С. Сверхпластичность жаропрочного никелевого сплава ЖС6-КП при высоких гидростатических давлениях // Технология легких сплавов. 2022. № 1. С. 67–75. DOI: 10.24412/0321-4664-2022-1-67-75.
19. Wen Hongning, Jin Junsong, Tang Xuefeng et al. Systematic analysis of distinct flow characteristics and underlying microstructural evolution mechanisms of a novel fine-grained P/M nickel-based superalloy during isothermal compression // Journal of Materials Science & Technology. 2023. Vol. 162. P. 57–73. DOI: 10.1016/j.jmst.2023.03.042.

20. Lu X.D., Zhang Y.W., Shi S.Y., Wen B., Su X., Du J.H. Hot deformation behavior of hard-to-deform Ni-based Alloy // Journal of Physics: Conference Series. 2021. Vol. 1777. Article number 012006. DOI: 10.1088/1742-6596/1777/1/012006.
21. Xu Xiao-yan, Ma Xiang-dong, Wang Hong, Ye Zhang, Chang Jian-wei, Xu Yao, Sun Guang-ai, Lu Wei-jie, Gao Yu-kui. Characterization of residual stresses and microstructural features in an Inconel 718 forged compressor disc // Transactions of Nonferrous Metals Society of China. 2019. Vol. 29. № 3. P. 569–578. DOI: 10.1016/S1003-6326(19)64965-4.
22. Galieva E.V., Akhunova A.Kh., Valitov V.A., Klassman E.Yu. Computer and physical modeling of multiple isothermal forging of EK61 superalloy // Letters on materials. 2022. Vol. 12. № 3. P. 243–248. DOI: 10.22226/2410-3535-2022-3-243-248.

Низкотемпературная сверхпластическая деформация никелевого сплава ЭК79 с ультрамелкозернистой структурой смешанного типа

Галиева Эльвина Венеровна*[1], кандидат технических наук, научный сотрудник
Классман Екатерина Юрьевна[2], аспирант, инженер
Валитов Венер Анварович[3], доктор технических наук, ведущий научный сотрудник
Институт проблем сверхпластичности металлов РАН, Уфа (Россия)

***E-mail: galieva_elvina_v@mail.ru**

[1]ORCID: https://orcid.org/0000-0002-1074-6274
[2]ORCID: https://orcid.org/0000-0003-1984-5137
[3]ORCID: https://orcid.org/0000-0002-1349-6047

Поступила в редакцию 22.09.2023 *Принята к публикации 03.11.2023*

Аннотация: Одним из наиболее эффективных способов повышения технологической пластичности современных суперсплавов – жаропрочных никелевых сплавов – является формирование в объемных полуфабрикатах ультрамелкозернистой (УМЗ) структуры, которая является необходимым условием для реализации эффекта структурной сверхпластичности в технологических процессах изготовления изделий из таких сплавов. Одним из наиболее перспективных методов получения УМЗ структуры является деформационно-термическая обработка (ДТО) по схеме всесторонней изотермической ковки. Показано, что ДТО сплава ЭК79 с постепенным снижением температуры обработки с 0,88 до 0,62 Ts (где Ts – температура растворения упрочняющей фазы) приводит к трансформации исходной мелкозернистой структуры типа микродуплекс в УМЗ структуру смешанного типа. Такая смешанная УМЗ микроструктура состоит из: 1) относительно крупных (наследственных от мелкозернистой структуры) частиц γ'-фазы размером 3,0±0,8 мкм; 2) зерна γ-фазы и некогерентных частиц γ'-фазы размером 0,3–0,5 мкм; 3) упрочняющих когерентных внутризеренных частиц γ'-фазы размером 0,05–0,1 мкм, выделяющихся при охлаждении с температуры ДТО до комнатной температуры. Сплав ЭК79, имеющий такую микроструктуру, при испытаниях на одноосное сжатие демонстрирует низкотемпературную сверхпластичность в диапазоне температур 800–1000 °С. Установлено, что повышение температуры деформации до 1000 °С приводит к укрупнению зерен γ-фазы до микронного размера. Сохранение сверхпластических свойств при наличии в структуре сравнительно крупных некогерентных частиц второй фазы (γ'-фазы), по-видимому, связано с тем, что деформация локализована в УМЗ компоненте.

Ключевые слова: жаропрочный никелевый сплав; ЭК79; упрочняющая фаза; микродуплексная структура; ультрамелкозернистая структура; низкотемпературная сверхпластичность; деформационно-термическая обработка; одноосное сжатие.

Благодарности: Работа выполнена при финансовой поддержке гранта РНФ № 22-79-00271, https://www.rscf.ru/project/22-79-00271/.

Электронно-микроскопические исследования и механические испытания проводились на базе Центра коллективного пользования ИПСМ РАН «Структурные и физико-механические исследования материалов».

Для цитирования: Галиева Э.В., Классман Е.Ю., Валитов В.А. Низкотемпературная сверхпластическая деформация никелевого сплава ЭК79 с ультрамелкозернистой структурой смешанного типа // Frontier Materials & Technologies. 2024. № 1. С. 19–27. DOI: 10.18323/2782-4039-2024-1-67-2.

doi: 10.18323/2782-4039-2024-1-67-3

The influence of hafnium on high-magnesium alloys doped with transition metals during heat treatment

Igor A. Zorin*[1,2,4], laboratory assistant-researcher, student,
II category electronic engineer
of the Laboratory of Mechanical Testing and Electron Microscopy
Evgeny V. Aryshenskiy[2,5], Doctor of Sciences (Engineering), Associate Professor,
senior researcher of the Laboratory of Electron Microscopy and Image Processing
Egor A. Kudryavtsev[3,6], PhD (Engineering),
researcher of the Common Use Center "Technologies and Materials
of the National Research University BelSU"
Aleksandr M. Drits[1,7], PhD (Engineering), leading researcher
Sergey V.Konovalov[2,8], Doctor of Sciences (Engineering), Professor,
Pro-rector for Research and Innovative Activities
[1]*Samara National Research University, Samara (Russia)*
[2]*Siberian State Industrial University, Novokuznetsk (Russia)*
[3]*Belgorod State National Research University, Belgorod (Russia)*

***E-mail: zorin.ia@ssau.ru**

[4]ORCID: https://orcid.org/0000-0001-9349-2494
[5]ORCID: https://orcid.org/0000-0003-3875-7749
[6]ORCID: https://orcid.org/0000-0003-1113-0807
[7]ORCID: https://orcid.org/0000-0002-9468-8736
[8]ORCID: https://orcid.org/0000-0003-4809-8660

Received 03.08.2023 *Accepted 20.11.2023*

Abstract: The purpose of the work is to study the influence of hafnium additives on the mechanical properties and thermal stability of particles at elevated temperature during heat treatment of aluminum alloys with a high magnesium content. Two modifications of 1570 alloy were chosen for the study: without hafnium content and with its addition of 0.5 % by weight. Both alloys were subjected to homogenizing annealing at a temperature of 440 °C with different exposure modes, which ranged from 2 to 100 h. Microhardness was studied for various heat treatment modes, and the fine microstructure was studied as well using transmission microscopy. As a result, it was possible to identify that during annealing at a short exposure time (2–8 h), the alloy with the hafnium addition has higher microhardness values exceeding those of 1570 alloy by an average of 20 HV units. This is associated with the fact that in 1570 alloy with hafnium additives, during heat treatment, the number of precipitated particles increases while their average size decreases compared to the base alloy. At the same time, in 1570 alloy without hafnium content, when annealed at a temperature of 440 °C, there is no increase in microhardness. This is caused by the fact that in 1570 alloy without hafnium content, when cooled after casting, discontinuous decomposition occurs, which resulted in the fact that most of the scandium precipitates from the supersaturated solid solution in the form of dispersoids. This phenomenon is not observed in the alloy with hafnium additives, which indicates its ability to stop discontinuous decomposition during cooling the ingot after casting.

Keywords: aluminum alloys; transition metals; scandium; hafnium; heat treatment; strengthening nanoparticles.

Acknowledgments: The study was supported by the grant of the Russian Science Foundation No. 22–29–01506, https://rscf.ru/project/22-29-01506/.

The work was carried out using the equipment of the Common Use Center "Technologies and Materials of the National Research University BelSU".

For citation: Zorin I.A., Aryshenskiy E.V., Kudryavtsev E.A., Drits A.M., Konovalov S.V. The influence of hafnium on high-magnesium alloys doped with transition metals during heat treatment. *Frontier Materials & Technologies*, 2024, no. 1, pp. 29–36. DOI: 10.18323/2782-4039-2024-1-67-3.

INTRODUCTION

Aluminum alloys are currently among the most desirable materials in many industries. One of the most popular additives to aluminum alloys is magnesium, alloying with which leads to a significant increase in strength properties due to solid solution strengthening. Another common additive, that increases the mechanical properties of aluminum alloys is scandium [1]. Its use leads to a significant refinement of the grain structure during casting [2–4]. Moreover, it promotes an increase in strength, due to the formation of coherent strengthening Al_3Sc nanoparticles with the $L1_2$ structure [5–7]. Considering the above, it is not surprising that magnesium-scandium joint doping is very common in modern industry.

At the same time, the use of scandium as an alloying element has certain disadvantages: firstly, it is very expensive, and secondly, due to the high rate of its diffusion in aluminum, Al_3Sc nanoparticles have low thermal stability and quickly coagulate when heated [8; 9]. To increase their thermal stability, zirconium is added to the alloys, which creates a shell around Al_3Sc preventing the transition of $L1_2$ to $D0_{23}$ and the decomposition of the supersaturated scandium solution [10; 11]. Moreover, zirconium reduces the amount of scandium required for effective modification of the cast structure [7; 12].

It is the principle of joint scandium-zirconium doping that was used to develop a number of aluminum alloys, with a high magnesium content. One of them is 1570 alloy, which is very popular in modern industry. Hafnium additives could further increase the effectiveness of strengthening particles. This element is also an effective grain refiner [13]. Moreover, like zirconium, it creates a shell around Al_3Sc particles preventing further diffusion of scandium, i. e., thermally stabilizes them [10; 14].

Recent studies [15; 16] showed that hafnium additions to 1570 alloy significantly slow down the decomposition of the supersaturated solid solution. Thus, in [16] it was found that when adding 0.5 % of hafnium to 1570 alloy, the discontinuous decomposition of the supersaturated solid solution in it completely stops. The study [15] showed that adding hafnium to 1570 alloy reduces the number of nanoparticles precipitated from it during annealing at a temperature of 370 °C and an exposure time of 4 h. This also indicates a slowdown in the decomposition of the supersaturated solid solution. It is worth noting that inhibiting the decomposition of a supersaturated solid solution at a temperature of 370 °C will not provide advantages, since due to a decrease in the number of nanoparticles, the strength characteristics of the alloy will also decrease. However, slowing down the rate of decomposition of a supersaturated solid solution of scandium in aluminum can be useful at higher temperatures, when the particles in the 1570 alloy begin to coagulate and coalesce, thereby losing their strengthening effect. At the same time, hafnium additives allow thermally stabilizing nanoparticles, thereby increasing their strength properties. Note, that increasing the thermal stability of particles is very important, since it will allow increasing the hot deformation temperature. This, in turn, will increase the ductility of the material and improve the energy efficiency of hot rolling [17].

The purpose of the work is to study the influence of hafnium additives on the mechanical properties and thermal stability of Al_3Sc particles at elevated temperature of heat treatment of high-magnesium aluminum alloys.

METHODS

To study the influence of hafnium on the formation of microstructure and mechanical properties during high-temperature annealing of rolled samples from aluminum alloys with a high magnesium content, 1570 and 1570 (+0.5 wt. % Hf) alloys were cast. To cast ingots of the studied alloys, a medium-frequency induction furnace was used; ingots with dimensions of 20×40×400 mm and a mass of 5 kg were cast into a steel mold, followed by cooling in water.

The following materials were used as charging materials for the alloy: aluminum of A85 grade, magnesium of MG90 grade, alloying composition of $Al–Sc_2$, $Al–Zr_5$, $Al–Hf_2$ grades, and alloying tablets of $Mn_{90}Al_{10}$ grade. First, aluminum was loaded and melted. After the aluminum melted and the temperature reached 730 °C, slag was removed from the melt surface. Next, the melt was heated to a temperature of 770–790 °C and $AlSc_2$, $AlZr_5$, $Al–Hf_2$ alloying compositions were added in portions weighing no more than 300 g, followed by stirring and holding the melt for 5 min. After introducing the above-mentioned alloying compositions, the melt was cooled to a temperature of 750 °C, after which new alloying components (Mg, Mn) were added. Next, the melt was stirred for 3 min, followed by heating the melt to a temperature of 740 °C and taking a sample for express analysis of the melt chemical composition. The chemical composition of the alloys (Table 1) was determined by the spectral method on an ARL 3460 atomic emission spectrometer (GOST 25086, GOST 7727, GOST 3221, ASTM E 716, ASTM E 1251). The Hf content was determined by calculation due to the absence of standard samples. Before pouring the molten metal into the mold, it was refined with carnallite flux introduced at the rate of 5 g per 1 kg of charging material. After this, slag was removed from the surface of the molten metal, and the metal was poured into a steel casting mold at a uniform pouring time of 20–30 s at a melt temperature of 730–750 °C. After solidification, the ingot was removed from the chill mold and cooled in water.

The ingots were annealed in an electric muffle furnace at a temperature of 440 °C and held for 2, 4, 8, 16, 24, 48, 72, and 100 h, followed by quenching in water to fix the supersaturated solid solution.

The microhardness of the studied alloy was measured using a Wolpert 402MVD automatic microhardness tester in accordance with GOST 9450–76 at a load of 0.2 N and a holding time of 10 s. Before testing began, one of the surfaces of the plane-parallel sample was ground and polished.

Using transmission microscopy on a JEM-2100 microscope (JEOL, Japan) equipped with an INCA energy dispersive analysis attachment (Oxford Instruments, UK), samples for both alloys considered in the work were studied after 4 h of holding at temperatures of 370 and 440 °C. Sample preparation for transmission electron microscopy was carried out in several stages. At the first stage, using a Sodick electroerosion machine (Sodick Co., Ltd, Japan),

Table 1. *Chemical composition of the studied alloys*
Таблица 1. *Химический состав исследуемых сплавов*

Alloy	Al	Si	Fe	Mn	Mg	Ti	Zr	Sc	Hf
1570	Base	0.13	0.21	0.44	6.25	0.02	0.06	0.25	–
1570–0.5Hf	Base	0.12	0.22	0.45	6.29	0.04	0.06	0.25	0.5

two blanks were cut for foils with a thickness of 500 μm. The indicated thickness is determined by possible deformation and bending of the foils during cutting, due to the possible presence of internal stresses in the samples. Next, the resulting blanks were mechanically thinned to a thickness of ~120 μm using Grid 2000 abrasive wheels (Struers, Denmark). Using a special punch, disks with a diameter of 3 mm were extruded from the resulting blanks and placed in a TenuPol-5 electrolytic thinning installation (Struers, Denmark). Thinning was carried out at a temperature of −30 °C in an electrolyte of the following composition: 75 % of CH_3OH, 25 % of HNO_3. As a result, at least 5 foil samples for TEM were produced from each of the 6 states. The fine structure of the samples was studied on a JEM-2100 TEM transmission electron microscope (JEOL, Japan), with an accelerating voltage of 200 kV equipped with an INCA EDX-analysis attachment (Oxford Instruments, UK). The resulting foils were immediately placed in a bi-inclined TEM holder with the ability to incline by ±30° along two axes. Due to the small size of the particles (5–10 nm), the shooting was carried out at a magnification of ×200,000 and a long exposure time (about 1 min), which made it possible to reliably record even such small coherent particles. In the resulting images, the number of particles and their chemical composition were considered using an EDX-detector.

RESULTS

The changes in the microhardness of the studied alloys are given below. According to Fig. 1, the mechanical characteristics of 1570 alloy generally remain unchanged and are in the range of 82–89 HV units. This points to the fact that all strengthening $Al_3(Sc,Zr)$ particles, which have a coherent $L1_2$ structure, precipitate during discontinuous decomposition, and their formation does not occur at subsequent stages of heat treatment.

At the same time, the alloy doped with hafnium shows the greatest increase in microhardness in the range of 2–8 h. This is associated with the fact that in the indicated time intervals, the active decomposition of the supersaturated solid solution begins and the precipitation of strengthening particles of the Al_3Sc type begins. After 16 h of holding, the alloy with the hafnium addition exhibits a decrease in microhardness, which is likely associated with the onset of loss of coherence and coalescence of particles of the Al_3Sc type.

Using transmission microscopy after annealing at 440 °C for 4 h, the fine structure in both alloys was studied. This annealing mode was chosen because, according to microhardness data (Fig. 1), its greatest increase was observed in the range from 2 to 8 h. Therefore, it is under these heat treatment modes, that the precipitation of the largest amount of strengthening nanoparticles is expected.

Fig. 2 presents the results of transmission electron microscopy for 1570 alloy after annealing at 440 °C for 4 h.

Superstructure $L1_2$ reflections in 1570 alloy are visible quite clearly, which indicates the presence of Al_3Sc nanoparticles coherent with the aluminum matrix. Shown in Fig. 2 b data indicate the presence of large (about 1 μm) particles precipitated in the alloy structure. These particles are close in their chemical composition to $Al_6(Mn,Fe)$ (Fig. 3) and, like Al_3Sc, appear during the decomposition of a supersaturated solid solution, since this alloy contains Mn and Fe. One should note that iron in aluminum alloys is an unavoidable impurity.

Al_3Sc nanoparticles are also observed in 1570 alloy, when it is heated to a temperature of 440 °C. Fig. 2 b shows a predominance of particles with sizes in the range from 1.6 to 13.3 nm in 1570 alloy. This indicates a predominantly finely dispersed phase in this sample, however, bigger particles, larger than 25 nm, are also observed. In general, the average particle size is 11.4 nm, and their average density is $2.2 \cdot 10^{10}$ cm^{-2}. It should be noted that the particles in the grain volume are distributed very unevenly, which is observed in Fig. 2 c, 2 d. One can assume that this is a consequence of discontinuous decomposition in this alloy during cooling of the cast blank.

In the presented state (Fig. 4), superstructural reflections are not visible so clearly, but they are present, which is associated with a decrease in the coefficient of diffusion of scandium in aluminum when doping the alloys with hafnium. A rather large number of relatively coarse particles can be observed (Fig. 4 b). These particles are also close in chemical composition to $Al_6(Mn,Fe)$ (Fig. 3 and Table 2) and are explained by the presence of manganese and iron in the alloy.

In the 1570–0.5Hf alloy, particles with sizes ranging from 5.2 to 14.5 nm prevail (Fig. 4 b). At the same time, dark-field images also show the precipitation of particles larger than 25 nm. The average particle size in this alloy is 10.5 nm, and the distribution density is 2.6×10^{10} cm^{-2}. In this case, the uneven distribution of particles in the grain volume is somewhat reduced.

DISCUSSION

It should be noted that a comparison of the average particle size observed in 1570 alloy after casting in [18] and obtained in this study after heating at a temperature of 440 °C with a holding time of 4 h indicates that heat treatment practically does not change the number and size of particles. In both cases, their size is around 10 nm. This leads to the fact that the microhardness of this alloy does not change over time. The latter occurs because the major share of scandium precipitates during the continuous decomposition of a supersaturated solid solution when cooling the ingot during casting, as well as during the formation of primary intermetallides at the crystallization of this alloy [16]. Therefore, for the process of continuous decomposition of a supersaturated solid solution when heating a given alloy, there is no longer enough scandium and the number of particles does not change. One can assume that zirconium still quite actively blocks the growth of particles when annealed at 440 °C for 4 h, which does not contradict the data [19].

It is worth noting that the particles formed during decomposition can also be coherent and make a rather large contribution to strengthening [8]. In this case, their strengthening effect is confirmed by the fact that the microhardness after casting is significantly higher in 1570 alloy containing nanoparticles formed as a result of discontinuous decomposition, than in 1570 alloy with a 0.5 % hafnium content, in which they are absent in this state [10].

A sharp increase in microhardness during heat treatment of 1570 alloy with a 0.5 % hafnium content is explained

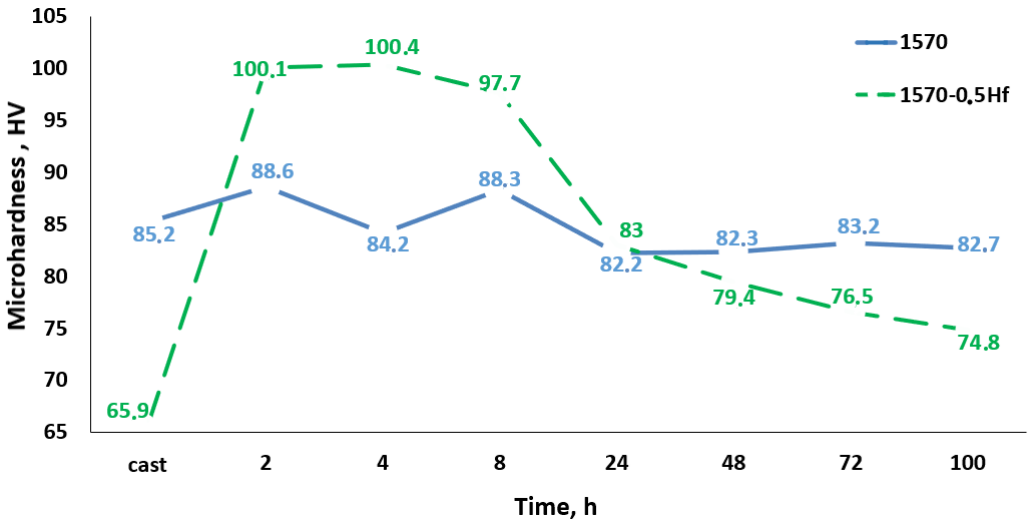

Fig. 1. *Change in microhardness during 440 °C annealing*
Рис. 1. *Изменение микротвердости при отжиге 440 °С*

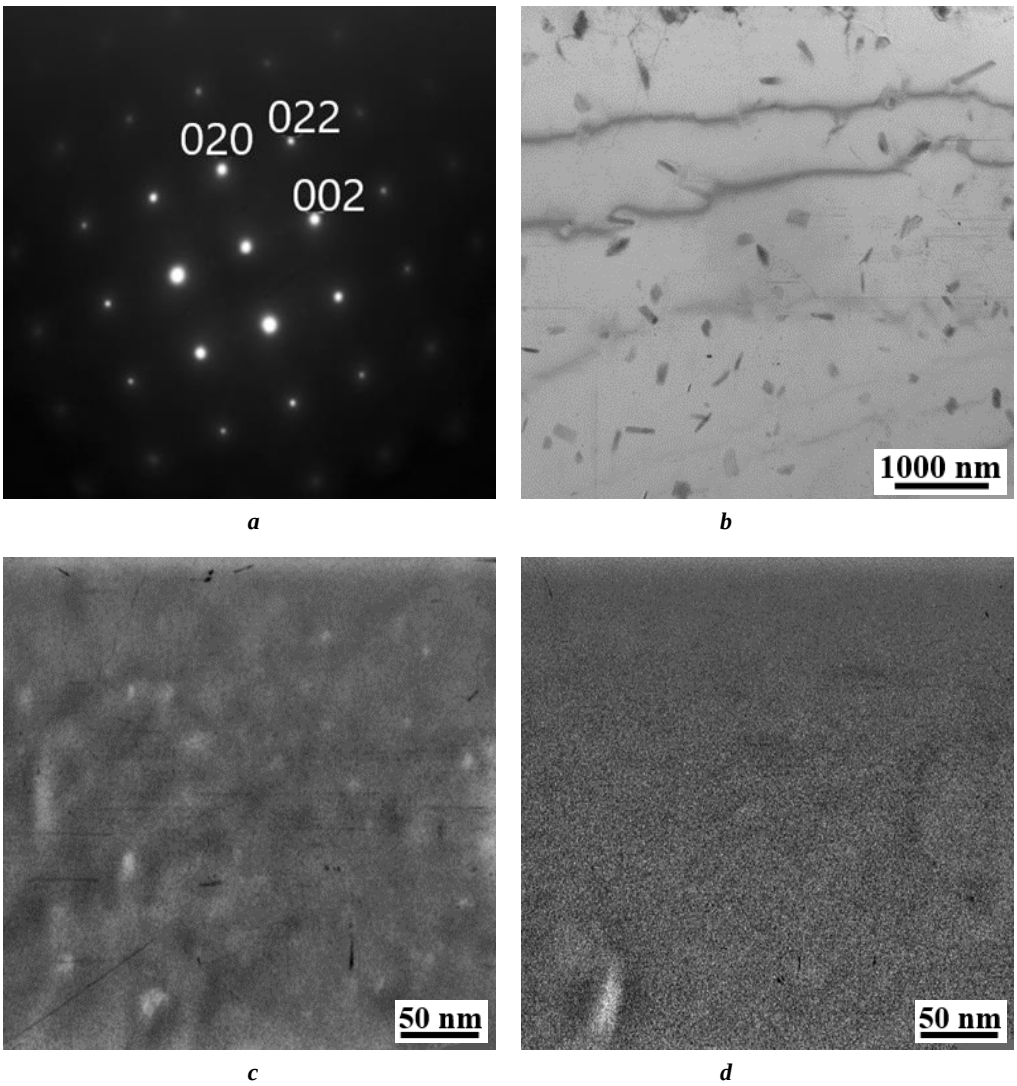

a ***b***

c ***d***

Fig. 2. *Fine structure of 1570 alloy during 440 °C annealing with a duration of 4 h:*
a *– microdifraction in the zone axis [001]$_\alpha$;* ***b*** *– bright field, ×20,000;* ***c, d*** *– dark field, ×200,000*
Рис. 2. *Тонкая структура сплава 1570 при отжиге при 440 °С длительностью 4 ч:*
а *– микродифракция в оси зоны [001]$_\alpha$;* ***b*** *– светлое поле, ×20 000;* ***c, d*** *– темное поле ×200 000*

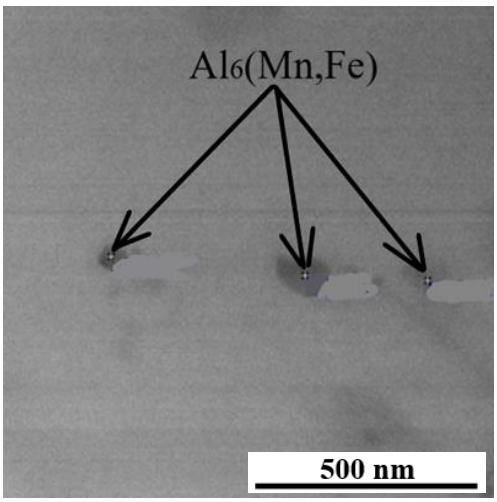

Fig. 3. *Areas of analysis of local chemical composition in a sample of 1570 alloy during 440 °C annealing with a duration of 4 h*
Рис. 3. *Участки анализа локального химического состава в образце сплава 1570 при отжиге 440 °С длительностью 4 ч*

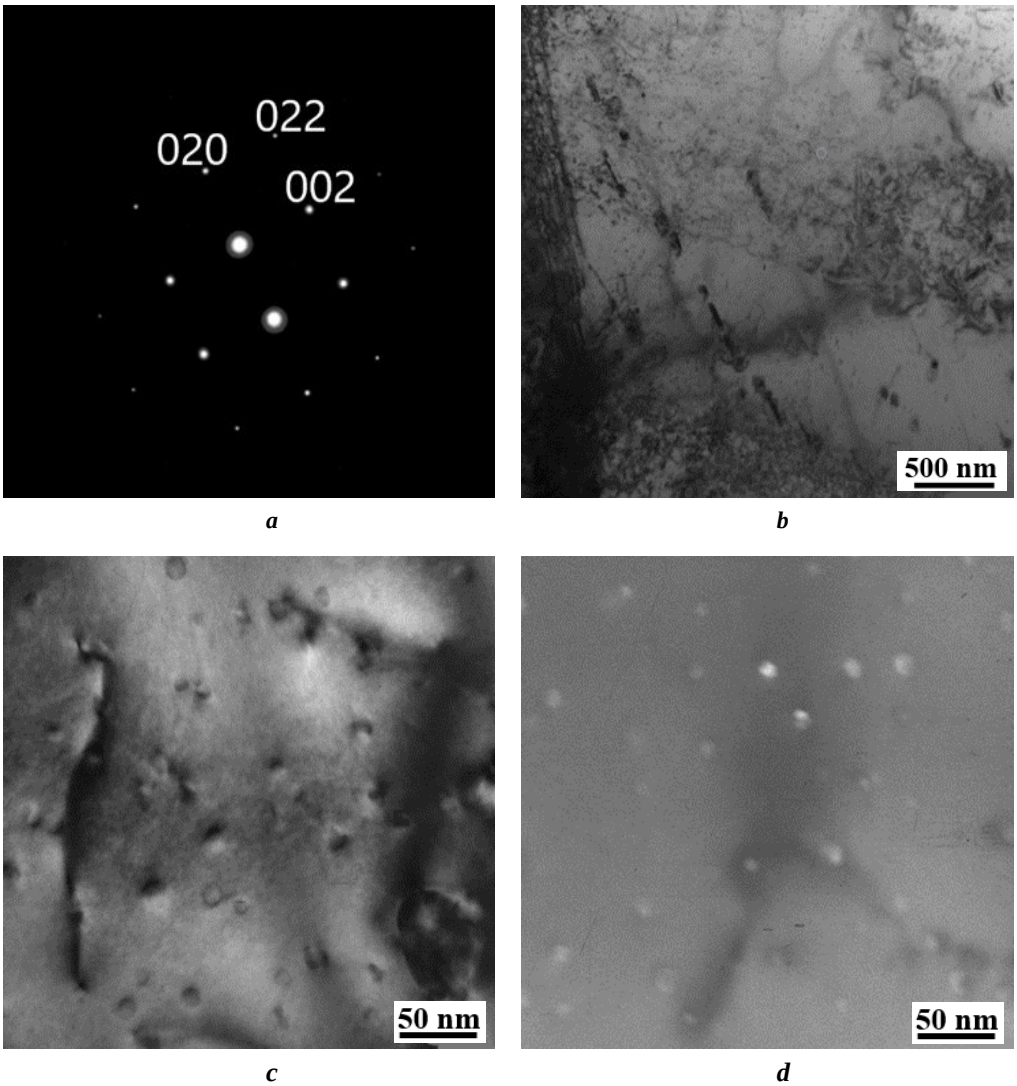

a ***b***

c ***d***

Fig. 4. *Fine structure of 1570–0.5Hf alloy during 440 °C annealing with a duration of 4 h:*
a *– microdifraction in the zone axis [001]$_\alpha$;* ***b*** *– bright field, ×20,000;* ***c, d*** *– dark field, ×200,000*
Рис. 4. *Тонкая структура сплава 1570–0,5Hf при отжиге при 440 °С длительностью 4 ч:*
а *– микродифракция в оси зоны [001]$_\alpha$;* ***b*** *– светлое поле, ×20 000;* ***c, d*** *– темное поле, ×200 000*

Table 2. *Local chemical composition of the particles in the 1570 alloy sample during 440 °C annealing with a duration of 4 h, at. %*
Таблица 2. *Локальный химический состав частиц в образце сплава 1570 при отжиге 440 °С длительностью 4 ч, ат. %*

Chemical elements	Al	Mn	Fe
Studied spectra	77.84	10.6	11.4

by the fact that active processes of precipitation of Al_3Sc particles from a supersaturated solid solution begin in it. This occurs because, unlike 1570 alloy, it retains enough scandium for continuous decomposition. Note that there are several possible reasons for suppressing the discontinuous decomposition of a supersaturated solid solution with the help of hafnium [16]. Not dwelling on the hypotheses in detail, one can state that the absence of discontinuous decomposition in alloys when doped with hafnium allows activating the formation of Al_3Sc nanoparticles, which as a result leads to an increase in microhardness. The higher properties of the 1570–0.5Hf alloy are generally explained by a larger number of nanoparticles and their more even precipitation. A more finely dispersed distribution of nanoparticles, in principle, distinguishes a solid solution with continuous decomposition from a discontinuous one [8]. With further heating for several hours, the microhardness remains at the same level, which means that the nanoparticles retain their size and number. However, after holding for more than 8 hours, the microhardness begins to decrease, which indicates a coagulation process. Then its decrease slows down significantly, which indicates the inhibition of coagulation processes. The lower microhardness values in 1570–0.5Hf alloy during long holding can be explained by the fact that a larger number of particles are available for the coalescence process in it than in 1570 alloy. Thus, hafnium additives make it possible to provide a significant advantage in strength properties during the first 8–10 h of heating, however, and then it is lost. It should also be noted that further study of the influence of hafnium additions on the thermal stability of Al_3Sc particles should be carried out in low-alloyed aluminum alloys (possibly with a lower scandium and zirconium content), which allow dissolving the discontinuous decomposition products. This will make it possible to distinguish the influence of an increase in strength properties resulting from the inhibition of discontinuous decomposition during the recrystallization process from the effect obtained by increasing the thermal stability of Al_3Sc nanoparticles.

CONCLUSIONS

1. Hafnium additives have a positive effect on the properties of 1570 alloy during heat treatment. Hafnium prevents the process of discontinuous decomposition of a supersaturated solid solution both during the ingot cooling after crystallization and during subsequent heat treatment.

2. It was found that in 1570 alloy with hafnium additives, during heat treatment, the total fraction of particles increases while their average size decreases in comparison with the original 1570 alloy.

3. Time intervals of 2–8 h are the most successful annealing mode for alloys with hafnium additives at a temperature of 440 °C. This is associated with the precipitation of strengthening Al_3Sc particles from the supersaturated solid solution; while for 1570 alloy, microhardness indicators remain unchanged, due to the fact that all nanosized dispersoids precipitate during the discontinuous decomposition of the solid solution.

REFERENCES

1. Ri E.Kh., Ri Kh., Deev V.B., Kolisova M.V. Effect of scandium on the structure, segregation and properties of the aluminium cast alloy AM4.5CD. *Tsvetnye metally*, 2019, no. 7, pp. 78–85. DOI: 10.17580/tsm.2019.07.10.
2. Zakharov V.V., Fisenko I.A., Kunyavskaya T.M. Prospects of alloying of aluminium alloys with scandium. *Tekhnologiya legkikh splavov*, 2020, no. 1, pp. 28–34. EDN: PDWRPX.
3. Lei Zhiguo, Wen Shengping, Huang Hui, Wei Wu, Nie Zuoren. Grain Refinement of Aluminum and Aluminum Alloys by Sc and Zr. *Metals*, 2023, vol. 13, no. 4, article number 751. DOI: 10.3390/met13040751.
4. Li Qinglin, Zhang Yushi, Lan Yefeng, Pei Ruijie, Feng Xiangyu, Xia Tiandong, Liu Dexue. Effect of scandium addition on microstructure and mechanical properties of as-cast Al–5%Cu alloys. *Vacuum*, 2020, vol. 177, article number 109385. DOI: 10.1016/j.vacuum.2020.109385.
5. Yu Kun, Li Wenxian, Li Songrui, Zhao Jun. Mechanical properties, and microstructure of aluminum alloy 2618 with Al_3(Sc, Zr) phases. *Materials Science and Engineering: A*, 2004, vol. 368, no. 1-2, pp. 88–93. DOI: 10.1016/j.msea.2003.09.092.
6. Rokhlin L.L., Bochvar N.R., Tarytina I.E. Joint effect of scandium and zirconium on the recrystallization of aluminum Al–Mg_2Si alloys. *Russian metallurgy (Metally)*, 2015, vol. 2015, no. 5, pp. 381–388. DOI: 10.1134/S0036029515050134.
7. Davydov V.G., Elagin V.I., Zakharov V.V., Rostova T.D. About scandium and zirconium additions in aluminium alloys. *Metal Science and Heat Treatment*, 1996, vol. 38, no. 7-8, pp. 347–352. DOI: 10.1007/bf01395323.
8. Zakharov V.V. The effect of scandium on the structure and properties of aluminum alloys. *Metal Science and Heat Treatment*, 2003, vol. 45, no. 7-8, pp. 246–253. DOI: 10.1023/A:1027368032062.
9. Zakharov V.V. Kinetics of decomposition of the solid solution of scandium in aluminum in binary Al–Sc alloys. *Metal Science and Heat Treatment*, 2015, vol. 57, no. 7-8, pp. 410–414. DOI: 10.1007/s11041-015-9897-z.
10. Forbord B., Lefebvre W., Danoix F., Hallem H., Marthinsen K. Three-dimensional atom probe investigation on the formation of Al_3(Sc, Zr)-dispersoids in aluminium

alloys. *Scripta materialia*, 2004, vol. 51, no. 4, pp. 333–337. DOI: 10.1016/j.scriptamat.2004.03.033.
11. Zakharov V.V. Stability of the solid solution of scandium in aluminum. *Metal Science and Heat Treatment*, 1997, vol. 39, no. 1-2, pp. 61–66. DOI: 10.1007/bf02467664.
12. Röyset J., Ryum N. Scandium in aluminium alloys. *International Materials Reviews*, 2005, vol. 50, no. 1, pp. 19–44. DOI: 10.1179/174328005X14311.
13. Li Hong-ying, Li De-wang, Zhu Zhi-xiang, Chen Bao-an, Chen Xin, Yang Chang-long, Zhang Hong-yu, Kang Wei. Grain refinement mechanism of as-cast aluminum by hafnium. *Transactions of Nonferrous Metals Society of China*, 2016, vol. 26, no. 12, pp. 3059–3069. DOI: 10.1016/S1003-6326(16)64438-2.
14. Jia Zhi-Hong, Huang Hui-Lan, Wang Xue-Li, Xing Yuan, Liu Qing. Hafnium in aluminum alloys: a review. *Acta Metallurgica Sinica*, 2016, vol. 29, pp. 105–119. DOI: 10.1007/s40195-016-0379-0.
15. Drits A.M., Aryshenskiy E.V., Kudryavtsev E.A., Zorin I.A., Konovalov S.V. The study of supersaturated solid solution decomposition in magnesium-rich aluminum alloys with scandium and hafnium additions. *Frontier Materials & Technologies*, 2022, no. 4, pp. 38–48. DOI: 10.18323/2782-4039-2022-4-38-48.
16. Zorin I.A., Aryshenskiy E.V., Drits A.M., Konovalov S.V., Komarov V.S. Effect of hafnium on cast microstructure in alloy 1570. *Izvestiya vysshikh uchebnykh zavedeniy. Tsvetnaya metallurgiya*, 2023, vol. 29, no. 1, pp. 56–65. DOI: 10.17073/0021-3438-2023-1-56-65.
17. Yashin V.V., Rushchits S.V., Aryshenskiy E.V., Latushkin I.A. Rheological behavior of 01570 and AA5182 wrought aluminum alloys under hot deformation conditions. *Tsvetnye metally*, 2019, no. 3, pp. 64–69. DOI: 10.17580/tsm.2019.03.09.
18. Zorin I.A., Drits A.M., Aryshenskiy E.V., Konovalov S.V., Grechnikov F.V., Komarov V.S. Effect of transition metals on as-cast aluminum alloys microstructure composition. *Fundamentalnye problemy sovremennogo materialovedeniya*, 2022, vol. 19, no. 4, pp. 520–531. DOI: 10.25712/ASTU.1811-1416.2022.04.011.
19. Zakharov V.V. About joint alloying of aluminum alloys with scandium and zirconium. *Metal Science and Heat Treatment*, 2014, vol. 56, no. 5-6, pp. 281–286. DOI: 10.1007/s11041-014-9746-5.

СПИСОК ЛИТЕРАТУРЫ

1. Ри Э.Х., Ри Х., Деев В.Б., Колисова М.В. Влияние скандия на структурообразование, ликвационные процессы и свойства литейного алюминиевого сплава АМ4,5Кд // Цветные металлы. 2019. № 7. С. 78–85. DOI: 10.17580/tsm.2019.07.10.
2. Захаров В.В., Фисенко И.А., Кунявская Т.М. Перспективы легирования алюминиевых сплавов скандием // Технология легких сплавов. 2020. № 1. С. 28–34. EDN: PDWRPX.
3. Lei Zhiguo, Wen Shengping, Huang Hui, Wei Wu, Nie Zuoren. Grain Refinement of Aluminum and Aluminum Alloys by Sc and Zr // Metals. 2023. Vol. 13. № 4. Article number 751. DOI: 10.3390/met13040751.
4. Li Qinglin, Zhang Yushi, Lan Yefeng, Pei Ruijie, Feng Xiangyu, Xia Tiandong, Liu Dexue. Effect of scandium addition on microstructure and mechanical properties of as-cast Al–5%Cu alloys // Vacuum. 2020. Vol. 177. Article number 109385. DOI: 10.1016/j.vacuum.2020.109385.
5. Yu Kun, Li Wenxian, Li Songrui, Zhao Jun. Mechanical properties, and microstructure of aluminum alloy 2618 with $Al_3(Sc, Zr)$ phases // Materials Science and Engineering: A. 2004. Vol. 368. № 1-2. P. 88–93. DOI: 10.1016/j.msea.2003.09.092.
6. Рохлин Л.Л., Бочвар Н.Р., Тарытина И.Е. Влияние скандия совместно с цирконием на рекристаллизацию алюминиевых сплавов системы Al–Mg_2Si // Металлы. 2015. № 3. С. 51–59. EDN: TNZOKN.
7. Davydov V.G., Elagin V.I., Zakharov V.V., Rostova T.D. About scandium and zirconium additions in aluminium alloys // Металловедение и термическая обработка металлов. 1996. № 8. С. 25–30. EDN: MOVQJR.
8. Захаров В.В. Влияние скандия на структуру и свойства алюминиевых сплавов // Металловедение и термическая обработка металлов. 2003. № 7. С. 7–15. EDN: QIWYNV.
9. Захаров В.В. Кинетика распада твердого раствора скандия в алюминии в двойных сплавах Al–Sc // Металловедение и термическая обработка металлов. 2015. № 7. С. 44–48. EDN: UAVTYF.
10. Forbord B., Lefebvre W., Danoix F., Hallem H., Marthinsen K. Three-dimensional atom probe investigation on the formation of $Al_3(Sc, Zr)$-dispersoids in aluminium alloys // Scripta materialia. 2004. Vol. 51. № 4. P. 333–337. DOI: 10.1016/j.scriptamat.2004.03.033.
11. Zakharov V.V. Stability of the solid solution of scandium in aluminum // Metal Science and Heat Treatment. 1997. Vol. 39. № 1-2. P. 61–66. DOI: 10.1007/bf02467664.
12. Röyset J., Ryum N. Scandium in aluminium alloys // International Materials Reviews. 2005. Vol. 50. № 1. P. 19–44. DOI: 10.1179/174328005X14311.
13. Li Hong-ying, Li De-wang, Zhu Zhi-xiang, Chen Bao-an, Chen Xin, Yang Chang-long, Zhang Hong-yu, Kang Wei. Grain refinement mechanism of as-cast aluminum by hafnium // Transactions of Nonferrous Metals Society of China. 2016. Vol. 26. № 12. P. 3059–3069. DOI: 10.1016/S1003-6326(16)64438-2.
14. Jia Zhi-Hong, Huang Hui-Lan, Wang Xue-Li, Xing Yuan, Liu Qing. Hafnium in aluminum alloys: a review // Acta Metallurgica Sinica. 2016. Vol. 29. P. 105–119. DOI: 10.1007/s40195-016-0379-0.
15. Дриц А.М., Арышенский Е.В., Кудрявцев Е.А., Зорин И.А., Коновалов С.В. Исследование распада пересыщенного твердого раствора в высокомагниевых алюминиевых сплавах со скандием, легированных гафнием // Frontier Materials & Technologies. 2022. № 4. С. 38–48. DOI: 10.18323/2782-4039-2022-4-38-48.
16. Зорин И.А., Арышенский Е.В., Дриц А.М., Коновалов С.В., Комаров В.С. Влияние гафния на литую микроструктуру в сплаве 1570 // Известия высших учебных заведений. Цветная металлургия. 2023. Т. 29. № 1. С. 56–65. DOI: 10.17073/0021-3438-2023-1-56-65.
17. Яшин В.В., Рущиц С.В., Арышенский Е.В., Латушкин И.А. Реологические свойства деформируемых алюминиевых сплавов 01570 и AA5182 в условиях горячей деформации // Цветные металлы. 2019. № 3. С. 64–69. DOI: 10.17580/tsm.2019.03.09.

18. Зорин И.А., Дриц А.М., Арышенский Е.В., Коновалов С.В., Гречников Ф.В., Комаров В.С. Влияние переходных металлов на микроструктурную композицию алюминиевых сплавов в литом состоянии // Фундаментальные проблемы современного материаловедения. 2022. Т. 19. № 4. С. 520–531. DOI: 10.25712/ASTU.1811-1416.2022.04.011.
19. Захаров В.В. О совместном легировании алюминиевых сплавов скандием и цирконием // Металловедение и термическая обработка металлов. 2014. № 6. С. 3–8. EDN: SJXNSD.

Влияние гафния на высокомагниевые сплавы, легированные переходными металлами, при термической обработке

Зорин Игорь Александрович[*1,2,4], лаборант-исследователь, студент,
инженер-электроник II категории лаборатории механических испытаний и электронной микроскопии
Арышенский Евгений Владимирович[2,5], доктор технических наук, доцент,
старший научный сотрудник лаборатории электронной микроскопии и обработки изображений
Кудрявцев Егор Алексеевич[3,6], кандидат технических наук,
научный сотрудник Центра коллективного пользования «Технологии и Материалы НИУ "БелГУ"»
Дриц Александр Михайлович[1,7], кандидат технических наук,
ведущий научный сотрудник
Коновалов Сергей Валерьевич[2,8], доктор технических наук, профессор,
проректор по научной и инновационной деятельности
[1]*Самарский национальный исследовательский университет имени академика С.П. Королева, Самара (Россия)*
[2]*Сибирский государственный индустриальный университет, Новокузнецк (Россия)*
[3]*Белгородский государственный национальный исследовательский университет, Белгород (Россия)*

***E-mail: zorin.ia@ssau.ru**

[4]ORCID: https://orcid.org/0000-0001-9349-2494
[5]ORCID: https://orcid.org/0000-0003-3875-7749
[6]ORCID: https://orcid.org/0000-0003-1113-0807
[7]ORCID: https://orcid.org/0000-0002-9468-8736
[8]ORCID: https://orcid.org/0000-0003-4809-8660

Поступила в редакцию 03.08.2023 *Принята к публикации 20.11.2023*

Аннотация: Целью работы является изучение влияния добавок гафния на механические свойства и термостабильность частиц при повышенной температуре термической обработки алюминиевых сплавов с высоким содержанием магния. Для изучения был выбран сплав 1570 в двух модификациях: без содержания гафния и с его добавкой 0,5 % по массе. Оба сплава были подвергнуты гомогенизационному отжигу при температуре 440 °С с различными режимами выдержки, которые составили от 2 до 100 ч. Для различных режимов термической обработки изучалась микротвердость, а также с помощью просвечивающей микроскопии исследовалась тонкая микроструктура. В результате удалось установить, что в процессе отжига при малом времени выдержки (2–8 ч) сплав с добавкой гафния имеет более высокие показатели микротвердости, превосходя показатели сплава 1570 в среднем на 20 HV. Это связано с тем, что в сплаве 1570 с добавками гафния при термообработке увеличивается количество выделяющихся частиц при одновременном уменьшении их среднего размера по сравнению с базовым сплавом. В то же время в сплаве 1570 без содержания гафния при его отжиге при температуре 440 °С роста микротвердости не происходит. Это обусловлено тем, что в сплаве 1570 без содержания гафния при остывании после литья происходит прерывистый распад, в результате которого большая часть скандия выделяется из пересыщенного твердого раствора в виде дисперсоидов. В сплаве с добавками гафния такого явления не наблюдается, что свидетельствует о его способности останавливать прерывистый распад в процессе охлаждения слитка после литья.

Ключевые слова: алюминиевые сплавы; переходные металлы; скандий; гафний; термообработка; упрочняющие наночастицы.

Благодарности: Исследование выполнено за счет гранта РНФ № 22–29–01506, https://rscf.ru/project/22-29-01506/.

Работа выполнена с использованием оборудования Центра коллективного пользования «Технологии и Материалы НИУ "БелГУ"».

Для цитирования: Зорин И.А., Арышенский Е.В., Кудрявцев Е.А., Дриц А.М., Коновалов С.В. Влияние гафния на высокомагниевые сплавы, легированные переходными металлами, при термической обработке // Frontier Materials & Technologies. 2024. № 1. С. 29–36. DOI: 10.18323/2782-4039-2024-1-67-3.

doi: 10.18323/2782-4039-2024-1-67-4

Special aspects of the microstructure evolution at the temperature-speed deformation of a medical purpose magnesium alloy of the Mg–Zn–Y alloying system

Kristina K. Kudasheva*, engineer of the Research Institute of Advanced Technologies
Mikhail L. Linderov[1], PhD (Physics and Mathematics),
senior researcher of the Research Institute of Advanced Technologies
Aleksandr I. Brilevskiy[2], junior researcher
of the Research Institute of Advanced Technologies
Aleksey V. Danyuk[3], PhD (Physics and Mathematics),
senior researcher of the Research Institute of Advanced Technologies
Igor S. Yasnikov[4], Doctor of Sciences (Physics and Mathematics), Associate Professor,
professor of Chair "General and Theoretical Physics",
leading researcher of the Research Institute of Advanced Technologies
Dmitry L. Merson[5], Doctor of Sciences (Physics and Mathematics), Professor,
Director of the Research Institute of Advanced Technologies
Togliatti State University, Togliatti (Russia)

***E-mail: a.abdugaffarova@gmail.com**

[1]ORCID: https://orcid.org/0000-0001-8655-4191
[2]ORCID: https://orcid.org/0000-0002-5780-6094
[3]ORCID: https://orcid.org/0000-0002-7352-9947
[4]ORCID: https://orcid.org/0000-0002-6120-7836
[5]ORCID: https://orcid.org/0000-0001-5006-4115

Received 15.06.2023 *Accepted 26.07.2023*

Abstract: Biocompatibility makes magnesium alloys attractive functional materials in terms of their use as biodegradable implants. However, the technologies for manufacturing semi-finished products carry a possible diversity of the local strain rate and temperature within a rather wide range, which affects the processed material structure and properties. The purpose of this study is to determine the range of temperatures and resistance to deformation, at which there is no negative effect on the main structural characteristics of the processed material, using the example of a medical purposes alloy of the Mg–Zn–Y alloying system. The authors carried out mechanical tests of a biodegradable Mg–1Zn–2.9Y magnesium alloy at various temperatures and strain rates. The influence of temperatures in the range of 20...400 °C on the structure and properties of the Mg–Zn–Y system alloy is disclosed. Starting from a temperature of 350 °C, the process of dynamic recrystallisation is accompanied both by the complete restoration (return) of the original microstructure and by coarsening of the grain size, which can adversely affect the material functional characteristics. The high thermal stability of the biodegradable Mg–1Zn–2.9Y magnesium alloy is revealed, which probably results from the presence of the LPSO phase in it. The study shows that the deformation process is accompanied by twinning. At a strain rate of $2 \cdot 10^{-2}$ s^{-1} over the entire temperature range, the grain size distribution slightly narrows and shifts towards smaller diameters. The application of the obtained results in technological processes for manufacturing medical semi-finished products will help to solve the issue of microstructure instability at the stage of transition from a semi-finished product to a finished product during subsequent thermomechanical treatments.

Keywords: medical purpose magnesium alloys; biodegradable magnesium alloys; Mg–1Zn–2.9Y; temperature-speed deformation; medical purpose alloy; magnesium alloys; dynamic recrystallisation; microstructure evolution.

Acknowledgements: The research is financially supported by the Russian Science Foundation within the scientific project No. 20-19-00585.

The paper was written using the reports of the participants of the XI International School of Physical Materials Science (SPM-2023), Togliatti, September 11–15, 2023.

For citation: Kudasheva K.K., Linderov M.L., Brilevskiy A.I., Danyuk A.V., Yasnikov I.S., Merson D.L. Special aspects of the microstructure evolution at the temperature-speed deformation of a medical purpose magnesium alloy of the Mg–Zn–Y alloying system. *Frontier Materials & Technologies*, 2024, no. 1, pp. 37–47. DOI: 10.18323/2782-4039-2024-1-67-4.

INTRODUCTION

Recently, biodegradable magnesium alloys have drawn the attention of developers of medical materials due to their attractive properties, including osteointegration [1; 2]. In fact, they formed a separate class of new generation biodegradable metal materials. Compared to other metal materials used as orthopaedic implants, such as titanium, titanium alloys, and stainless steels, the elastic modulus of magnesium alloys is closest in value

to that of human bone tissue [3]. Moreover, magnesium and its alloys are already used as temporary implants that are completely degradable in a biological environment (*in vivo*), and are replaced by newly formed bone, which eliminates the necessity of repeated surgical interference to remove the implant. Many studies have proven that magnesium alloys are safe, and effective materials for medical implants [3–5]. Magnesium ions released from the alloy showed good biological activity [6–8]. The magnesium alloy implanted in the human body is gradually destroyed (dissolved) and absorbed [9], and excess magnesium ions are removed from the human body due to metabolism. The absence of the necessity of repeated operations to remove implants significantly reduces morbidity and the risk of injury. This feature makes them extremely attractive to the market of biodegradable metal implants designed to restore bones that require temporary support.

Despite all the advantages, magnesium and its alloys are characterised by relatively low strength and corrosion resistance. Many studies have been carried out to improve their mechanical properties and corrosion resistance by alloying [10; 11]. For example, the addition of rare-earth metals promotes dynamic recrystallisation of magnesium alloys and increases tensile strength without loss of ductility [12; 13]. The addition of yttrium (Y) can simultaneously improve both ductility [14] and corrosion resistance [15] of a magnesium alloy. Moreover, a significant improvement in the properties of magnesium alloys is possible due to surface modification [16].

At present, much attention is paid to the hardening of magnesium and its alloys by methods based on severe plastic deformation (SPD), in particular, multi-axial isothermal forging [17]. Magnesium and its alloys are poorly deformed, since they have a hexagonal close-packed lattice, and only two primary slip systems: (0001)<1120> and (1010)<1120> [18]. To increase the number of possible slip systems, it is usually necessary to increase the deformation processing temperature, which naturally negatively affects the final properties of the material [19].

The modern technology for manufacturing macroscopic products from magnesium and its alloys is quite well deveoped, however, for most medical products, semi-finished products of small sizes in one or two dimensions (foil, thin-walled tubes, wire, etc.) are required. The manufacture of such semi-finished products is associated with the application of large deformation technologies (drawing, rolling, and extrusion). The development of a technology for the production of medical devices is impossible without knowing the temperature-velocity behaviour of alloys in the process of active deformation. At the same time, the ultimate goal is both to develop a technology for manufacturing thin-walled semi-finished products and to form the required functional properties, which are largely determined by the microstructure characteristics.

Since the microstructure of metals and alloys is formed as a result of dynamic rearrangements of a defective ensemble, and acoustic emission (AE) arising during their deformation is a unique phenomenon capable of precisely reflecting defect dynamics [20], in this work, we will use AE as an experimental method of controlling and diagnosing the evolution of a defective ensemble *in situ*, including for monitoring possible recrystallisation processes.

The purpose of this work is to determine the influence of temperature-velocity factors on possible recrystallisation processes and microstructure parameters of a medical purpose alloy of the Mg–Zn–Y alloying system.

METHODS

Material and test samples

To carry out the research, a low alloy with a nominal composition of Mg–1Zn–2.9Y (at. %) was selected, which was manufactured based on Mg95V pig magnesium at SOMZ LLC (Solikamsk).

The chemical composition of the produced alloy was determined using an ARL 4460-1632 high-precision optical emission spectrometer. The results of the chemical composition analysis are shown in Table 1.

End sections containing casting defects were cut off from the resulting castings, and to remove surface defects, the castings were machined on a lathe. After mechanical treatment, the blanks were subjected to homogenising at 430 °C for 24 h.

Multi-axial isothermal forging (MIF) was carried out at the production base of the IMSP RAS (Ufa). When performing each forging cycle, the total degree of deformation ε was about 1.4. MIF was implemented using a PA2638 hydraulic press (630 tf) equipped with a UIShB 510 isothermal die block with flat dies and an induction heater. In total, the blank underwent 16 forging cycles in the temperature range of 325...400 °C. At the final stage, to obtain plates, the blank was upset on a press at 325 °C.

The mechanical properties of the resulting material were evaluated using two types of cylindrical specimens made according to the drawings (Fig. 1). For mass testing, the samples had a working part with a diameter of 5 mm and a length of 25 mm (Fig. 1 a), and for tests with AE registration, the samples were more massive: 8 mm in diameter, 40 mm long, and with a flat for installing an AE sensor (Fig. 1 b). The longitudinal axis of the samples corresponded to the expanding direction (RD) after upsetting.

Experimental technique

Samples were tested for uniaxial tension on an Instron 8802 universal servohydraulic testing system (England) with nominal strain rates: $5\cdot10^{-4}$, $5\cdot10^{-3}$, $2\cdot10^{-2}$ s^{-1}, using an Instron 3119-406 climate chamber at temperatures: 20, 100, 150, 200, 250, 300, and 400 °C (heating uniformity was controlled using thermocouples).

Additional tests were carried out:

1) the alloy in the initial state was kept in a furnace at 400 °C (the holding time was chosen to be equal to the time of testing the sample with a strain rate of $5\cdot10^{-3}$ s^{-1} by 8 %);

2) the alloy in the initial state was deformed by 8 % with a strain rate of $5\cdot10^{-3}$ s^{-1} at room temperature, and then kept in a furnace at 400 °C (the holding time was chosen to be equal to the time of testing the sample with a strain rate of $5\cdot10^{-3}$ s^{-1} by 8 %).

Table 1. *Chemical composition of the Mg–Zn–Y system alloy*
Таблица 1. *Химический состав сплава системы Mg–Zn–Y*

Name of alloy	Alloying elements, at. %				
	Mg	Zn	Y	Zr*	Other elements' amount
Mg–1Zn–2.9Y	Base	0.8	2.2	0.076	0.1

*Note. *Zirconium is added to a melt to reduce the content of iron impurities and grain refinement.*
*Примечание. *Цирконий добавляется в расплав для снижения содержания примесей железа и измельчения зерна.*

a ***b***

Fig. 1. *Specimens for mechanical tests:* ***a*** *– for mass temperature-speed tests;*
b *– with a flat for tests with simultaneous recording of an acoustic emission signal*
Рис. 1. *Образцы для механических испытаний:* ***a*** *– для массовых температурно-скоростных испытаний;*
b *– с лыской для испытаний с одновременной регистрацией сигнала акустической эмиссии*

Deformation was measured using an Epsilon 3448 extensometer (item 3, Fig. 2).

To record the AE signal, the authors used the equipment consisting of a MSAE-1300WB broadband piezoelectric transducer (Microsensors, Sarov) with an operating frequency range of 50...1300 kHz; a PAC 2/4/6 low-noise preamplifier (USA) with a bandwidth of 10...1200 kHz and an amplification of +60 dB; a PAC PCI-2 low-noise registration system, which allows recording a signal into the computer memory in streaming mode (stream) with a resolution of 16 bits and a signal sampling frequency of 2 MHz, input filter bandwidth of 100...1000 kHz, and additional amplification of +6 dB. After testing, the recorded stream was sequentially divided into frames with a duration of 4096 samples, for each of which the energy (E) and median frequency (fm) (the frequency dividing the area under the spectral density power curve into two equal parts) were calculated and synchronized with the deformation curve. The AE technique is described in more detail in our earlier work [20].

The microstructure study was carried out on cross-sectional tensile specimens (TD) in the middle of the working base. Microstructure analysis was performed using the EBSD method. The metallographic specimens were prepared by grinding on a sandpaper of different grain sizes, polishing using a diamond suspension (with a particle size ranging from 9 μm to 0.25 μm) and Hitachi IM4000 Plus finishing ion polishing (Japan) (the inclination of 3° to the surface, acceleration of 6 kV and discharge of 1.5 kV, argon gas 0.1 cm^3/min and 25 rpm 1–2 h).

To estimate the microstructure parameter, the authors used a Zeiss Sigma scanning electron microscope (Carl Zeiss, Germany) equipped with a TFE cathode and an EDAX/TSL backscattered electron diffraction detector (EDAX, Mahwa, New Jersey, USA). Microstructure scanning was carried out with a step of 250...350 nm, the structural element reliability criterion was 6÷8 points, with a codirectional orientation within 5°. Based on the obtained structure maps, histograms of grain-boundary angles and grain sizes were constructed. The diameter of a circle with an equivalent area was chosen as the grain size estimate.

RESULTS

The initial microstructure of the Mg–1Zn–2.9Y alloy (Fig. 3 a) consists of fine grains (average diameter is (1.5±0.7) μm) slightly elongated as a result of alloy upsetting after MIF. The grain size distribution is lognormal (Fig. 3 b), and the histogram of grain-boundary angles (Fig. 3 c) reveals a maximum around a 30° angle.

As an example, Fig. 4 shows mechanical diagrams for uniaxial tensile tests of specimens at temperatures of 20 (Fig. 4 a) and 200 °C (Fig. 4 b) with three strain rates.

Due to the fact that the level of AE signals turned out to be very low even at room temperature, it was possible to carry out correct tests only for the highest strain rate ($2\cdot10^{-2}$ s^{-1}). As an example, Fig. 5 shows diagrams of the AE parameters combined with the uniaxial tension curve in the test temperature range of 20–250 °C and at a strain rate of $2\cdot10^{-2}$ s^{-1}.

At elevated temperatures of mechanical tests, the presented diagrams (Fig. 5 b–d) show a sharp transition to plastic deformation resembling a yield tooth, which is not observed in tests at room temperature. The presence of two kinks is also visible in the diagram. In this interval (from the "yield tooth" to the last "kink"), the deformation is accompanied by a rather powerful AE.

The study of the microstructure in specimens tested at a maximum strain rate of $2\cdot10^{-2}$ s^{-1} at temperatures of 150, 200, 250, and 300 °C was carried out after loading was stopped at a total strain of 4, 8, and 16 %. As an example, a view of the microstructure (Fig. 6 a) is shown, as well as the histograms of grain size distributions (Fig. 6 b) and grain-boundary angles (Fig. 6 c) after tests at a temperature of 250 °C and with a degree of deformation of 16 %.

According to the results of the studies, no significant changes in the structure compared to the initial state (Fig. 3) at all temperatures and degrees of deformation were revealed. The investigated alloy has a high thermal stability, which is probably related to the presence of the LPSO phase in it.

Since no significant changes occurred in the structure in the temperature range of 20–300 °C, to find the boundary of such "insensitivity", it was decided to additionally test the specimens with a strain rate of $5\cdot10^{-3}$ s^{-1} up to a strain of 8 % at 350 and 400 °C. As can be seen, in these cases, the microstructure (Fig. 7, 8) consists of larger grains and the peak in the histogram of distribution of grain boundaries over the grain-boundary angles shifted closer to ~90°.

To identify the reasons for the growth of average grain size, which may be associated with dynamic or static recrystallisation, the authors carried out additional studies. Fig. 9 and 10 show the microstructures of the samples, as well as the grain size distributions and distributions of grain-boundary angles after soaking at 400 °C (Fig. 9) and after soaking at 400 °C of the Mg–1Zn–2.9Y alloy predeformed by 8 % at room temperature with a strain rate of $5\cdot10^{-3}$ s^{-1} (Fig. 10).

DISCUSSION

At the highest temperature of tests with AE registration (250 °C), the dependence of the median frequency on time (of strain) is of oscillatory character (Fig. 5 d). According to our hypothesis, this may be related to the recrystallisation nature, in particular, to the fact that, the dynamic recrystallisation process in the Mg–1Zn–2.9Y alloy proceeds continuously (does not coincide in time in spatially separated regions of the metal) due to the presence of the LPSO phase in it.

The study of the microstructure in samples tested at a maximum strain rate of $2\cdot10^{-2}$ s^{-1} at temperatures of 150, 200, 250, and 300 °C of testing carried out after the loading was stopped, and at a total strain of 4, 8, and 16 % (Fig. 6) showed no significant changes compared to the initial state (Fig. 3). The investigated alloy has a high thermal stability, which is probably related to the presence of the LPSO phase in it. However, the following peculiarities were identified:

1) in all cases, except for the initial state, the histograms of the grain-boundary angles show a high-angle component (a peak near 90°) associated with twin boundaries (Fig. 6 c), i. e., mechanical twinning was present in all the cases studied;

2) at the highest strain rate at all temperatures, the grain size distribution narrows and shifts towards smaller diameters in relation to the initial state, which has a positive effect on the material functional characteristics.

Comparing the results of action of a temperature of 400 °C on a material in the static state (in the initial (Fig. 9) and deformed by 8 % (Fig. 10) states) with the result of exposure to the same temperature, but in the dynamic mode (at active deformation (Fig. 8)) demonstrates fundamental changes. If in the dynamic mode at a temperature of 400 °C, compared to lower temperatures, the average grain size grows, but at a low grain size nonhomogeneity (Fig. 8 a, 8 b), then in the static mode at a temperature of 400 °C, the process of inhomogeneous recrystallisation occurs with the formation of interlayers of large grains (Fig. 9 a, 9 b), which is even more pronounced after a preliminary deformation of 8 % (Fig. 10 a, 10 b).

Thus, starting from a temperature of 350 °C, the process of dynamic recrystallisation in the alloy under study is accompanied both by the complete restoration (return) of the initial microstructure and by coarsening of the grain size, which can adversely affect the Mg–1Zn–2.9Y alloy functional parameters.

CONCLUSIONS

Based on the results of mechanical tests of a medical purpose magnesium alloy of the Mg–Zn–Y alloying system, it was found that in the range of test temperature (150÷300) °C and rate ($5\cdot10^{-4}$÷$2\cdot10^{-2}$) s^{-1}, no significant changes occur in the structure compared to the initial state (after multi-axial isothermal forging). The investigated alloy has a high thermal stability, which is obviously attributed to the presence of the LPSO phase in it. The formation of a peak near the 90° angle on the histograms of the distribution of grain-boundary angles indicates a significant role of the twinning process in the overall deformation process. Moreover, at the highest strain rate over the entire temperature range, the grain size distribution narrows slightly and shifts towards smaller diameters, which positively affects the Mg–1Zn–2.9Y alloy microstructure and the material functional characteristics.

Starting from a temperature of 350 °C, the process of dynamic recrystallisation is accompanied both by

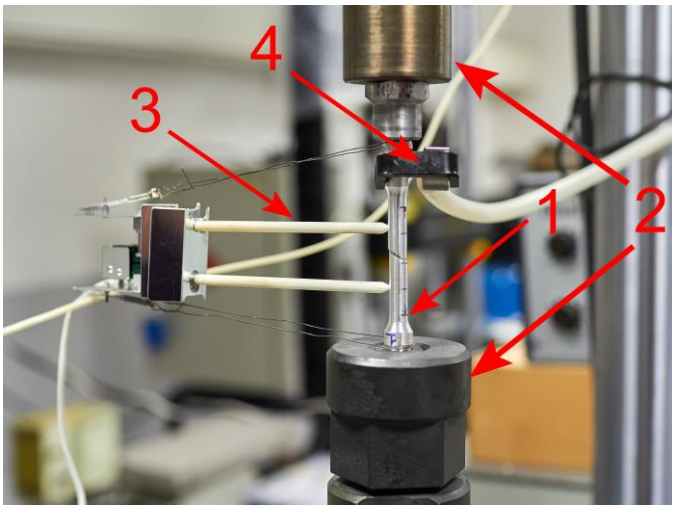

Fig. 2. *A unit for uniaxial tensile tests of specimens:*
1 – specimen; 2 – jaws; 3 – extensometer; 4 – acoustic emission sensor
Рис. 2. *Установка для испытаний на одноосное растяжение образцов:*
1 – образец; 2 – захваты; 3 – экстензометр; 4 – датчик акустической эмиссии

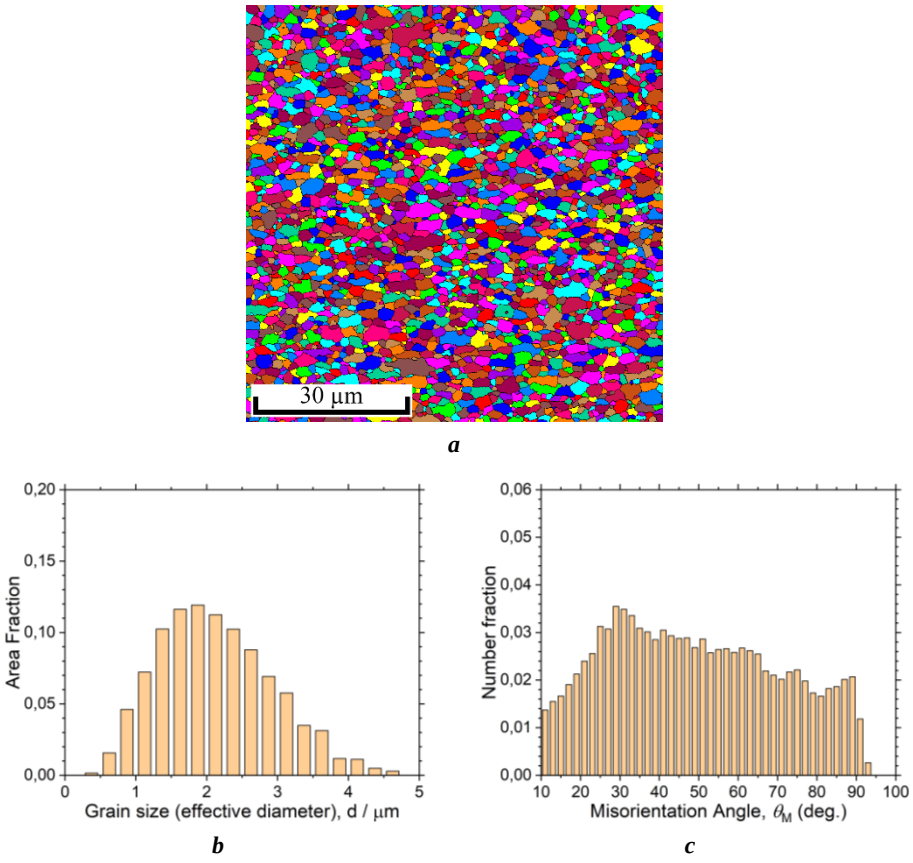

Fig. 3. *Microstructure (**a**), grain size distribution (**b**), and grain-boundary angle distribution (**c**) of the Mg–1Zn–2.9Y alloy in the initial state*
Рис. 3. *Микроструктура (**a**), распределение зерен по размерам (**b**) и распределение по углам разориентировки (**c**) сплава Mg–1Zn–2,9Y в исходном состоянии*

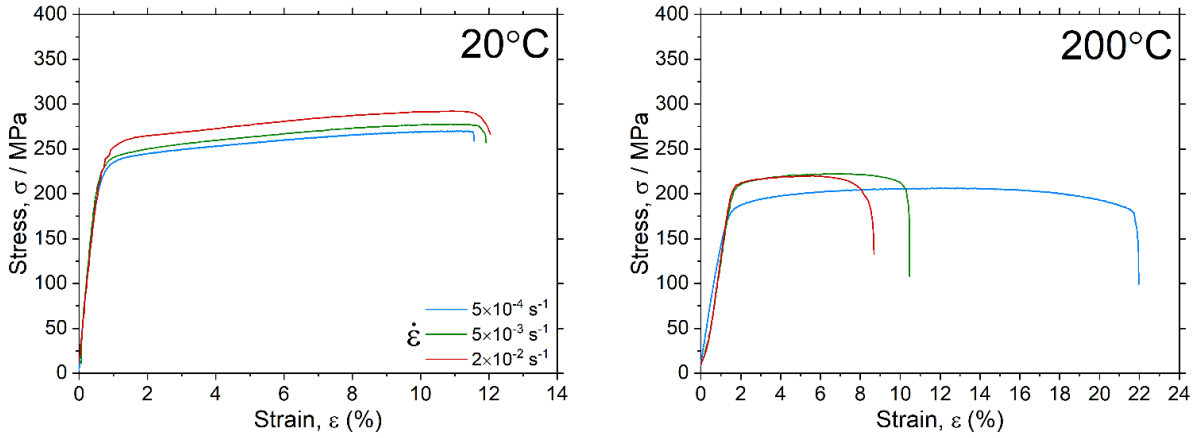

a *b*

Fig. 4. *Diagrams of mechanical tests in the "stress – strain" coordinates for three rates of deformation at temperatures of 20 °C (**a**) and 200 °C (**b**)*
Рис. 4. *Диаграммы механических испытаний в координатах «напряжение – деформация» для трех скоростей деформации при температурах 20 °C (**a**) и 200 °C (**b**)*

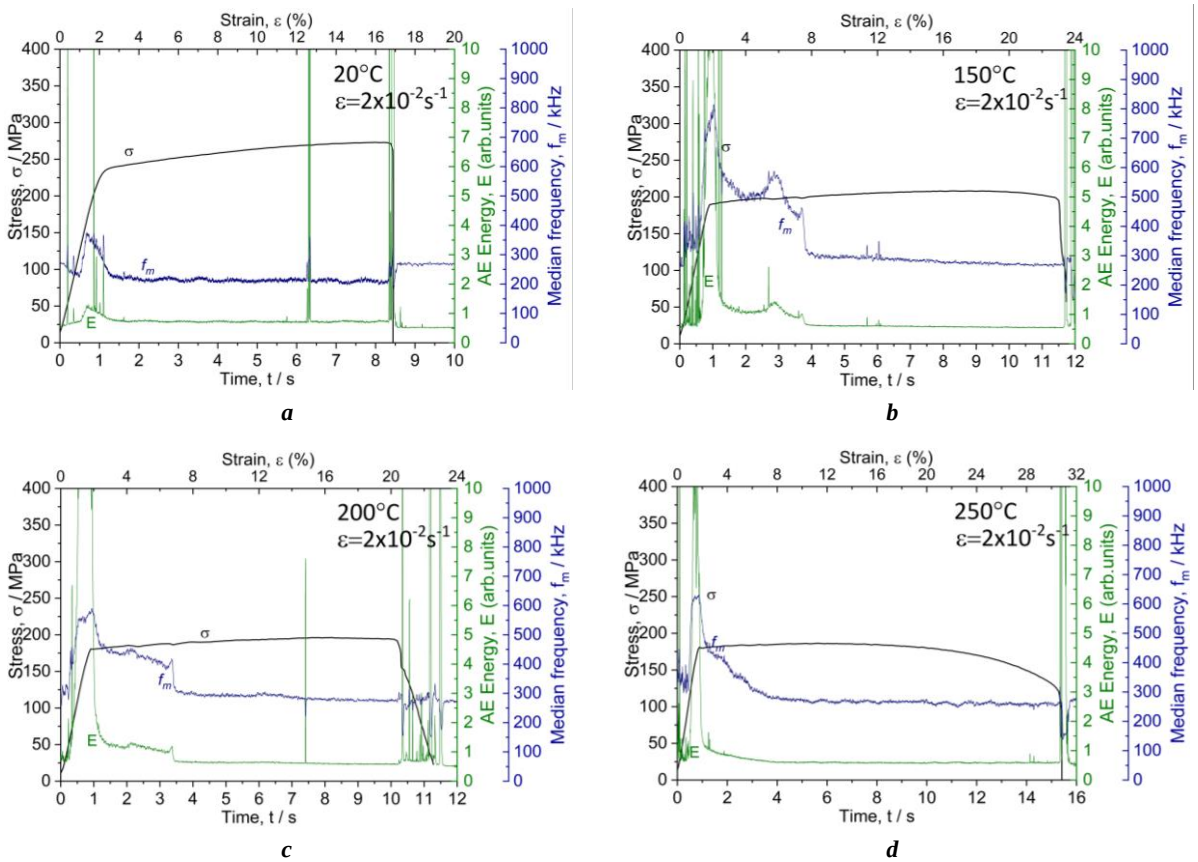

a *b*

c *d*

Fig. 5. *Diagrams of acoustic emission signal parameters brought in coincidence with the curve of uniaxial tension at test temperatures of 20 °C (**a**), 150 °C (**b**), 200 °C (**c**), and 250 °C (**d**) and deformation rate of $2 \cdot 10^{-2}$ s^{-1}*
Рис. 5. *Диаграммы параметров сигнала акустической эмиссии, совмещенные с кривой одноосного растяжения при температурах испытаний 20 °C (**a**), 150 °C (**b**), 200 °C (**c**) и 250 °C (**d**) и скоростью деформирования $2 \cdot 10^{-2}$ c^{-1}*

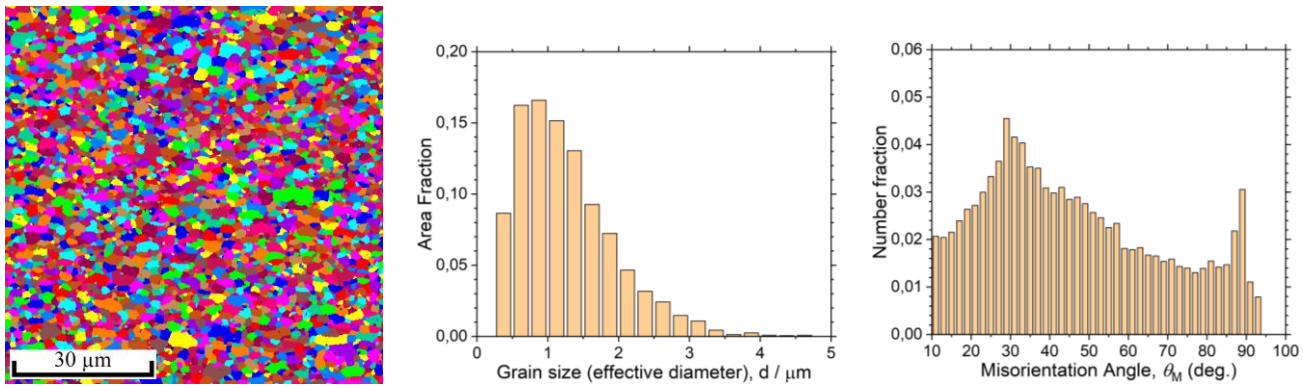

a *b* *c*

Fig. 6. *Microstructure (**a**), grain size distribution (**b**), and grain-boundary angle distribution (**c**) of the Mg–1Zn–2.9Y alloy after temperature tests at 250 °C with a deformation rate of $2 \cdot 10^{-2}$ s^{-1} and deformation degree of 16 %*
Рис. 6. *Микроструктура (**a**), распределение зерен по размерам (**b**) и распределение по углам разориентировки (**c**) сплава Mg–1Zn–2,9Y после температурных испытаний при 250 °C со скоростью деформации $2 \cdot 10^{-2}$ $с^{-1}$ и степенью деформации 16 %*

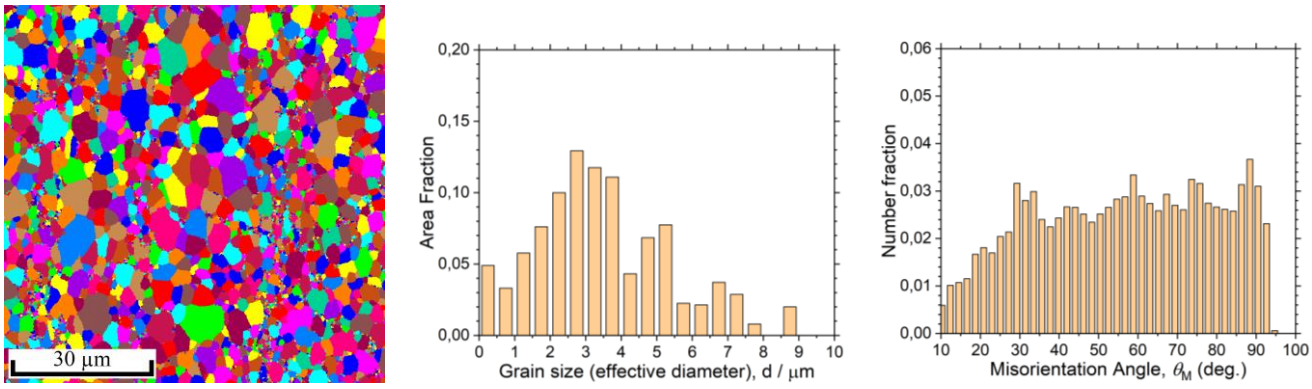

a *b* *c*

Fig. 7. *Microstructure (**a**), grain size distribution (**b**), and grain-boundary angle distribution (**c**) of the Mg–1Zn–2.9Y alloy after temperature tests at 350 °C with a deformation rate of $5 \cdot 10^{-3}$ s^{-1} and deformation degree of 8 %*
Рис. 7. *Микроструктура (**a**), распределение зерен по размерам (**b**) и распределение по углам разориентировки (**c**) сплава Mg–1Zn–2,9Y после температурных испытаний при 350 °C со скоростью деформации $5 \cdot 10^{-3}$ $с^{-1}$ и степенью деформации 8 %*

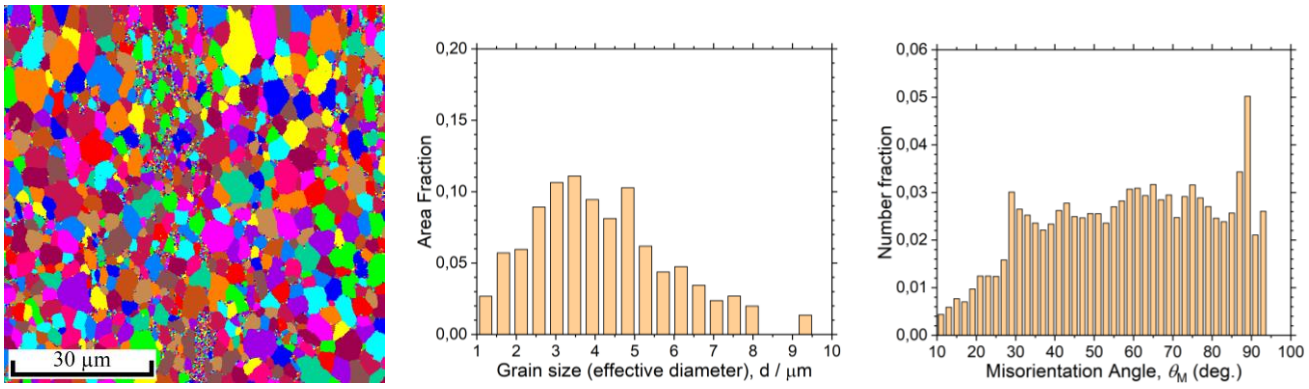

a *b* *c*

Fig. 8. *Microstructure (**a**), grain size distribution (**b**), and grain-boundary angle distribution (**c**) of the Mg–1Zn–2.9Y alloy after temperature tests at 400 °C with a deformation rate of $5 \cdot 10^{-3}$ s^{-1} and deformation degree of 8 %*
Рис. 8. *Микроструктура (**a**), распределение зерен по размерам (**b**) и распределение по углам разориентировки (**c**) сплава Mg–1Zn–2,9Y после температурных испытаний при 400 °C со скоростью деформации $5 \cdot 10^{-3}$ $с^{-1}$ и степенью деформации 8 %*

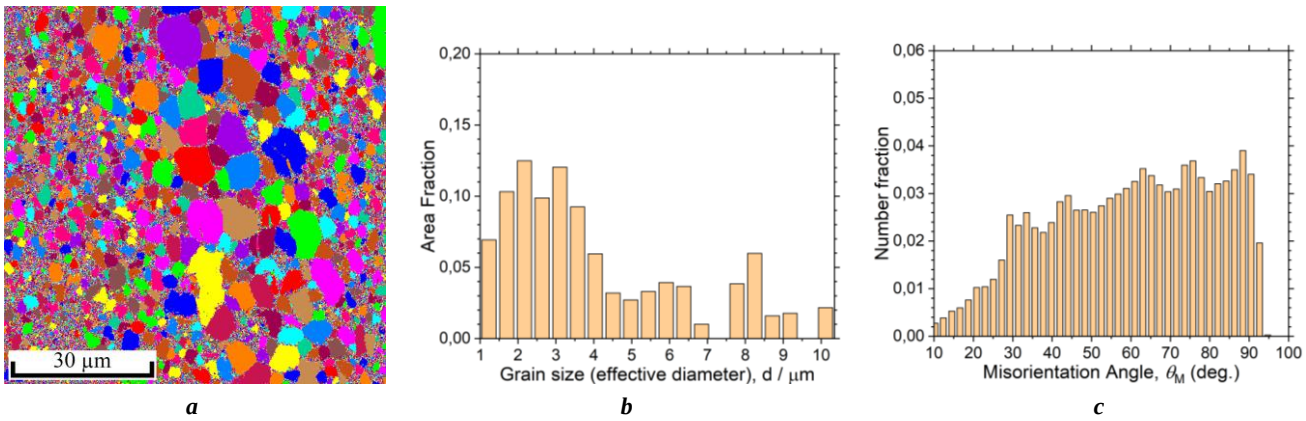

a *b* *c*

Fig. 9. *Microstructure (**a**), grain size distribution (**b**), and grain-boundary angle distribution (**c**) of the Mg–1Zn–2.9Y alloy after soaking at a temperature of 400 °C*

Рис. 9. *Микроструктура (**a**), распределение зерен по размерам (**b**) и распределение по углам разориентировки (**c**) сплава Mg–1Zn–2,9Y после выдержки при температуре 400 °C*

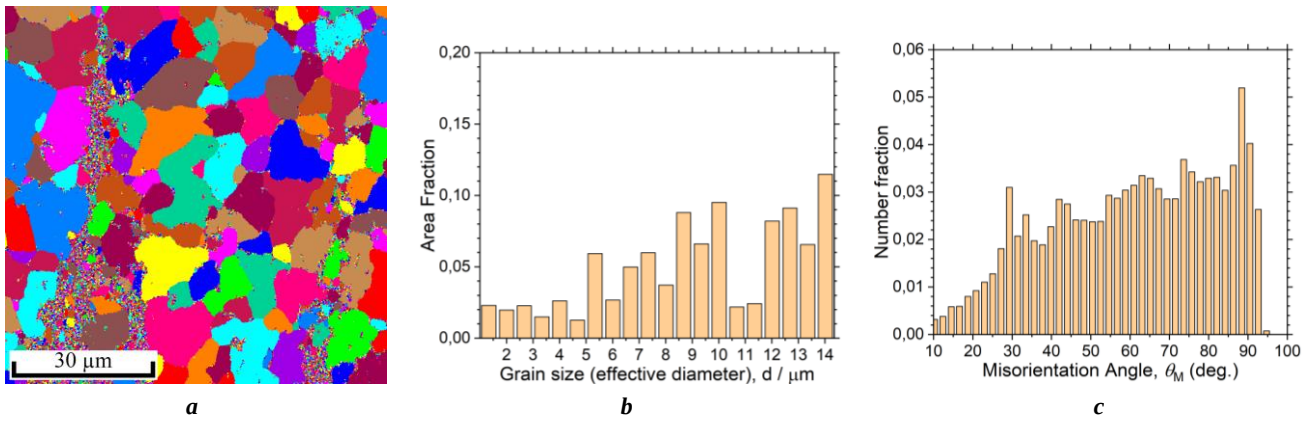

a *b* *c*

Fig. 10. *Microstructure (**a**), grain size distribution (**b**), and grain-boundary angle distribution (**c**) of the Mg–1Zn–2.9Y alloy after 8 % deformation at room temperature with a deformation rate of $5 \cdot 10^{-3}$ s^{-1} and further soaking at 400 °C*

Рис. 10. *Микроструктура (**a**), распределение зерен по размерам (**b**) и распределение по углам разориентировки (**c**) сплава Mg–1Zn–2,9Y после деформации 8 % при комнатной температуре со скоростью деформации $5 \cdot 10^{-3}$ c^{-1} и дальнейшей выдержке при 400 °C*

the complete restoration (return) of the original microstructure and by coarsening of the grain size, which can adversely affect the material functional characteristics and is unacceptable with regard to the variability of technological parameters.

Thus, the Mg–1Zn–2.9Y alloy in the state after multiaxial isothermal forging has a thermally stable fine-grained structure, which allows leveling the negative effect of possible fluctuations in the technological parameters of shaping in the range of strain temperature (150÷300) °C and rates $(5 \cdot 10^{-4} \div 2 \cdot 10^{-2})$ s^{-1}.

REFERENCES

1. Prakasam M., Locs J., Salma-Ancane K., Loca D., Largeteau A., Berzina-Cimdina L. Biodegradable materials and metallic implants-A review. *Journal of Functional Biomaterials*, 2017, vol. 8, no. 4, article number 44. DOI: 10.3390/jfb8040044.
2. Li Nan, Zheng Yufeng. Novel Magnesium Alloys Developed for Biomedical Application: A Review. *Journal of Materials Science & Technology*, 2013, vol. 29, no. 6, pp. 489–502. DOI: 10.1016/j.jmst.2013.02.005.
3. Kumar K., Gill R.S., Batra U. Challenges and opportunities for biodegradable magnesium alloy implants. *Materials Technology*, 2018, vol. 33, no. 2, pp. 153–172. DOI: 10.1080/10667857.2017.1377973.
4. Hort N., Huang Y., Fechner D. et al. Magnesium alloys as implant materials – Principles of property design for Mg–RE alloys. *Acta Biomaterialia*, 2010, vol. 6, no. 5, pp. 1714–1725. DOI: 10.1016/j.actbio.2009.09.010.
5. Song Guang-Ling, Song Shizhe. A Possible Biodegradable Magnesium Implant Material. *Advanced Engineering Materials*, 2007, vol. 9, no. 4, pp. 298–302. DOI: 10.1002/adem.200600252.
6. Ali W., Mehboob A., Han Min-Gu, Chang Seung-Hwan. Experimental study on degradation of mechanical properties of biodegradable magnesium alloy (AZ31)

wires/poly(lactic acid) composite for bone fracture healing applications. *Composite Structures*, 2019, vol. 210, pp. 914–921. DOI: 10.1016/j.compstruct.2018.12.011.
7. Bommala V.K., Krishna M.G., Rao C.T. Magnesium matrix composites for biomedical applications: A review. *Journal of Magnesium and Alloys*, 2019, vol. 7, no. 1, pp. 72–79. DOI: 10.1016/j.jma.2018.11.001.
8. Suljevic O., Fischerauer S.F., Weinberg A.M., Sommer N.G. Immunological reaction to magnesium-based implants for orthopedic applications. What do we know so far? A systematic review on in vivo studies. *Materials Today Bio*, 2022, vol. 15, article number 100315. DOI: 10.1016/j.mtbio.2022.100315.
9. Liu Wenwen, Guo Shuo, Tang Zhen, Wei Xinghui, Gao Peng, Wang Ning, Li Xiaokang, Guo Zheng. Magnesium promotes bone formation and angiogenesis by enhancing MC3T3-E1 secretion of PDGF-BB. *Biochemical and Biophysical Research Communications*, 2020, vol. 528, no. 4, pp. 664–670. DOI: 10.1016/j.bbrc.2020.05.113.
10. Xia Yu, Wu Liang, Yao Wen-hui et al. In-situ layered double hydroxides on Mg−Ca alloy: Role of calcium in magnesium alloy. *Transactions of Nonferrous Metals Society of China*, 2021, vol. 31, no. 6, pp. 1612–1627. DOI: 10.1016/S1003-6326(21)65602-9.
11. Dong Jianhui, Lin Tao, Shao Huiping, Wang Hao, Wang Xueting, Song Ke, Li Qianghua. Advances in degradation behaviour of biomedical magnesium alloys: A review. *Journal of Alloys and Compounds*, 2022, vol. 908, article number 164600. DOI: 10.1016/j.jallcom.2022.164600.
12. Chen Junxiu, Kolawole S.K., Wang Jianhua, Su Xuping, Tan Lili, Yang Ke. Systems, Properties, Surface Modification and Applications of Biodegradable Magnesium-Based Alloys: A Review. *Materials*, 2022, vol. 15, no. 14, p. 5031. DOI: 10.3390/ma15145031.
13. Tekumalla S., Seetharaman S., Almajid A., Gupta M. Mechanical Properties of Magnesium-Rare Earth Alloy Systems: A Review. *Metals*, 2015, vol. 5, no. 1, pp. 1–39. DOI: 10.3390/met5010001.
14. Das A.K. Recent trends in laser cladding and alloying on magnesium alloys: A review. *Materials Today: Proceedings*, 2022, vol. 51, part 1, pp. 723–727. DOI: 10.1016/j.matpr.2021.06.217.
15. Gao Jia-cheng, Wu Sha, Qiao Li-ying, Wang Yong. Corrosion behavior of Mg and Mg-Zn alloys in simulated body fluid. *Transactions of Nonferrous Metals Society of China*, 2008, vol. 18, no. 3, pp. 588–592. DOI: 10.1016/S1003-6326(08)60102-8.
16. Jagadeesh G.V., Setti S.G. Surface Modification of Biodegradable Magnesium Alloy by Ball Burnishing Process. *Recent Advances in Materials Technologies: Select Proceedings of ICEMT 2021*. Springer Nature Singapore, 2023, pp. 327–334. DOI: 10.1007/978-981-19-3895-5_26.
17. Figueiredo R.B., Langdon T.G. Achieving Microstructural Refinement in Magnesium Alloys through Severe Plastic Deformation. *Materials Transactions*, 2009, vol. 50, no. 1, pp. 111–116. DOI: 10.2320/matertrans.MD200818.
18. Bryła K., Dutkiewicz J., Lityńska-Dobrzyńska L., Rokhlin L.L., Kurtyka P. Influence of number of ECAP passes on microstructure and mechanical properties of AZ31 magnesium alloy. *Archives of Metallurgy and Materials*, 2012, vol. 57, no. 3, pp. 711–717. DOI: 10.2478/v10172-012-0077-5.
19. Aksenov D.A., Nazarov A.A., Raab G.I., Raab A.G., Fakhretdinova E.I., Asfandiyarov R.N., Shishkunova M.A., Sementeeva Yu.R. Effects of Severe Plastic Deformation and Ultrasonic Treatment on the Structure, Strength, and Corrosion Resistance of Mg–Al–Zn Alloy. *Materials*, 2022, vol. 15, no. 20, p. 7200. DOI: 10.3390/ma15207200.
20. Merson D., Linderov M., Brilevsky A., Danyuk A., Vinogradov A. Monitoring Dynamic Recrystallisation in Bioresorbable Alloy Mg–1Zn–0.2Ca by Means of an In Situ Acoustic Emission Technique. *Materials*, 2022, vol. 15, no. 1, p. 328. DOI: 10.3390/ma15010328.

СПИСОК ЛИТЕРАТУРЫ

1. Prakasam M., Locs J., Salma-Ancane K., Loca D., Largeteau A., Berzina-Cimdina L. Biodegradable materials and metallic implants-A review // Journal of Functional Biomaterials. 2017. Vol. 8. № 4. Article number 44. DOI: 10.3390/jfb8040044.
2. Li Nan, Zheng Yufeng. Novel Magnesium Alloys Developed for Biomedical Application: A Review // Journal of Materials Science & Technology. 2013. Vol. 29. № 6. P. 489–502. DOI: 10.1016/j.jmst.2013.02.005.
3. Kumar K., Gill R.S., Batra U. Challenges and opportunities for biodegradable magnesium alloy implants // Materials Technology. 2018. Vol. 33. № 2. P. 153–172. DOI: 10.1080/10667857.2017.1377973.
4. Hort N., Huang Y., Fechner D. et al. Magnesium alloys as implant materials – Principles of property design for Mg–RE alloys // Acta Biomaterialia. 2010. Vol. 6. № 5. P. 1714–1725. DOI: 10.1016/j.actbio.2009.09.010.
5. Song Guang-Ling, Song Shizhe. A Possible Biodegradable Magnesium Implant Material // Advanced Engineering Materials. 2007. Vol. 9. № 4. P. 298–302. DOI: 10.1002/adem.200600252.
6. Ali W., Mehboob A., Han Min-Gu, Chang Seung-Hwan. Experimental study on degradation of mechanical properties of biodegradable magnesium alloy (AZ31) wires/poly(lactic acid) composite for bone fracture healing applications // Composite Structures. 2019. Vol. 210. P. 914–921. DOI: 10.1016/j.compstruct.2018.12.011.
7. Bommala V.K., Krishna M.G., Rao C.T. Magnesium matrix composites for biomedical applications: A review // Journal of Magnesium and Alloys. 2019. Vol. 7. № 1. P. 72–79. DOI: 10.1016/j.jma.2018.11.001.
8. Suljevic O., Fischerauer S.F., Weinberg A.M., Sommer N.G. Immunological reaction to magnesium-based implants for orthopedic applications. What do we know so far? A systematic review on in vivo studies // Materials Today Bio. 2022. Vol. 15. Article number 100315. DOI: 10.1016/j.mtbio.2022.100315.
9. Liu Wenwen, Guo Shuo, Tang Zhen, Wei Xinghui, Gao Peng, Wang Ning, Li Xiaokang, Guo Zheng. Magnesium promotes bone formation and angiogenesis by enhancing MC3T3-E1 secretion of PDGF-BB // Biochemical and Biophysical Research Communications. 2020. Vol. 528. № 4. P. 664–670. DOI: 10.1016/j.bbrc.2020.05.113.

10. Xia Yu, Wu Liang, Yao Wen-hui et al. In-situ layered double hydroxides on Mg−Ca alloy: Role of calcium in magnesium alloy // Transactions of Nonferrous Metals Society of China. 2021. Vol. 31. № 6. P. 1612–1627. DOI: 10.1016/S1003-6326(21)65602-9.
11. Dong Jianhui, Lin Tao, Shao Huiping, Wang Hao, Wang Xueting, Song Ke, Li Qianghua. Advances in degradation behavior of biomedical magnesium alloys: A review // Journal of Alloys and Compounds. 2022. Vol. 908. Article number 164600. DOI: 10.1016/j.jallcom.2022.164600.
12. Chen Junxiu, Kolawole S.K., Wang Jianhua, Su Xuping, Tan Lili, Yang Ke. Systems, Properties, Surface Modification and Applications of Biodegradable Magnesium-Based Alloys: A Review // Materials. 2022. Vol. 15. № 14. P. 5031. DOI: 10.3390/ma15145031.
13. Tekumalla S., Seetharaman S., Almajid A., Gupta M. Mechanical Properties of Magnesium-Rare Earth Alloy Systems: A Review // Metals. 2015. Vol. 5. № 1. P. 1–39. DOI: 10.3390/met5010001.
14. Das A.K. Recent trends in laser cladding and alloying on magnesium alloys: A review // Materials Today: Proceedings. 2022. Vol. 51. Part 1. P. 723–727. DOI: 10.1016/j.matpr.2021.06.217.
15. Gao Jia-cheng, Wu Sha, Qiao Li-ying, Wang Yong. Corrosion behavior of Mg and Mg-Zn alloys in simulated body fluid // Transactions of Nonferrous Metals Society of China. 2008. Vol. 18. № 3. P. 588–592. DOI: 10.1016/S1003-6326(08)60102-8.
16. Jagadeesh G.V., Setti S.G. Surface Modification of Biodegradable Magnesium Alloy by Ball Burnishing Process // Recent Advances in Materials Technologies: Select Proceedings of ICEMT 2021. Singapore: Springer Nature Singapore, 2023. P. 327–334. DOI: 10.1007/978-981-19-3895-5_26.
17. Figueiredo R.B., Langdon T.G. Achieving Microstructural Refinement in Magnesium Alloys through Severe Plastic Deformation // Materials Transactions. 2009. Vol. 50. № 1. P. 111–116. DOI: 10.2320/matertrans.MD200818.
18. Bryła K., Dutkiewicz J., Lityńska-Dobrzyńska L., Rokhlin L.L., Kurtyka P. Influence of number of ECAP passes on microstructure and mechanical properties of AZ31 magnesium alloy // Archives of Metallurgy and Materials. 2012. Vol. 57. № 3. P. 711–717. DOI: 10.2478/v10172-012-0077-5.
19. Aksenov D.A., Nazarov A.A., Raab G.I., Raab A.G., Fakhretdinova E.I., Asfandiyarov R.N., Shishkunova M.A., Sementeeva Yu.R. Effects of Severe Plastic Deformation and Ultrasonic Treatment on the Structure, Strength, and Corrosion Resistance of Mg–Al–Zn Alloy // Materials. 2022. Vol. 15. № 20. P. 7200. DOI: 10.3390/ma15207200.
20. Merson D., Linderov M., Brilevsky A., Danyuk A., Vinogradov A. Monitoring Dynamic Recrystallisation in Bioresorbable Alloy Mg–1Zn–0.2Ca by Means of an In Situ Acoustic Emission Technique // Materials. 2022. Vol. 15. № 1. P. 328. DOI: 10.3390/ma15010328.

Особенности эволюции микроструктуры при температурно-скоростном деформировании магниевого сплава медицинского назначения системы легирования Mg–Zn–Y

Кудашева Кристина Камильевна*, инженер НИИ прогрессивных технологий
Линдеров Михаил Леонидович[1], кандидат физико-математических наук,
старший научный сотрудник НИИ прогрессивных технологий
Брилевский Александр Игоревич[2], младший научный сотрудник НИИ прогрессивных технологий
Данюк Алексей Валериевич[3], кандидат физико-математических наук,
старший научный сотрудник НИИ прогрессивных технологий
Ясников Игорь Станиславович[4], доктор физико-математических наук, доцент,
профессор кафедры «Общая и теоретическая физика»,
ведущий научный сотрудник НИИ прогрессивных технологий
Мерсон Дмитрий Львович[5], доктор физико-математических наук, профессор,
директор НИИ прогрессивных технологий
Тольяттинский государственный университет, Тольятти (Россия)

***E-mail: a.abdugaffarova@gmail.com**

[1]ORCID: https://orcid.org/0000-0001-8655-4191
[2]ORCID: https://orcid.org/0000-0002-5780-6094
[3]ORCID: https://orcid.org/0000-0002-7352-9947
[4]ORCID: https://orcid.org/0000-0002-6120-7836
[5]ORCID: https://orcid.org/0000-0001-5006-4115

Поступила в редакцию 15.06.2023 *Принята к публикации 26.07.2023*

Аннотация: Биосовместимость делает сплавы магния привлекательными функциональными материалами с точки зрения их использования в качестве биорезорбируемых имплантатов. Однако технологии изготовления полуфабрикатов несут в себе возможное варьирование локальной скорости деформации и температуры в достаточно широком диапазоне, что сказывается на структуре и свойствах обрабатываемого материала. Цель исследования состоит в определении диапазона температур и стойкостей деформации, при которых не происходит

отрицательного влияния на основные структурные характеристики обрабатываемого материала, на примере сплава медицинского назначения системы легирования Mg–Zn–Y. Проведены механические испытания биоразлагаемого магниевого сплава Mg–1Zn–2,9Y при различных температурах и скоростях деформации. Раскрыто влияние температур в диапазоне 20…400 °C на структуру и свойства сплава системы Mg–Zn–Y. Начиная с температуры 350 °C, процесс динамической рекристаллизации сопровождается не только полным восстановлением (возвратом) исходной микроструктуры, но и укрупнением размеров зерна, что может негативно сказаться на функциональных характеристиках материала. Выявлена высокая термостабильность биоразлагаемого магниевого сплава Mg–1Zn–2,9Y, что, вероятно, объясняется наличием в нем LPSO-фазы. Показано, что деформационный процесс сопровождается двойникованием. При скорости деформации $2 \cdot 10^{-2}$ $с^{-1}$ во всем температурном диапазоне распределение зерен по размерам несколько сужается и смещается в сторону меньших диаметров. Использование полученных результатов в технологических процессах изготовления полуфабрикатов медицинского назначения поможет решить проблему нестабильности микроструктуры на стадии перехода от полуфабриката в изделие при последующих термомеханических обработках.

Ключевые слова: магниевые сплавы медицинского назначения; биоразлагаемые магниевые сплавы; Mg–1Zn–2,9Y; температурно-скоростная деформация; сплав медицинского назначения; магниевые сплавы; динамическая рекристаллизация; эволюция микроструктуры.

Благодарности: Исследование выполнено при финансовой поддержке Российского научного фонда в рамках реализации научного проекта № 20-19-00585.

Статья подготовлена по материалам докладов участников XI Международной школы «Физическое материаловедение» (ШФМ-2023), Тольятти, 11–15 сентября 2023 года.

Для цитирования: Кудашева К.К., Линдеров М.Л., Брилевский А.И., Данюк А.В., Ясников И.С., Мерсон Д.Л. Особенности эволюции микроструктуры при температурно-скоростном деформировании магниевого сплава медицинского назначения системы легирования Mg–Zn–Y // Frontier Materials & Technologies. 2024. № 1. С. 37–47. DOI: 10.18323/2782-4039-2024-1-67-4.

doi: 10.18323/2782-4039-2024-1-67-5

Electrospark modification of the surface of additive VT6 alloy with high-entropy and amorphous electrodes

Samat K. Mukanov*[1], PhD (Engineering), junior researcher
of Scientific-Educational Center of Self-Propagating High-Temperature Synthesis
Pavel A. Loginov[2], PhD (Engineering), senior researcher
of Scientific-Educational Center of Self-Propagating High-Temperature Synthesis
Mikhail I. Petrzhik[3], Doctor of Sciences (Engineering),
professor of Chair of Powder Metallurgy and Functional Coatings,
leading researcher of Scientific-Educational Center of Self-Propagating High-Temperature Synthesis
Evgeny A. Levashov[4], Doctor of Sciences (Engineering), Professor,
Head of Chair of Powder Metallurgy and Functional Coatings,
Head of Scientific-Educational Center of Self-Propagating High-Temperature Synthesis
National University of Science and Technology MISIS, Moscow (Russia)

***E-mail: smukanov@misis.ru**

[1]ORCID: https://orcid.org/0000-0001-6719-6237
[2]ORCID: https://orcid.org/0000-0003-2505-2918
[3]ORCID: https://orcid.org/0000-0002-1736-8050
[4]ORCID: https://orcid.org/0000-0002-0623-0013

Received 23.06.2023 *Accepted 16.11.2023*

Abstract: Unsatisfactory quality of the surface layer of additive products, in particular increased surface roughness, prevents the widespread use of electron beam powder bed fusion (EBPBF). Electrospark treatment (EST) is one of the methods for smoothing and hardening the surface layer. The work shows the possibility of modifying the surface of additive VT6 alloy samples by reactive EST with multicomponent electrodes. For this purpose, the authors used electrodes made of the $Fe_{48}Cr_{15}Mo_{14}Y_2C_{15}B_6$ bulk metallic glass forming alloy and the $FeCoCrNi_2$ high-entropy alloy. Based on the results of scanning electron microscopy, it was identified that after EST, both modified layers have a thickness of about 16 μm. X-ray diffraction phase analysis showed that in the case of treatment with an amorphous electrode they contain carboborides of the Ti(B,C) type, and in the case of treatment with a high-entropy electrode – intermetallic of the Ti_2(Fe,Ni) type. The modified layers have average hardness values of 19 and 10 GPa and elastic modulus of 234 and 157 GPa, respectively, which significantly exceeds the values of these parameters for the EBPBF-grown VT6 alloy. Electric discharge modification of the surface with multicomponent electrodes led to a decrease in roughness by 8...11 times due to the melting of the protrusions and filling of the dimples with the melt to a depth of more than 50 μm. A comparative analysis of the results of tribological tests showed a change in the wear mechanism as a result of EST of the additive VT6 alloy. Wear resistance increased by 4 and 3 orders of magnitude when using electrodes made of a bulk metallic glass and high-entropy alloy, respectively.

Keywords: titanium alloy; electron beam powder bed fusion; surface roughness; smoothing; hardening; wear resistance; electrospark treatment; bulk metallic glass forming alloy; high-entropy alloys.

Acknowledgements: The work was financially supported by the Ministry of Science and Higher Education of the Russian Federation within the state assignment in the sphere of science (project No. 0718-2020-0034).

The paper was written on the reports of the participants of the XI International School of Physical Materials Science (SPM-2023), Togliatti, September 11–15, 2023.

For citation: Mukanov S.K., Loginov P.A., Petrzhik M.I., Levashov E.A. Electrospark modification of the surface of additive VT6 alloy with high-entropy and amorphous electrodes. *Frontier Materials & Technologies*, 2024, no. 1, pp. 49–60. DOI: 10.18323/2782-4039-2024-1-67-5.

INTRODUCTION

Poor surface quality is one of the main factors limiting the development of additive technologies (AT) [1; 2]. Electron beam powder bed fusion (EBPBF), used to grow titanium products allows obtaining good properties in bulk, however, defects (unmelted particles, pores, cracks) are formed on their surface, which reduces surface-sensitive properties, such as wear resistance [3; 4]. Taken together, surface defects determine increased roughness [5; 6], which has a critical impact on the service life and reliability of manufactured products [7]. Currently, to improve the quality of additive surfaces, various post-processing methods are used, which are divided into processing with [8–10], and without [11–13] surface layer removal.

The first group includes methods of mechanical processing and electrochemical processing, which allow obtaining rather smooth surfaces with a roughness of less than 0.5 μm. The latter includes laser processing, and surface modification by deposition of coatings. In particular, in [13], the possibility of using laser polishing of the Inconel 718 nickel alloy was demonstrated, which allows reducing the surface roughness *Ra* from 7.5 to 1 μm. It was shown that laser exposure led to a decrease in grain

size and an increase in microhardness from 345 to 440 HV. The main disadvantage of such methods is uncontrolled heating of the blank part, which leads to bulk recrystallization [14; 15]. The application of electrospark treatment (EST) of EBPBF-grown products is free of this disadvantage, since the supplied energy leads to insignificant heating [16; 17].

The application of electrodes made of multicomponent alloys, such as bulk metallic glass forming alloys (BMG), and so-called high-entropy alloys (HEA), in the reactive EST technology is of particular interest.

Bulk metallic glass forming alloys are based on near-eutectic compositions of multicomponent systems, in which the melt solidifies during deep supercooling with the formation of amorphous or metastable phases [18]. The advantage of these electrodes is their chemical and structural homogeneity, characteristic of metallic glasses, and the near-eutectic composition of low-melting electrodes ensures deep supercooling of the melt, formed during local melting of the electrode, spreading of melt drops over the substrate surface, filling of dimples and obtaining modified surfaces with an amorphous/nanocrystalline structure.

The prospects of using in EST technology of multicomponent cast electrodes with high glass-forming ability produced by vacuum metallurgy, were experimentally shown in [18; 19]. In particular, in [18], $Fe_{48}Cr_{15}Mo_{14}Y_2C_{15}B_6$ and $Fe_{61}Ni_4Cr_3Nb_8Mn_4Si_2B_{18}$ cast electrodes were used to perform EST of substrates made of carbon steel, and VT20 grade titanium alloy (Ti–6.5Al–V–Mo–2Zr). EST with amorphous electrodes allowed increasing the hardness of the VT20 titanium alloy by 3 times, and increasing the wear resistance by 3 orders of magnitude. In [19], as a result of vacuum EST of an AISI 420S steel substrate using a $Fe_{41}Co_7Cr_{15}Mo_{14}C_{15}B_6Y_2$ electrode, a surface with an amorphous structure was obtained. It was noted that the low roughness of the electric discharge surfaces was ensured, due to the formation of melt drops that spread over the substrate surface.

Due to the high configurational entropy of mixing components, HEAs [20] tend to form a structure of a single solid solution. However, it is metastable, and when heated by an electric spark discharge, it experiences decomposition, the products of which, interacting with the substrate elements, can form a modified layer strengthened by intermetallic compounds.

The studies discussed above show that the application of multicomponent electrodes in the EST technology to improve the quality of additive surfaces is promising, but requires additional study.

The purpose of this study is to test multicomponent alloys with high glass-forming ability, and high mixing entropy as electrodes for the reactive EST of the additive VT6 titanium alloy.

METHODS

EBPBF-grown VT6 alloy (Ti–6Al–4V) was used as substrates (cathodes). Table 1 presents the chemical composition of the alloy.

Rod electrodes (anodes), with a diameter of 3 mm made of bulk metallic glass forming $Fe_{48}Cr_{15}Mo_{14}Y_2C_{15}B_6$ alloy, were produced by induction melting followed by casting the melt into a copper mold at an argon pressure of 0.2 atm. Multicomponent electrodes made of high-entropy $FeCoCrNi_2$ alloy powder were produced, by hot pressing (HP) on a DSP-515 SA press (Dr. Fritsch, Germany) in a vacuum, at a temperature of 950 °C, a pressure of 35 MPa, and an isobaric holding for 3 min.

Electrospark treatment was carried out on an Alier-Metal 303 machine in an argon environment, using a vibrating anode holder according to the following mode: current strength – 120 A; pulse duration – 20 μs; voltage – 20 V; pulse energy – 48 mJ; pulse frequency – 3200 Hz.

The kinetics of mass transfer of multicomponent electrodes onto a titanium substrate during EST (specific anode erosion ΔA_i and specific weight gain of the cathode ΔK_i), was measured by the gravimetric method for 5 min on a KERN 770 analytical balance (KERN, Germany) with an accuracy of 10^{-5} g. Measuring of the cathode and anode mass was carried out every minute after EST on an Alier-Metal 303 machine.

X-ray diffraction (XRD) phase analysis was carried out using spectra obtained on a D2 PHASER diffractometer (Bruker AXS, Germany) in monochromatic Cu-Kα ($\lambda K\alpha$=0.15418 nm) radiation in the 2θ angle range from 10° to 120°. Microstructural studies were performed on an S-3400N scanning electron microscope (SEM) (Hitachi High-Technology Corporation, Japan), equipped with a NORAN System 7 X-ray energy-dispersive spectrometer (Thermo Scientific, USA).

Tribological tests were carried out on a Tribometer friction machine (CSM Instruments, Switzerland), at room temperature with reciprocating motion according to the "pin – plate" scheme. A fixed ball with a diameter of 3 mm made of 100Cr6 grade steel (analogous to ShH15) was used as a counterbody. Test conditions: track length is 4 mm, applied load is 1 and 2 N, maximum speed is 5 cm/s. Observation of counterbody wear spot was carried out using an AXIOVERT CA25 optical microscope (ZEISS, Germany) at ×100 magnification. Wear tracks and surface roughness

Table 1. *Composition of the VT6 titanium alloy (Ti–6Al–4V) according to GOST 19807–91*
Таблица 1. *Состав титанового сплава ВТ6 (Ti–6Al–4V) по ГОСТ 19807–91*

Concentration, at. %						
Ti	**Al**	**V**	**O**	**Si**	**Fe**	**Zr**
83.74	10.98	4.08	0.57	0.24	0.24	0.15

were studied using a WYKO NT1100 optical profilometer (Veeco, USA). Mechanical properties (hardness and elastic modulus), were studied using a Nano-HardnessTester instrument (CSM Instruments, Switzerland) at a maximum load of 10 mN.

RESULTS

The surface of the substrates was characterized by a "loose" relief (Fig. 1 a), which was formed by unmelted spherical particles of the original powder with a size of 70...90 μm representing typical defects for EBPBF technology.

The substrate structure was two-phase, and consisted of α and β phases of titanium with lattice parameter of 0.2913 and 0.3152 nm, respectively (Fig. 1 b).

The curves of mass transfer kinetics for both types of electrodes presented in Fig. 2 indicate an increase in the thickness of the electric spark layer throughout the entire duration of treatment (5 min/cm^2). The curves of mass increase of titanium alloy substrates, described by a power function, indicate a low contribution of reverse transfer. The greatest weight gain ($\Delta K_5=5.0\cdot10^{-4}$ g) is observed during treatment with a BMG-electrode. At the same time, the HEA-electrode erosion during treatment of the titanium substrate additive surface was more intense.

Fig. 3 shows images of microstructure of cross-section of the EBPBF-titanium alloy after treatment with a BMG-electrode. The modified layer, about 16 μm thick, has a gradient structure with pronounced dark inclusions.

According to energy dispersive X-ray spectroscopy (EDX) data presented in Table 2, these inclusions are TiC carbide particles. As the distance from the surface increases, the size of the carbide particles increases from 100 to 300 nm. Dark region 3 (Fig. 3 b) at the boundary of the modified layer, and the substrate contains several elements (Ti, Fe, Cr, Mo, Al, Y, C) with a predominance of Ti (51.0 at. %) and corresponds to the zone of primary interaction between the electrode and the substrate.

Images of the titanium substrate microstructure, after treatment with a HEA-electrode are shown in Fig. 4. Treatment of the titanium alloy additive surface with a HEA-electrode also led to the formation of a modified layer 16 μm thick (Fig. 4 a). One can observe that the modified layer has a structure without inclusions compared to the layer formed by a BMG-electrode. This layer is characterized by a high Ti content (60...75 at. %) throughout the entire thickness. EDX (Table 3) showed that the concentration of elements in the surface layer (region 1) and the melt-filled dimples (region 3) is almost the same, which indicates a uniform distribution of elements throughout the entire thickness.

Fig. 4 b shows that, due to the action of electric spark pulses, local melting of both the electrode and the substrate occurred. The resulting melt filled the surface dimples of the substrate. The depth of filling of the dimples with the melt is in the range of 52.3±1.8 μm.

Fig. 5 and Table 4 show the results of XRD phase analysis of modified layers, formed during EST with

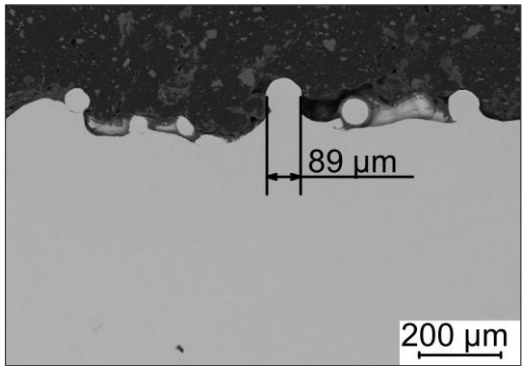

a

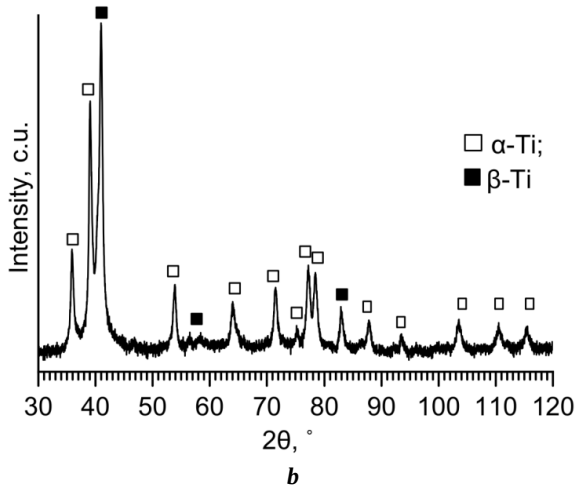

b

Fig. 1. *Cross-section image (**a**) and diffraction pattern (**b**) of a VT6 EBPBF sample in the initial state*
Рис. 1. *Изображение поперечного шлифа (**a**) и дифрактограмма (**b**) СЭЛС-образца ВТ6 в исходном состоянии*

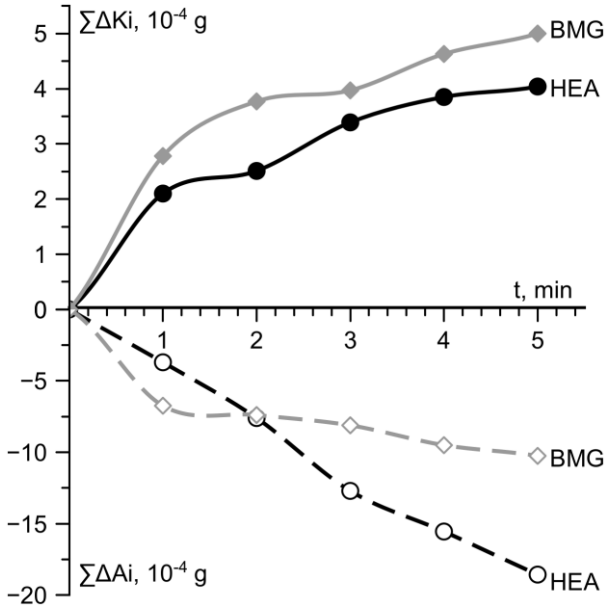

Fig. 2. *Cathode weight gain and anode erosion during EST of a titanium alloy with BMG and HEA electrodes: solid line is substrate weight gain, dashed line is electrode erosion*
Рис. 2. *Привес катода и эрозия анода при ЭИО титанового сплава ОАС- и ВЭС-электродами: сплошная линия – привес массы подложки, пунктирная линия – эрозия электрода*

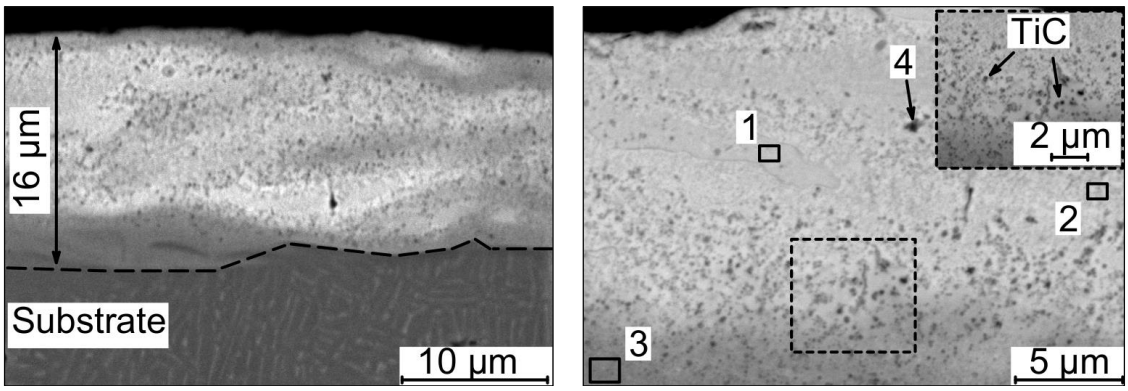

a ***b***

Fig. 3. *SEM image in the backscattered electron (BSE) mode of the cross-section of the VT6 EBPBF sample after EST with a BMG-electrode (**a**); EDX analysis area (inset contains a magnified image of the selected area) (**b**)*
Рис. 3. *РЭМ-изображение в режиме обратно отраженных электронов (BSE) поперечного шлифа СЭЛС-образца ВТ6 после ЭИО ОАС-электродом (**а**); области ЭДС-анализа (на вставке увеличенное изображение выделенной области) (**b**)*

Table 2. *EDX analysis results of areas shown at Fig. 3 b*
Таблица 2. *Результаты ЭДС-анализа областей, показанных на рис. 3 b*

No.	Concentration, at. %							
	Fe	C	Ti	Cr	Mo	Al	V	Y
1	33.4	24.4	19.6	10.7	8.0	2.7	0.9	0.4
2	32.7	25.5	19.0	10.5	9.1	2.0	0.8	0.4
3	15.6	19.3	51.0	5.4	4.3	4.0	–	0.4
4	16.1	35.4	34.1	6.0	5.8	1.3	–	–

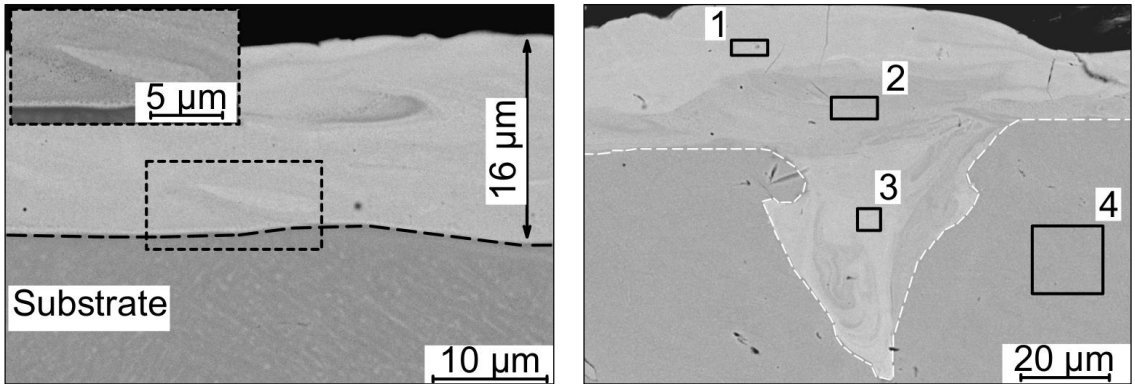

a *b*

Fig. 4. *SEM images in the backscattered electron (BSE) mode: modified layer of the VT6 EBPBF sample after EST with a HEA-electrode (insert contains a magnified image of the selected area) (**a**); a deep dimple filled with the melt during EST (**b**)*
Рис. 4. *РЭМ-изображения в режиме обратно отраженных электронов (BSE): модифицированный слой СЭЛС-образца ВТ6 после ЭИО ВЭС-электродом (на вставке увеличенное изображение выделенной области) (**a**); глубокая впадина, заполненная расплавом при ЭИО (**b**)*

Table 3. *EDX analysis results of areas shown at Fig. 4 b*
Таблица 3. *Результаты ЭДС-анализа областей, показанных на рис. 4 b*

No.	Concentration, at. %						
	Ti	Ni	Fe	Al	Cr	Co	V
1	59.4	10.8	8.3	7.1	6.1	5.5	2.8
2	74.5	4.7	4.0	8.7	2.4	2.2	3.6
3	65.0	8.9	6.8	7.8	4.3	4.2	3.0
4	86.3	–	–	9.5	–	–	4.2

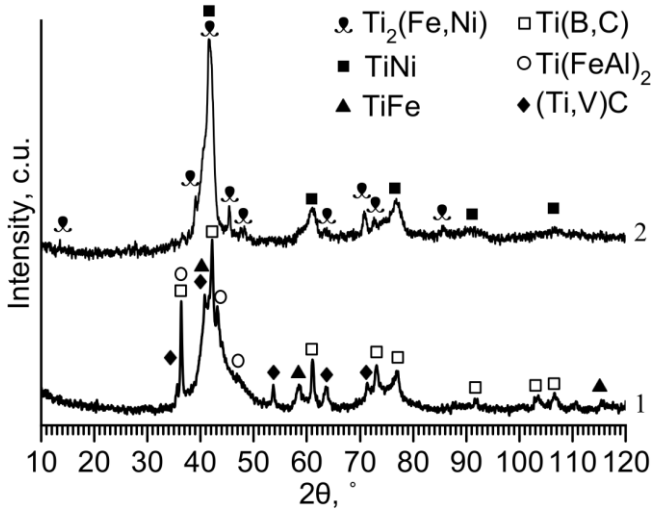

Fig. 5. *X-ray diffraction pattern of the VT6 EBPBF sample after EST with an electrode: 1 – $Fe_{48}Cr_{15}Mo_{14}Y_2C_{15}B_6$ BMG-electrode; 2 – $FeCoCrNi_2$ HEA-electrode*
Рис. 5. *Дифрактограмма СЭЛС-образца ВТ6 после ЭИО электродом: 1 – ОАС-электрод $Fe_{48}Cr_{15}Mo_{14}Y_2C_{15}B_6$; 2 – ВЭС-электрод $FeCoCrNi_2$*

Table 4. *Phase composition of samples subjected to EST*
Таблица 4. *Фазовый состав образцов, подвергнутых ЭИО*

Electrode used at EST	Phase	Portion, wt. %	Lattice parameter, nm		
			(a)	(b)	(c)
$Fe_{48}Cr_{15}Mo_{14}Y_2C_{15}B_6$	Ti(B,C)	44.8	0.8558	–	–
	$Ti(FeAl)_2$	27.5	0.4920	–	0.7988
	(Ti,V)C	14.6	0.2904	–	0.4640
	TiFe	13.1	0.3153	–	–
$FeCoCrNi_2$	$Ti_2(Fe,Ni)$	60.1	1.1296	–	–
	TiNi	39.9	0.3039	–	–

multicomponent electrodes. At processing with a BMG-electrode, chemically active titanium interacted with the electrode elements resulting in the formation of cubic phases: carbides and intermetallics. According to the EDX data (Table 2), the carbide particles contain Ti and C. Considering that the EDX resolution does not allow identifying boron contained in the BMG-electrode, these particles (Fig. 3 b) are probably carboborides of the Ti(B,C) type. The interaction of the Al and V substrate elements with the electrode leading to the formation of hexagonal $Ti(FeAl)_2$ and (Ti,V)C phases was also discovered.

The structure of the layer modified by the HEA-electrode consists of two phases; the diffraction peaks in the diffraction pattern can be attributed to the $Ti_2(Fe,Ni)$ and TiNi cubic phases. One should note that there is a halo in both diffraction patterns, confirming the formation of an amorphous phase during EST, as was found in [18], which is more pronounced for the sample treated with a BMG-electrode.

Table 5 presents the results of studying the surface topography of the modified layers. The initial titanium sample additive surface was characterized by a high roughness (*Ra*) of 38.75±3.00 μm. One can see that treatment with multicomponent electrodes noticeably reduces the values of the arithmetic average of profile height deviations (*Ra*) and maximum peak to valley height of the profile (*Rz*) compared to the additive surface of the original titanium alloy. The minimum surface roughness of 3.53±0.31 μm is observed when processed with a BMG-electrode, and is probably determined by the high fluidity of the electrode material.

The effect of the titanium alloy EST, with multicomponent electrodes on the tribological and mechanical properties can be traced in Fig. 6 and 7. As one can see in Fig. 6 a, the starting friction coefficient (FC) for the titanium substrate is 0.23, and it increases monotonically to 0.33 at the end of the test. When the counterbody slides over the layer formed by a BMG-electrode, three stages can be seen: up to 1000 cycles, a low FC (0.09...0.12) remains unchanged; during the breaking-in period (up to 1500 cycles), a FC monotonically increases from 0.15 to 0.32, and the steady-state friction coefficient reaches 0.36. Increasing the applied load from 1 to 2 N on the steel ball led to an increase in FC up to 0.39. When testing a layer formed by a HEA-electrode, the starting FC is the highest (0.25), and after 500 cycles, a more significant increase in FC up to 0.48 is observed.

The results of measuring mechanical properties (Fig. 6 b, Table 6) showed that EST leads to an increase in both hardness (4 times for BMG and 2 times for HEA) and elastic modulus (1.7 times for BMG and 1.2 times for HEA) of the titanium alloy. The average hardness values of the layers formed by the BMG- and HEA-electrodes were 18.7±2.5 and 10.0±0.9 GPa, respectively.

To study the nature of wear of the samples, the areas of tribocontact on the counterbody, and the sample were studied (Fig. 7). Fig. 7 a–c shows the wear spot of the steel ball. The adhering of wear debris to the ball, while maintaining its spherical shape, confirms the higher hardness of the counterbody compared to the titanium alloy.

The presence of deep grooves in the counterbody wear spot (Fig. 7 b, 7 c) indicates a greater hardness of the layer formed on VT6, during processing with multicomponent electrodes compared to the counterbody material.

The reduced wear of the untreated titanium alloy is the highest (10^{-3} $mm^3/(N \cdot m)$). After treating the titanium alloy with a BMG-electrode, no wear groove was detected at a load of 1 N, which corresponds to a reduced wear value of less than 10^{-7} $mm^3/(N \cdot m)$. Therefore, to test samples with a modified layer, the load was increased up to 2 N. With an increase in the applied load from 1 to 2 N (Table 6), the wear of the steel counterbody increased from 3.18 to $3.84 \cdot 10^{-5}$ $mm^3/(N \cdot m)$, while the wear of the modified layer did not change ($<10^{-7}$ $mm^3/(N \cdot m)$).

DISCUSSION

As known [21], erosion of electrodes during an electric spark discharge depends on a number of factors: density, heat capacity, specific heat of fusion, thermal coefficient of electrical resistance, etc. Their porosity has a great influence on the erosion resistance of electrodes. Previously [22], to increase erosion and accelerate mass transfer during EST, electrodes with increased porosity (5–10 %) produced by powder metallurgy methods were used. In this study, HEA-electrodes were produced using HP technology,

Table 5. *Surface roughness of the VT6 alloy EBPBF samples before and after EST*
Таблица 5. *Шероховатость поверхности СЭЛС-образцов сплава ВТ6 до и после ЭИО*

Sample	*Ra*, μm	*Rz*, μm
EBPBF of the VT6 alloy	38.75±3.00	221.72±38.00
EST with a BMG-electrode	3.53±0.31	36.19±5.00
EST with a HEA-electrode	4.66±0.28	37.26±3.98

Table 6. *Tribological and mechanical properties of samples*
Таблица 6. *Трибологические и механические свойства образцов*

Sample	I, 10^{-5}·mm^3/(N·m)		FC (final)	H, GPa	E, GPa
	of a sample	of a counterbody			
EBPBF of the VT6 alloy	159.60	sticking	0.33	4.7±0.3	136±7
+ EST with a BMG-electrode	<10^{-7}	3.18	0.36	18.7±2.5	234±32
+ EST with a BMG-electrode*	<10^{-7}	3.84	0.39		
+ EST with a HEA-electrode*	3.24	3.33	0.48	10.0±0.9	157±15

Note. *******Applied load is 2 N.*
Примечание. *******Приложенная нагрузка – 2 Н.*

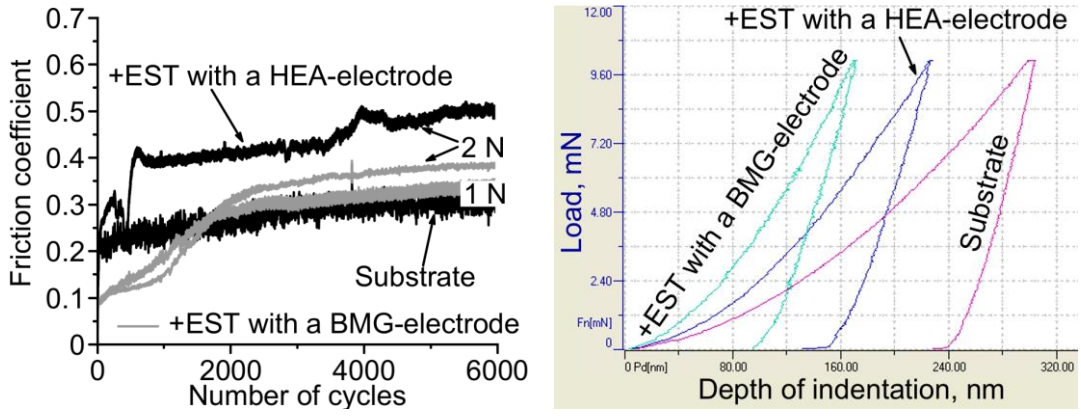

a ***b***

Fig. 6. *Experimental dependences of the friction coefficient on the number of cycles* ***(a)*** *and nanoindentation curves* ***(b)***
Рис. 6. *Экспериментальные зависимости коэффициента трения от количества циклов* ***(а)*** *и кривые наноиндентирования* ***(b)***

so large erosion values (Fig. 2) can be explained by the presence of pores in them (porosity is 3.8±0.2 %). The increase in the cathode weight gain (ΔK_5=5.0·10^{-4} g) during treatment with a BMG-electrode, can be explained by a lower melting point, higher ability melt to undercooling (ΔT=38 °C) and better fluidity [18].

Modified layers, formed during EST with multicomponent electrodes, have a gradient or layered structure. Probably, such a structure is associated with the mixing of melt droplets, containing substrate and electrode elements, as a result of repeated exposure to pulsed electric spark discharges. During EST, spark pulses with a duration of 20 μs, cause local heating and melting of the anode and cathode, ensuring their chemical and diffusion interaction leading to reaction phase formation. Heat removal by the metal substrate provides a high quenching rate of melt (10^5–10^7) K/s [18; 23], which leads to surface layer hardening.

The modified layer produced by EST, with an amorphous $Fe_{48}Cr_{15}Mo_{14}Y_2C_{15}B_6$ electrode significantly differs in structure from the layer produced by EST with

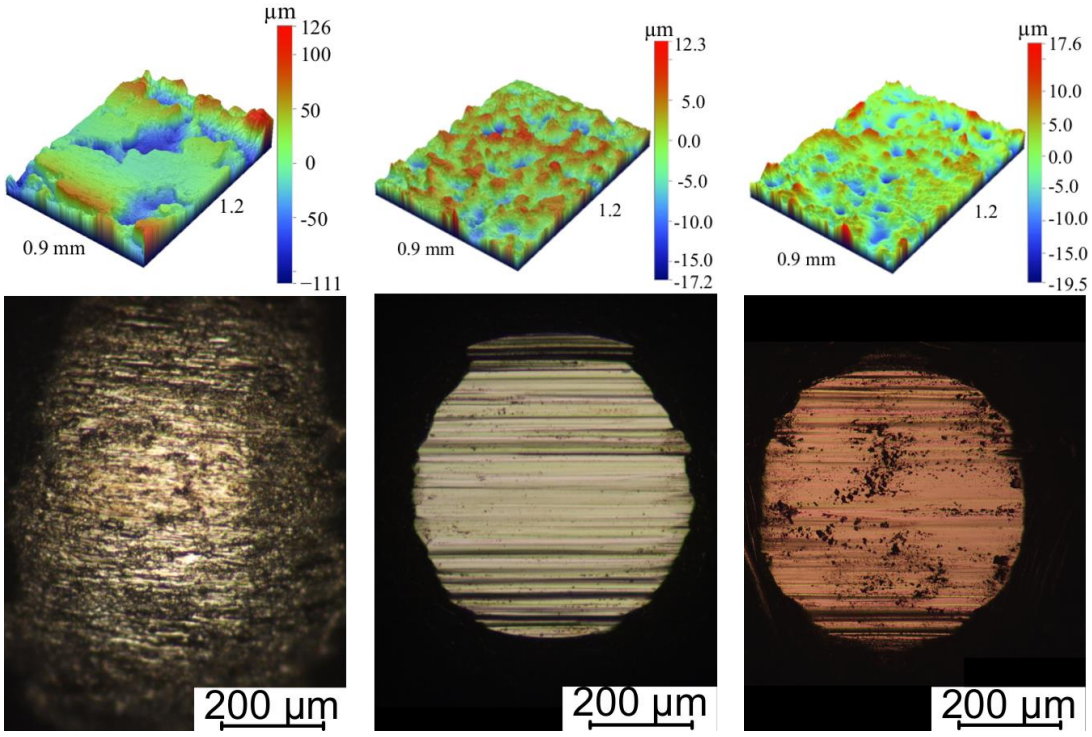

Fig. 7. *Micrographs of counterbodies and 3D-images of wear tracks after tribotestins of samples: the VT6 alloy tested at the load of 1 N* ***(a)****; of modified layers formed with BMG-electrode* ***(b)****; HEA-electrode* ***(c)*** *(both tested at 2 N)*

Рис. 7. *Микрофотографии контртел и 3D-изображения дорожек износа образцов после трибоиспытаний: исходный сплав ВТ6 (при нагрузке 1 Н)* ***(a)****; модифицированные слои, сформированные: ОАС-электродом* ***(b)****; ВЭС-электродом* ***(c)*** *(оба при нагрузке 2 Н)*

a $FeCoCrNi_2$ electrode. A characteristic feature of the first one (Fig. 3) is its gradient structure; the size of Ti(B,C) carboboride particles varies within 100...500 nm, with larger particles located further from the surface. When treated with a $FeCoCrNi_2$ electrode, a layer is formed with a predominant proportion of the $Ti_2(Fe,Ni)$ intermetallic. The increased Ti content (Table 3) in this modified layer is caused by the processing electrode composition. The amorphous electrode composition, in contrast to HEA, contains active metalloids (carbon, boron), which react with Ti forming new phases (in particular, Ti(B,C)).

As can be observed from Table 5, the roughness of modified layers, just as the starting FC (Fig. 6 a), was much lower than that of the additive surface of the original EBPBF VT6.

As shown in Fig. 7 b, 7 c, in the area of contact of the counterbody with the modified layers, the wear mechanism changes. It is observed not the adhering of wear products, but the formation of deep grooves, which is more pronounced after testing a sample treated with a BMG-electrode, the structure of which contains TiC carbide particles (Fig. 3). This indicates that the counterbody is scratched by solid particles crumbled from the modified layer of the sample at the initial stage of testing, where the abrasive wear mechanism may predominate. Wear of a sample treated with a HEA-electrode, occurs both through crumbling at the beginning of the test and through further grinding of particles of the solid and brittle $Ti_2(Fe,Ni)$ phase, which leads to smoothing of the counterbody central part by wear products. In this case, the monotonic increase in the friction coefficient up to 0.48, with sliding counterbody occurs due to an increase in the contact area.

Based on the comprehensive tribological study, Fig. 8 shows a schematic representation of the wear mechanism of the original titanium alloy, and samples with modified layers. Reduced FC (0.33) when the counterbody slides along the untreated sample surface is probably caused by the occurrence of a solid-phase reaction of chemically active Ti, with the counterbody ShH15 steel (100Cr6) material. As a result of this sliding of the ball, wear products adhere to its surface (Fig. 7 a). Compaction of wear products under the load, leads to the tribolayer formation in the contact zone providing a reduced friction coefficient.

Increasing the load up to 2 N, when testing a layer after treatment with a BMG-electrode, practically, does not lead to a change in the final friction coefficient (Table 6). This indicates that the wear of this layer during the entire test occurred according to the same mechanism. In this case, an increase in the counterbody wear is observed, but the wear of the modified layer remains unchanged.

Comparing the XRD results with tribological tests, one can conclude that the increase in the wear resistance of the titanium sample treated with a BMG-electrode by 4 orders of magnitude is caused by the formation of Ti(B,C) carboboride. In the case of treatment with a HEA-electrode, despite the high volume fraction of $Ti_2(Fe,Ni)$, the modified layer has a rather high reduced wear value of $3.24 \cdot 10^{-5}$ $mm^3/(N \cdot m)$ compared to the surface treated with

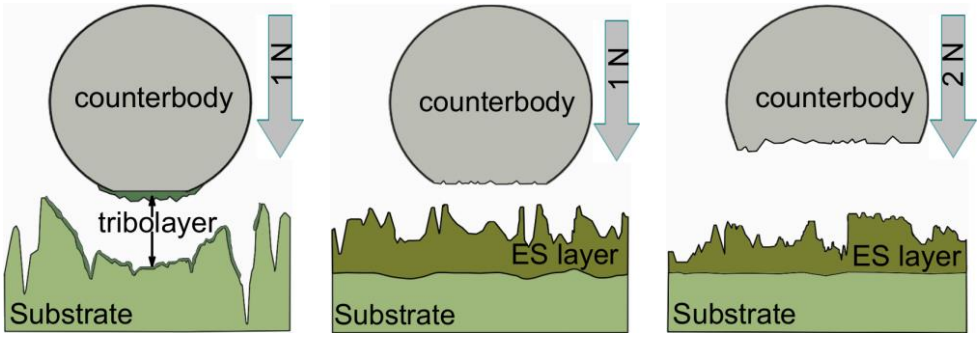

Fig. 8. *Schematic diagram of the wear mechanism of samples before and after EST*
Рис. 8. *Схематическое изображение механизма износа образцов до и после ЭИО*

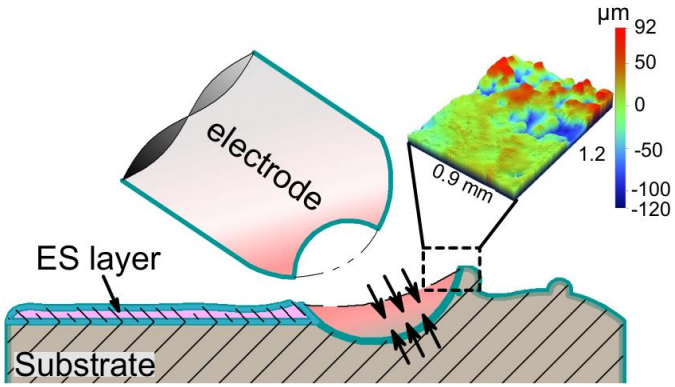

Fig. 9. *Scheme and 3D-image of the surface of the VT6 EBPBF sample after EST with multicomponent electrodes*
Рис. 9. *Схема и 3D-изображение поверхности СЭЛС-образца ВТ6 после ЭИО многокомпонентными электродами*

a BMG-electrode. Thus, the phase composition and microstructure of the modified layers correlate with mechanical and tribological characteristics. The presence of high-hardness phases (Ti(B,C), Ti_2(Fe,Ni)) in the modified layers, in combination with a fine-crystalline structure, led to a significant increase in hardness and elastic modulus compared to the VT6 alloy.

Fig. 9 presents the scheme for smoothing the additive surface of a titanium alloy (substrate). Based on the study of the structure and morphology of the additive sample surface before (Fig. 1) and after EST (Fig. 3, 4), one can assume that when processing the EBPBF sample with multicomponent electrodes, local melting of the protrusions on their surface occurs with the formation of a melt consisting of electrode and substrate elements. This melt spreads over the surface and fills dimples more than 50 μm deep. Thus, the shown in table 5 decrease in the average surface roughness *Ra* by 8 and 11 times for the HEA and BMG electrodes, respectively, can be explained.

CONCLUSIONS

1. Electrospark treatment of additive surface of the titanium alloy with electrodes made of multicomponent alloys, led to the formation of modified layers about 16 μm thick with a submicron structure. When treated with an amorphous electrode, a gradient structure layer is formed, the size of Ti(B,C) carboboride particles varies within 100...500 nm with larger particles located further from the surface.

2. The results of comparative tribological tests of an EBPBF sample with modified layers showed that EST with multicomponent electrodes allows increasing the wear resistance of a titanium alloy. It has been found that an increase by 4 orders of magnitude in the wear resistance of EBPBF samples of titanium alloy, treated with an amorphous electrode, is associated with the formation of Ti(B,C) carboboride in the surface layer due to the interaction of the chemically active melt with the substrate.

3. The results of studying the mechanical properties showed, that EST leads to an increase in both the hardness (2 and 4 times) and the elastic modulus (1.2 and 1.7 times) of the VT6 alloy when treated with high-entropy, and amorphous electrodes, respectively. The quenching of melt droplets with the formation of hard and wear-resistant intermetallics or carboborides plays a key role in the hardening of modified layers during EST.

4. It has been demonstrated that during EST with multicomponent electrodes, a melt is formed, which spreads over the titanium alloy surface filling dimples more than 50 μm deep, which leads to a decrease in surface roughness by 8 and 11 times for the HEA and BMG electrodes, respectively.

REFERENCES

1. Murr L.E., Gaytan S.M., Ceylan A. et al. Characterization of titanium aluminide alloy components fabricated by additive manufacturing using electron beam melting. *Acta Materialia*, 2010, vol. 58, no. 5, pp. 1887–1894. DOI: 10.1016/j.actamat.2009.11.032.
2. Leary M. Surface roughness optimisation for selective laser melting (SLM): Accommodating relevant and irrelevant surfaces. *Laser Additive Manufacturing: Materials, Design, Technologies and Applications*. Sawston, Woodhead Publishing, 2017, pp. 99–118. DOI: 10.1016/B978-0-08-100433-3.00004-X.
3. Karlsson J., Snis A., Engqvist H., Lausmaa J. Characterization and comparison of materials produced by Electron Beam Melting (EBM) of two different Ti–6Al–4V powder fractions. *Journal of Materials Processing Technology*, 2013, vol. 213, no. 12, pp. 2109–2118. DOI: 10.1016/j.jmatprotec.2013.06.010.
4. Calignano F., Manfredi D., Ambrosio E.P. et al. Overview on Additive Manufacturing Technologies. *Proceedings of the IEEE*, 2017, vol. 105, no. 4, pp. 593–612. DOI: 10.1109/JPROC.2016.2625098.
5. Nasab M.H., Gastaldi D., Lecis N.F., Vedani M. On morphological surface features of the parts printed by selective laser melting (SLM). *Additive Manufacturing*, 2018, vol. 24, pp. 373–377. DOI: 10.1016/j.addma.2018.10.011.
6. Leuders S., Thöne M., Riemer A., Niendorf T., Tröster T., Richard H.A., Maier H.J. On the mechanical behaviour of titanium alloy TiAl6V4 manufactured by selective laser melting: Fatigue resistance and crack growth performance. *International Journal of Fatigue*, 2013, vol. 48, pp. 300–307. DOI: 10.1016/j.ijfatigue.2012.11.011.
7. Fé-Perdomo I.L., Ramos-Grez J., Mujica R., Rivas M. Surface roughness Ra prediction in Selective Laser Melting of 316L stainless steel by means of artificial intelligence inference. *Journal of King Saud University - Engineering Sciences*, 2023, vol. 35, no. 2, pp. 148–156. DOI: 10.1016/j.jksues.2021.03.002.
8. Asfandiyarov R.N., Raab G.I., Gunderov D.V., Aksenov D.A., Raab A.G., Gunderova S.D., Shishkunova M.A. Roughness and microhardness of UFG grade 4 titanium under abrasive-free ultrasonic finishing. *Frontier Materials & Technologies*, 2022, no. 3-1, pp. 41–49. DOI: 10.18323/2782-4039-2022-3-1-41-49.
9. Bagehorn S., Wehr J., Maier H.J. Application of mechanical surface finishing processes for roughness reduction and fatigue improvement of additively manufactured Ti-6Al-4V parts. *International Journal of Fatigue*, 2017, vol. 102, pp. 135–142. DOI: 10.1016/j.ijfatigue.2017.05.008.
10. Tan K.L., Yeo S.H. Surface modification of additive manufactured components by ultrasonic cavitation abrasive finishing. *Wear*, 2017, vol. 378-379, pp. 90–95. DOI: 10.1016/j.wear.2017.02.030.
11. Yasa E., Kruth J.-P. Microstructural investigation of Selective Laser Melting 316L stainless steel parts exposed to laser re-melting. *Procedia Engineering*, 2011, vol. 19, pp. 389–395. DOI: 10.1016/j.proeng.2011.11.130.
12. Zhang Baicheng, Zhu Lin, Liao Hanlin, Coddet C. Improvement of surface properties of SLM parts by atmospheric plasma spraying coating. *Applied Surface Science*, 2012, vol. 263, pp. 777–782. DOI: 10.1016/j.apsusc.2012.09.170.
13. Fang Zhihao, Lu Libin, Chen Longfei, Guan Yingchun. Laser Polishing of Additive Manufactured Superalloy. *Procedia CIRP*, 2018, vol. 71, pp. 150–154. DOI: 10.1016/j.procir.2018.05.088.
14. Barile C., Casavola C., Pappalettera G., Renna G. Advancements in Electrospark Deposition (ESD) Technique: A Short Review. *Coatings*, 2022, vol. 12, no. 10, article number 1536. DOI: 10.3390/coatings12101536.
15. Wang De, Deng Shaojun, Chen Hui, Chi Changtai, Hu Dean, Wang Wengin, He Wen, Liu Xiubo. Microstructure and properties of TiC particles planted on single crystal superalloy by electrospark discharging. *Surface and Coatings Technology*, 2023, vol. 461, article number 129438. DOI: 10.1016/j.surfcoat.2023.129438.
16. Liu Xiao-Qin, Zhang Yu-Xing, Wang Xiao-Rong, Wang Zhao-Qin, He Peng. Microstructure and corrosion properties of AlCrxNiCu0.5Mo (x = 0, 0.5, 1.0, 1.5, 2.0) high entropy alloy coatings on Q235 steel by electrospark – Computer numerical control deposition. *Materials Letters*, 2021, vol. 292, article number 129642. DOI: 10.1016/j.matlet.2021.129642.
17. Mukanov S.K., Baskov F.A., Petrzhik M.I., Levashov E.A. Electro-spark treatment with low-melting Al–Si and Al–Ca electrodes in order to improve wear and oxidation resistance of EP741NP alloy prepared by selective laser melting. *Metallurgist*, 2022, vol. 66, no. 3, pp. 317–326. DOI: 10.1007/s11015-022-01331-0.
18. Petrzhik M., Molokanov V., Levashov E. On conditions of bulk and surface glass formation of metallic alloys. *Journal of Alloys and Compounds*, 2017, vol. 707, pp. 68–72. DOI: 10.1016/j.jallcom.2016.12.293.
19. Sheveyko A.N., Kuptsov K.A., Antonyuk M.N., Bazlov A.I., Shtansky D.V. Electro-spark deposition of amorphous Fe-based coatings in vacuum and in argon controlled by surface wettability. *Materials Letters*, 2022, vol. 318, article number 132195. DOI: 10.1016/j.matlet.2022.132195.
20. Mukanov S., Loginov P., Fedotov A., Bychkova M., Antonyuk M., Levashov E. The Effect of Copper on the Microstructure, Wear and Corrosion Resistance of CoCrCuFeNi High-Entropy Alloys Manufactured by Powder Metallurgy. *Materials*, 2023, vol. 16, no. 3, article number 1178. DOI: 10.3390/ma16031178.
21. Gitlevich A.E., Mikhaylov V.V., Parkanskiy N.Ya., Revutskiy V.M. *Elektroiskrovoe legirovanie metallicheskikh poverkhnostey* [Electric-Spark Alloying of Metal Surfaces]. Kishinev, Shtiintsa Publ., 1985. 196 p.
22. Levashov E.A., Merzhanov A.G., Shtansky D.V. Advanced Technologies, Materials and Coatings Developed in Scientific-Educational Center of SHS. *Galvanotechnik*, 2009, vol. 100, no. 9, pp. 2102–2114. EDN: MWXQPL.
23. Zhao Wang, Su Hao, He Weifeng, Wang Xiaorong, Cui Xiaoyu, Luo Sihai. Defect Control of Electro-spark Deposition WC–Co Coatings via Adjusting Pulse Energy and Deposited Layer Number. *Journal of Materials Engineering and Performance*, 2023, vol. 32, pp. 1402–1411. DOI: 10.1007/s11665-022-07204-6.

СПИСОК ЛИТЕРАТУРЫ

1. Murr L.E., Gaytan S.M., Ceylan A. et al. Characterization of titanium aluminide alloy components fabricated by additive manufacturing using electron beam melting // Acta Materialia. 2010. Vol. 58. № 5. P. 1887–1894. DOI: 10.1016/j.actamat.2009.11.032.
2. Leary M. Surface roughness optimisation for selective laser melting (SLM): Accommodating relevant and irrelevant surfaces // Laser Additive Manufacturing: Materials, Design, Technologies and Applications. Sawston: Woodhead Publishing, 2017. P. 99–118. DOI: 10.1016/B978-0-08-100433-3.00004-X.
3. Karlsson J., Snis A., Engqvist H., Lausmaa J. Characterization and comparison of materials produced by Electron Beam Melting (EBM) of two different Ti–6Al–4V powder fractions // Journal of Materials Processing Technology. 2013. Vol. 213. № 12. P. 2109–2118. DOI: 10.1016/j.jmatprotec.2013.06.010.
4. Calignano F., Manfredi D., Ambrosio E.P. et al. Overview on Additive Manufacturing Technologies // Proceedings of the IEEE. 2017. Vol. 105. № 4. P. 593–612. DOI: 10.1109/JPROC.2016.2625098.
5. Nasab M.H., Gastaldi D., Lecis N.F., Vedani M. On morphological surface features of the parts printed by selective laser melting (SLM) // Additive Manufacturing. 2018. Vol. 24. P. 373–377. DOI: 10.1016/j.addma.2018.10.011.
6. Leuders S., Thöne M., Riemer A., Niendorf T., Tröster T., Richard H.A., Maier H.J. On the mechanical behaviour of titanium alloy TiAl6V4 manufactured by selective laser melting: Fatigue resistance and crack growth performance // International Journal of Fatigue. 2013. Vol. 48. P. 300–307. DOI: 10.1016/j.ijfatigue.2012.11.011.
7. Fé-Perdomo I.L., Ramos-Grez J., Mujica R., Rivas M. Surface roughness Ra prediction in Selective Laser Melting of 316L stainless steel by means of artificial intelligence inference // Journal of King Saud University - Engineering Sciences. 2023. Vol. 35. № 2. P. 148–156. DOI: 10.1016/j.jksues.2021.03.002.
8. Асфандияров Р.Н., Рааб Г.И., Гундеров Д.В., Аксенов Д.А., Рааб А.Г., Гундерова С.Д., Шишкунова М.А. Шероховатость и микротвердость ультрамелкозернистого титана Grade 4, подвергнутого безабразивной ультразвуковой финишной обработке // Frontier Materials & Technologies. 2022. № 3-1. С. 41–49. DOI: 10.18323/2782-4039-2022-3-1-41-49.
9. Bagehorn S., Wehr J., Maier H.J. Application of mechanical surface finishing processes for roughness reduction and fatigue improvement of additively manufactured Ti-6Al-4V parts // International Journal of Fatigue. 2017. Vol. 102. P. 135–142. DOI: 10.1016/j.ijfatigue.2017.05.008.
10. Tan K.L., Yeo S.H. Surface modification of additive manufactured components by ultrasonic cavitation abrasive finishing // Wear. 2017. Vol. 378-379. P. 90–95. DOI: 10.1016/j.wear.2017.02.030.
11. Yasa E., Kruth J.-P. Microstructural investigation of Selective Laser Melting 316L stainless steel parts exposed to laser re-melting // Procedia Engineering. 2011. Vol. 19. P. 389–395. DOI: 10.1016/j.proeng.2011.11.130.
12. Zhang Baicheng, Zhu Lin, Liao Hanlin, Coddet C. Improvement of surface properties of SLM parts by atmospheric plasma spraying coating // Applied Surface Science. 2012. Vol. 263. P. 777–782. DOI: 10.1016/j.apsusc.2012.09.170.
13. Fang Zhihao, Lu Libin, Chen Longfei, Guan Yingchun. Laser Polishing of Additive Manufactured Superalloy // Procedia CIRP. 2018. Vol. 71. P. 150–154. DOI: 10.1016/j.procir.2018.05.088.
14. Barile C., Casavola C., Pappalettera G., Renna G. Advancements in Electrospark Deposition (ESD) Technique: A Short Review // Coatings. 2022. Vol. 12. № 10. Article number 1536. DOI: 10.3390/coatings12101536.
15. Wang De, Deng Shaojun, Chen Hui, Chi Changtai, Hu Dean, Wang Wengin, He Wen, Liu Xiubo. Microstructure and properties of TiC particles planted on single crystal superalloy by electrospark discharging // Surface and Coatings Technology. 2023. Vol. 461. Article number 129438. DOI: 10.1016/j.surfcoat.2023.129438.
16. Liu Xiao-Qin, Zhang Yu-Xing, Wang Xiao-Rong, Wang Zhao-Qin, He Peng. Microstructure and corrosion properties of AlCrxNiCu0.5Mo (x = 0, 0.5, 1.0, 1.5, 2.0) high entropy alloy coatings on Q235 steel by electrospark – Computer numerical control deposition // Materials Letters. 2021. Vol. 292. Article number 129642. DOI: 10.1016/j.matlet.2021.129642.
17. Муканов С.К., Басков Ф.А., Петржик М.И., Левашов Е.А. Электроискровая обработка легкоплавкими электродами Al–Si И Al–Ca для повышения стойкости к износу и окислению сплава ЭП741НП, полученного селективным лазерным сплавлением // Металлург. 2022. № 3. С. 70–77. DOI: 10.52351/00260827_2022_03_70.
18. Petrzhik M., Molokanov V., Levashov E. On conditions of bulk and surface glass formation of metallic alloys // Journal of Alloys and Compounds. 2017. Vol. 707. P. 68–72. DOI: 10.1016/j.jallcom.2016.12.293.
19. Sheveyko A.N., Kuptsov K.A., Antonyuk M.N., Bazlov A.I., Shtansky D.V. Electro-spark deposition of amorphous Fe-based coatings in vacuum and in argon controlled by surface wettability // Materials Letters. 2022. Vol. 318. Article number 132195. DOI: 10.1016/j.matlet.2022.132195.
20. Mukanov S., Loginov P., Fedotov A., Bychkova M., Antonyuk M., Levashov E. The Effect of Copper on the Microstructure, Wear and Corrosion Resistance of CoCrCuFeNi High-Entropy Alloys Manufactured by Powder Metallurgy // Materials. 2023. Vol. 16. № 3. Article number 1178. DOI: 10.3390/ma16031178.
21. Гитлевич А.Е., Михайлов В.В., Парканский Н.Я., Ревуцкий В.М. Электроискровое легирование металлических поверхностей. Кишинев: Штиинца, 1985. 196 с.
22. Levashov E.A., Merzhanov A.G., Shtansky D.V. Advanced Technologies, Materials and Coatings Developed in Scientific-Educational Center of SHS // Galvanotechnik. 2009. Vol. 100. № 9. P. 2102–2114. EDN: MWXQPL.
23. Zhao Wang, Su Hao, He Weifeng, Wang Xiaorong, Cui Xiaoyu, Luo Sihai. Defect Control of Electro-spark Deposition WC–Co Coatings via Adjusting Pulse Energy and Deposited Layer Number // Journal of Materials Engineering and Performance. 2023. Vol. 32. P. 1402–1411. DOI: 10.1007/s11665-022-07204-6.

Электроискровое модифицирование поверхности аддитивного сплава ВТ6 высокоэнтропийным и аморфным электродами

Муканов Самат Куандыкович*[*1], кандидат технических наук, младший научный сотрудник научно-учебного центра самораспространяющегося высокотемпературного синтеза
Логинов Павел Александрович[2], кандидат технических наук, старший научный сотрудник научно-учебного центра самораспространяющегося высокотемпературного синтеза
Петржик Михаил Иванович[3], доктор технических наук, профессор кафедры порошковой металлургии и функциональных покрытий, ведущий научный сотрудник научно-учебного центра самораспространяющегося высокотемпературного синтеза
Левашов Евгений Александрович[4], доктор технических наук, профессор, заведующий кафедрой порошковой металлургии и функциональных покрытий, директор научно-учебного центра самораспространяющегося высокотемпературного синтеза
Университет науки и технологий МИСИС, Москва (Россия)

***E-mail: smukanov@misis.ru**

[1]ORCID: https://orcid.org/0000-0001-6719-6237
[2]ORCID: https://orcid.org/0000-0003-2505-2918
[3]ORCID: https://orcid.org/0000-0002-1736-8050
[4]ORCID: https://orcid.org/0000-0002-0623-0013

Поступила в редакцию 23.06.2023 *Принята к публикации 16.11.2023*

Аннотация: Неудовлетворительное качество поверхностного слоя аддитивных изделий, в частности повышенная шероховатость поверхности, препятствует широкому применению селективного электронно-лучевого сплавления (СЭЛС). Одним из способов выглаживания, а также упрочнения поверхностного слоя является электроискровая обработка (ЭИО). В работе показана возможность модифицирования поверхности аддитивных образцов из сплава ВТ6 путем реакционной ЭИО многокомпонентными электродами. Для этого были использованы электроды из объемноаморфизуемого сплава $Fe_{48}Cr_{15}Mo_{14}Y_2C_{15}B_6$ и высокоэнтропийного сплава $FeCoCrNi_2$. По результатам растровой электронной микроскопии установлено, что после ЭИО оба модифицированных слоя имеют толщину около 16 мкм. Рентгеноструктурный фазовый анализ показал, что в случае обработки аморфным электродом они содержат карбобориды типа Ti(B,C), а в случае обработки высокоэнтропийным электродом – интерметаллиды типа $Ti_2(Fe,Ni)$. Модифицированные слои имеют средние значения твердости 19 и 10 ГПа и модуля упругости 234 и 157 ГПа соответственно, что значительно превышает значения этих параметров для сплава ВТ6, выращенного СЭЛС. Электроискровое модифицирование поверхности многокомпонентными электродами привело к уменьшению шероховатости в 8…11 раз за счет оплавления выступов и заполнения впадин расплавом на глубину более 50 мкм. Сравнительный анализ результатов трибологических испытаний показал изменение механизма износа в результате ЭИО аддитивного сплава ВТ6. Износостойкость повысилась на 4 и 3 порядка величины при применении электродов из объемноаморфизуемого и высокоэнтропийного сплава соответственно.

Ключевые слова: титановый сплав; селективное электронно-лучевое сплавление; шероховатость поверхности; выглаживание; упрочнение; износостойкость; электроискровая обработка; объемноаморфизуемые сплавы; высокоэнтропийные сплавы.

Благодарности: Работа выполнена при финансовой поддержке Министерства науки и высшего образования Российской Федерации в рамках государственного задания в сфере науки (проект № 0718-2020-0034).

Статья подготовлена по материалам докладов участников XI Международной школы «Физическое материаловедение» (ШФМ-2023), Тольятти, 11–15 сентября 2023 года.

Для цитирования: Муканов С.К., Логинов П.А., Петржик М.И., Левашов Е.А. Электроискровое модифицирование поверхности аддитивного сплава ВТ6 высокоэнтропийным и аморфным электродами // Frontier Materials & Technologies. 2024. № 1. С. 49–60. DOI: 10.18323/2782-4039-2024-1-67-5.

doi: 10.18323/2782-4039-2024-1-67-6

The study of end milling temperature of low-alloy steel in coarse-grained and ultrafine-grained states

Dmitry A. Rastorguev[1], PhD (Engineering),
assistant professor of Chair "Equipment and Technologies of Machine Building Production"
Aleksandr A. Sevastyanov*[2], postgraduate student
of Chair "Equipment and Technologies of Machine Building Production"
Gennady V. Klevtsov, Doctor of Sciences (Engineering),
professor of Chair "Nanotechnologies, Materials Science and Mechanics"
Togliatti State University, Togliatti (Russia)

***E-mail: alex-119977@yandex.ru, a.sevastyanov@tltsu.ru**

[1]ORCID: https://orcid.org/0000-0001-6298-1068
[2]ORCID: https://orcid.org/0000-0002-7465-650X

Received 05.07.2023 *Accepted 29.01.2024*

Abstract: The paper presents the results of the study of the end milling temperature of low-alloy steel depending on the cutting modes and the type of crystalline structure. The experiment was carried out on a PROMA FHV-50PD universal milling machine. The blanks were processed using a 12-12D-30C-75L-4F HRC55 carbide milling cutter. No cooling was used during processing. The obtained data were statistically analyzed to identify the dependence of the end milling temperature of low-alloy steel on the processing modes and the steel crystalline structure. When creating a mathematical model of cutting temperature, the authors carried out a bootstrap analysis to identify the significance of the parameters of the processing modes. The mathematical model was chosen using the Akaike informative criterion. It was found that mathematical models of the temperature dependence on processing modes for both types of crystalline structure include the cutting depth in the second power. At the same time, for steel in an ultrafine-grained state, both the cutting depth and the feed are statistically significant. It was not possible to detect the influence of cutting speed on temperature in the studied range of processing modes. Thus, when milling this group of materials, the force component primarily determined by the cutting depth exerts the predominant influence on the temperature regime. The level of cutting temperature when processing steel in an ultrafine-grained state is generally higher than when processing steel in a coarse-grained state, which should be associated with the increased physical and mechanical properties of steel with an ultrafine-grained crystalline structure.

Keywords: material cutting; coarse-grained (CG) and ultrafine-grained (UFG) structure; low-alloy steel; cutting temperature; end milling.

Acknowledgments: The authors thank Professor R.Z. Valiev, the Director of the Research Institute of Physics of Advanced Materials at Ufa University of Science and Technology (Ufa), for kindly provided materials for the study.

The work was financially supported by the Russian Science Foundation (project No. 20-69-47059, https://rscf.ru/project/20-69-47059/).

For citation: Rastorguev D.A., Sevastyanov A.A., Klevtsov G.V. The study of end milling temperature of low-alloy steel in coarse-grained and ultrafine-grained states. *Frontier Materials & Technologies*, 2024, no. 1, pp. 61–69. DOI: 10.18323/2782-4039-2024-1-67-6.

INTRODUCTION

The study of the properties of bulk nanostructured metal materials with an ultrafine-grained (UFG) structure is one of the most promising areas of modern materials science [1; 2]. However, despite the growing interest in such materials on the part of researchers and engineers, there is insufficient data on the cutting machinability of materials with a UFG structure. There is data on the surface roughness dependence on the type of crystalline structure of the material being processed when milling B95 aluminum alloy [3]. It follows from the results of the study [3] that when processing an alloy with a UFG structure, the surface quality is higher as compared to an alloy with a coarse-grained (CG) structure. Similar studies were carried out for turning 12H18N10T stainless steel [4]. The paper also notes a significant decrease in roughness parameters when processing materials with a UFG structure. It follows from work [5], that the microhardness and microstructure of the near-surface layer of the blank, after milling, differ for steel with coarse and fine grains. In work [6] dealing with the study of end milling of microchannels in a UFG low-carbon steel blank, a decrease in surface roughness parameters when processing UFG material is also observed.

The work [7] proposes a convenient and effective method to determine the constants of the Johnson – Cook model for UFG titanium. The authors subsequently, used the obtained values of the constants, to calculate the cutting forces when processing UFG titanium [8]. The work [9] describes a fast and accurate algorithm for calculating the temperature when cutting UFG titanium, and notes that the cutting temperature of the VT6 titanium alloy, with an UFG structure, is significantly lower than the cutting temperature of an alloy with a CG structure. The authors of [10] note an increase in cutting force when processing UFG VT6

titanium alloy, as well as a decrease in the size of burrs compared to CG titanium. In [11], based on a study of the chip parameters, and thermal conductivity of CG and UFG titanium, the authors concluded on a potential increase in cutting machinability, and reduction in cutting tool wear when changing to a structure with fine grains.

At the same time, there is no data on the influence of steel structure, and processing modes, on cutting temperature. Cutting temperature is an important factor that must be taken into account by a technologist, when designing operations for mechanical machining of materials [12]. Cutting temperature affects the cutting tool durability, the machined surface roughness, the dimensional accuracy of processing, and many other parameters of the cutting process [13; 14]. Moreover, cutting temperature can be used as one of the main diagnostic signals along with cutting force [15; 16]. The use of cutting temperature, as a feedback signal when developing automatic control systems for the treatment process, is worth noting individually [17; 18].

The purpose of this work is to study the influence of the coarse-grained, and ultrafine-grained crystalline structure of 09G2S steel, and its processing modes on the cutting temperature during end milling.

METHODS

09G2S low-carbon low-alloy steel, GOST 19281-2014 (Table 1) was chosen as the material for the study.

Two samples with dimensions of 40×15×10 mm each in one of two states were studied: as-delivered state with a CG structure, and after equal channel angular pressing (ECAP) according to the Conform scheme (ECAP-C) with a UFG structure. The ECAP-C technology included: homogenizing annealing of steel at 820 °C followed by quenching in water + tempering at 350 °C + cold ECAP-C, 4 passes along the Vs (*Bc*) route + additional annealing at 350 °C, with a holding time of 10 min. The production technology and properties of the UFG steel are given in more detail in [19; 20]. Table 2 gives the mechanical properties of 09G2S steel before and after ECAP-C.

The experiment was carried out on a PROMA FHV-50PD universal milling machine. The blanks were processed using a 12-12D-30C-75L-4F HRC55 carbide milling cutter. No cooling was used during processing. The cutting temperature was recorded using a Seek Thermal Compact XR thermal imager. Thermal imager characteristics: temperature range is from −40 °C to +330 °C, viewing angle is 20°, resolution is 412×312 pixels, and frame refresh rate is 9 Hz.

When creating a model using a limited amount of data, bootstrap analysis was used. By creating multiple random samples with replacement from the original sample, a test statistic is created to find confidence intervals. Bootstrap analysis was carried out for a confidence interval of 0.95, with a number of samples of 999, the type of confidence intervals is BCa (corrected percentile), and the sampling method is sample of objects. All calculations were carried out in the R programming environment.

To search for the best structure of the mathematical model of cutting temperature, the method of automatic processing of models and discarding insignificant parameters, was used. The selection of the regression model was carried out, using the technique of stepwise forward/backward search, assessing the effectiveness of the model, according to the AIC criterion, and discarding insignificant parameters. The Akaike Informative Criterion (commonly called AIC), is a criterion for choosing between statistical models. The informative criterion considers the fit of the model to the data, taking into account the number of model parameters. When evaluating, preference is given to the model with the minimum criterion value.

Table 1. *Chemical composition of the 09G2S steel (wt. %)*
Таблица 1. *Химический состав стали 09Г2С (мас. %)*

Steel	C	Si	Mn	P	S	Ni	Cr	Al	Cu	Fe
09G2S	0.09	0.64	1.26	0.007	<0.003	0.1	0.08	0.02	0.14	the rest

Table 2. *Average grain size (d_{av}) and mechanical properties of the 09G2S steel in different states*
Таблица 2. *Средний размер зерна (d_{av}) и механические свойства стали 09Г2С в различных состояниях*

Steel state	d_{av}, μm	HB	$\sigma_в$, MPa	$\sigma_{0.2}$, MPa	δ, %
Initial (CG state)	20.00	143	485±3	354±11	25±1.8
After ECAP-C (UFG state)	0.45	331	838±12	655±44	10±1.5

RESULTS

The results of measuring the cutting temperature for the 09G2S steel with CG and UFG structure, are given in Tables 3, 4. It can be observed, that the cutting temperature depends on both the modes and the type of crystalline structure, of the alloy.

Fig. 1 shows distribution graphs (box plot) of cutting temperature for the 09G2S steel in CG and UFG states. In the graphs, one can see the extreme values (range), outliers, quartile boundaries, and a median. The graph for steel in the CG state shows the cutting temperature distribution, with possible outliers for experiments No. 3 and 5 (Fig. 1 a). For steel in the UFG state, no outliers were detected (Fig. 1 b). Fig. 1 shows that the interquartile range (rectangle height) for UFG steel is 2 times larger, and the median is significantly higher. Thus, the temperatures when processing 09G2S steel in the UFG state, are generally higher, than when processing 09G2S steel in the CG state.

Fig. 2, 3 show bootstrap analysis graphs. Bootstrap analysis displays an assessment of the significance of processing parameters when calculating cutting temperature. Thus, for steel in the CG state, the cutter rotation speed *n* and the feed *s* are insignificant, as can be observed from Fig. 2 b, 2 c (the abscissa of the peak value of the graph is near zero for *n* and *s*). Therefore, for steel in the coarse-grained state, the only significant parameter of the model is the cutting depth t. For the model of the cutting temperature of steel in the UFG state, the feed *s* (Fig. 3 c), as well as the depth of cut in the first and second degrees (Fig. 3 b, 3 d) are significant.

The model of the cutting temperature dependence, on processing modes, for 09G2S steel in the CG state is expressed by the formula

$$T = k + c \cdot t + d \cdot t^2,$$

where T is temperature, °C;
t is cutting depth, mm;
k, c, d are adjustable model parameters.

Fig. 4 shows a diagram of the model parameters with residuals for CG steel. The graphs represent the convergence of the model for all parameters. This is evident from the closeness of the values with residuals (solid line) and the model values (dashed line).

The model of the cutting temperature dependence on processing modes for 09G2S steel in the UFG state is expressed by the formula

$$T = t + s + I \cdot t^2,$$

where I is the model parameter.

Fig. 5 shows a diagram of model parameters with residuals for UFG steel. High model convergence is observed.

While studying the influence of processing modes on the temperature during end milling of blanks made of 09G2S steel in the CG and UFG states, the authors obtained the following results: for steel in the CG state, the cutting depth *t* has the greatest influence on the cutting temperature; for steel in the UFG state – the cutting depth *t* and feed *s*. In both cases, the dependence of temperature on cutting depth is described by a second-degree polynomial.

DISCUSSION

The experimental data analysis showed a different nature of the cutting temperature dependence on processing modes for steel in CG and UFG states. Probably, the higher temperature when processing steel in the UFG state can be explained by the increased level of physical and mechanical properties of this steel. This result is opposite to that obtained in [7] for the cutting temperature of titanium.

Apparently, to answer fully the question about the influence of the type of alloy crystalline structure on the cutting temperature, it is necessary to take into account the complex of physical and mechanical properties of the material. Thus, the 09G2S steel studied in this work is characterized by a significant increase in mechanical properties with grain refinement. This is most evident from the increase in the strength of the 09G2S steel, which increases by 1.7 times (from 485 to 838 MPa) during ECAP, as well as from the increase in the yield strength of steel by 1.85 times (from 354 to 655 MPa). At the same time, the thermal conductivity of steel is higher than that of titanium. Therefore, one can expect different patterns of temperature distribution, when cutting steel and titanium. The process of end milling of 09G2S steel, in the CG and UFG states is characterized by the absence of influence of the cutting speed on the temperature, in the studied range of processing modes. Thus, when milling this group of materials, the force component primarily determined by the cutting depth, exerts the predominant influence on the temperature regime. Further research could be aimed at investigating the milling temperature of steel, with different types of crystalline structure, within a wider range of cutting speeds. In this case, to carry out experiments, one may need both higher-speed machining equipment, and a thermal imager with a wider temperature measurement range, since the cutting temperature increases with increasing cutting speed.

The research is also complicated by the fact that at present, blanks from alloys with a UFG structure for cutting experiments, are produced in single-piece quantities. The shortage of processed material greatly limits the range of research carried out. Therefore, one can expect that in the near future, a lack of experimental data on the cutting processing of alloys with a UFG structure will continue to be. Partially, mathematical modeling of experimental results, with a small number of experiments, helps to find a way out of the situation. Statistical methods similar to the bootstrap analysis, used in this work, allow identifying the significance of factors, and formulating analytical dependencies for processing parameters, based on a relatively small sample of experimental data. Thus, the approach proposed in this study will help, in the future, to continue research into the cutting of alloys with different types of a crystalline structure. These studies will be necessary to design technological processes, for the production of parts from alloys, with an ultrafine-grained crystalline structure.

Table 3. *Milling temperature of the 09G2S steel in the initial state*
Таблица 3. *Температура фрезерования стали 09Г2С в исходном состоянии*

No. of experiment	Spindle speed *n*, rpm	Feed *s*, mm/min	Cutting depth *t*, mm	Cutting temperature, *T*, °C
1	720	65	0.6	91.3
2	875	65	0.8	84.5
3	720	65	1.0	198.0
4	720	100	0.6	94.0
5	875	100	1.0	259.0*
6	720	470	0.6	90.0
7	720	470	1.0	130.3
8	875	470	0.8	126.3
9	875	185	0.6	115.5
10	720	65	0.8	110.3

*Note. *A higher temperature value is possible, since the obtained value is close to the upper limit of the instrument measurement range (300 °C).*

*Примечание. *Возможно большее значение температуры, поскольку полученное значение близко к верхней границе диапазона измерения прибора (300 °C).*

Table 4. *Milling temperature of the 09G2S steel after ECAP-C*
Таблица 4. *Температура фрезерования стали 09Г2С после РКУП-К*

No. of experiment	Spindle speed *n*, rpm	Feed *s*, mm/min	Cutting depth *t*, mm	Cutting temperature, *T*, °C
1	720	65	0.6	95.5
2	875	65	0.8	97.3
3	720	65	1.0	163.0
4	720	100	0.6	94.3
5	875	100	0.8	109.5
6	875	100	1.0	195.3
7	720	185	0.6	168.8
8	875	185	0.8	170.3
9	875	185	1.0	258.3*

*Note. *A higher temperature value is possible, since the obtained value is close to the upper limit of the instrument measurement range (300 °C).*

*Примечание. *Возможно большее значение температуры, поскольку полученное значение близко к верхней границе диапазона измерения прибора (300 °C).*

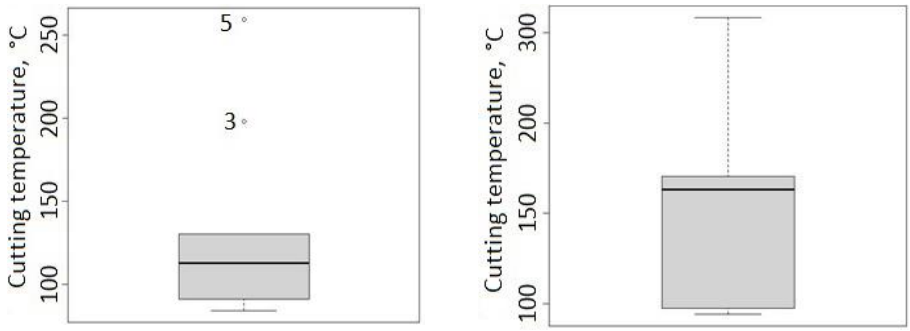

a ***b***

Fig. 1. *Box plots for cutting temperature of the 09G2S steel in CG and UFG states. The rectangle shows the boundaries of the lower and upper quartiles, the median is indicated by a dash:* ***a*** *– for CG state;* ***b*** *– for UFG state*

Рис. 1. *Графики распределения температуры резания для стали 09Г2С в КЗ и УМЗ состояниях. Прямоугольник отображает границы нижнего и верхнего квартилей, чертой обозначена медиана:* ***a*** *– для КЗ состояния;* ***b*** *– для УМЗ состояния*

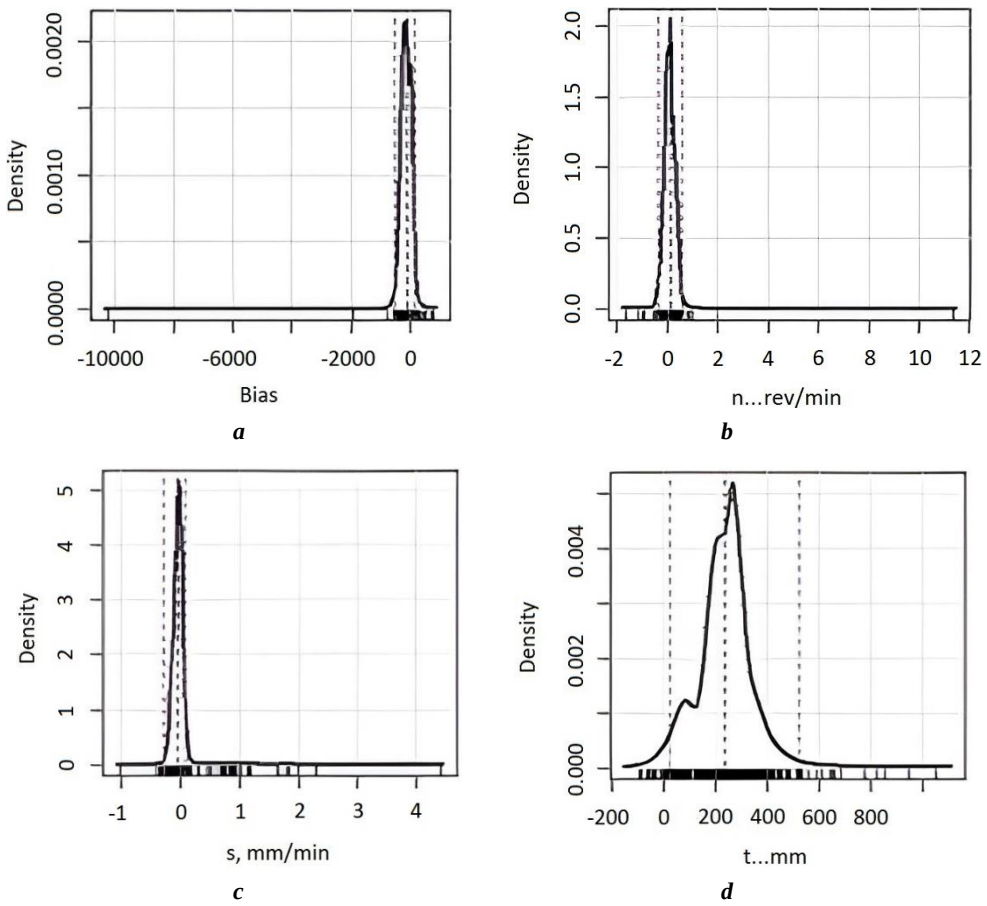

a ***b*** ***c*** ***d***

Fig. 2. *Bootstrap-analysis graphs for CG steel:* ***a*** *– bias;* ***b*** *– n, rev/min;* ***c*** *– s, mm/min;* ***d*** *– t, mm*

Рис. 2. *Графики бутстреп-анализа для КЗ стали:* ***a*** *– смещение;* ***b*** *– n, об/мин;* ***c*** *– s, мм/мин;* ***d*** *– t, мм*

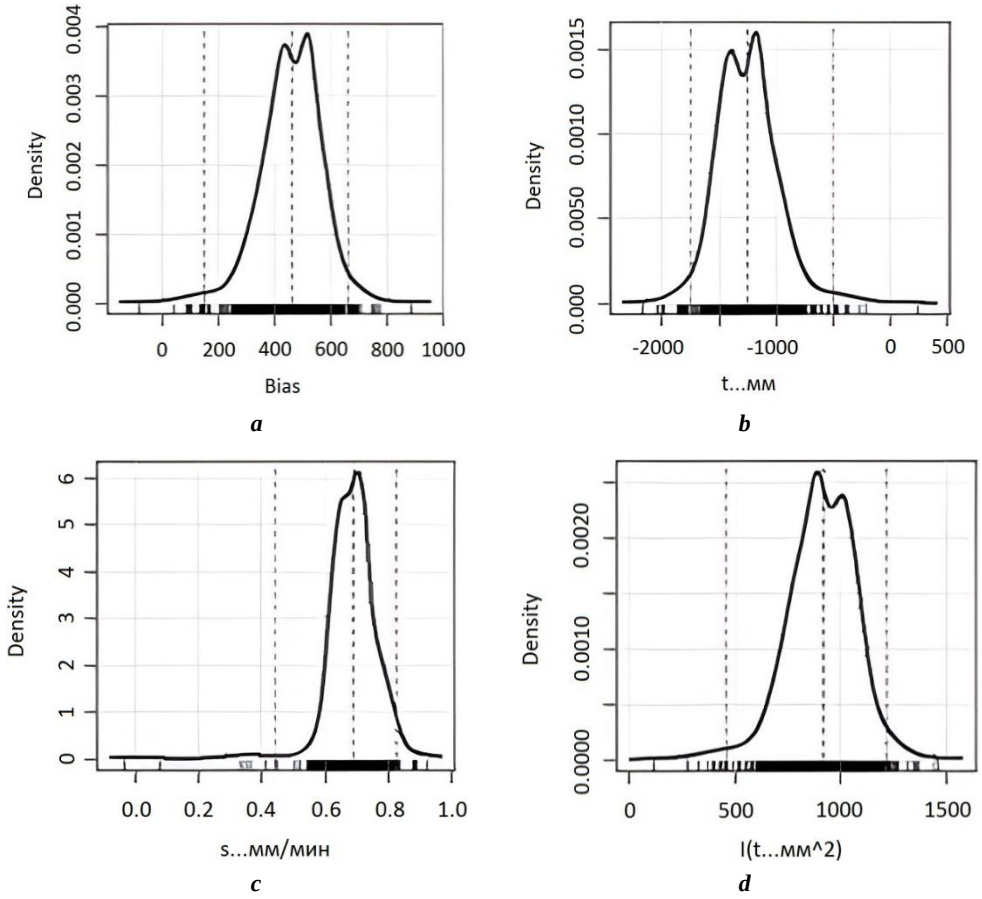

Fig. 3. *Bootstrap-analysis graphs for UFG steel:*
a *– bias;* ***b*** *– t, mm;* ***c*** *– s, mm/min;* ***d*** *– I(t, mm^2)*
Рис. 3. *Графики бутстреп-анализа для УМЗ стали:*
a *– смещение;* ***b*** *– t, мм;* ***c*** *– s, мм/мин;* ***d*** *– I(t, мм^2)*

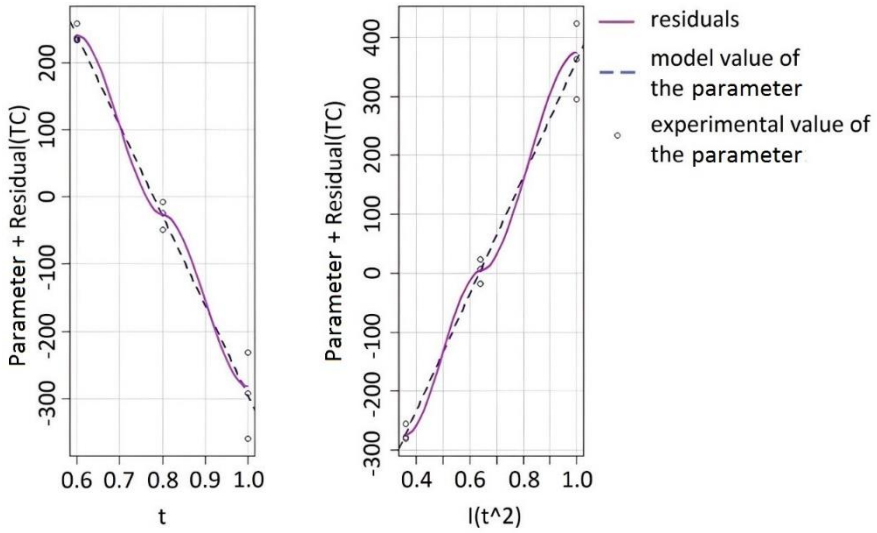

Fig. 4. *Diagram of the model parameters with residuals for CG steel*
Рис. 4. *Диаграмма параметров модели с остатками для КЗ стали*

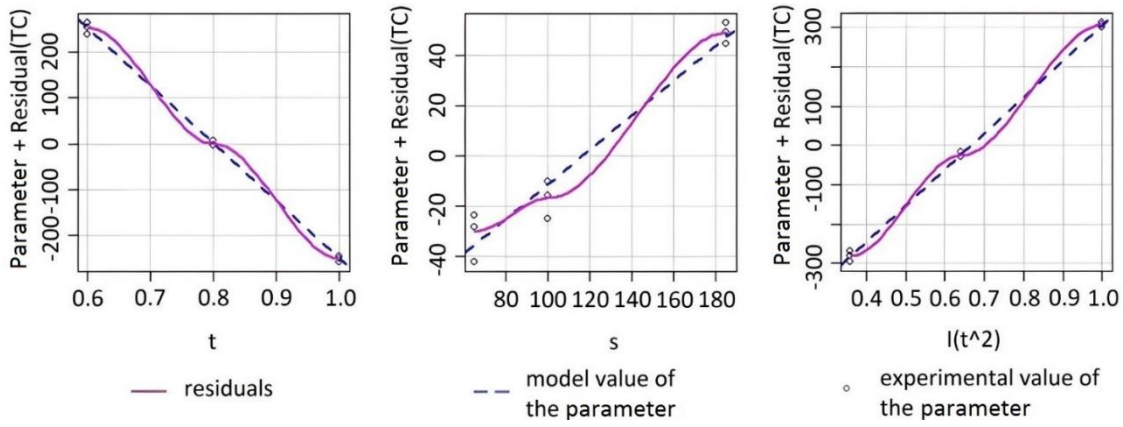

Fig. 5. *Diagram of the model parameters with residuals for UFG steel*
Рис. 5. *Диаграмма параметров модели с остатками для УМЗ стали*

CONCLUSIONS

The main factor influencing the end milling temperature of 09G2S steel in coarse-grained and ultrafine-grained states, is the cutting depth. For steel in the ultrafine-grained state, a significant factor in calculating the cutting temperature, aside from the cutting depth, is the feed, and its cutting temperature level is generally higher than that of steel in the coarse-grained state.

REFERENCES

1. Elias C.N., Meyers M.A., Valiev R.Z., Monteiro S.N. Ultra fine grained titanium for biomedical applications: an overview of performance. *Journal of Materials Research and Technology*, 2013, vol. 2, no. 4, pp. 340–350. DOI: 10.1016/j.jmrt.2013.07.003.
2. Lowe T.C., Valiev R.Z., Xiaochun Li, Ewing B.R. Commercialization of bulk nanostructured metals and alloys. *MRS Bulletin*, 2021, vol. 46, pp. 265–272. DOI: 10.1557/s43577-021-00060-0.
3. Filippov A.V., Tarasov S.Yu., Podgornykh O.A., Shamarin N.N., Vorontsov A.V. The Effect of Equal-Channel Angular Pressing on the Surface Quality of Aluminum Alloy 7075 after Milling. *Obrabotka metallov (Metal Working and Material Science)*, 2018, vol. 20, no. 4, pp. 96–106. DOI: 10.17212/1994-6309-2018-20.4-96-106.
4. Shamarin N.N., Filippov A.V., Tarasov S.Yu., Podgornykh O.A., Utyaganova V.R. The Effect of the Structural State of AISI 321 Stainless Steel on Surface Quality During Turning. *Obrabotka metallov (Metal Working and Material Science)*, 2020, vol. 22, no. 1, pp. 102–113. DOI: 10.17212/1994-6309-2020-22.1-102-113.
5. Rodrigues A.R., Balancin O., Gallego J., de Assis C.L.F., Matsumoto H., de Oliveira F.B., da Silva Moreira S.R., da Silva Neto O.V. Surface Integrity Analysis when Milling Ultrafine-grained Steels. *Materials Research*, 2012, vol. 15, no. 1, pp. 125–130. DOI: 10.1590/S1516-14392011005000094.
6. de Assis C.L.F., Jasinevicius R.G., Rodrigues A.R. Micro end-milling of channels using ultrafine-grained low-carbon steel. *The International Journal of Advanced Manufacturing Technology*, 2015, vol. 77, pp. 1155–1165. DOI: 10.1007/s00170-014-6503-2.
7. Ning Jinqiang, Nguyen Vinh, Huang Yong, Hartwig K.T., Liang S.Y. Inverse determination of Johnson–Cook model constants of ultra-fine-grained titanium based on chip formation model and iterative gradient search. *The International Journal of Advanced Manufacturing Technology*, 2018, vol. 99, pp. 1131–1140. DOI: 10.1007/s00170-018-2508-6.
8. Ning Jinqiang, Nguyen Vinh, Liang S.Y. Analytical modeling of machining forces of ultra-fine-grained titanium. *The International Journal of Advanced Manufacturing Technology*, 2019, vol. 101, pp. 627–636. DOI: 10.1007/s00170-018-2889-6.
9. Ning Jinqiang, Nguyen Vinh, Huang Yong, Hartwig K.T., Liang S.Y. Constitutive modeling of ultra-fine-grained titanium flow stress for machining temperature prediction. *Bio-design and Manufacturing*, 2019, vol. 2, pp. 153–160. DOI: 10.1007/s42242-019-00044-9.
10. Rastorguev D.A., Sevastyanov A.A., Klevtsov G.V., Bokov I.A., Dema R.R., Amirov R.N., Latypov O.R. Investigation of cutting force during face milling of coarse-grained and ultrafine-grained titanium alloys VT-6. *Russian metallurgy (Metally)*, 2022, vol. 2022, no. 13, pp. 1857–1863. DOI: 10.1134/s0036029522130316.
11. Lapovok R., Molotnikov A., Levin Y., Bandaranayake A., Estrin Y. Machining of coarse grained and ultra fine grained titanium. *Journal of Materials Science*, 2012, vol. 47, pp. 4589–4594. DOI: 10.1007/s10853-012-6320-7.
12. Storchak M., Kushner V., Möhling H.-C., Stehle T. Refinement of temperature determination in cutting zones. *Journal of Mechanical Science and Technology*, 2021, vol. 35, pp. 3659–3673. DOI: 10.1007/s12206-021-0736-4.
13. Cheng Hu, Zhuang Kejia, Weng Jian, Zhang Xiaoming, Ding Han. Cutting temperature prediction in negative-rake-angle machining with chamfered insert based on a modified slip-line field model. *International Journal of Mechanical Sciences*, 2020, vol. 167, article number 105273. DOI: 10.1016/j.ijmecsci.2019.105273.
14. Aliev M.M., Fomenko A.V., Fominov E.V., Shuchev K.G., Mironenko A.E. Influence of Wear-Resistant Coatings on Processes in the Contact Zone during Metal

Cutting. *Russian Engineering Research*, 2023, vol. 43, pp. 1101–1105. DOI: 10.3103/S1068798X23090034.
15. Rastorguev D.A., Sevastyanov A.A. Development of turning process digital twin based on machine learning. *Frontier Materials & Technologies*, 2021, no. 1, pp. 32–41. DOI: 10.18323/2073-5073-2021-1-32-41.
16. Grigorev S.N. *Diagnostika avtomatizirovannogo proizvodstva* [Diagnostics of automated production]. Moscow, Mashinostroenie Publ., 2011. 600 p.
17. Reka N.G., Kourov G.N., Lyutov A.G. Temperature Control Channel in the Metal-Cutting Zone of a Lathe. *Russian Engineering Research*, 2016, vol. 36, no. 2, pp. 163–167. DOI: 10.3103/S1068798X16020192.
18. Kuznetsov A.P. Temperature Control of Metal-Cutting Machines. *Russian Engineering Research*, 2015, vol. 35, pp. 46–50. DOI: 10.3103/S1068798X15010165.
19. Merson E.D., Myagkikh P.N., Klevtsov G.V., Merson D.L., Vinogradov A. Effect of fracture mode on acoustic emission behavior in the hydrogen embrittled low-alloy steel. *Engineering Fracture Mechanics*, 2019, vol. 210, pp. 342–357. DOI: 10.1016/j.engfracmech.2018.05.026.
20. Valiev R.Z., Zhilyaev A.P., Langdon T.G. *Bulk Nanostructured Materials: Fundamentals and Applications*. Hoboken, John Wiley & Sons Publ., 2014. 440 p. DOI: 10.1002/9781118742679.

СПИСОК ЛИТЕРАТУРЫ

1. Elias C.N., Meyers M.A., Valiev R.Z., Monteiro S.N. Ultra fine grained titanium for biomedical applications: an overview of performance // Journal of Materials Research and Technolgy. 2013. Vol. 2. № 4. P. 340–350. DOI: 10.1016/j.jmrt.2013.07.003.
2. Lowe T.C., Valiev R.Z., Xiaochun Li, Ewing B.R. Commercialization of bulk nanostructured metals and alloys // MRS Bulletin. 2021. Vol. 46. P. 265–272. DOI: 10.1557/s43577-021-00060-0.
3. Филиппов А.В., Тарасов С.Ю., Подгорных О.А., Шамарин Н.Н., Воронцов А.В. Влияние равноканального углового прессования на качество поверхности алюминиевого сплава В95 после фрезерования // Обработка металлов (технология, оборудование, инструменты). 2018. Т. 20. № 4. С. 96–106. DOI: 10.17212/1994-6309-2018-20.4-96-106.
4. Шамарин Н.Н., Филиппов А.В., Тарасов С.Ю., Подгорных О.А., Утяганова В.Р. Влияние структурного состояния коррозионно-стойкой стали 12Х18Н10Т на качество поверхности после точения // Обработка металлов (технология, оборудование, инструменты). 2020. Т. 22. № 1. С. 102–113. DOI: 10.17212/1994-6309-2020-22.1-102-113.
5. Rodrigues A.R., Balancin O., Gallego J., de Assis C.L.F., Matsumoto H., de Oliveira F.B., da Silva Moreira S.R., da Silva Neto O.V. Surface Integrity Analysis when Milling Ultrafine-grained Steels // Materials Research. 2012. Vol. 15. № 1. P. 125–130. DOI: 10.1590/S1516-14392011005000094.
6. de Assis C.L.F., Jasinevicius R.G., Rodrigues A.R. Micro end-milling of channels using ultrafine-grained low-carbon steel // The International Journal of Advanced Manufacturing Technology. 2015. Vol. 77. P. 1155–1165. DOI: 10.1007/s00170-014-6503-2.
7. Ning Jinqiang, Nguyen Vinh, Huang Yong, Hartwig K.T., Liang S.Y. Inverse determination of Johnson–Cook model constants of ultra-fine-grained titanium based on chip formation model and iterative gradient search // The International Journal of Advanced Manufacturing Technology. 2018. Vol. 99. P. 1131–1140. DOI: 10.1007/s00170-018-2508-6.
8. Ning Jinqiang, Nguyen Vinh, Liang S.Y. Analytical modeling of machining forces of ultra-fine-grained titanium // The International Journal of Advanced Manufacturing Technology. 2019. Vol. 101. P. 627–636. DOI: 10.1007/s00170-018-2889-6.
9. Ning Jinqiang, Nguyen Vinh, Huang Yong, Hartwig K.T., Liang S.Y. Constitutive modeling of ultra-fine-grained titanium flow stress for machining temperature prediction // Bio-design and Manufacturing. 2019. Vol. 2. P. 153–160. DOI: 10.1007/s42242-019-00044-9.
10. Расторгуев Д.А., Севастьянов А.А., Клевцов Г.В., Боков И.А., Дёма Р.Р., Амиров Р.Н., Латыпов О.Р. Исследование силы резания при торцовом фрезеровании крупнозернистого и ультрамелкозернистого титанового сплава ВТ6 // Технология металлов. 2021. № 7. С. 21–28. EDN: DBJMWH.
11. Lapovok R., Molotnikov A., Levin Y., Bandaranayake A., Estrin Y. Machining of coarse grained and ultra fine grained titanium // Journal of Materials Science. 2012. Vol. 47. P. 4589–4594. DOI: 10.1007/s10853-012-6320-7.
12. Storchak M., Kushner V., Möhling H.-C., Stehle T. Refinement of temperature determination in cutting zones // Journal of Mechanical Science and Technology. 2021. Vol. 35. P. 3659–3673. DOI: 10.1007/s12206-021-0736-4.
13. Cheng Hu, Zhuang Kejia, Weng Jian, Zhang Xiaoming, Ding Han. Cutting temperature prediction in negative-rake-angle machining with chamfered insert based on a modified slip-line field model // International Journal of Mechanical Sciences. 2020. Vol. 167. Article number 105273. DOI: 10.1016/j.ijmecsci.2019.105273.
14. Aliev M.M., Fomenko A.V., Fominov E.V., Shuchev K.G., Mironenko A.E. Influence of Wear-Resistant Coatings on Processes in the Contact Zone during Metal Cutting // Russian Engineering Research. 2023. Vol. 43. P. 1101–1105. DOI: 10.3103/S1068798X23090034.
15. Расторгуев Д.А., Севастьянов А.А. Разработка цифрового двойника процесса точения на основе машинного обучения // Frontier Materials & Technologies. 2021. № 1. С. 32–41. DOI: 10.18323/2073-5073-2021-1-32-41.
16. Григорьев С.Н. Диагностика автоматизированного производства. М.: Машиностроение, 2011. 600 с.
17. Reka N.G., Kourov G.N., Lyutov A.G. Temperature Control Channel in the Metal-Cutting Zone of a Lathe // Russian Engineering Research. 2016. Vol. 36. № 2. P. 163–167. DOI: 10.3103/S1068798X16020192.
18. Kuznetsov A.P. Temperature Control of Metal-Cutting Machines // Russian Engineering Research. 2015. Vol. 35. P. 46–50. DOI: 10.3103/S1068798X15010165.
19. Merson E.D., Myagkikh P.N., Klevtsov G.V., Merson D.L., Vinogradov A. Effect of fracture mode on acoustic emission behavior in the hydrogen embrittled low-alloy steel // Engineering Fracture Mechanics. 2019. Vol. 210. P. 342–357. DOI: 10.1016/j.engfracmech.2018.05.026.
20. Valiev R.Z., Zhilyaev A.P., Langdon T.G. Bulk Nanostructured Materials: Fundamentals and Applications. Hoboken: John Wiley & Sons, Inc., 2014. 440 p. DOI: 10.1002/9781118742679.

Исследование температуры концевого фрезерования низколегированной стали в крупнозернистом и ультрамелкозернистом состояниях

Расторгуев Дмитрий Александрович[1], кандидат технических наук,
доцент кафедры «Оборудование и технологии машиностроительного производства»
Севастьянов Александр Александрович*[2], аспирант
кафедры «Оборудование и технологии машиностроительного производства»
Клевцов Геннадий Всеволодович, доктор технических наук,
профессор кафедры «Нанотехнологии, материаловедение и механика»
Тольяттинский государственный университет, Тольятти (Россия)

***E-mail: alex-119977@yandex.ru,**
a.sevastyanov@tltsu.ru

[1]ORCID: https://orcid.org/0000-0001-6298-1068
[2]ORCID: https://orcid.org/0000-0002-7465-650X

Поступила в редакцию 05.07.2023 *Принята к публикации 29.01.2024*

Аннотация: Представлены результаты исследования температуры концевого фрезерования низколегированной стали в зависимости от режимов резания и типа кристаллической структуры. Эксперимент проводился на универсальном фрезерном станке PROMA FHV-50PD. Обработку заготовок осуществляли твердосплавной фрезой 12-12D-30C-75L-4F HRC55. В ходе обработки охлаждение не использовалось. Полученные данные подвергались статистическому анализу с целью выявления зависимости температуры концевого фрезерования низколегированной стали от режимов обработки и кристаллической структуры стали. При создании математической модели температуры резания проводился бутстреп-анализ для определения значимости параметров режимов обработки. Выбор математической модели производился с использованием информационного критерия Акаике. Обнаружено, что математические модели зависимости температуры от режимов обработки для обоих типов кристаллической структуры включают глубину резания во второй степени. При этом для стали в ультрамелкозернистом состоянии статистически значима не только глубина резания, но и подача. Влияния скорости резания на температуру в исследуемом диапазоне режимов обработки обнаружить не удалось. Таким образом, при обработке фрезерованием данной группы материалов преобладающее влияние на температурный режим оказывает силовая составляющая, в первую очередь определяемая глубиной резания. Уровень температуры резания при обработке стали в ультрамелкозернистом состоянии в целом выше, чем при обработке стали в крупнозернистом состоянии, что должно быть связано с повышенными физико-механическими свойствами стали с ультрамелкозернистой кристаллической структурой.

Ключевые слова: резание материалов; крупнозернистая (КЗ) и ультрамелкозернистая (УМЗ) структура; низколегированная сталь; температура резания; концевое фрезерование.

Благодарности: Авторы благодарят директора НИИ ФПМ при Уфимском университете науки и технологий (г. Уфа) профессора Р.З. Валиева за любезное предоставление материалов для исследования.

Работа выполнена при финансовой поддержке РНФ (проект № 20-69-47059, https://rscf.ru/project/20-69-47059/).

Для цитирования: Расторгуев Д.А., Севастьянов А.А., Клевцов Г.В. Исследование температуры концевого фрезерования низколегированной стали в крупнозернистом и ультрамелкозернистом состояниях // Frontier Materials & Technologies. 2024. № 1. С. 61–69. DOI: 10.18323/2782-4039-2024-1-67-6.

doi: 10.18323/2782-4039-2024-1-67-7

On the possibility of local measurement of crack resistance of structural steels taking into account the structure

Maxim I. Sergeyev*, postgraduate student
Egor V. Pogorelov[1], postgraduate student
Artemiy A. Dudarev, graduate student
Elina A. Sokolovskaya[2], PhD (Engineering), Associate Professor,
assistant professor of Chair of Metal Science and Physics of Strength
Aleksandr V. Kudrya, Doctor of Sciences (Engineering), Professor,
professor of Chair of Materials Science and Strength Physics
University of Science and Technology MISIS, Moscow (Russia)

***E-mail: m1600219@edu.misis.ru**

[1]ORCID: https://orcid.org/0000-0002-6768-5038
[2]ORCID: https://orcid.org/0000-0001-9381-9223

Received 27.06.2023 *Accepted 04.03.2024*

Abstract: The scale of heterogeneity of the structures of steels and alloys can be rather large both within one sample and within a product. The procedure adopted in practice for determining the integral values of crack resistance characteristics cannot always reflect this circumstance. In this regard, it is necessary to develop methods for assessing the crack resistance of a medium with a heterogeneous structure. In this work, the authors determined the crack resistance of large forgings made of heat-hardenable 38KhN3MFA-Sh steel (0.38%C–Cr–3%Ni–Mo–V) based on the critical crack opening δ_c and the *J*-integral. The presence of critical stages in the development of a ductile crack during testing was assessed by acoustic emission measurements. In combination with the obtained methods of digital fractography of 3D images of fractures, this allowed relating the shape and position of the leading edge of each crack jump to the load-displacement diagram. Measuring the crack opening geometry during the test showed the possibility of determining directly the coefficient of crack face rotation when estimating δ_c. In general, this allowed constructing a map of the distribution of parameter δ_c values over the thickness of the sample and estimating the scale of the scatter in crack resistance within one sample – up to 30 %. Such a localization of measurements, primarily of the δ_c parameter, is comparable to the scale of heterogeneity in the morphology of various types of structures, which was assessed based on the measurement of digital images of the dendritic structure, the Bauman sulfur print, non-metallic inclusions on an unetched section, and ferrite-pearlite banding in the microstructure. This makes it possible to link local crack resistance values to various fracture mechanisms and their accompanying structural components.

Keywords: heterogeneity of structures; crack resistance; acoustic emission; fractography; quality prediction in metallurgy; critical crack opening; Cherepanov–Rice integral; nonlinear fracture mechanics.

Acknowledgments: The paper was written on the reports of the participants of the XI International School of Physical Materials Science (SPM-2023), Togliatti, September 11–15, 2023.

For citation: Sergeyev M.I., Pogorelov E.V., Dudarev A.A., Sokolovskaya E.A., Kudrya A.V. On the possibility of local measurement of crack resistance of structural steels taking into account the structure. *Frontier Materials & Technologies*, 2024, no. 1, pp. 71–81. DOI: 10.18323/2782-4039-2024-1-67-7.

INTRODUCTION

The production of materials, in particular steels, is characterized by technological heredity – a mechanism for the evolution of structure and defects determined by the technological process trajectory [1; 2]. Within the tolerance limit of standard technology, a wide range of technological process trajectories is usually observed, the implementation of which leads to the formation of various structures in the material, nominally identical, but differing in the geometry of their structure [3; 4]. This is the reason for the scatter in properties, primarily viscosity (material's resistance to crack propagation), often significant [3; 5].

Within the current GOST 25.506-85, BS 7448-Part 1, and ASTM E1290 standards, it is assumed that the force criterion K_{1c} should be determined under the conditions of plane deformation, the deformation criterion – critical crack opening δ_c and the energy criterion – *J*-integral should be determined under conditions of developed plastic deformation and ductile crack undergrowth. All of them give crack resistance values when testing a sample with a preinduced fatigue crack. It is obvious that in the presence of a heterogeneous structure, the integral value of crack resistance is the result of the "addition" of the crack resistance values of individual structural components, the level of which is determined, among other things, by the size, shape of similar structural elements, and their spatial configuration. In this regard, the determination of crack resistance should provide for the possibility of linking it to the structure, the heterogeneity of its structure, for example, as was implemented within the local assessment of cold brittleness on samples whose dimensions are comparable to the scale of individual structural components [3]. The updating of regulatory documents related to the determination of crack resistance on massive samples has actually maintained the approaches to its assessment proposed several

decades ago. Until recently, the solution to this problem was complicated by difficulties associated with the correct description of the topography of fractures, in particular, its labor intensity, which makes their assessment qualitative [6; 7]. Therefore, for example, it is impossible to identify objectively the positions of the leading front of a growing crack in a fracture at the time of its successive jumps. Understanding this is necessary to identify the patterns of ductile crack propagation kinetics, in particular, in connection with the need to determine the critical stages of its development [7; 8]. Due to the morphology diversity of similar structures, which determines differences in the mechanisms and, consequently, in the crack propagation kinetics, it is not always clear to what extent the use of the maximum load value during testing as a critical value recommended by regulatory documents corresponds to reality [3; 6]. The use of acoustic emission (AE) for this purpose is not always accompanied by a comparison with direct results of measuring the topography of fractures, which complicates the interpretation of the results obtained [9; 10]. It is obvious that the development of digital methods for measuring structures and fractures can allow progressing in this direction, but a number of issues related to their metrological support still remain unresolved, which complicates the assessment of the reproducibility and comparability of the results obtained [3; 11]. However, the consistent development and application of methods for digitalization of measurements in crack resistance tests should provide a deeper understanding of the patterns of crack opening and propagation, which will allow developing refined approaches to determining fracture toughness, including assessing the possibility of linking the results to the structure heterogeneity. This is important for developing justified technology solutions aimed at increasing the consistent quality of metal [3; 5; 12].

The purpose of this work is to clarify the methods for determining criteria for nonlinear fracture mechanics based on measuring the crack geometry and opening, and to assess the possibility of linking crack resistance values to the structure heterogeneity.

METHODS

The metal of large forgings made of heat-hardenable steels of 38KhN3MFA-Sh (0.38%C–Cr–3%Ni–Mo–V) and 15Kh2NMFA (0.15%C–2%Cr–Ni–Mo–V) types with varying degrees of preserved cast structure and 09G2S (0.09%C–2%Mn–Si) sheet steel (Table 1) produced according to current industrial technologies was used as research objects.

Deep etching in a 50 % aqueous HCl solution (for ~30 min), 3 % HNO_3 solution (up to 3–5 s) was used to identify the dendritic structure and microstructure, respectively, and the Bauman method was used to obtain a sulfur print.

Digital images (in 256 shades of gray) of microstructures and non-metallic inclusions (NMI) on unetched sections were obtained using light microscopy (Axio Observer D1m Carl Zeiss class in the magnification range of 50–1000 times). To convert the images of macrostructures and the sulfur print into digital form, the authors also used an AGFA 1280 digital camera with a CCD matrix and a DUOSCAN T1200 scanner at a resolution of 500 dpi (film negatives at a magnification of ×0.5, the sulfur print at the sample scale).

To measure the geometry of structures and fractures, their primary digital 2D images (in 256 shades of gray) were converted into a "1-0" matrix (black and white) based on an analysis of the image brightness field. The illumination unevenness in the field of view was eliminated by subtracting an optimal degree polynomial; noise (not definitely identifiable small objects) was removed by filtration (taking into account the nature of the object's structure, usually ≤5–10 μm^2) [11].

Assessment of the heterogeneity of the placement of dark spots of sulfur prints was carried out by dividing the image into Voronoi polyhedra – polygons, in each of which all points are closer to its center than the points in neighboring polyhedra. In this case, the distribution of distances between neighboring polyhedra will objectively reflect the location of the sulfur print dark spots [3]. The difference in measurement results was assessed based on the nonparametric Smirnov criterion [13].

Digital three-dimensional images of fractures were obtained at the sample scale using the component module for the "Optofract – 5M" optical microscope (Russia), as well as optical units of the MBS-9 microscope (Russia) and a Nikon J1 digital system camera, resolution 10.1 megapixels. The method resolution was 5–10 μm for each of the three coordinates, the total analyzed volume corresponded to the fracture area in plan (taking into account measurements in the third direction) [15].

A digital three-dimensional triangulation model based on the obtained series of photographs was created using the OpenMVG, OpenMVS software packages and specially developed service modules in the C++ and Python programming languages. As a result of software reconstruction of the surface, non-textured triangulation models were obtained in the Stanford PLY and Wavefront OBJ formats. Visualization and editing (surfaces and point clouds) were carried out using MeshLab and CloudCompare software, the main 3D relief characteristics were calculated using Gwyddion software [1].

Fracture toughness tests were carried out using a three-point bending scheme in accordance with the GOST 25.506-85 standard on an Instron 150LX testing machine (USA) using rectangular specimens of type 4 (with dimensions of 15×20×120 mm) with a notch and a pre-grown fatigue crack, at loading speed of not more than 0.2 mm/min at room test temperature.

The force (K_{IC}) and energy (J-integral) crack resistance criteria were assessed in accordance with the GOST 25.506 standard. The value of the critical crack opening δ_c was also determined based on the concept that assumes that crack opening occurs by rotating its edges around a certain center (axis) [15, p. 86]:

$$\delta_c = V_c \frac{1}{1 + n\frac{l+z}{B-l}},$$

where V_c is the sensor displacement at critical load;
l is the crack length;
n is the rotation coefficient;

z is the distance from the displacement sensor location to the sample;
B is the height of the sample.

The coefficient *n* was determined experimentally based on finding the position of the center of rotation of the crack edges along the sample height (*L*) [14]:

$$n_{exp} = \frac{B-l}{L-(l+z)}.$$

The kinetics of stepped crack propagation was studied using the AE method and quantitative analysis of fractures. With a large number $N>>1$ of small AE pulses, informative emission signals corresponding to crack jumps, linked to the "Bending load *(P)* – Displacement *(V)*" diagram, were separated from the cumulative distribution $N(A)$ – the total number of pulses *N* with amplitude less than *A* [16].

The values of the critical crack opening δ_c and the *J*-integral were determined for each of the first crack jumps, δ_c – also for individual points of the leading crack edge.

RESULTS

The presence of different-scale structures in materials, from dendritic patterns of different geometries to microstructures of different morphologies, leads to a significant scatter in properties due to the influence of heterogeneity of structures on fracture mechanisms. Heterogeneity of structures at all scale observation levels was also present in the steels under study. It was observed both within one sample and from sample to sample. For example, a pair-wise comparison of samples of the results of measuring the NMI areas (at least 2000 pieces per option) at a 100-fold increase in four equal areas (not less than 80 mm^2 each) of the surface of an unetched section (total area ~340 mm^2) made of 38KhN3MFA-Sh (0.38%C–Cr–3%Ni–Mo–V) steel based on the Smirnov *D* criterion identified a significant difference with a risk of 0.05 (with a table value of $D_{0.05}$=1.36[1]) (Table 2).

The difference in the criterion experimental values reflects the difference in the statistics of the distribution of non-metallic inclusions areas in the studied parts of the section, which, in turn, is a consequence of the heterogeneity of the forging dendritic structure. This heterogeneity in the geometry of inclusions may be one of the reasons for the scatter in fracture toughness values.

The Bauman sulfur print morphology evidences the existence of NMI heterogeneity of a different scale in the same forgings associated with the presence in their structure of separate dendritic liquation zones (Fig. 1): columnar dendrites reflecting the heat removal direction to the surface of the forging (peripheral zone), a mixture of equiaxial small dendrites in the intermediate zone and coarse equiaxial dendrites in the central one (Fig. 2 a).

For the development of ductile fracture, both the size of sulfides and their placement on the surface of the polished section are important: their close location to each other facilitates the ductile fracture initiation, and an increase in their sparseness promotes the development of plastic deformation. The selection of the nearest neighbors on the plane was obtained based on partitioning the sulfur print image into Voronoi polyhedra (Fig. 2 b, 2 c). Partitioning the image into Voronoi polyhedra showed that the average distances between the centers of the polyhedra for different liquation zones (peripheral, intermediate and central) were close and amounted to 3.70±0.02; 3.70±0.01; 3.39±0.02 mm, respectively. The heterogeneity of the placement of the sulfur print dark spots of the forging of 38KhN3MFA-Sh (0.38%C–Cr–3%Ni–Mo–V) steel is evidenced, in particular, by the distribution of distances between their centers for forging areas corresponding to different zones of liquation (peripheral, intermediate and central) reflecting differences in the dendritic pattern morphology (Table 3).

With a similar distribution of distances between spots in each of the areas of the forgings, as evidenced by the values of the skewness and kurtosis coefficients (Table 4), differences are observed between the samples related to the results of measuring the distances between dark neighboring spots. This may be one of the reasons for the scatter of properties over the forging cross-section. The reason for such heterogeneity in the distribution of sulfides (sulfur print dark spots) was most likely liquation. A comparison of samples – the results of measuring the pitch of dendrites, for example, in the central and intermediate regions of the forging according to the Smirnov criterion, revealed their significant difference (D_{exp}=1.121 > $D_{0.118}$=1.19)[2]. The dendrite pitch varied from 60 to 3820 μm.

The remote consequences of liquation were also reflected in the microstructure of 38KhN3MFA-Sh (0.38%C–Cr–3%Ni–Mo–V) steel (a mixture of ferrite and bainite), in which large ferrite areas were observed. Their diameter varied from 95 to 386 μm.

The presence of a dendritic structure in forgings made of 15Kh2NMFA (0.15%C–2%Cr–Ni–Mo–V) steel also contributed to the formation of uneven distribution of sulfur print dark spots and the appearance of different grain sizes in the structure. Etching of samples selected at random revealed austenite grains in the structure differing in the range of maximum diameter *D* values ($\Delta=D_{max}-D_{min}$): 250 and 90 μm, respectively.

Heterogeneity of microstructures is characteristic not only of steels with a remained cast structure – its remote consequences can be observed, for example, in rolled products. The result of this may be differences in the scale of banding in the microstructure over the cross section of an impact sample made of sheet 09G2S (0.09%C–2%Mn–Si) steel (Fig. 3). Comparison of samples of the results of measuring the pitch of pearlite bands in two fields cut out from a panoramic image (along the cross section of an impact sample) using the Smirnov criterion showed that they differ with a risk of 0.05 (D_{exp}=1.37 > $D_{0.05}$=1.36).

Thus, it is obvious that the scale of heterogeneity of different-scale structures can be very large; this is typical when producing the materials, primarily the most widespread – steels. In this regard, assessing the viscosity of a medium with a heterogeneous structure, which allows

[1] *Bolshev L.N., Smirnov N.V. Mathematical Statistics Tables. Nauka, 1965. 464 p.*

[2] *See 1.*

Table 1. *Chemical compositions of steels under study*
Таблица 1. *Химические составы исследуемых сталей*

Steel	Weight fraction of elements, %									
	C	**Mn**	**Si**	**P**	**S**	**Cr**	**Ni**	**Mo**	**V**	**Cu**
38KhN3MFA (0.38%C–Cr–3%Ni–Mo–V)	0.41	0.22	0.22	0.02	0.02	0.87	3.32	0.58	0.14	0.03
09G2S (0.09%C–2%Mn–Si)	0.12	1.3	0.5	0.04	0.04	0.3	0.3	–	–	0.3
15Kh2NMFA (0.15%C–2%Cr–Ni–Mo–V)	0.13	0.3	0.17	0.02	0.02	1.8	1.0	0.5	0.01	0.03

Table 2. *Experimental values of the Smirnov criterion when comparing the results of measuring non-metallic inclusions areas on four equal-area sections of 38KhN3MFA-Sh (0.38%C–Cr–3%Ni–Mo–V) steel*
Таблица 2. *Экспериментальные значения критерия Смирнова при сравнении результатов измерения площадей неметаллических включений на четырех равных по площади участках шлифа из стали 38ХН3МФА-Ш (0,38%C–Cr–3%Ni–Mo–V)*

Panorama section	1	2	3	4
1	–	5.57	2.52	1.85
2	5.57	–	7.18	4.39
3	2.52	7.18	–	3.28
4	1.85	4.39	3.28	–

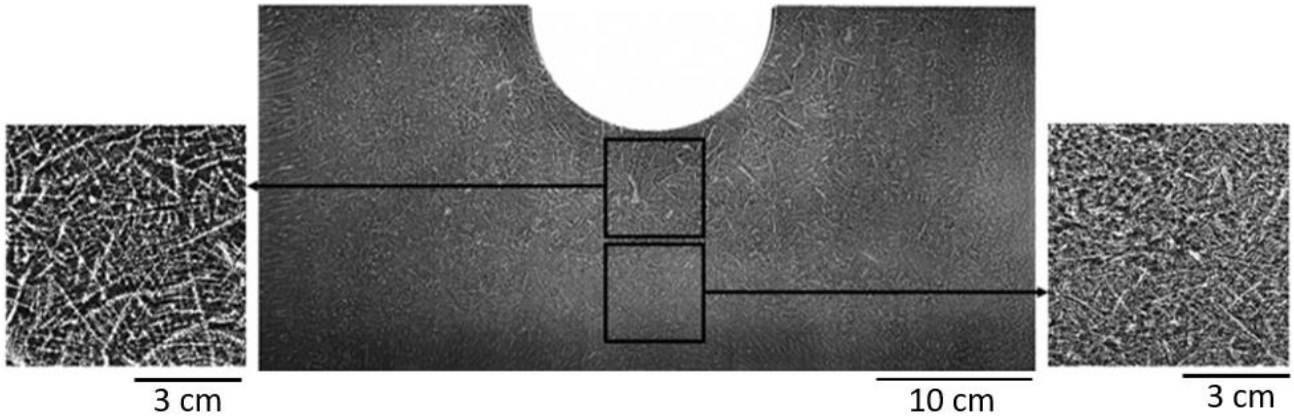

Fig. 1. *Morphology of the dendritic pattern of forging made of 38KhN3MFA-Sh (0.38%C–Cr–3%Ni–Mo–V) steel and its structure in the central and intermediate regions of the forging*
Рис. 1. *Морфология дендритного рисунка поковки из стали 38ХН3МФА-Ш (0,38%C–Cr–3%Ni–Mo–V) и его строение в центральной и промежуточной областях поковки*

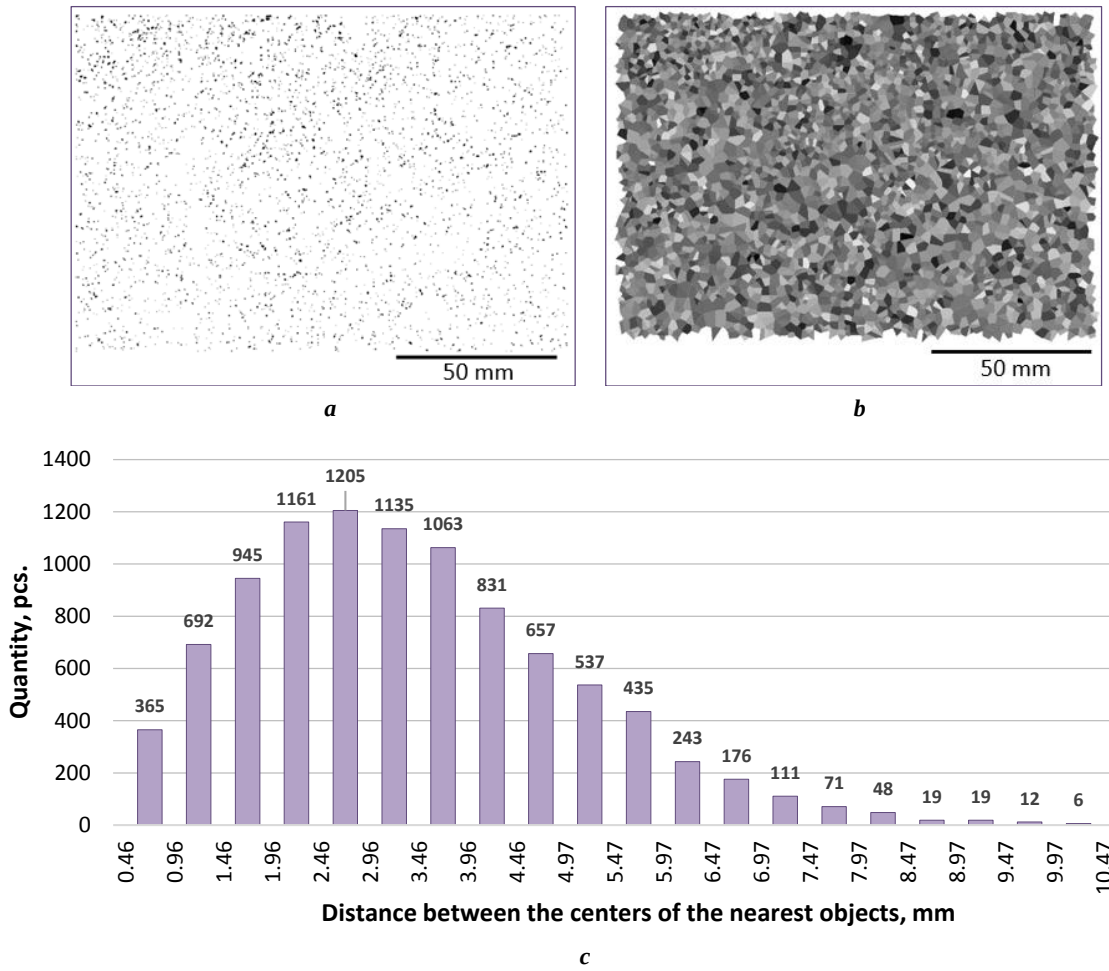

Fig. 2. *Sulfur print image decomposition (**a**) into Voronoi polyhedra (**b**) using the example of the central region of a forging made of tempered 38KhN3MFA-Sh steel (0.38% C–Cr–3% Ni–Mo–V) and the distribution of distances between the centers of gravity of the nearest dark spots (**c**)*

Рис. 2. *Разбиение изображения серного отпечатка (**а**) на полиэдры Вороного (**b**) на примере центральной области поковки из улучшаемой стали 38ХН3МФА-Ш (0,38%C–Cr–3%Ni–Mo–V) и распределение расстояний между центрами тяжести ближайших темных пятен (**c**)*

Table 3. *Experimental values of the Smirnov criterion obtained when comparing the distribution of the number of the nearest dark neighbor spots and the distances between their centers for different fragments of the sulfur print image of the forging made of 38KhN3MFA-Sh (0.38%C–Cr–3%Ni–Mo–V) steel*

Таблица 3. *Экспериментальные значения критерия Смирнова, полученные при сравнении распределений числа ближайших темных пятен-соседей и расстояний между их центрами, для различных фрагментов изображения серного отпечатка поковки из стали 38ХН3МФА-Ш (0,38%C–Cr–3%Ni–Mo–V)*

Forging area under study	Peripheral	Central	Intermediate
Peripheral	–	0.724 (0.6) 7.361 (0.05)	0.629 (0.8) 2.307 (0.05)
Central	0.724 (0.6) 7.361 (0.05)	–	0.588 (0.9) 9.356 (0.05)
Intermediate	0.629 (0.8) 2.307 (0.05)	0.588 (0.9) 9.356 (0.05)	–

Note. The numerator and denominator indicate the experimental values of the Smirnov criterion for the distribution of the number of the nearest dark spots of the sulfur print and the distance between their centers, respectively. The risks of the hypothesis about their differences are indicated in parentheses.

Примечание. В числителе и знаменателе указаны экспериментальные значения критерия Смирнова для распределения числа ближайших темных пятен серного отпечатка и расстояния между их центрами соответственно. В скобках указаны риски гипотезы об их отличии.

Table 4. *Values of the coefficients of skewness and kurtosis of the distributions of the number of neighbors of the nearest sulfur print dark spots and the distances between them in different areas along the cross-section of a forging made of 38KhN3MFA-Sh (0.38%C–Cr–3%Ni–Mo–V) steel*

Таблица 4. *Значения коэффициентов асимметрии и эксцесса распределений числа соседей ближайших темных пятен серного отпечатка и расстояний между ними в различных областях по сечению поковки из стали 38ХН3МФА-Ш (0,38%C–Cr–3%Ni–Mo–V)*

Parameter	Coefficient of	Peripheral region	Central region	Intermediate region
Number of neighbors	skewness	0.456	0.329	0.410
	kurtosis	0.167	−0.045	0.183
Distance between the centers of the nearest dark spots of sulfur print	skewness	0.719	0.737	0.674
	kurtosis	0.421	0.518	0.379

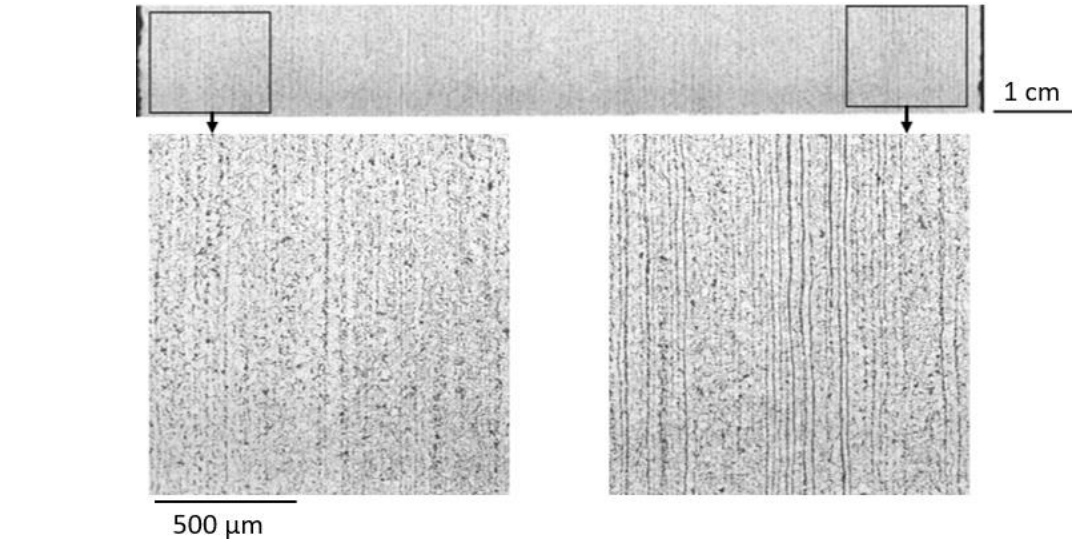

a

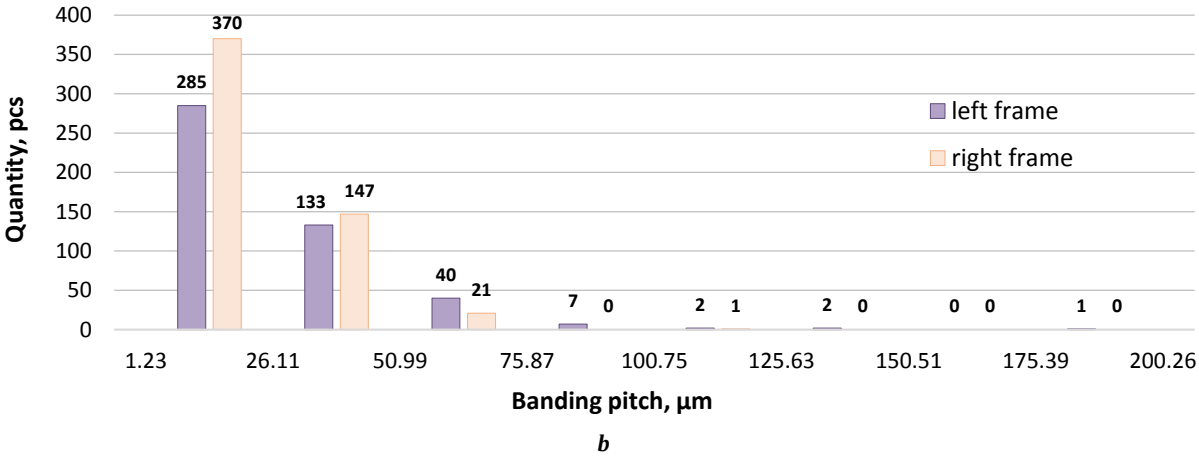

b

Fig. 3. *The observed difference in the scale of banding in the microstructure along the cross-section of an impact sample made of sheet 09G2S (0.09%C–2%Mn–Si) steel in the panorama as a whole and in its different sections (left and right) (**a**) and the corresponding distribution of values of a pitch of perlite strips (**b**)*

Рис. 3. *Наблюдаемое различие в масштабах полосчатости в микроструктуре по сечению ударного образца из листовой стали 09Г2С (0,09%C–2%Mn–Si) на панораме в целом и на отдельных ее участках (левом и правом) (**а**) и соответствующее им распределение значений шага полос перлита (**b**)*

determining the influence of heterogeneity on the fracture resistance, becomes relevant.

When determining fracture toughness based on the *J*-integral and δ_c, the authors assessed the crack propagation kinetics using AE, which made it possible to record pulses during the fracture process (Fig. 4 a). Most of the recorded pulses were of a noise nature. Filtering of AE signals allowed separating signals corresponding to crack jumps (with reference to the "*P* – *V*" diagram, Fig. 4 b).

The obtained results allowed identifying the scale of differences in crack resistance values (critical crack opening) both within each sample and from forging to forging, including the result of crack resistance calculation according to GOST: $\Delta^{\delta c}=\delta_c^{max}-\delta_c^{min}$; $\Delta_1^{\delta c}=|\delta_c^{GOST}-\delta_{c1}|$; $\Delta_{max}^{\delta c}=|\delta_c^{GOST}-\delta_c^{max}|$; $\Delta_{min}^{\delta c}=|\delta_c^{GOST}-\delta_c^{min}|$ (Table 5).

The difference between the δ_c values calculated in accordance with GOST within one sample compared to the CCO value determined experimentally (δ_c^{max}) varied from 3 to 40 % for 38KhN3MFA-Sh (0.38%C–Cr–3%Ni–Mo–V) steel, from 15 to 17 % for 15Kh2NMFA (0.15%C–2%Cr–Ni–Mo–V) steel; it reached 22 and 43 %, respectively, compared to the δ_c^{min} minimum opening value.

The *J*-integral values were also determined for each of the first five crack jumps, taking into account its undergrowth. The obtained results allowed identifying the scale of differences in the *J*-integral values both within each sample and from sample to sample, including with GOST: $\Delta^J=J^{max}-J^{min}$; $\Delta_1^J=|J^{GOST}-J_1|$; $\Delta_{max}^J=|J^{GOST}-J^{max}|$; $\Delta_{max}^J=|J^{GOST}-J^{max}|$; $\Delta_{min}^J=|J^{GOST}-J^{min}|$ (Table 6).

To assess the crack resistance heterogeneity over the sample section, a map of the distribution of critical crack opening values for the second – fourth jumps along the contours of the crack leading edge was compiled (Fig. 5). The first jump from a fatigue crack was not taken into account, since the fracture relief was measured only at the stage of static crack undergrowth.

Therefore, the use of a refined technique for local assessment of the critical crack opening allowed determining the values of crack resistance δ_c over the cross section of the sample.

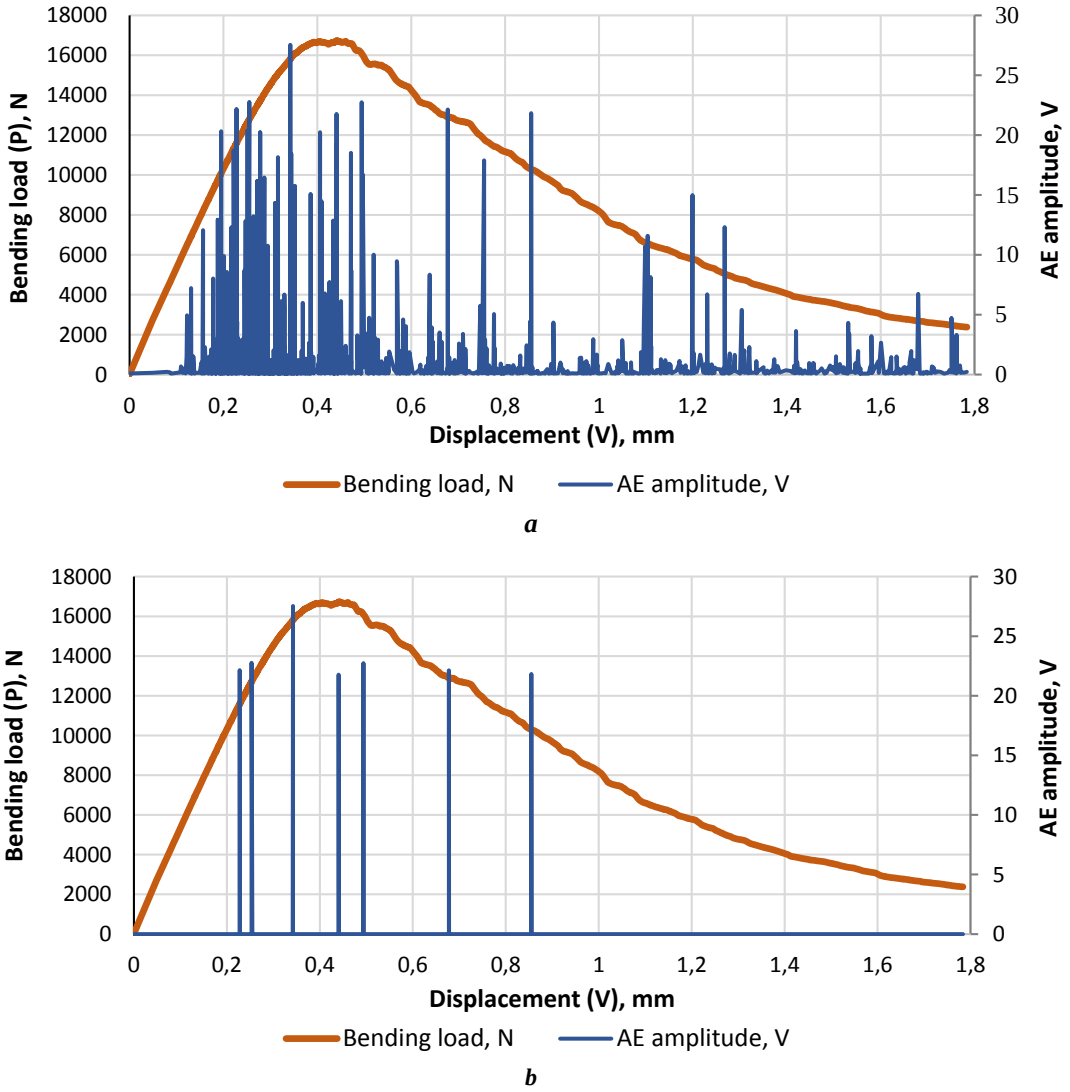

Fig. 4. *Loading – displacement diagram and AE signals during the destruction of a sample made of 38KhN3MFA-Sh (0.38%C–Cr–3%Ni–Mo–V) steel before (**a**) and after (**b**) filtration*
Рис. 4. *Диаграмма «нагрузка – смещение» и сигналы АЭ при разрушении образца из стали 38ХН3МФА-Ш (0,38%C–Cr–3%Ni–Mo–V) до (**a**) и после (**b**) фильтрации*

Table 5. *Scale of heterogeneity of δ_c values (mm) of metal forgings with a heterogeneous structure made of 38KhN3MFA-Sh (0.38%C–Cr–3%Ni–Mo–V) and 15Kh2NMFA (0.15%C–2%Cr–Ni–Mo–V) steels*
Таблица 5. *Масштаб неоднородности значений δ_c (мм) металла поковок с неоднородной структурой из стали 38ХН3МФА-Ш (0,38%C–Cr–3%Ni–Mo–V) и 15Х2НМФА (0,15%C–2%Cr–Ni–Mo–V)*

Steel	Sample number	$\Delta_1^{\delta c}$	$\delta_c^{\max}$	$\delta_c^{\min}$	$\Delta^{\delta c}$	$\Delta_{\max}^{\delta c}$	$\Delta_{\min}^{\delta c}$
38KhN3MFA-Sh (0.38%C–Cr–3%Ni–Mo–V)	1	0.005	0.108	0.079	0.029	0.031	0.002
	2	0.016	0.098	0.077	0.021	0.016	0.005
	3	0.031	0.121	0.091	0.030	0.031	0.001
	4	0.002	0.065	0.052	0.013	0.002	0.015
	5	0.007	0.093	0.068	0.025	0.007	0.018
15Kh2NMFA (0,15%C–2%Cr–Ni–Mo–V)	6	0.023	0.347	0.298	0.049	0.051	0.002
	7	0.089	0.228	0.152	0.076	0.040	0.116

Table 6. *Scale of heterogeneity of J-интеграла values (MJ/m^2) of 38KhN3MFA-Sh (0.38%C–Cr–3%Ni–Mo–V) and 15Kh2NMFA (0.15%C–2%Cr–Ni–Mo–V) steels*
Таблица 6. *Масштаб неоднородности значений J-интеграла (МДж/м^2) сталей 38ХН3МФА-Ш (0,38%C–Cr–3%Ni–Mo–V) и 15Х2НМФА (0,15%C–2%Cr–Ni–Mo–V)*

Steel	Sample number	J_{GOST}	$J_{\max}$	$J_{\min}$	Δ^J	Δ_1^J	$\Delta_{\max}^J$	$\Delta_{\min}^J$
38KhN3MFA-Sh (0.38%C–Cr–3%Ni–Mo–V)	1	0.057	0.097	0.066	0.031	0.009	0.040	0.009
	2	0.099	0.081	0.047	0.034	0.044	0.018	0.052
	3	0.070	0.135	0.083	0.052	0.025	0.065	0.013
	4	0.062	0.102	0.079	0.023	0.026	0.040	0.017
	5	0.067	0.064	0.039	0.025	0.028	0.003	0.028
15Kh2NMFA (0,15%C–2%Cr–Ni–Mo–V)	6	0.298	0.587	0.336	0.251	0.038	0.289	0.038
	7	0.274	0.189	0.122	0.067	0.106	0.085	0.152

DISCUSSION

The observed difference in crack resistance values within one sample and between samples showed that taking into account crack undergrowth, including shape restoration of its leading edge (according to AE measurements and fracture topography), provides a wider range of crack resistance values, both the critical crack opening δ_c and the Cherepanov–Rice integral (compared to GOST 25.506). This is significant, since for large forgings made of heat-hardenable 38KhN3MFA-Sh (0.38%C–Cr–3%Ni–Mo–V) and 15Kh2NMFA (0.15%C–2%Cr–Ni–Mo–V) steels, it was shown that the δ_c values within one sample varied from 25 to 37 % and from 16 to 50 %, respectively. At the same time, the values determined in accordance with GOST 25.506 differed from 3 to 34 % for 38KhN3MFA-Sh (0.38%C–Cr–3%Ni–Mo–V) steel and from 8 to 33 % for 15Kh2NMFA (0.15%C–2%Cr–Ni–Mo–V) steel compared to the δ_c values characteristic of the first static crack jump (according to AE measurements).

The *J*-integral value gives the integral value of the fracture energy for each crack jump. It was shown that the *J*-integral values within one sample varied from 29 to 72 % and from 55 to 75 %, respectively. The study revealed a significant difference between the values of the Cherepanov–Rice

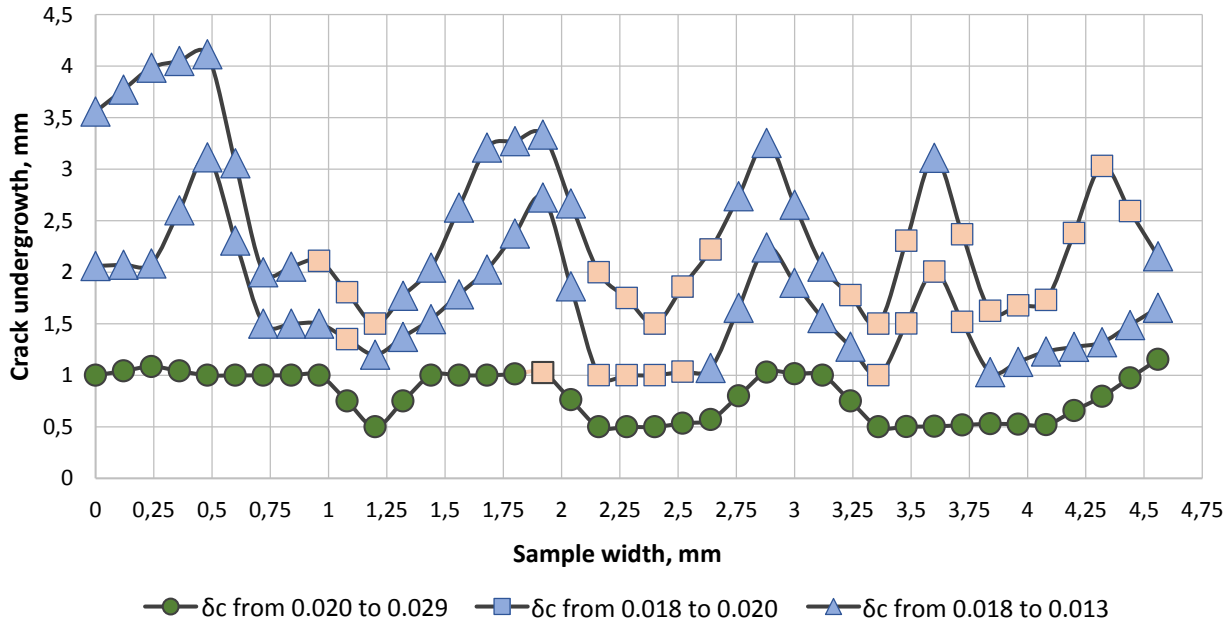

Fig. 5. *Map of the heterogeneity of crack resistance distribution (δ_c values) based on measurements at the bottom of a macrobrittle square for the second – fourth jumps of a ductile crack (the first jump from a fatigue crack was not taken into account), 38KhN3MFA-Sh (0.38%C–Cr–3%Ni–Mo–V)*
Рис. 5. *Карта неоднородности распределения трещиностойкости (значений δ_c) по измерениям на дне макрохрупкого квадрата для второго – четвертого скачков вязкой трещины (первый скачок от усталостной трещины не учитывался), сталь 38ХН3МФА-Ш (0,38%C–Cr–3%Ni–Mo–V)*

integral determined in accordance with GOST 25.506 and the *J*-integral values characteristic of the first static crack jump (according to AE measurements). It was 16–44 % for 38KhN3MFA-Sh (0.38%C–Cr–3%Ni–Mo–V) steel, 13–39 % for 15Kh2NMFA (0.15%C–2%Cr–Ni–Mo–V) steel. This means that using maximum load values as critical values when determining fracture toughness is not always valid.

It is important to note that critical crack opening has the advantage of being able to actually pinpoint the crack opening within each of the leading edges of a growing crack (taking into account their curvature and irregular shape). Hence, the possibility of linking δ_c values to one or another destruction mechanism, which is determined by the type of structure or the features of its local structure. This is important when identifying the causes of the scatter in viscosity, determining its structural and metallurgical factors, and it will allow improving the objectivity of the prediction of metal destruction as a whole. Identifying critical elements of structures is also necessary for managing the quality of metal products, including in real time, changing from selecting structures for given properties to designing structures of optimal configuration [17; 18].

CONCLUSIONS

Direct measurements of images of heterogeneous structures in large forgings made of 38KhN3MFA-Sh (0.38%C–Cr–3%Ni–Mo–V), 15Kh2NMFA (0.15%C–2%Cr–Ni–Mo–V) steels and sheet of 09G2S (0.09%C–2%Mn–Si) steel were used to assess the degree of heterogeneity of their structure, the scale of which should definitely be taken into account when determining their crack resistance. The boundaries of effective application of the criteria of nonlinear fracture mechanics are compared: deformation criterion – critical crack opening δ_c and energy criterion – *J*-integral. The study showed that, in the case the geometry and kinetics of ductile crack development are measured during fracture toughness testing, it is possible to expand the range of values of crack resistance characteristics (for each crack jump on one sample), which is essential for a more complete description of the viscosity reserve of a medium with a heterogeneous structure. The advantage of critical crack opening δ_c – the possibility of relating crack resistance values to the structure – has been identified when assessing structural steels with different-scale structural heterogeneity.

REFERENCES

1. Shtremel M.A. *Razrushenie. Razrushenie materiala* [Destruction. Rupture of material]. Moscow, MISiS Publ., 2015. Kn. 1, 975 p.
2. Shtremel M.A. *Razrushenie. Razrushenie struktur* [Destruction. Rupture of structures]. Moscow, MISiS Publ., 2015. Kn. 2, 975 p.
3. Kudrya A.V., Sokolovskaya E.A., Tang V.F. Possibility of predicting the destruction of metal materials with a heterogeneous structure. *Russian metallurgy (Metally)*, 2022, vol. 2022, no. 10, pp. 1318–1331. DOI: 10.1134/S0036029522100160.
4. Kazakov A.A., Kiselev D.V., Kazakova E.I. Quantitative methods for assessing the microstructure of steel

and alloys for revising outdated GOST standards. *Lite i metallurgiya*, 2021, no. 2, pp. 42–48. DOI: 10.21122/1683-6065-2021-2-42-48.
5. Kudrya A.V., Nikulin S.A., Nikolaev Y.A., Arsenkin A.M., Sokolovskaya E.A., Skorodumov S.V., Chernobaeva A.A., Kuzko E.I., Khoreva E.G. Nonuniformity of the ductility of 15X2HMFA low-alloy steel. *Steel in Translation*, 2009, vol. 39, no. 9, pp. 742–747. EDN: QCKREZ.
6. Tan Long, Li Songyang, Zhao Liangyin, Wang Lulu, Zhao Xiuxiu. The effect of mechanical inhomogeneity in microzones of welded joints on CTOD fracture toughness of nuclear thick-walled steel. *Nuclear Engineering and Technology*, 2023, vol. 55, no. 11, pp. 4112–4119. DOI: 10.1016/j.net.2023.07.031.
7. Li Ai, Soltangharaei V., Greer B., Bayat M., Ziehl P. Structural health monitoring of stainless-steel nuclear fuel storage canister using acoustic emission. *Developments in the Built Environment*, 2024, vol. 17, article number 100294. DOI: 10.1016/j.dibe.2023.100294.
8. Xu Jie, Sun Tong, Xu Yantao, Han Qinghua. Fracture toughness research of G20Mn5QT cast steel based on the acoustic emission technique. *Construction and Building Materials*, 2020, vol. 230, article number 116904. DOI: 10.1016/j.conbuildmat.2019.116904.
9. Vorontsov V.B., Pershin V.K. Correlation between Acoustic Emission and the Local Structural Restructuring in the Nonequilibrium Aluminum Melt. *Russian Metallurgy (Metally)*, 2020, vol. 2020, no. 2, pp. 92–101. DOI: 10.1134/S0036029520020160.
10. Botvina L.R., Tyutin M.R., Bolotnikov A.I., Petersen T.B. effect of preliminary cycling on the acoustic emission characteristics of structural 15Kh2GMF steel. *Russian Metallurgy (Metally)*, 2021, vol. 2021, no. 1, pp. 32–41. EDN: INTJOA.
11. Sokolovskaya E.A., Kudrya A.V., Kodirov D.F., Sergeev M.I., Budanova E.S., Samoshina M.E. On the reliability of the results of digital measurements of images of structures in metal science. *Metallurg*, 2024, no. 1, pp. 36–39. EDN: DGYMXQ.
12. Makhutov N.A. Evolution of laboratory researches and diagnostics of materials. *Zavodskaya laboratoriya. Diagnostika materialov*, 2022, vol. 88, no. 1-1, pp. 5–13. DOI: 10.26896/1028-6861-2022-88-1-I-5-13.
13. Nikitin Y. *Asymptotic efficiency of nonparametric tests*. New York, Cambridge University Press Publ., 1995. 274 p.
14. Kudrya A.V., Sokolovskaya E.A., Ngo Kh.N., Kuzko E.I., Kotishevskiy G.V. Fracture forecasting of large-size forged pieces with multi-scale structure. *Russian metallurgy (metally)*, 2019, vol. 12, no. 12, pp. 1304–1308. DOI: 10.1134/S0036029519120115.
15. Rabotnov Yu.N., ed. *Novye metody otsenki soprotivleniya metallov khrupkomu razrusheniyu* [New methods for assessing the resistance of metals to brittle fracture]. Moscow, Mir Publ., 1972. 438 p.
16. Khanzhin V.G., Shtremel M.A. Quantitative information on fracture processes obtained by measurement of acoustic emission. *Metal Science and Heat Treatment*, 2009, vol. 51, no. 5-6, pp. 250–255. DOI: 10.1007/s11041-009-9146-4.
17. Shtremel M.A., Karabasova L.V., Chizhikov V.I., Vodeniktov S.I. About optimal alloying of high-vanadium high-speed steel. *Metal Science and Heat Treatment*, 1999, vol. 41, no. 3-4, pp. 146–150. DOI: 10.1007/bf02465798.
18. Shtremel M.L., Belomyttsev M.Yu., Medvedev V.V., Mochalov B.V., Chernukha L.G. The structure and features of composite materials having web structure on the base of NiAl intermetallide. *Izvestiya. Ferrous metallurgy*, 2006, no. 1, pp. 40–44. EDN: HTDWRB.

СПИСОК ЛИТЕРАТУРЫ

1. Штремель М.А. Разрушение. В 2 кн. Кн. 1: Разрушение материала. М.: МИСиС, 2015. 975 с.
2. Штремель М.А. Разрушение. В 2 кн. Кн. 2: Разрушение структур. М.: МИСиС, 2015. 975 с.
3. Кудря А.В., Соколовская Э.А., Танг В.Ф. Возможность прогноза разрушения металлических материалов с неоднородной структурой // Деформация и разрушение материалов. 2022. № 6. С. 2–19. EDN: BSVQQW.
4. Казаков А.А., Киселев Д.В., Казакова Е.И. Количественные методы оценки микроструктуры стали и сплавов для пересмотра устаревших ГОСТ // Литье и металлургия. 2021. № 2. С. 42–48. DOI: 10.21122/1683-6065-2021-2-42-48.
5. Кудря А.В., Никулин С.А., Николаев Ю.А., Арсенкин А.М., Соколовская Э.А., Скородумов С.В., Чернобаева А.А., Кузько Е.И., Хорева Е.Г. Факторы неоднородности вязкости низколегированной стали 15Х2НМФА // Известия высших учебных заведений. Черная металлургия. 2009. № 9. С. 23–28. EDN: QCKREZ.
6. Tan Long, Li Songyang, Zhao Liangyin, Wang Lulu, Zhao Xiuxiu. The effect of mechanical inhomogeneity in microzones of welded joints on CTOD fracture toughness of nuclear thick-walled steel // Nuclear Engineering and Technology. 2023. Vol. 55. № 11. P. 4112–4119. DOI: 10.1016/j.net.2023.07.031.
7. Li Ai, Soltangharaei V., Greer B., Bayat M., Ziehl P. Structural health monitoring of stainless-steel nuclear fuel storage canister using acoustic emission // Developments in the Built Environment. 2024. Vol. 17. Article number 100294. DOI: 10.1016/j.dibe.2023.100294.
8. Xu Jie, Sun Tong, Xu Yantao, Han Qinghua. Fracture toughness research of G20Mn5QT cast steel based on the acoustic emission technique // Construction and Building Materials. 2020. Vol. 230. Article number 116904. DOI: 10.1016/j.conbuildmat.2019.116904.
9. Vorontsov V.B., Pershin V.K. Correlation between Acoustic Emission and the Local Structural Restructuring in the Nonequilibrium Aluminum Melt // Russian Metallurgy (Metally). 2020. Vol. 2020. № 2. P. 92–101. DOI: 10.1134/S0036029520020160.
10. Ботвина Л.Р., Тютин М.Р., Болотников А.И., Петерсен Т.Б. Влияние предварительного циклирования на характеристики акустической эмиссии конструкционной стали 15Х2ГМФ // Металлы. 2021. № 1. С. 32–41. EDN: KYXDHW.
11. Соколовская Э.А., Кудря А.В., Кодиров Д.Ф., Сергеев М.И., Буданова Е.С., Самошина М.Е. О достоверности результатов цифровых измерений изображений структур в металловедении // Металлург. 2024. № 1. С. 36–39. EDN: DGYMXQ.
12. Махутов Н.А. Развитие лабораторных исследований и диагностики материалов // Заводская лаборатория.

Диагностика материалов. 2022. Т. 88. № 1-1. С. 5–13. DOI: 10.26896/1028-6861-2022-88-1-I-5-13.
13. Nikitin Y. Asymptotic efficiency of nonparametric tests. New York: Cambridge University Press, 1995. 274 p.
14. Кудря А.В., Соколовская Э.А., Нго Х.Н., Кузько Е.И., Котишевский Г.В. Прогноз разрушения крупных поковок с неоднородной структурой // Электрометаллургия. 2019. № 6. С. 33–39. EDN: XLIBHK.
15. Новые методы оценки сопротивления металлов хрупкому разрушению / под ред. Ю.Н. Работнова. М.: Мир, 1972. 438 с.
16. Ханжин В.Г., Штремель М.А. Количественная информация о процессах разрушения, получаемая при измерениях акустической эмиссии // Металловедение и термическая обработка металлов. 2009. № 5. С. 53–59. EDN: JTSNZB.
17. Shtremel M.A., Karabasova L.V., Chizhikov V.I., Vodeniktov S.I. About optimal alloying of high-vanadium high-speed steel // Металловедение и термическая обработка металлов. 1999. № 4. С. 16–20. EDN: MPCVSV.
18. Штремель М.Л., Беломытцев М.Ю., Медведев В.В., Мочалов Б.В., Чернуха Л.Г. Структура и свойства композиционных материалов на основе интерметаллида NiAl // Известия высших учебных заведений. Черная металлургия. 2006. № 1. С. 40–44. EDN: HTDWRB.

О возможности локального измерения трещиностойкости конструкционных сталей с привязкой к структуре

Сергеев Максим Иванович*, аспирант
Погорелов Егор Васильевич[1], аспирант
Дударев Артемий Александрович, магистр
Соколовская Элина Александровна[2], кандидат технических наук, доцент,
доцент кафедры металловедения и физики прочности
Кудря Александр Викторович, доктор технических наук, профессор,
профессор кафедры металловедения и физики прочности
Университет науки и технологий МИСИС, Москва (Россия)

***E-mail: m1600219@edu.misis.ru**

[1]ORCID: https://orcid.org/0000-0002-6768-5038
[2]ORCID: https://orcid.org/0000-0001-9381-9223

Поступила в редакцию 27.06.2023 *Принята к публикации 04.03.2024*

Аннотация: Масштаб неоднородности структур сталей и сплавов может быть достаточно велик в пределах как одного образца, так и изделия. Принятая на практике процедура определения интегральных значений характеристик трещиностойкости не всегда может отразить это обстоятельство. В этой связи необходимо развитие методов оценки трещиностойкости среды с неоднородной структурой. В работе трещиностойкость крупных поковок из улучшаемой стали 38ХН3МФА-Ш (0,38%C–Cr–3%Ni–Mo–V) определяли на основе критического раскрытия трещины δ_c и *J*-интеграла. Наличие критических этапов в развитии вязкой трещины при испытании оценивали по измерениям акустической эмиссии. В сочетании с полученными методами цифровой фрактографии 3D-изображениями изломов это позволило привязать форму и положение переднего фронта каждого скачка трещины к диаграмме «нагрузка – смещение». Измерение геометрии раскрытия трещины в процессе испытания показало возможность прямого определения коэффициента вращения берегов трещины при оценке δ_c. В целом это позволило построить карту распределения значений параметра δ_c по толщине образца и оценить масштаб разброса трещиностойкости в пределах одного образца – до 30 %. Такая локализация измерений, в первую очередь параметра δ_c, сопоставима с масштабом неоднородности строения морфологии различных типов структур, который был оценен на основе измерения цифровых изображений дендритной структуры, серного отпечатка по Бауману, неметаллических включений на нетравленом шлифе, феррито-перлитной полосчатости в микроструктуре. Это дает возможность для привязки локальных значений трещиностойкости к различным механизмам разрушения и сопутствующим им структурным составляющим.

Ключевые слова: неоднородность структур; трещиностойкость; акустическая эмиссия; фрактография; прогноз качества в металлургии; критическое раскрытие трещины; интеграл Черепанова – Райса; нелинейная механика разрушения.

Благодарности: Статья подготовлена по материалам докладов участников XI Международной школы «Физическое материаловедение» (ШФМ-2023), Тольятти, 11–15 сентября 2023 года.

Для цитирования: Сергеев М.И., Погорелов Е.В., Дударев А.А., Соколовская Э.А., Кудря А.В. О возможности локального измерения трещиностойкости конструкционных сталей с привязкой к структуре // Frontier Materials & Technologies. 2024. № 1. С. 71–81. DOI: 10.18323/2782-4039-2024-1-67-7.

doi: 10.18323/2782-4039-2024-1-67-8

The influence of tungsten carbide and boride additives on the structure and microhardness of CrFeNi equiatomic coating formed by short-pulse laser cladding

Aleksandr K. Stepchenkov*[1,4], junior researcher
Aleksey V. Makarov[1,5], Doctor of Sciences (Engineering), Corresponding member of RAS, Head of Department of Materials Science, Head of Laboratory of Mechanical Properties
Elena G. Volkova[1,6], PhD (Physics and Mathematics), senior researcher
Svetlana Kh. Estemirova[2,7], PhD (Chemistry), senior researcher
Evgeny V. Kharanzhevskiy[3,8], Doctor of Sciences (Engineering), Professor, Head of Laboratory of Physics and Chemistry of Materials
[1]*M.N. Mikheev Institute of Metal Physics of the Ural Branch of RAS, Yekaterinburg (Russia)*
[2]*Institute of Metallurgy of the Ural Branch of RAS, Yekaterinburg (Russia)*
[3]*Udmurt State University, Izhevsk (Russia)*

***E-mail: stepchenkov@imp.uran.ru, alexander.stepchenkov@gmail.com**

[4]ORCID: https://orcid.org/0000-0001-9431-0170
[5]ORCID: https://orcid.org/0000-0002-2228-0643
[6]ORCID: https://orcid.org/0000-0003-4958-3027
[7]ORCID: https://orcid.org/0000-0001-7039-1420
[8]ORCID: https://orcid.org/0000-0002-1525-2169

Received 27.06.2023 *Accepted 30.01.2024*

Abstract: A coating based on a single-phase medium-entropy CrFeNi alloy with a face centered cubic (fcc) structure has good ductility, relatively high anti-corrosion properties, low cost, but insufficient strength for its widespread use. It is assumed that adding strengthening particles in the form of tungsten carbides and borides to the CrFeNi equiatomic coating will lead to an increase in its mechanical properties. This work studies the influence of tungsten carbide and boride additives on the structure and microhardness of a CrFeNi equiatomic coating. The coatings were formed by layer-by-layer short-pulse laser cladding with preplaced powder on a multifunctional laser installation equipped with a solid-state laser with a lamp pump based on an Nd:YAG crystal. The change in phase composition when adding strengthening particles was detected using X-ray diffraction analysis and transmission electron microscopy (TEM). Both methods confirmed the precipitation of $Cr_{23}C_6$ chromium carbide in the deposited coatings. TEM photographs indicate that the precipitated phase is distributed along the grain boundaries of the γ-solid solution. The study found that the addition of 6 wt. % WC and 3 wt. % WB increases the level of microhardness of the CrFeNi coating by 26 % (from 340±6 to 430±12 HV 0.025). This occurs due to the presence of $Cr_{23}C_6$, WC particles in the structure and possible microdistortions of the crystal lattice of the γ-phase as a result of doping with tungsten atoms released during the dissolution of tungsten borides and carbides in the process of high-temperature short-pulse laser heating.

Keywords: CrFeNi coating; medium-entropy alloys; tungsten carbides/borides; short-pulse laser cladding; equiatomic coatings; microhardness.

Acknowledgments: The work was carried out within the state assignment to M.N. Mikheev Institute of Metal Physics of the Ural Branch of the Russian Academy of Sciences (IMP UB RAS) on the topic “Structure” No. 122021000033-2. The research was carried out using the equipment of the Electron Microscopy and Mechanical Testing Departments of the Collaborative Access Center “Testing Center of Nanotechnology and Advanced Materials” of IMP UB RAS.

A.K. Stepchenkov thanks M.N. Mikheev Institute of Metal Physics for the support of the work under the state assignment to IMP UB RAS on the topic “Structure” No. 122021000033-2, which was carried out within the framework of the IMP UB RAS youth project No. 22-13/mol.

The paper was written on the reports of the participants of the XI International School of Physical Materials Science (SPM-2023), Togliatti, September 11–15, 2023.

For citation: Stepchenkov A.K., Makarov A.V., Volkova E.G., Estemirova S.Kh., Kharanzhevskiy E.V. The influence of tungsten carbide and boride additives on the structure and microhardness of CrFeNi equiatomic coating formed by short-pulse laser cladding. *Frontier Materials & Technologies*, 2024, no. 1, pp. 83–94. DOI: 10.18323/2782-4039-2024-1-67-8.

INTRODUCTION

One of the most rapidly developing areas of modern metal science is associated with the development of a new class of materials – high-entropy alloys (HEAs). These alloys appeared relatively recently, in 2004, usually contain at least five elements, and the amount of each of them should not be less than 5 at. % [1; 2]. Due to

significant differences in the processes of structure and phase formation, HEAs are classified as a separate group of materials, that have mechanical and functional properties, as well as thermal stability, different from traditional alloys (the main element as a matrix and a set of alloying elements). As a result, HEAs can have unique strength, tribological and corrosion properties in a wide temperature range [3–5].

Medium-entropy alloys (MEAs) consist of three or more main elements with approximately equal atomic percentages, and their configuration entropy is in the range of 1–1.5 R (R is the universal gas constant) [6]. Due to the high mixing entropy associated with a disordered solution of several elements, both MEAs and HEAs can form stable single-phase solid solutions in which, in an ideal situation, atoms of different sizes are uniformly distributed.

Most industrial equipment is exposed to aggressive external influence, such as high thermal and mechanical loads. To ensure long-term operability, and stability of this equipment, a functional surface layer (coating) with high mechanical, anti-corrosion and other properties is required. It is the surface layers, in which the processes of wear, corrosion, cavitation damage and the initiation of fatigue cracks develop, which are the main reasons for the failure of the bulk of parts and mechanisms. Therefore, the use of expensive HEAs and MEAs, in the form of thin laser coatings, and not in the form of an entirely manufactured part, will provide a significant economic effect due to material saving [7].

At the same time, the technology of laser surfacing, using short-pulse radiation, has a number of significant advantages. These include the possibility of producing a homogeneous, and dense layer of coating material of a specified thickness with a good metallurgical bonding, with the substrate material [8], as well as the possibility of forming nonequilibrium microstructures with unique physical, and mechanical properties [9]. Due to high energy densities, the thermal effect on the substrate is minimized [9; 10]. The continuous development of laser technologies makes them attractive for use, due to relative ease of operation, low cost, and high processing efficiency.

The system of Cr–Fe–Ni components is the basis for a large number of MEAs and HEAs. Taken together, these components form a medium-entropy equiatomic alloy with relatively high anti-corrosion, mechanical and wear-resistant properties, as well as low cost compared to other multicomponent alloys.

Generally, single-phase face centered cubic (fcc) structure HEAs and MEAs have good ductility, but low strength [11]. Therefore, the development of ways to improve the mechanical properties of these alloys is an up-to-date area for further research. The strength of multicomponent alloys can be increased through solid solution strengthening, by adding elements with a large atomic radius. The second phase precipitation in the fcc matrix can also improve the mechanical properties of the alloy [12].

To increase the hardness of traditional alloys, additives of various strengthening particles are used – carbides, borides, etc. Tungsten carbide WC is well known for its high hardness, high chemical stability and oxidation resistance, which makes it possible to use it as a reinforcing phase in composite coatings to increase wear resistance [13–15]. It is known that tungsten borides have good chemical inertness, high wear resistance and hardness, as well as a high fusion temperature [16; 17]. Based on this, it can be assumed that the addition of strengthening particles in the form of tungsten carbides and borides during short-pulse laser cladding of the CrFeNi alloy can be an effective way to increase its strength characteristics.

The purpose of this work is to study changes in the structural-phase state and microhardness of a coating based on an equiatomic CrFeNi alloy, formed by short-pulse laser cladding with the addition of tungsten carbides and borides.

METHODS

Multicomponent coatings, based on medium-entropy alloys, were formed by layer-by-layer short-pulse laser cladding, with preplaced powder on a LRS AU multifunctional laser system (manufactured by the "OKB BULAT"), equipped with a solid-state Nd:YAG laser (wavelength is 1.065 μm).

The substrate material, was plates of AISI 1035 (chemical composition: Fe–C0.38–Si0.34–Mn0.65–Cr0.13–Ni0.06–Cu0.09 wt. %; as-delivered state), with dimensions of 45×45×10 mm^3. Before applying the coating, the surface of the plates was cleaned from oxides using sandpaper. As the base coating material, an equiatomic alloy of the Cr–Fe–Ni system was used in the form of a spherical powder, with a fraction of 50–150 μm (supplied by PJSC "Ashinsky Metallurgical Plant", Asha, Russia), the chemical composition of which is given in Table 1. To strengthen the CrFeNi matrix of the coating, GP10BN powder (60 % WC + 30 % WB + 10 % Co) with the fraction of 10–30 μm was used produced by Luoyang Golden Egret Geotools Co., Ltd (China). The surfacing material of the multicomponent coating was obtained by mechanically mixing CrFeNi alloy powder, and the GP10BN powder in amounts of 3 and 10 wt. %. Consequently, CrFeNi + 1.8 % WC + 0.9 % WB + 0.3 % Co and CrFeNi + 6 % WC + 3 % WB + 1 % Co coatings were obtained (wt. %). A coating without adding the alloying elements (CrFeNi), acted as a base coating to compare the resulting structural features and micromechanical properties.

Laser cladding with preplaced powder was used to apply the coating. A preplaced layer of the material was produced by applying a suspension (10 g of a mixture of CrFeNi powder and alloying additive (GP10BN powder); 2 ml of alcohol-rosin solution) and subsequent levelling with a special device ("knife") to achieve a uniform thickness (~200 μm) of the layer over the entire deposited area. Then, the plate with the applied layer of suspension was dried with a heat gun for 15–20 s. After this, the plate was placed in a chamber with continuous inert gas (argon) purging. Laser scanning of the deposited layer of the material was carried out according to the scheme shown in Fig. 1 a.

The following laser cladding parameters were used: pulse duration – 3.5 ms; pulse frequency – 20 Hz; pulse energy – 8.3 J; distance between scanning lines – 0.8 mm;

Table 1. *Chemical composition of CrFeNi powder, wt. %*
Таблица 1. *Химический состав порошка CrFeNi, мас. %*

Fe	Ni	Cr	C	S	P	Si
Base	35.6	29.8	0.37	<0.001	0.008	1.62

the diameter of the laser spot in the focal plane was ~1 mm. After this, the deposited coating was re-exposed to laser action, but with a greater degree of laser defocusing in order to obtain a surface with less roughness. To reduce the effect of mixing the coating material with the substrate material, the coating was applied in three layers.

Measurements of Vickers microhardness (HV) of coatings, as well as the construction of 2*D* maps of its distribution, were carried out on a cross-section using a Q10A+ automated microhardness tester (Qness, Austria). The load on the Vickers indenter was 0.245 N (25 gf), and the holding time was 10 s. The measurement error was determined by the standard deviation with a confidence level of p=0.95. The presence of an optical system, with magnifying lenses, made it possible to use this equipment for studying the macrostructure.

X-ray diffraction analysis (XRD) was performed using a XRD-7000 diffractometer (Shimadzu, Japan) in Cu–K_α radiation, using a graphite monochromator. X-ray tube voltage U=40 kV, current I=30 mA, focus size 1×10 mm^2, external standard is silicon powder. The diffraction spectrum was recorded in the angular range of 2Θ=30–120°, in a step-by-step mode with a scanning step of Δθ=0.03° and a pulse accumulation duration of 2 s. Phase identification was carried out using the PDF-2 database of the International Centre for Diffraction Data (ICDD). The ICDD data bank also contains a program of quantitative analysis using the corundum number method, which was applied to determine the relative content of the phases. Corundum numbers (the ratio of the intensities of the maximum lines of phases, and the reference phase of corundum (α-Al_2O_3) in a 1:1 mixture), are accumulated in the ICDD data bank along with X-ray phase standards. This method is a semi-quantitative estimation.

Measurements of the half-width (full width at half maximum) of diffraction lines, were performed using the "New_profile" software package (free distribution). The package includes a set of means for preliminary processing of diffraction spectra, (background separation, elimination of the $K\alpha_2$ component of the doublet). Background separation was carried out using the least squares method (LSM); to determine the single maxima parameters, the Lorentz quadratic function was used. The software package uses the residual value as a criterion for the quality of fitting. In the process of fitting the Lorentz function to the experimental profiles of single maxima, data on the position of these maxima were obtained, which were then used to calculate the elementary cell parameters of the detected phases.

Since the X-ray diffraction spectrum contained broadened diffraction maxima, we analysed the line broadening using the Williamson–Hall method, which assumes that the broadening is caused by the small sizes of coherent scattering regions (CSR) and microdistortions (ε) of crystalline structure (type II residual stress). The method is based on the following relation:

$$\beta = 4 \cdot \varepsilon \cdot \tan\Theta + \frac{\lambda}{D \cdot \cos\Theta},$$

where β is the physical broadening, rad.;
ε is an average value of microstrains (dimensionless value);
Θ is Bragg angle;
λ is the radiation wavelength (for Cu–K_α λ=1.54051 Å);
D is the CSR size, nm.

Electron microscopy studies were carried out using a JEM-200CX transmission electron microscope (JEOL, Japan). Samples (~300 μm thick) for the production of thin foils were cut out on an electric spark machine, followed by grinding to a thickness of 50–70 μm. Then, they were subjected to double-sided thinning by electropolishing.

RESULTS

Fig. 2 shows a cross-section of a CrFeNi + 6 % WC + + 3 % WB + 1 % Co (wt. %) medium-entropy alloy coating obtained by optical microscopy. As can be seen, the coating thickness value after three-layer laser cladding varies from approximately 620 to 710 μm. The macrostructure of the studied sample shown in Fig. 2 confirms that during the laser cladding, a relatively dense, uniform coating is formed without large defects in the form of cracks. The coating contains isolated continuity defects in the form of pores, which are predominantly round-shaped. It is also worth noting that during laser cladding, an almost defect-free transition zone was formed, between the coating material and the substrate material: there are no peelings of the coating, only isolated elongated pores are observed.

The Vickers microhardness test results indicate an increase in the microhardness of coatings up to 26 %, with the addition of strengthening additives in the form of tungsten carbides and borides. As can be seen from Table 2 and the graph presented in Fig. 3, the average microhardness of the CrFeNi coating formed by laser cladding is 340±6 HV 0.025.

An increase in the mass fraction of WC and WB in coatings, leads to an increase in the microhardness level. The average microhardness level of the CrFeNi + 1.8 % WC + + 0.9 % WB + 0.3 % Co sample is approximately 380±11 HV 0.025, while this feature for the CrFeNi + + 6 % WC + 3 % WB + 1 % Co sample is 430±12 HV 0.025, which is 12 and 26 %, respectively, higher than that of the original sample without strengthening additives.

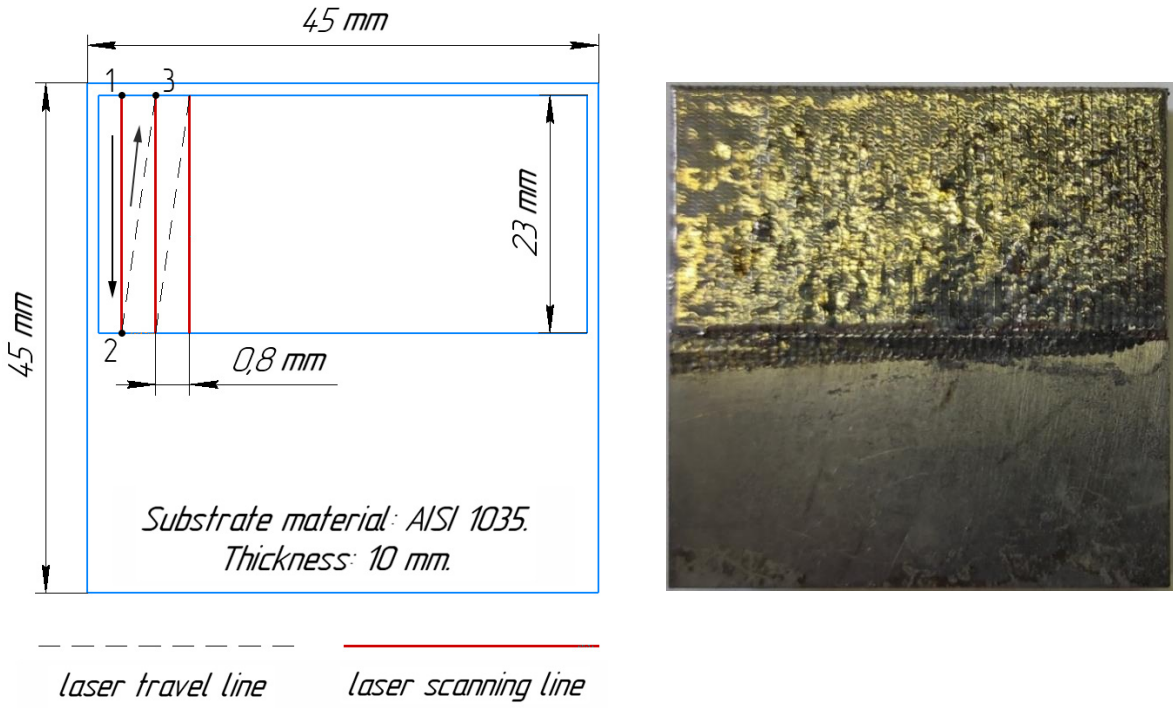

Fig. 1. *Scheme of laser scanning of pre-applied powder (**a**) and appearance of a steel sample with a fused coating (**b**)*
Рис. 1. *Схема лазерного сканирования предварительно нанесенного порошка (**a**) и внешний вид стального образца с наплавленным покрытием (**b**)*

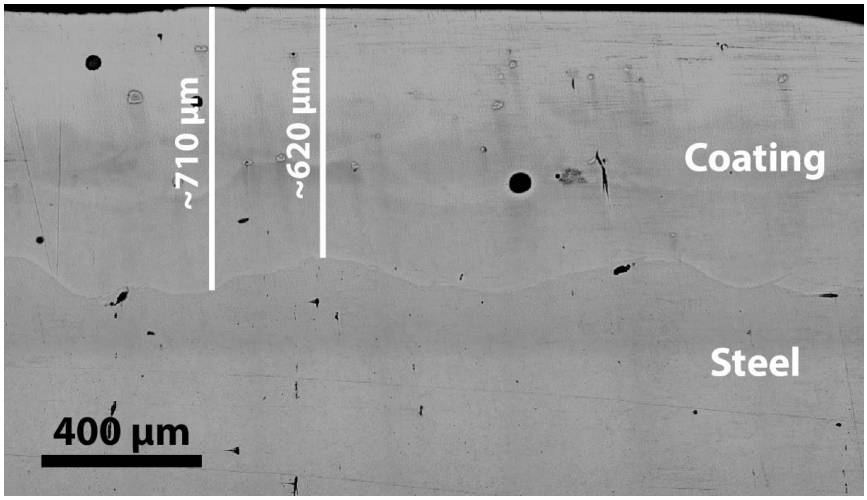

Fig. 2. *Macrostructure of a fused coating based on CrFeNi + 6 % WC + 3 % WB + 1 % Co medium-entropy alloy in the cross-section plane*
Рис. 2. *Макроструктура наплавленного покрытия на основе среднеэнтропийного сплава CrFeNi + 6 % WC + 3 % WB + 1 % Co в плоскости поперечного сечения*

Fig. 4 shows 2D maps of microhardness distribution in the cross-sectional plane of the studied samples, where areas with high microhardness values (465–500 HV 0.025 and above) are marked in red, and areas with the lowest microhardness values (150–200 HV 0.025) are marked in blue. As can be seen, the CrFeNi sample is characterised by a relatively uniform microhardness distribution, in the cross-sectional plane (Fig. 4 a). Slight deviations in the microhardness distribution are observed in the CrFeNi + 1.8 % WC + + 0.9 % WB + 0.3 % Co coating (Fig. 4 b): areas of the coating near the "coating – steel" transition zone have a slightly higher microhardness level.

Fig. 5 presents the XRD results for the CrFeNi + + 6 % WC + 3 % WB + 1 % Co sample. Phase analysis showed, that the sample contains three phases: γ-phase (CrFeNi-based solid solution), chromium carbide $Cr_{23}C_6$

Table 2. *The results of measuring microhardness of the studied samples*
Таблица 2. *Результаты измерения микротвердости исследованных образцов*

Coating	Average value, HV	RMS deviation σ, HV	Range *R*, HV	Coefficient of variation V_σ, %
CrFeNi	340±6	37	175	10.6
CrFeNi + 1.8 % WC + + 0.9 % WB + 0.3 % Co	380±11	51	263	13.4
CrFeNi + 6 % WC + + 3 % WB + 1 % Co	430±12	61	328	14.2

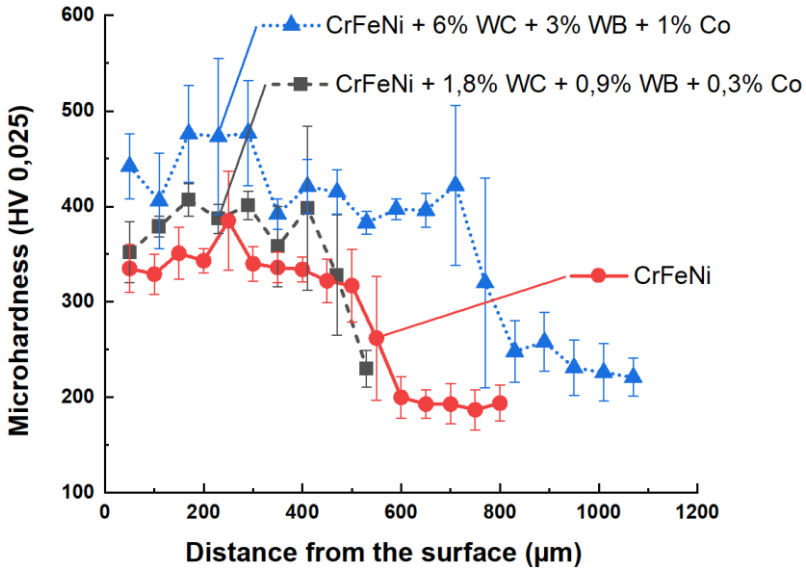

Fig. 3. *Graph of changes in microhardness of samples with deposited coatings depending on the distance from the surface*
Рис. 3. *График изменения микротвердости образцов с наплавленными покрытиями в зависимости от расстояния от поверхности*

(Fm-3m space group), and WC tungsten carbide. The ratio of the diffraction maxima indicates that the γ-phase has a distinct texture with the [200] zone axis. Analysis of the diffraction peak profiles, showed that their width significantly exceeds the instrumental width. As a result of the calculations, it was found that the average size of the γ-phase CSR is 59 nm, and the average value of microstrains (<ε>) was 0.26 %.

The elementary cell parameters calculated using the least squares method (RTP 32 programme), and the quantitative composition are shown in Table 3. It can be observed that the lattice parameter of the CrFeNi-based γ-solid solution practically did not change, when adding the tungsten carbides and borides (a=3.598 Å and a=3.599 Å, respectively). The presented quantitative analysis results for the CrFeNi + 6 % WC + 3 % WB + 1 % Co coating (~86 wt. % of γ, ~13 wt. % of $Cr_{23}C_6$, ~1 wt. % of WC), are estimating due to the presence of the γ-phase crystallite texture.

The TEM method was used to study the structure of a CrFeNi alloy formed by short-pulse laser cladding. Fig. 6 a, 6 b show the sample microstructure features. Elongated subgrains are observed, inside of which there are individual dislocations or dislocation cells. The subgrain boundaries are wide, consisting of clusters of dislocations. The reflections in the microdiffraction image (Fig. 6 a) belong only to the γ-phase, which is also confirmed by the obtained results in [18; 19]. In general, the sample structure is characteristic of samples obtained by selective laser melting and is single-phase.

Fig. 7 shows the structural features of the CrFeNi + + 6 % WC + 3 % WB + 1 % Co sample. In Fig. 7 a, 7 c, fcc grains of 1–2 μm in size, with an elongated or rounded shape are visible. There are a small number of dislocations inside the grains. The $Me_{23}C_6$ phase precipitated along the grain boundaries. In the microdiffraction patterns, except for the fcc reflections of the solid solution, there is a network of $Me_{23}C_6$ reflections (Fig. 7 b). In the dark-field image (Fig. 7 d), precipitates of the $Me_{23}C_6$ phase glow along the grain boundaries.

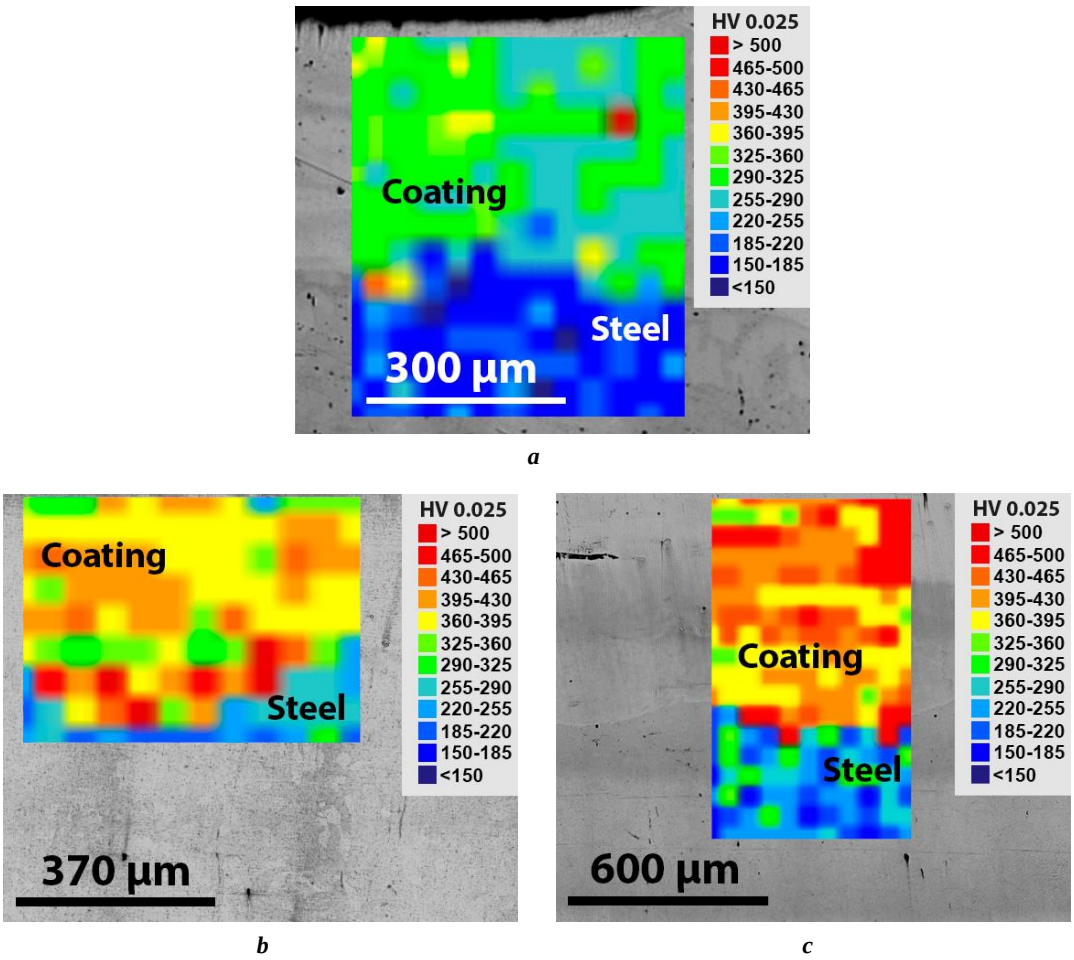

Fig. 4. *2D distribution maps of microhardness of deposited coatings in the cross-sectional plane of the samples:* ***a*** *– CrFeNi;* ***b*** *– CrFeNi + 1.8 % WC + 0.9 % WB + 0.3 % Co;* ***c*** *– CrFeNi + 6 % WC + 3 % WB + 1 % Co*

Рис. 4. *2D-карты распределения микротвердости наплавленных покрытий в плоскости поперечного сечения образцов:* ***a*** *– CrFeNi;* ***b*** *– CrFeNi + 1,8 % WC + 0,9 % WB + 0,3 % Co;* ***c*** *– CrFeNi + 6 % WC + 3 % WB + 1 % Co*

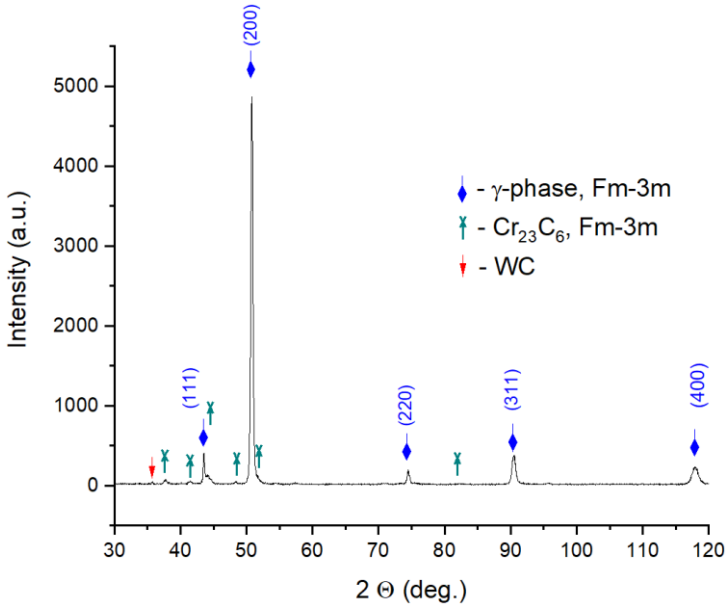

Fig. 5. *X-ray diffraction pattern of the CrFeNi + 6 % WC + 3 % WB + 1 % Co sample*

Рис. 5. *Рентгеновская дифрактограмма образца CrFeNi + 6 % WC + 3 % WB + 1 % Co*

Table 3. *Phase composition, elementary cell parameters of the studied samples*
Таблица 3. *Фазовый состав, параметры элементарной ячейки исследованных образцов*

Phase	Content, wt. %	Elementary cell parameters, Å	
		a	V
CrFeNi coating			
γ-phase, Fm-3m	100.0	3.598	46.58
CrFeNi + 6 % WC + 3 % WB + 1 % Co coating			
γ-phase, Fm-3m	86.2	3.599	46.62
$Cr_{23}C_6$, Fm-3m	12.7	10.660	1 214.20
WC	1.0	–	–

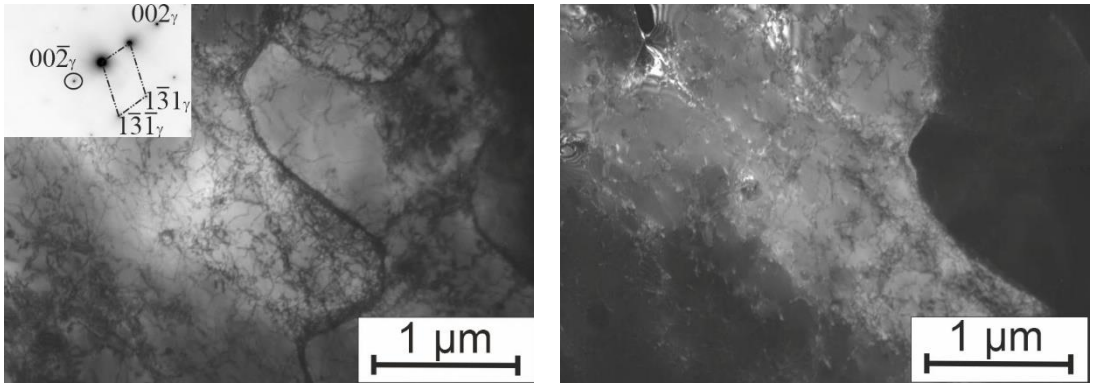

a ***b***

Fig. 6. *Structure of the CrFeNi sample:*
a *– bright-field image; in the insert – microdiffraction pattern, [130]$_\gamma$ zone axis;*
b *– dark-field image in the $00\bar{2}_\gamma$ reflection*

Рис. 6. *Структура образца CrFeNi:*
a *– светлопольное изображение; на вкладке – картина микродифракции, ось зоны [130]$_\gamma$;*
b *– темнопольное изображение в рефлексе $00\bar{2}_\gamma$*

DISCUSSION

It is important to emphasise that the results of this work confirm the fundamental possibility of using a CrFeNi equiatomic alloy as a surface layer formed by laser cladding. This allows saving expensive material. Moreover, to produce a dense coating and a transition zone (from the coating to the steel substrate), without continuity defects (pores), a more careful selection of surfacing technological modes is apparently required.

The microhardness of the CrFeNi alloy depends on the manufacturing technology. For comparison, technologies for producing CrFeNi alloy, not using laser radiation, are characterised by lower microhardness values. Thus, in [18], the CrFeNi alloy produced by the spark plasma sintering technology had an average microhardness of 267 HV. The microhardness of CrFeNi samples produced by vacuum-arc melting in an argon atmosphere was approximately 200 HV [19], while the microhardness of the CrFeNi coating formed by laser cladding is on average 340±6 HV 0.025.

During this work, it was identified that the addition of tungsten carbides and borides has a positive influence on the microhardness values of deposited coatings. A similar approach, to increasing the strength properties of a CrFeNi alloy by adding particles, is mentioned in [20]: adding 1 wt. % of yttrium oxide Y_2O_3 and 1 wt. % of zirconium Zr to the CrFeNi alloy, leads to an increase in microhardness to 474 HV.

Based on the results of the study of the structure and phase composition, one can assume that this strengthening effect is caused by the precipitates of special $Cr_{23}C_6$ chromium carbide formed along the grain boundaries of the γ-solid solution. The hardness of $Cr_{23}C_6$ carbide is 1000–1150 HV [21]. The X-ray method did not reveal the presence of WB tungsten borides in the deposited coating, which in an amount of 3 wt. % was added to the CrFeNi equiatomic alloy powder. However, the XRD method identified a small amount (1 wt. %) of WC tungsten carbide in the coating (Fig. 5, Table 3), which, along with chromium

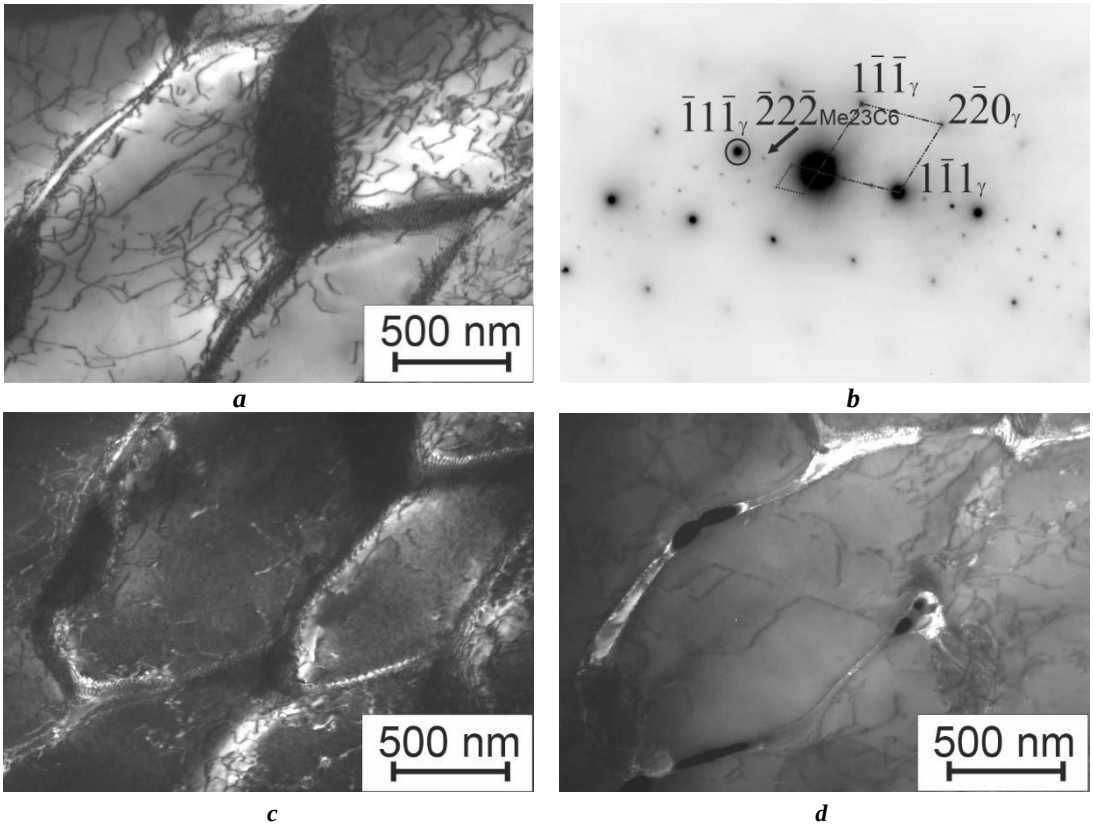

a *b*

c *d*

Fig. 7. *Structure of the CrFeNi + 6 % WC + 3 % WB + 1 % Co sample:*
a *– bright-field image;* ***b*** *– microdiffraction pattern, axis of* $[110]_\gamma$ *and* $[110]_{Me_{23}C_6}$ *zones;*
c *– dark-field image in the* $\bar{1}1\bar{1}_\gamma$ *reflection;* ***d*** *– dark-field image in the* $\bar{2}2\bar{2}_{Me_{23}C_6}$ *reflection*

Рис. 7. *Структура образца CrFeNi + 6 % WC + 3 % WB + 1 % Co:*
a *– светлопольное изображение;* ***b*** *– картина микродифракции, оси зон* $[110]_\gamma$ *и* $[110]_{Me_{23}C_6}$ *;*
c *– темнопольное изображение в рефлексе* $\bar{1}1\bar{1}_\gamma$ *;* ***d*** *– темнопольное изображение в рефлексе* $\bar{2}2\bar{2}_{Me_{23}C_6}$

carbides, causes dispersion strengthening of the coating. From these data, it follows that tungsten boride completely dissolved during laser cladding of the coating, and tungsten carbide dissolved only partially. This is facilitated by the larger amount of added WC carbide (6 wt. %), as well as the higher melting point of tungsten carbide ($Tmelt_{WC}$=2870 °C), than that of tungsten boride ($Tmelt_{WB}$=2660 °C).

To form $Cr_{23}C_6$ chromium carbide, the presence of free carbon is necessary. Despite the fact that the CrFeNi powder for surfacing contains 0.37 wt. % of C, when surfacing the CrFeNi coating without additives, a single-phase structure of a γ-solid solution is formed. Precipitates of $Cr_{23}C_6$ chromium carbide were found only in coatings with additives. This may lead to the assumption, that part of the WC tungsten carbides (possibly significant) dissolved due to high instantaneous power values during the process of short-pulse laser cladding. In addition, during the crystallization process, carbon formed compounds with chromium, as a more active chemical element.

When WC and WB particles dissolve, as a result of laser cladding, tungsten atoms move into a γ-solid solution based on the Cr–Fe–Ni alloying system, replacing individual chromium, iron or nickel atoms at the crystal lattice sites. This leads to microdistortions of the lattice and corresponding additional coating strengthening.

CONCLUSIONS

This study demonstrated the fundamental possibility of producing relatively high-quality coatings (with the presence of isolated pores) based on a CrFeNi equiatomic alloy with a thickness of 600–700 μm using short-pulse laser cladding with preplaced powder.

TEM method identified that the coating formed from the CrFeNi alloy without strengthening additives using short-pulse laser cladding, is characterised by a single-phase structure (γ-solid solution), with a grain size of 1–2 μm. The addition of strengthening particles in the form of tungsten carbides and borides (WC and WB) to the CrFeNi matrix, leads to the $Me_{23}C_6$ second phase precipitation in the laser coating along the grain boundaries. The results of X-ray diffraction phase analysis confirm the presence of the $Cr_{23}C_6$ phase, in the CrFeNi + 6 % WC+3 % WB + + 1 % Co coating, complete dissolution of WB boride and partial dissolution of WC carbide during laser cladding. According to approximate calculations (due to the presence of texture in the γ-phase), the content of the $Cr_{23}C_6$ phase

precipitated during crystallization is 12.7 wt. %. The elementary cell parameter of the γ-phase does not change significantly, when adding strengthening particles to the CrFeNi-based coating. In both cases it is (3.598–3.599) Å.

The results of Vickers microhardness test indicate that the microhardness in the cross-sectional plane of the samples is characterised by relative homogeneity. Only in the CrFeNi + 6 % WC + 3 % WB + 1 % Co coating, individual areas with an increased microhardness level are observed. The obtained results indicate the strengthening of CrFeNi-based coatings by adding tungsten carbides and borides. The CrFeNi + 1.8 % WC + 0.9 % WB + 0.3 % Co sample has an average microhardness of 380±11 HV 0.025, which is 12 % higher than the initial value. The average microhardness of the CrFeNi + 6 % WC + 3 % WB + 1 % Co sample is 430±12 HV 0.025, which is 26 % higher than the average microhardness level of the CrFeNi coating (340±6 HV 0.025) without strengthening additives.

The strengthening of the CrFeNi + 6 % WC + 3 % WB + + 1 % Co coating is caused by the presence of chromium carbides ($Cr_{23}C_6$), and tungsten carbides (WC) particles in the laser coating structure, as well as, apparently, the occurrence of microdistortions of the crystalline lattice of the γ-solid CrFeNi-based solution due to its doping with tungsten atoms precipitated during the dissolution of tungsten borides, and carbides in the process of high-temperature short-pulse laser heating.

REFERENCES

1. Cantor B., Chang I.T.H., Knight P., Vincent A.J.B. Microstructural development in equiatomic multicomponent alloys. *Materials Science and Engineering: A*, 2004, vol. 375-377, pp. 213–218. DOI: 10.1016/j.msea.2003.10.257.
2. Yeh Jien-Wei, Lin Su-Jien, Chin Tsung-Shune, Gan Jon-Yiew, Chen Swe-Kai, Shun Tao-Tsung, Tsau Chung-Huei, Chou Shou-Yi. Formation of simple crystal structures in Cu–Co–Ni–Cr–Al–Fe–Ti–V alloys with multiprincipal metallic elements. *Metallurgical and Materials Transactions A*, 2004, vol. 35, pp. 2533–2536. DOI: 10.1007/s11661-006-0234-4.
3. Zhang Yong, Zuo Ting Ting, Tang Zhi, Gao M.C., Dahmen K.A., Liaw P.K., Lu Zhao Ping. Microstructures and properties of high-entropy alloys. *Progress in Materials Science*, 2014, vol. 61, pp. 1–93. DOI: 10.1016/j.pmatsci.2013.10.001.
4. Butler T.M., Weaver M.L. Influence of annealing on the microstructures and oxidation behaviors of $Al_8(CoCrFeNi)_{92}$, $Al1_5(CoCrFeNi)_{85}$, and $Al_{30}(CoCrFeNi)_{70}$ high-entropy alloys. *Metals*, 2016, vol. 6, no. 9, article number 222. DOI: 10.3390/met6090222.
5. Daoud H.M., Manzoni A.M., Völkl R., Wanderka N., Glatzel U. Oxidation behavior of $Al_8Co_{17}Cr_{17}Cu_8Fe_{17}Ni_{33}$, $Al_{23}Co_{15}Cr_{23}Cu_8Fe_{15}Ni_{15}$, and $Al_{17}Co_{17}Cr_{17}Cu_{17}Fe_{17}Ni_{17}$ compositionally complex alloys (high-entropy alloys) at elevated temperatures in air. *Advanced Engineering Materials*, 2015, vol. 17, no. 8, pp. 1134–1141. DOI: 10.1002/adem.201500179.
6. Gludovatz B., Hohenwarter A., Thurston K.V.S., Bei Hongbin, Wu Zhenggang, George E.P., Ritchie R.O. Exceptional damage-tolerance of a medium-entropy alloy CrCoNi at cryogenic temperatures. *Nature Communications*, 2016, vol. 7, article number 10602. DOI: 10.1038/ncomms10602.
7. Arif Z.U., Khalid M.Y., Rashid A.A., Rehman E.U., Atif M. Laser deposition of high-entropy alloys: A comprehensive review. *Optics & Laser Technology*, 2022, vol. 145, article number 107447. DOI: 10.1016/j.optlastec.2021.107447.
8. Xiang Kang, Chai Linjiang, Wang Yueyuan, Wang Hao, Guo Ning, Ma Yanlong, Murty K.L. Microstructural characteristics and hardness of CoNiTi medium-entropy alloy coating on pure Ti substrate prepared by pulsed laser cladding. *Journal of Alloys and Compounds*, 2020, vol. 849, article number 156704. DOI: 10.1016/j.jallcom.2020.156704.
9. Geng Yanfei, Konovalov S.V., Chen Xizhang. Research status and application of the high-entropy and traditional alloys fabricated via the laser cladding. *Progress in Physics of Metals*, 2020, vol. 21, no. 1, pp. 26–45. DOI: 10.15407/ufm.21.01.026.
10. Juan Yongfei, Zhang Jiao, Dai Yongbing, Dong Qing, Han Yanfeng. Designing rules of laser-clad high-entropy alloy coatings with simple solid solution phases. *Acta Metallurgica Sinica (English Letters)*, 2020, vol. 33, pp. 1064–1076. DOI: 10.1007/s40195-020-01040-0.
11. Chen Zhao, Wen Xiaoli, Wang Weili, Lin Xin, Yang Haiou, Jiang Ze, Chen Lianyang, Wu Haibin, Li Wenhui, Li Nan. Engineering fine grains, dislocations and precipitates for enhancing the strength of TiB_2-modified CoCrFeMnNi high-entropy alloy using Laser Powder Bed Fusion. *Journal of Materials Research and Technology*, 2023, vol. 26, pp. 1198–1213. DOI: 10.1016/j.jmrt.2023.07.244.
12. He Junyang, Makineni S.K., Lu Wenjun, Shang Yuanyuan, Lu Zhaoping, Li Zhiming, Gault B. On the formation of hierarchical microstructure in a Mo-doped NiCoCr medium-entropy alloy with enhanced strength-ductility synergy. *Scripta Materialia*, 2020, vol. 175, pp. 1–6. DOI: 10.1016/j.scriptamat.2019.08.036.
13. Ren Mengfei, Li Ruifen, Zhang Xiaoqiang, Gu Jiayang, Jiao Chen. Effect of WC particles preparation method on microstructure and properties of laser cladded Ni60-WC coatings. *Journal of Materials Research and Technology*, 2023, vol. 22, pp. 605–616. DOI: 10.1016/j.jmrt.2022.11.120.
14. Cao Qizheng, Fan Li, Chen Haiyan, Hou Yue, Dong Lihua, Ni Zhiwei. Wear behavior of laser cladded WC-reinforced Ni-based coatings under low temperature. *Tribology International*, 2022, vol. 176, article number 107939. DOI: 10.1016/j.triboint.2022.107939.
15. Sabzi M., Dezfuli S.M., Mirsaeedghazi S.M. The effect of pulse-reverse electroplating bath temperature on the wear/corrosion response of Ni-Co/tungsten carbide nanocomposite coating during layer deposition. *Ceramics International*, 2018, vol. 44, no. 16, pp. 19492–19504. DOI: 10.1016/j.ceramint.2018.07.189.
16. Dash T., Nayak B.B. Preparation of multi-phase composite of tungsten carbide, tungsten boride and carbon by arc plasma melting: characterization of melt-cast product. *Ceramics International*, 2016, vol. 42, no. 1-A, pp. 445–459. DOI: 10.1016/j.ceramint.2015.08.129.

17. Chen Hai-Hua, Bi Yan, Cheng Yan, Ji Guangfu, Peng Fang, Hu Yan-Fei. Structural and thermodynamic properties of WB at high pressure and high temperature. *Physica B: Condensed Matter*, 2012, vol. 407, no. 24, pp. 4760–4764. DOI: 10.1016/j.physb.2012.08.016.
18. Liang Dingshan, Zhao Cancan, Zhu Weiwei, Wei Pengbo, Jiang Feilong, Ren Fuzeng. Significantly enhanced wear resistance of an ultrafine-grained CrFeNi medium-entropy alloy at elevated temperatures. *Metallurgical and Materials Transactions A*, 2020, vol. 51, pp. 2834–2850. DOI: 10.1007/s11661-020-05755-8.
19. Zhang Hongbin, Chen Kang, Wang Zhongwei, Zhou Haiping, Gao Kuidong, Du Yichang, Su Yukuo. Microstructure and mechanical properties of novel Si-added CrFeNi medium-entropy alloy prepared via vacuum arc-melting. *Journal of Alloys and Compounds*, 2022, vol. 904, article number 164136. DOI: 10.1016/j.jallcom.2022.164136.
20. Peng Shibo, Lu Zheng, Yu Li. Control of microstructure and hardness of ODS-CrFeNi MEAs by Y_2O_3/Zr addition. *Materials Characterization*, 2022, vol. 186, article number 111816. DOI: 10.1016/j.matchar.2022.111816.
21. Makarov A.V., Soboleva N.N., Malygina I.Yu. Role of the strengthening phases in abrasive wear resistance of laser-clad NiCrBSi coatings. *Journal of Friction and Wear*, 2017, vol. 38, no. 4, pp. 272–278. DOI: 10.3103/S1068366617040080.

СПИСОК ЛИТЕРАТУРЫ

1. Cantor B., Chang I.T.H., Knight P., Vincent A.J.B. Microstructural development in equiatomic multicomponent alloys // Materials Science and Engineering: A. 2004. Vol. 375-377. P. 213–218. DOI: 10.1016/j.msea.2003.10.257.
2. Yeh Jien-Wei, Lin Su-Jien, Chin Tsung-Shune, Gan Jon-Yiew, Chen Swe-Kai, Shun Tao-Tsung, Tsau Chung-Huei, Chou Shou-Yi. Formation of simple crystal structures in Cu–Co–Ni–Cr–Al–Fe–Ti–V alloys with multiprincipal metallic elements // Metallurgical and Materials Transactions A. 2004. Vol. 35. P. 2533–2536. DOI: 10.1007/s11661-006-0234-4.
3. Zhang Yong, Zuo Ting Ting, Tang Zhi, Gao M.C., Dahmen K.A., Liaw P.K., Lu Zhao Ping. Microstructures and properties of high-entropy alloys // Progress in Materials Science. 2014. Vol. 61. P. 1–93. DOI: 10.1016/j.pmatsci.2013.10.001.
4. Butler T.M., Weaver M.L. Influence of annealing on the microstructures and oxidation behaviors of $Al_8(CoCrFeNi)_{92}$, $Al_{15}(CoCrFeNi)_{85}$, and $Al_{30}(CoCrFeNi)_{70}$ high-entropy alloys // Metals. 2016. Vol. 6. № 9. Article number 222. DOI: 10.3390/met6090222.
5. Daoud H.M., Manzoni A.M., Völkl R., Wanderka N., Glatzel U. Oxidation behavior of $Al_8Co_{17}Cr_{17}Cu_8Fe_{17}Ni_{33}$, $Al_{23}Co_{15}Cr_{23}Cu_8Fe_{15}Ni_{15}$, and $Al_{17}Co_{17}Cr_{17}Cu_{17}Fe_{17}Ni_{17}$ compositionally complex alloys (high-entropy alloys) at elevated temperatures in air // Advanced Engineering Materials. 2015. Vol. 17. № 8. P. 1134–1141. DOI: 10.1002/adem.201500179.
6. Gludovatz B., Hohenwarter A., Thurston K.V.S., Bei Hongbin, Wu Zhenggang, George E.P., Ritchie R.O. Exceptional damage-tolerance of a medium-entropy alloy CrCoNi at cryogenic temperatures // Nature Communications. 2016. Vol. 7. Article number 10602. DOI: 10.1038/ncomms10602.
7. Arif Z.U., Khalid M.Y., Rashid A.A., Rehman E.U., Atif M. Laser deposition of high-entropy alloys: A comprehensive review // Optics & Laser Technology. 2022. Vol. 145. Article number 107447. DOI: 10.1016/j.optlastec.2021.107447.
8. Xiang Kang, Chai Linjiang, Wang Yueyuan, Wang Hao, Guo Ning, Ma Yanlong, Murty K.L. Microstructural characteristics and hardness of CoNiTi medium-entropy alloy coating on pure Ti substrate prepared by pulsed laser cladding // Journal of Alloys and Compounds. 2020. Vol. 849. Article number 156704. DOI: 10.1016/j.jallcom.2020.156704.
9. Geng Yanfei, Konovalov S.V., Chen Xizhang. Research status and application of the high-entropy and traditional alloys fabricated via the laser cladding // Progress in Physics of Metals. 2020. Vol. 21. № 1. P. 26–45. DOI: 10.15407/ufm.21.01.026.
10. Juan Yongfei, Zhang Jiao, Dai Yongbing, Dong Qing, Han Yanfeng. Designing rules of laser-clad high-entropy alloy coatings with simple solid solution phases // Acta Metallurgica Sinica (English Letters). 2020. Vol. 33. P. 1064–1076. DOI: 10.1007/s40195-020-01040-0.
11. Chen Zhao, Wen Xiaoli, Wang Weili, Lin Xin, Yang Haiou, Jiang Ze, Chen Lianyang, Wu Haibin, Li Wenhui, Li Nan. Engineering fine grains, dislocations and precipitates for enhancing the strength of TiB_2-modified CoCrFeMnNi high-entropy alloy using Laser Powder Bed Fusion // Journal of Materials Research and Technology. 2023. Vol. 26. P. 1198–1213. DOI: 10.1016/j.jmrt.2023.07.244.
12. He Junyang, Makineni S.K., Lu Wenjun, Shang Yuanyuan, Lu Zhaoping, Li Zhiming, Gault B. On the formation of hierarchical microstructure in a Mo-doped NiCoCr medium-entropy alloy with enhanced strength-ductility synergy // Scripta Materialia. 2020. Vol. 175. P. 1–6. DOI: 10.1016/j.scriptamat.2019.08.036.
13. Ren Mengfei, Li Ruifen, Zhang Xiaoqiang, Gu Jiayang, Jiao Chen. Effect of WC particles preparation method on microstructure and properties of laser cladded Ni60-WC coatings // Journal of Materials Research and Technology. 2023. Vol. 22. P. 605–616. DOI: 10.1016/j.jmrt.2022.11.120.
14. Cao Qizheng, Fan Li, Chen Haiyan, Hou Yue, Dong Lihua, Ni Zhiwei. Wear behavior of laser cladded WC-reinforced Ni-based coatings under low temperature // Tribology International. 2022. Vol. 176. Article number 107939. DOI: 10.1016/j.triboint.2022.107939.
15. Sabzi M., Dezfuli S.M., Mirsaeedghazi S.M. The effect of pulse-reverse electroplating bath temperature on the wear/corrosion response of Ni-Co/tungsten carbide nanocomposite coating during layer deposition // Ceramics International. 2018. Vol. 44. № 16. P. 19492–19504. DOI: 10.1016/j.ceramint.2018.07.189.
16. Dash T., Nayak B.B. Preparation of multi-phase composite of tungsten carbide, tungsten boride and carbon by arc plasma melting: characterization of melt-cast product // Ceramics International. 2016. Vol. 42. № 1-A. P. 445–459. DOI: 10.1016/j.ceramint.2015.08.129.

17. Chen Hai-Hua, Bi Yan, Cheng Yan, Ji Guangfu, Peng Fang, Hu Yan-Fei. Structural and thermodynamic properties of WB at high pressure and high temperature // Physica B: Condensed Matter. 2012. Vol. 407. № 24. P. 4760–4764. DOI: 10.1016/j.physb.2012.08.016.
18. Liang Dingshan, Zhao Cancan, Zhu Weiwei, Wei Pengbo, Jiang Feilong, Ren Fuzeng. Significantly enhanced wear resistance of an ultrafine-grained CrFeNi medium-entropy alloy at elevated temperatures // Metallurgical and Materials Transactions A. 2020. Vol. 51. P. 2834–2850. DOI: 10.1007/s11661-020-05755-8.
19. Zhang Hongbin, Chen Kang, Wang Zhongwei, Zhou Haiping, Gao Kuidong, Du Yichang, Su Yukuo. Microstructure and mechanical properties of novel Si-added CrFeNi medium-entropy alloy prepared via vacuum arc-melting // Journal of Alloys and Compounds. 2022. Vol. 904. Article number 164136. DOI: 10.1016/j.jallcom.2022.164136.
20. Peng Shibo, Lu Zheng, Yu Li. Control of microstructure and hardness of ODS-CrFeNi MEAs by Y_2O_3/Zr addition // Materials Characterization. 2022. Vol. 186. Article number 111816. DOI: 10.1016/j.matchar.2022.111816.
21. Makarov A.V., Soboleva N.N., Malygina I.Yu. Role of the strengthening phases in abrasive wear resistance of laser-clad NiCrBSi coatings // Journal of Friction and Wear. 2017. Vol. 38. № 4. P. 272–278. DOI: 10.3103/S1068366617040080.

Влияние добавок карбида и борида вольфрама на структуру и микротвердость эквиатомного CrFeNi-покрытия, сформированного короткоимпульсной лазерной наплавкой

Степченков Александр Константинович*[1,4], младший научный сотрудник
Макаров Алексей Викторович[1,5], доктор технических наук, член-корреспондент РАН, заведующий отделом материаловедения и лабораторией механических свойств
Волкова Елена Георгиевна[1,6], кандидат физико-математических наук, старший научный сотрудник
Эстемирова Светлана Хусаиновна[2,7], кандидат химических наук, старший научный сотрудник
Харанжевский Евгений Викторович[3,8], доктор технических наук, профессор, заведующий лабораторией физики и химии материалов

[1]*Институт физики металлов имени М.Н. Михеева Уральского отделения РАН, Екатеринбург (Россия)*
[2]*Институт металлургии Уральского отделения РАН, Екатеринбург (Россия)*
[3]*Удмуртский государственный университет, Ижевск (Россия)*

***E-mail: stepchenkov@imp.uran.ru, alexander.stepchenkov@gmail.com**

[4]ORCID: https://orcid.org/0000-0001-9431-0170
[5]ORCID: https://orcid.org/0000-0002-2228-0643
[6]ORCID: https://orcid.org/0000-0003-4958-3027
[7]ORCID: https://orcid.org/0000-0001-7039-1420
[8]ORCID: https://orcid.org/0000-0002-1525-2169

Поступила в редакцию 27.06.2023 *Принята к публикации 30.01.2024*

Аннотация: Покрытие на основе однофазного среднеэнтропийного сплава CrFeNi с гранецентрированной кубической (ГЦК) структурой обладает хорошей пластичностью, относительно высокими антикоррозионными свойствами, низкой стоимостью, но недостаточной прочностью для его широкого применения. Предполагается, что добавление упрочняющих частиц в виде карбидов и боридов вольфрама в эквиатомное CrFeNi-покрытие приведет к повышению его механических свойств. В работе изучено влияние добавок карбида и борида вольфрама на структуру и микротвердость эквиатомного CrFeNi-покрытия. Формирование покрытий осуществлялось путем послойного короткоимпульсного лазерного оплавления предварительно нанесенного порошка на многофункциональной лазерной установке, оснащенной твердотельным лазером с ламповой накачкой на основе кристалла Nd:YAG. Изменение фазового состава при добавлении упрочняющих частиц выявлялось с помощью методов рентгеновского дифракционного анализа и просвечивающей электронной микроскопии (ПЭМ). Оба метода подтвердили выделение в наплавленных покрытиях карбида хрома $Cr_{23}C_6$. Фотографии, полученные при помощи ПЭМ, указывают на то, что выделяемая фаза распределена по границам зерен γ-твердого раствора. Установлено, что добавление 6 мас. % WC и 3 мас. % WB повышает уровень микротвердости CrFeNi-покрытия на 26 % (с 340±6 до 430±12 HV 0,025) вследствие наличия в структуре частиц $Cr_{23}C_6$, WC и возможных микроискажений кристаллической решетки γ-фазы в результате легирования атомами вольфрама, высвободившимися при растворении боридов и карбидов вольфрама в процессе высокотемпературного короткоимпульсного лазерного нагрева.

Ключевые слова: CrFeNi-покрытие; среднеэнтропийные сплавы; карбиды/бориды вольфрама; короткоимпульсная лазерная наплавка; эквиатомные покрытия; микротвердость.

Благодарности: Работа выполнена в рамках государственного задания ИФМ УрО РАН по теме «Структура» № 122021000033-2. Исследования проводились с использованием оборудования отделов электронной микроскопии и механических испытаний ЦКП «Испытательный центр нанотехнологий и перспективных материалов» ИФМ УрО РАН.

А.К. Степченков благодарит Институт физики металлов имени М.Н. Михеева за поддержку работы по государственному заданию ИФМ УрО РАН по теме «Структура» № 122021000033-2, которая выполнялась в рамках молодежного проекта ИФМ УрО РАН № 22-13/мол.

Статья подготовлена по материалам докладов участников XI Международной школы «Физическое материаловедение» (ШФМ-2023), Тольятти, 11–15 сентября 2023 года.

Для цитирования: Степченков А.К., Макаров А.В., Волкова Е.Г., Эстемирова С.Х., Харанжевский Е.В. Влияние добавок карбида и борида вольфрама на структуру и микротвердость эквиатомного CrFeNi-покрытия, сформированного короткоимпульсной лазерной наплавкой // Frontier Materials & Technologies. 2024. № 1. С. 83–94. DOI: 10.18323/2782-4039-2024-1-67-8.

doi: 10.18323/2782-4039-2024-1-67-9

Digital measurements of non-metallic inclusions in steel

Natalia A. Stukalova[1,3], postgraduate student
Davronjon F. Kodirov*[1,4], postgraduate student
Valeriy I. Alekseev[1], postgraduate student
Elina A. Sokolovskaya[1,5], PhD (Engineering), Associate Professor,
assistant professor of Chair of Metal Science and Physics of Strength
Irina G. Rodionova[2,6], Doctor of Sciences (Engineering), Associate Professor,
Deputy Director of the Scientific Center for Physical and Chemical Fundamentals and Technologies of Metallurgy
[1]*University of Science and Technology MISIS, Moscow (Russia*)
[2]*State Research Center FSUE I.P. Bardin Central Research Institute of Ferrous Metallurgy, Moscow (Russia)*

***E-mail: DFKodirov@yandex.ru**

[3]ORCID: https://orcid.org/0009-0007-3455-4457
[4]ORCID: https://orcid.org/0009-0003-5380-5558
[5]ORCID: https://orcid.org/0000-0001-9381-9223
[6]ORCID: https://orcid.org/0000-0003-4201-4665

Received 19.07.2023 *Accepted 13.11.2023*

Abstract: The experience of many-year research has shown that optimizing the steel chemical composition and microstructural characteristics, as well as reducing its contamination with non-metallic inclusions (NMI), it is possible to significantly increase the corrosion resistance of oilfield pipeline steels and increase the time of their trouble-free operation. The influence of complex NMIs on the steel corrosion resistance is determined by both the chemical composition of NMIs and their quantitative ratios. Therefore, obtaining metal products of the required quality is possible only when using the "control by structure" principle. In the work, based on the analysis of brightness fields of images (on a sample scale) in 256 shades of gray, the authors proposed digital, metrologically supported procedures for measuring the NMI heterogeneity of low-carbon oilfield steels: eliminating the heterogeneity of field illumination, justifying the criteria for binarization and noise filtering. For low-carbon steels of various types of melting, the authors identified the key role of dispersed non-metallic inclusions ranging in size from 5–10 μm^2 to 2 nm^2 in the formation of the corrosion resistance of steels. This may explain why, in some cases, there is no interrelation between the corrosion rate and the fracture resistance of steels, the formation of which is determined by larger particles. When representing the NMI as a set of random points on the plane, the distribution of distances between the nearest ones is estimated based on Voronoi polyhedra statistics. The study shows that an increase in the kurtosis coefficient of distributions of polyhedra areas is accompanied by an increase in the corrosion rate of the steels under study. This indicates the negative impact of heterogeneity in the arrangement of dispersed NMIs on the corrosion resistance of steels.

Keywords: digital measurements of structures; quality management by structure; non-metallic inclusions in steel; corrosion resistance of oilfield pipes.

Acknowledgments: The paper was written on the reports of the participants of the XI International School of Physical Materials Science (SPM-2023), Togliatti, September 11–15, 2023.

For citation: Stukalova N.A., Kodirov D.F., Alekseev V.I., Sokolovskaya E.A., Rodionova I.G. Digital measurements of non-metallic inclusions in steel. *Frontier Materials & Technologies*, 2024, no. 1, pp. 95–103. DOI: 10.18323/2782-4039-2024-1-67-9.

INTRODUCTION

Producing high-quality steel is possible only when controlling the non-metallic inclusions (NMI) present in it, which are an inevitable product of the technological process [1; 2]. The size of inclusions in steel depends on their origin and can vary from 0.01 microns to 10 mm. Due to their small volume fraction, NMIs primarily affect the destruction processes, but each size group affects in its own way [1]. Large inclusions visible to an unaided eye contribute to the formation of areas of destruction or corrosion. Small inclusions (less than 1 mm) can lead to the formation of fatigue failure sites. Dispersed inclusions can affect the plastic properties, and susceptibility to the austenite grain growth [3]. The quality of the metal is determined both by the NMI volume fraction, and size and by their shape and heterogeneity of location. In turn, analysis of the NMI chemical and phase composition, makes it possible to diagnose their origin for further elimination of the negative impact. The works [4–6] reflect the peculiarities of the influence of the size, shape and type of inclusions, on the mechanical properties of structural steels. NMI contamination is one of the main reasons for the rapid failure of oil pipes [7]. The corrosion activity of complex Nis, present in modern steels, depends on their chemical and phase composition, the optimization of which can prevent the negative impact of NMIs on the corrosion resistance of steels, under service conditions of oilfield pipelines [8].

Due to the significant influence of NMIs on the properties of steel, various methods are used to analyze them. To study the chemical composition of single NMIs, scanning electron microscopy, with the possibility of performing

X-ray spectral microanalysis is used. To determine the size and shape of inclusions, and estimate the distance between them, the extreme value method, Spark-DAT, thermodynamic calculations, etc. are used [9–11]. However, the ranking of structures based on comparison of their images, obtained by the light microscopy methods with reference scales is the most common. The GOST 1778, 5639 and 3443 reference scales have an empirical nature; this indicator is complex, and difficult to formalize. The statistical nature of images of "score" structures is often not taken into account; therefore, there are difficulties when determining a one-to-one correspondence between GOST "scores" and the quantitative characteristics of the geometric elements of their images. Digitalization makes it possible to document quickly measurements of structures, which allows collecting measurement statistics, and formulating recommendations on product quality management based on it [12].

Through digitalization, it became possible to provide mass measurements and obtain statistical estimates of the geometric parameters of structural elements, which was previously difficult to achieve due to the large amount of manual work. The obtained representative volume of measurement results, allows evaluating the influence of structural heterogeneity on the properties of steels, taking into account their different scales. An assessment of the variation in contamination of the 38KhN3MFA steel (from large forgings) with NMIs, showed that the scale of observation is of great importance, and affects the reproducibility of the measurement results of the NMI geometry [13].

Segmentation, i. e., dividing an image into its constituent areas or objects, is one of the important stages of quantitative analysis. Non-trivial image segmentation is one of the most challenging image processing problems. Most existing image segmentation algorithms are based on one of two basic properties of the luminance signal: discontinuity and uniformity. In the first case, the approach consists in the image partition based on sudden changes in the signal, such as luminance differences in the image. The second category of methods uses dividing the image into areas that are homogeneous in terms of pre-selected criteria. Threshold processing (binarization) is an example of such methods [14]. In the standards existing today (ASTM E45–18a and DIN EN 10247:2017-09), it is recommended to use the flicker method as a binarization method for quantitative assessment of NMIs, but it is manual, and as a consequence, subjective. In turn, most image analyzers have built-in global methods. The use of global binarization methods when processing panoramas of NMI images, can lead to the binary image distortion. The reasons for this are the small size, and number of objects to study, and the feature of automatic "stitching" of image panoramas, leading to illumination heterogeneity. Therefore, it remains relevant to develop physically justified binarization methods that allow identifying objectively the informative objects in images of structures.

The practice of developing digital procedures for measuring structures and fractures shows that considering the physical laws of the formation of the brightness field of their images, when identifying binarization and filtering criteria, and a reasonable choice of the measurement object representative volumes. Taking into account their statistical nature, can provide virtually the only trajectory for preparing images for their subsequent measurement. Consequently, one cannot expect significant differences from the results of measurements of the geometry of structural elements, obtained in different laboratories, on the same metallographic specimens [15]. It is obvious that digital metallography using image analyzers that have undergone interlaboratory round-robin comparisons, will significantly simplify acceptance tests, between the supplier and consumer of metal products [16].

The purpose of this study is to develop a methodology for quantitative analysis of non-metallic inclusions on a thin section scale, to identify patterns of their influence on the corrosion resistance of oilfield pipe metal.

METHODS

Sheets of five low-carbon steels of various melts were the objects of the study. The sheets intended for oilfield pipes were produced using standard technology. Table 1 presents the chemical composition of the steels under study.

The chemical composition of steels was determined using an OBLF QSN 750 automatic analyzer and complied with the requirements of regulatory documents. The microstructure was studied on longitudinal samples cut from sheets in the as-delivered condition. The cut samples were hot pressed into resin using a CitoPress-5 automatic electrohydraulic press. Grinding and polishing were carried out on an AutoMet 250 Buehler machine. For the structure metallographic examination, the authors used an Axio Observer D1m Carl Zeiss optical microscope.

To assess the steel contamination with NMIs in our study, panoramas were obtained on the scale of a metallographic specimen (the studied area for all samples was at least 170 mm^2). Image panoramas of non-metallic inclusions were obtained on unetched metallographic specimens, using Thixomet software at a magnification of ×50. The chemical composition of complex NMIs was determined using a JSM-6610LV scanning electron microscope at a magnification of ×500 (the analyzed area was at least 3.5 mm^2 on the sample scale). Nanosized precipitates of carbide (carbonitride) excess phases were studied by transmission electron microscopy using a JEM-200CX microscope.

Tensile tests to determine strength and plastic characteristics were carried out in accordance with GOST 1497-84. Electrochemical studies to determine corrosion characteristics and subsequent calculations were carried out in accordance with ASTM G3, G5, G59, G102, ISO 17475:2005, and GOST 9.912-89 standards.

Image panoramas were processed in prepared software using C#. The color image was converted to shades of gray (from 0 to 255) using the formula:

$$I=0.299\cdot R+0.587\cdot G+0.114\cdot B,$$

where R, G and B are the intensity values of red, green and blue colors, respectively [17].

To process image panoramas, a complex algorithm was developed, which includes the elimination of illumination

Table 1. *Chemical composition of the steels under study*
Таблица 1. *Химический состав исследуемых сталей*

Steel	Element content, mass fraction, %										
	C	**Mn**	**Si**	**S**	**P**	**Cr**	**Ni**	**Mo**	**V**	**Nb**	**N**
1	0.052	0.466	0.150	0.002	0.005	0.054	0.091	0.009	0.099	0.002	0.022
2	0.054	0.653	0.214	0.001	0.005	0.067	0.104	0.009	0.044	0.024	0.007
3	0.049	1.090	0.248	0.001	0.005	0.244	0.076	0.095	0.002	0.033	0.008
4	0.049	0.920	0.230	0.001	0.004	0.651	0.071	0.008	0.004	0.040	0.007
5	0.044	0.635	0.258	0.001	0.003	0.538	0.070	0.009	0.044	0.025	0.007

heterogeneity of various natures and subsequent analysis of the brightness field to determine the binarization threshold. Illumination heterogeneity was eliminated using a method based on subtracting the 1st or 2nd degree surface from the original 3D distribution of image luminance intensities. The binarization algorithm included the construction of distribution histograms of intensities of the halftone image pixels $f(x,y)$. Dark objects were identified against a light background by determining the value of T threshold, which delimits the brightness distribution modes. Any point in the image with coordinates x_i and y_i, at which $f(x_i,y_i)>T$, was called the background, points with lower brightness were called the object. Geometric parameters were calculated according to the four-connection principle; boundary objects were not taken into account.

The authors calculated the following NMI parameters: density, volume fraction and average area, as well as the skewness and kurtosis coefficients of area distribution. To identify the "object – noise" threshold value, the authors relied on the parameters of the equipment used, and the nature of the object. For this purpose, in particular, the filtering threshold was varied, sequentially removing from the primary image the inclusions with an area of less than 5, 10, 25, 50, 75, and 100 μm^2, respectively. To assess the NMI location heterogeneity, the construction of Voronoi polyhedra [18] based on the method of perpendicular bisectors was proposed. After constructing the polyhedra and determining the nearest neighbors, the distances between the centers of objects (NMI), the areas of the polyhedra and the number of their nearest neighbors, as well as the kurtosis and skewness coefficients, of the distributions of the obtained values were calculated.

RESULTS

The variation of the threshold filter led to the following changes in the values of the NMI geometry parameters: a natural decrease in the density and volume fraction of particles, an increase in the average values of their area for the five steels under study (Fig. 1). It was identified that at high filter values, the difference in the density of the NMIs of the studied samples is leveled out. The difference in the density of large inclusions (from 100 μm^2 and above) for all samples was minimal – 29 pcs/mm^2, and for all inclusions (without filtering) – 218 pcs/mm^2.

The results of the NMI quantitative analysis were compared to the acceptance properties of steels. The results of tensile and corrosion resistance tests are given in Table 2.

The sheets studied corresponded to K52 and K55 strength classes, the scatter of strength and plastic parameters was insignificant. However, the corrosion resistance of the samples differed by a factor of 3. Fig. 2 shows the relationship between the NMI density, and the corrosion resistance of the steels under study, taking into account different levels of noise filtration.

Fig. 3 shows the dependences of Voronoi polyhedra parameters on the corrosion resistance values of the samples under study, from which it follows that these characteristics significantly correlate with each other.

Steels 4 and 5 have the lowest density and more uniform distribution of NMIs, and as a consequence, the best corrosion resistance. In turn, for steels 1, 2 and 3, the statistics of Voronoi polyhedra do not differ, but for steels 2 and 3, a correlation with the NMI density was revealed. For steel 1, no significant relationship was found between the NMI density and corrosion resistance.

Table 3 presents the results of the quantitative assessment and chemical composition of NMI using scanning microscopy.

Fig. 4 shows images of nanosized particles obtained using transmission microscopy.

DISCUSSION

The change in the characteristics of steel contamination with inclusions with increasing filtration threshold (Fig. 1), is associated with the removal of small objects, the number of which prevails over large ones. Fig. 2 shows that the greatest strength of the relationship between corrosion resistance and NMI density (correlation coefficient is 0.95), is observed in the absence of their filtration. Increasing the filtration threshold and the accompanying screening out of small inclusions leads to a decrease in the correlation coefficient. This indicates that corrosion resistance is mainly affected by small inclusions (<10 μm^2). One should

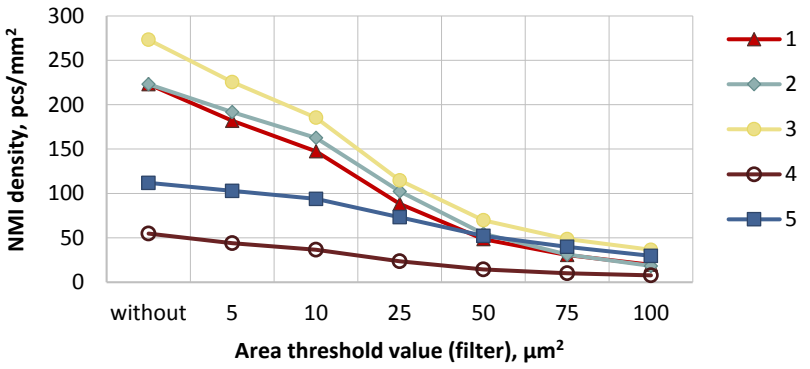

a

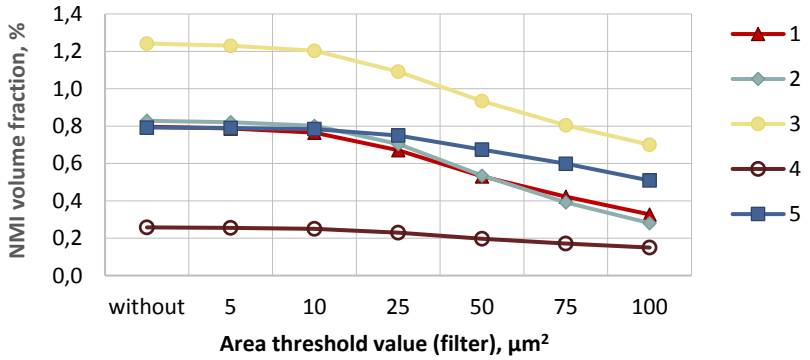

b

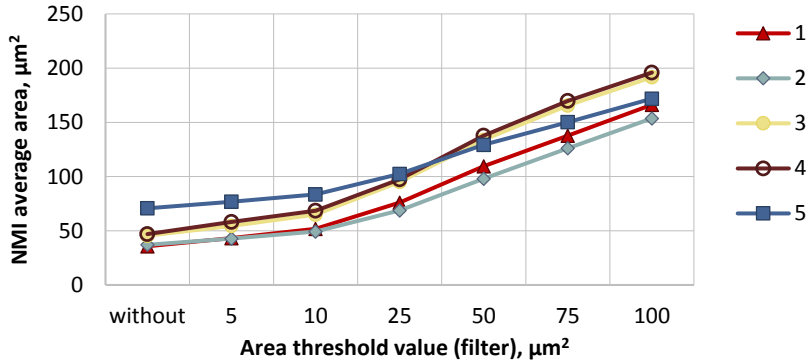

c

Fig. 1. *Statistical parameters of NMIs of the steels under study at different filtration levels:*
a *– density;* ***b*** *– volume fraction;* ***c*** *– average area*
Рис. 1. *Статистические параметры НВ изучаемых сталей при разных уровнях фильтрации:*
a *– плотность;* ***b*** *– объемная доля;* ***c*** *– средняя площадь*

Table 2. *Mechanical and corrosive properties of the steels under study*
Таблица 2. *Механические и коррозионные свойства исследуемых сталей*

Steel	Yield strength, MPa	Tensile strength, MPa	Ultimate elongation, %	Corrosion rate, mm/year
1	441.0	510.9	24.9	1.67
2	413.8	504.4	25.9	1.35
3	469.8	547.4	21.5	1.57
4	454.0	556.2	21.5	0.59
5	445.7	524.7	26.3	0.75

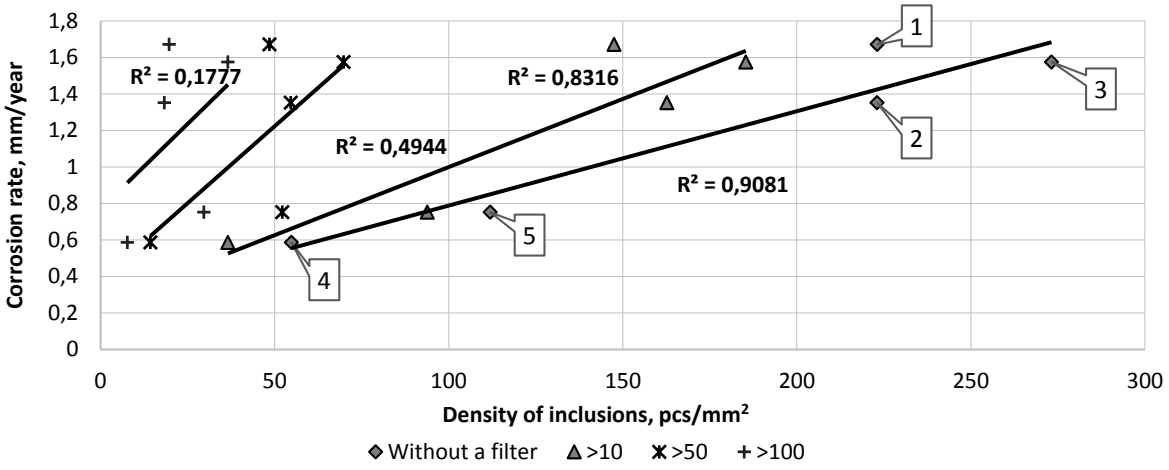

Fig. 2. *Correlation of NMI density and corrosion rate in the steels under study when varying the inclusion filtration level (by their area)*
Рис. 2. *Соотношение плотности НВ и скорости коррозии в исследуемых сталях при вариации уровня фильтрации включений (по величине их площади)*

consider this fact during "noise – object" filtering, since an incorrect choice of threshold can lead to the loss of a significant part of the information. Despite the fact that the volume fraction of small NMIs is low, they have a higher density compared to large ones. In this regard, there is an increased likelihood that small inclusions will form clusters, which, in turn, will contribute to a decrease in the corrosion resistance of steels.

It is unlikely that the absence of a significant relationship between the NMI density and corrosion resistance for steel 1 may be associated with the chemical composition of inclusions and the release of nanosized particles. Therefore, further analysis of the contamination of steels with NMIs was carried out using scanning and transmission microscopy. Microanalysis of inclusions using SEM showed that, unlike other steels under study, steel 1 is distinguished by a high density of complex NMIs based on aluminum-magnesium spinel and a high Al/(Mg+Ca) ratio. It is known [19] that with an increase in the proportion of the Al_2O_3 phase in a complex NMI, the tendency to the appearance of microfractures around the NMIs increases, which leads to a decrease in the corrosion resistance of steel. In turn, modifying steel with calcium allows giving a globular shape to such inclusions and thereby reduce their negative impact [20].

Transmission electron microscopy showed that steel 1 contains a large number of nanosized carbonitride particles. The belonging of particles to one type or another was assessed by the nature of the mutual arrangement of the particles, the presence of a regular orientation correspondence between the particles, and the ferrite matrix, and by the shape of reflections of the particles in the microdiffraction patterns. Nanoparticles were detected in almost all areas of the sample tested for their presence. Particles of all known types were observed, most of all particles were of the interphase/mixed type; their volume density was high (Fig. 4). Thus, the presence in steel 1 of nanoparticles of a different (than in steels 2–5) nature, determined the deviation from the found general patterns reflecting the relationship between the NMI density and corrosion resistance.

The results of the work showed the importance of an integrated approach to the study of the morphology of nonmetallic inclusions. This involves the combination of a physically supported image-processing algorithm to get ideas about the geometry of inclusions, and the patterns of their arrangement in the volume of metal with an analysis of their composition using transmission and scanning microscopy, including submicroscopic and nanoscale observations. It appears to be essential for understanding the differences in corrosion resistance of oilfield steels.

CONCLUSIONS

1. The authors proposed a method for processing panoramic images of NMIs (on a metallographic specimen) based on an analysis of the patterns of their brightness fields (in 256 shades of gray) to compile reasonable algorithms for illumination, equalization and binarization of images, which is necessary to obtain metrologically assured results. The study shows the importance of justifying the choice of filtering threshold for objects of noise nature, to obtain significant results.

2. The study shows the effectiveness of using the statistics of Voronoi polyhedra to assess the heterogeneity of NMIs location, which includes obtaining statistical estimates of the type of distribution of parameter values.

3. Comparing the results of corrosion tests, and quantitative assessment of the NMIs of samples of the steels under study, the influence of density, values of the polyhedron area distribution kurtosis coefficient, and the average distance between the centers of inclusions (in the size range from 2 nm^2 to 10 μm^2) on corrosion resistance was discovered. The coefficients of determination of linear dependencies

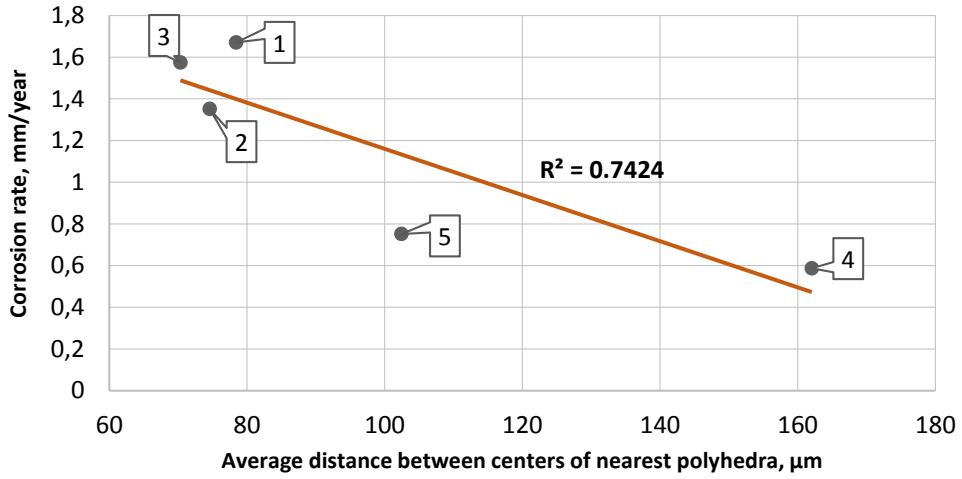

a

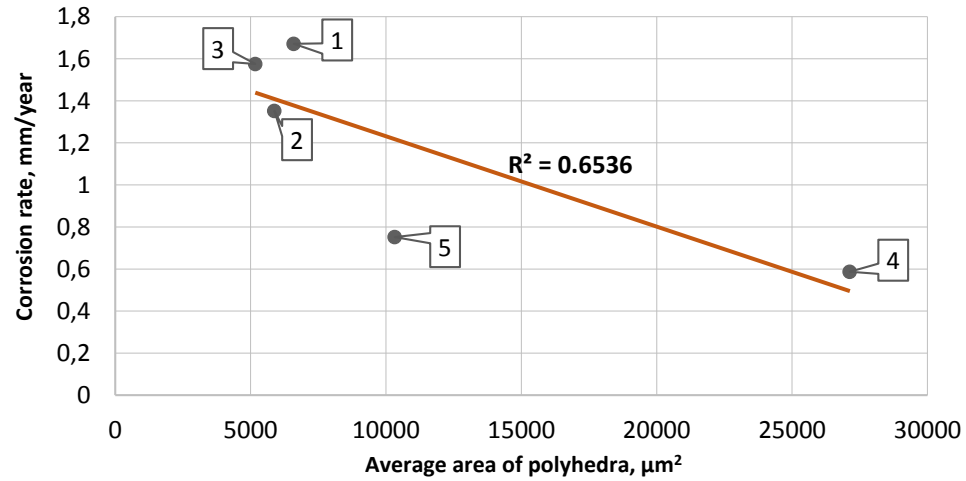

b

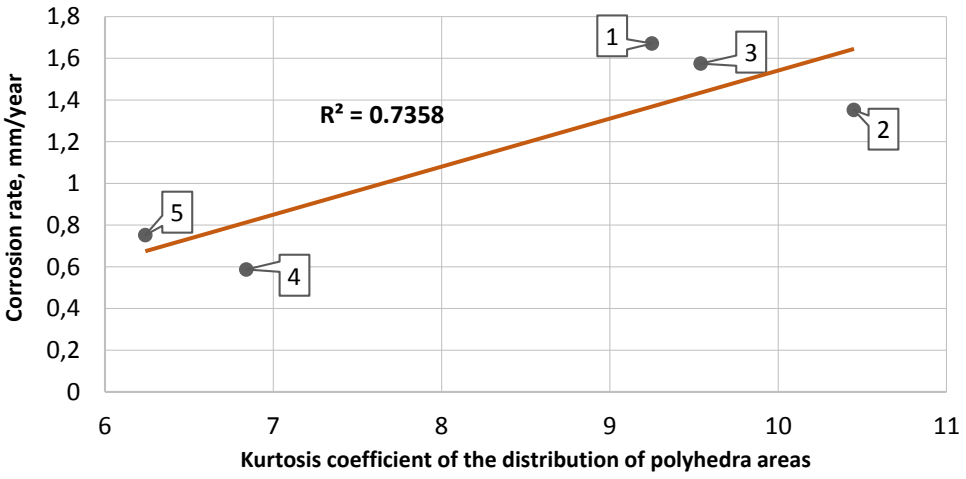

c

Fig. 3. *Correlation of the results of determining the NMI geometry (according to the Voronoi polyhedra statistics) and the corrosion rate:* ***a*** *– average distance between centers;* ***b*** *– average area of polyhedra;* ***c*** *– kurtosis coefficient of the distribution of polyhedra areas*

Рис. 3. *Соотношение результатов определения геометрии НВ (по статистике полиэдров Вороного) и скорости коррозии:* ***a*** *– среднее расстояние между центрами;* ***b*** *– средняя площадь полиэдров;* ***c*** *– коэффициент эксцесса распределения площадей полиэдров*

Table 3. *The results of NMI analysis using scanning microscopy*
Таблица 3. *Результаты анализа НВ методом сканирующей микроскопии*

Steel	Area of analyzed surface of a metallographic specimen, mm^2	NMI density, pcs/mm^2	Chemical element average content in inclusions, wt. %				Al/(Mg+Ca)
			Mg	Al	S	Ca	
1	3.79	51	3.75	10.60	2.95	6.04	1.18
2	4.54	37	6.73	6.95	2.73	7.14	0.53
3	3.57	48	3.40	3.11	1.32	8.38	0.32
4	3.90	35	4.03	7.92	5.48	4.60	0.97
5	3.82	43	4.17	3.00	3.11	9.19	0.35

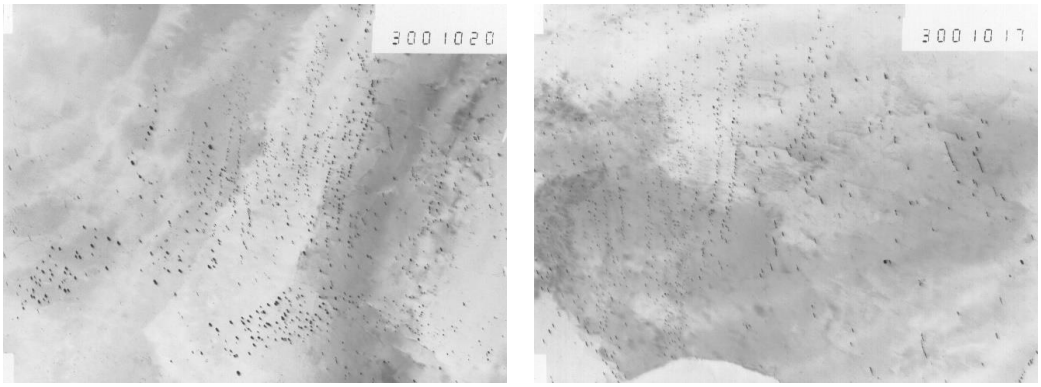

a ***b***

Fig. 4. *Nanosize particles of carbonitrides in the steel 1:*
a *– formed according to the interphase mechanism;* ***b*** *– formed in ferrite*
Рис. 4. *Наноразмерные частицы карбонитридов в стали 1:*
а *– сформировавшиеся по межфазному механизму;* ***b*** *– образовавшиеся в феррите*

were 0.91, 0.74, and 0.74, respectively. At the same time, the influence of inclusions on the fracture resistance was not revealed, which can be explained by the absence of differences in the contamination of steels with larger NMIs playing a decisive role in fracture.

4. Using SEM methods, the composition of the NMIs was revealed – predominantly aluminum-magnesium spinel; using TEM methods, the authors identified the presence of a large number of nanosized particles having a significant impact on the development of the corrosion rate of the steels under study.

REFERENCES

1. Shtremel M.A. The issues of metallurgical quality of steel (non-metallic inclusions). *Metal Science and Heat Treatment*, 1980, no. 8, C. 2–6.
2. Gulyaev A.P. *Chistaya stal* [Pure steel]. Moscow, Metallurgiya Publ., 1975. 184 p.
3. Vinograd M.I. *Vklyucheniya v stali i ee svoystva* [Steel inclusions and its properties]. Moscow, Metallurgizdat Publ., 1963. 252 p.
4. Zerbst U., Madia M., Klinger C., Bettge D., Murakami Y. Defects as a root cause of fatigue failure of metallic components. II: Non-metallic inclusions. *Engineering Failure Analysis*, 2019, vol. 98, C. 228–239. DOI: 10.1016/j.engfailanal.2019.01.054.
5. Liu Hanze, Zhang Shikun, Zhang Jing, Ren Qiang, Zhang Lifeng, Ge Yanfeng. Properties of typical non-metallic inclusions in steel: First-principles calculations. *Materials Today Communications*, 2023, vol. 34, article number 105118. DOI: 10.1016/j.mtcomm.2022.105118.
6. Costa e Silva A. The effects of non-metallic inclusions on properties relevant to the performance of steel in structural and mechanical applications. *Journal of Materials Research and Technology*, 2019, vol. 8, no. 2, C. 2408–2422. DOI: 10.1016/j.jmrt.2019.01.009.
7. Vyboyshchik M.A., Ioffe A.V. Scientific basis of development and the methodology of creation of steels for the production of oilfield casing and tubular goods with the increased strength and corrosion resistance. *Vektor nauki Tolyattinskogo gosudarstvennogo universiteta*, 2019, no. 1, C. 13–20. DOI: 10.18323/2073-5073-2019-1-13-20.

8. Amezhnov A.V., Rodionova I.G. Influence of chemical and phase composition of non-metallic inclusions on corrosion resistance of carbon and low alloy steels in water mediums typical for oilfield pipelines operating conditions. *Metallurgist*, 2019, vol. 63, no. 7-8, pp. 717–726. EDN: KBDKLV.
9. Kazakov A.A., Murysev V.A., Kiselev D.V. Interpretation of nature of non-metallic inclusions in assessing the quality of metal products in the industrial conditions. *Chernye metally*, 2021, no. 9, C. 47–54. DOI: 10.17580/chm.2021.09.08.
10. Passigatti S.T.P., de Oliveira M.S., de Oliveira J.R., de Souza R.M., Vieira E.A. On the comparative inclusion analysis in steels: Spark-DAT, ASCAT and optical microscopy. *Journal of Materials Research and Technology*, 2022, vol. 19, C. 4745–4755. DOI: 10.1016/j.jmrt.2022.06.155.
11. Barbosa C., de Campos J.B., do Nascimento J.L., Caminha I.M.V. Quantitative study on nonmetallic inclusion particles in steels by automatic image analysis with extreme values method. *Journal of Iron and Steel Research International*, 2009, vol. 16, C. 18–21. DOI: 10.1016/S1006-706X(09)60054-6.
12. Kudrya A.V., Sokolovskaya E.A., Perezhogin V.Yu., Kodirov D.F. On taking into account the statistical nature of objects in structural analysis in metals science. *Russian metallurgy (Metally)*, 2020, vol. 2020, no. 12, pp. 1435–1438. DOI: 10.1134/S0036029520120149.
13. Kudrya A.V., Sokolovskaya E.A., Perezhogin V.Yu., Kha N.N. Some practical concerns related to computer procedures of processing images in material science. *Vektor nauki Tolyattinskogo gosudarstvennogo universiteta*, 2019, no. 4, C. 35–44. DOI: 10.18323/2073-5073-2019-4-35-44.
14. Gonsales R.S., Vuds R.E. *Tsifrovaya obrabotka izobrazheniy* [Digital Image Processing]. Moscow, Tekhnosfera Publ., 2012. 1104 p.
15. Sokolovskaya E.A., Kudrya A.V., Perezhogin V.Yu., Tang V.P., Kodirov D.F.U., Sergeyev M.I. Possibilities of measurement digitalization in metal science for the introduction of quantitative measurement to the evaluation of structures and fractures. *Metallurgist*, 2022, vol. 66, no. 7, C. 792–804. DOI: 10.1007/s11015-022-01390-3.
16. Kazakov A.A., Kiselev D.V., Kazakova E.I. Quantitative methods for assessing the microstructure of steel and alloys for revising outdated GOST standards. *Lite i metallurgiya*, 2021, no. 2, C. 42–48. DOI: 10.21122/1683-6065-2021-2-42-48.
17. McHugh S.T. *Understanding Photography. Master Your Digital Camera and Capture That Perfect*. San Francisco, No Starch Press Publ., 2018. 240 p.
18. Voronoi G.F. Nouvelles applications des paramètres continus à la théorie de formes quadratiques. *Journal für die reine und angewandte Mathematik*, 2009, vol. 1908, no. 134, C. 198–287. DOI: 10.1515/crll.1908.134.198.
19. Jo Sung-Koo, Kim Seon-Hyo, Song Bo. Thermodynamics on the Formation of Spinel ($MgO \times Al_2O_3$). Inclusion in Liquid Iron Containing Chromium. *Metallurgical and Materials Transactions B*, 2002, vol. 33, C. 703–709. DOI: 10.1007/s11663-002-0023-4.
20. Osio A.S., Liu S., Olson D.L. The effect of solidification on the formation and growth of inclusions in low carbon steel welds. *Material Science and Engineering A*, 1996, vol. 221, no. 1-2, C. 122–133. DOI: 10.1016/S0921-5093(96)10466-4.

СПИСОК ЛИТЕРАТУРЫ

1. Штремель М.А. Проблемы металлургического качества стали (неметаллические включения) // Металловедение и термическая обработка металлов. 1980. № 8. С. 2–6.
2. Гуляев А.П. Чистая сталь. М.: Металлургия, 1975. 184 с.
3. Виноград М.И. Включения в стали и ее свойства. М.: Металлургиздат, 1963. 252 с.
4. Zerbst U., Madia M., Klinger C., Bettge D., Murakami Y. Defects as a root cause of fatigue failure of metallic components. II: Non-metallic inclusions // Engineering Failure Analysis. 2019. Vol. 98. P. 228–239. DOI: 10.1016/j.engfailanal.2019.01.054.
5. Liu Hanze, Zhang Shikun, Zhang Jing, Ren Qiang, Zhang Lifeng, Ge Yanfeng. Properties of typical non-metallic inclusions in steel: First-principles calculations // Materials Today Communications. 2023. Vol. 34. Article number 105118. DOI: 10.1016/j.mtcomm.2022.105118.
6. Costa e Silva A. The effects of non-metallic inclusions on properties relevant to the performance of steel in structural and mechanical applications // Journal of Materials Research and Technology. 2019. Vol. 8. № 2. P. 2408–2422. DOI: 10.1016/j.jmrt.2019.01.009.
7. Выбойщик М.А., Иоффе А.В. Научные основы разработки и методология создания сталей для производства нефтепромысловых труб повышенной прочности и коррозионной стойкости // Вектор науки Тольяттинского государственного университета. 2019. № 1. С. 13–20. DOI: 10.18323/2073-5073-2019-1-13-20.
8. Амежнов А.В., Родионова И.Г. Влияние химического и фазового состава неметаллических включений на коррозионную стойкость углеродистых и низколегированных сталей в водных средах, характерных для условий эксплуатации нефтепромысловых трубопроводов // Металлург. 2019. № 7. С. 45–52. EDN: PEQWNK.
9. Казаков А.А., Мурысев В.А., Киселев Д.В. Интерпретация природы неметаллических включений при оценке качества металлопродукции в условиях заводской практики // Черные металлы. 2021. № 9. С. 47–54. DOI: 10.17580/chm.2021.09.08.
10. Passigatti S.T.P., de Oliveira M.S., de Oliveira J.R., de Souza R.M., Vieira E.A. On the comparative inclusion analysis in steels: Spark-DAT, ASCAT and optical microscopy // Journal of Materials Research and Technology. 2022. Vol. 19. P. 4745–4755. DOI: 10.1016/j.jmrt.2022.06.155.
11. Barbosa C., de Campos J.B., do Nascimento J.L., Caminha I.M.V. Quantitative study on nonmetallic inclusion particles in steels by automatic image analysis with extreme values method // Journal of Iron and Steel Research International. 2009. Vol. 16. P. 18–21. DOI: 10.1016/S1006-706X(09)60054-6.
12. Кудря А.В., Соколовская Э.А., Пережогин В.Ю., Кодиров Д.Ф. Об учете статистической природы объектов при анализе структур в металловедении // Электрометаллургия. 2020. № 7. С. 22–27. EDN: DTRDTP.
13. Кудря А.В., Соколовская Э.А., Пережогин В.Ю., Ха Н.Н. Некоторые практические соображения, свя-

занные с компьютерными процедурами обработки изображений в материаловедении // Вектор науки Тольяттинского государственного университета. 2019. № 4. С. 35–44. DOI: 10.18323/2073-5073-2019-4-35-44.
14. Гонсалес Р.С., Вудс Р.Е. Цифровая обработка изображений. М.: Техносфера, 2012. 1104 с.
15. Соколовская Э.А., Кудря А.В., Пережогин В.Ю., Танг В.Ф., Кодиров Д.Ф.У., Сергеев М.И. Возможности цифровизации измерений в металловедении для внесения в оценку структур и разрушения количественной меры // Металлург. 2022. № 7. С. 48–57. DOI: 10.52351/00260827_2022_07_48.
16. Казаков А.А., Киселев Д.В., Казакова Е.И. Количественные методы оценки микроструктуры стали и сплавов для пересмотра устаревших ГОСТ // Литье и металлургия. 2021. № 2. С. 42–48. DOI: 10.21122/1683-6065-2021-2-42-48.
17. McHugh S.T. Understanding Photography. Master Your Digital Camera and Capture That Perfect. San Francisco: No Starch Press, 2018. 240 p.
18. Voronoi G.F. Nouvelles applications des paramètres continus à la théorie de formes quadratiques // Journal für die reine und angewandte Mathematik. 2009. Vol. 1908. № 134. P. 198–287. DOI: 10.1515/crll.1908.134.198.
19. Jo Sung-Koo, Kim Seon-Hyo, Song Bo. Thermodynamics on the Formation of Spinel ($MgO \times Al_2O_3$). Inclusion in Liquid Iron Containing Chromium // Metallurgical and Materials Transactions B. 2002. Vol. 33. P. 703–709. DOI: 10.1007/s11663-002-0023-4.
20. Osio A.S., Liu S., Olson D.L. The effect of solidification on the formation and growth of inclusions in low carbon steel welds // Material Science and Engineering A. 1996. Vol. 221. № 1-2. P. 122–133. DOI: 10.1016/S0921-5093(96)10466-4.

Цифровые измерения неметаллических включений в стали

Стукалова Наталья Анатольевна[1,3], аспирант
Кодиров Давронжон Фарходжон угли*[1,4], аспирант
Алексеев Валерий Игоревич[1], аспирант
Соколовская Элина Александровна[1,5], кандидат технических наук, доцент,
доцент кафедры металловедения и физики прочности
Родионова Ирина Гавриловна[2,6], доктор технических наук, доцент,
заместитель директора научного центра физико-химических основ и технологий металлургии
[1]*Университет науки и технологий МИСИС, Москва (Россия)*
[2]*ГНЦ ФГУП «ЦНИИчермет им. И.П. Бардина», Москва (Россия)*

***E-mail: DFKodirov@yandex.ru**

[3]ORCID: https://orcid.org/0009-0007-3455-4457
[4]ORCID: https://orcid.org/0009-0003-5380-5558
[5]ORCID: https://orcid.org/0000-0001-9381-9223
[6]ORCID: https://orcid.org/0000-0003-4201-4665

Поступила в редакцию 19.07.2023 *Принята к публикации 13.11.2023*

Аннотация: Опыт многолетних исследований показал, что существенно повысить коррозионную стойкость сталей нефтепромысловых трубопроводов и увеличить сроки их безаварийной эксплуатации можно, оптимизируя химический состав и микроструктурные особенности стали, а также понижая ее загрязненность неметаллическими включениями (НВ). Влияние комплексных НВ на коррозионную стойкость стали обусловлено как химическим составом НВ, так и их количественных соотношением. Поэтому получение металлопродукции требуемого качества возможно только с применением принципа «управления по структуре». В работе на основе анализа полей яркости изображений (в масштабе образцов) в 256 оттенках серого предложены цифровые метрологически обеспеченные процедуры измерения неоднородности НВ низкоуглеродистых сталей нефтепромыслового назначения, такие как устранение неоднородности освещения поля зрения, обоснование критериев бинаризации и фильтрации шумов. Для низкоуглеродистых сталей различной выплавки выявлена ключевая роль дисперсных неметаллических включений размером от 5–10 мкм^2 до 2 нм^2 в формировании коррозионной стойкости сталей. Это может объяснить, почему в ряде случаев отсутствует взаимосвязь между скоростью коррозии и сопротивлением сталей разрушению, в формировании которого определяющее влияние оказывают частицы большего размера. В представлении НВ как множества случайных точек на плоскости распределение расстояний между ближайшими из них оценено на основе статистики полиэдров Вороного. Показано, что повышению коэффициента эксцесса распределений площадей полиэдров сопутствует увеличение скорости коррозии исследуемых сталей. Это указывает на отрицательное влияние неоднородности в размещении дисперсных НВ на коррозионную стойкость сталей.

Ключевые слова: цифровые измерения структур; управление качеством по структуре; неметаллические включения в стали; коррозионная стойкость нефтепромысловых труб.

Благодарности: Статья подготовлена по материалам докладов участников XI Международной школы «Физическое материаловедение» (ШФМ-2023), Тольятти, 11–15 сентября 2023 года.

Для цитирования: Стукалова Н.А., Кодиров Д.Ф., Алексеев В.И., Соколовская Э.А., Родионова И.Г. Цифровые измерения неметаллических включений в стали // Frontier Materials & Technologies. 2024. № 1. С. 95–103. DOI: 10.18323/2782-4039-2024-1-67-9.

doi: 10.18323/2782-4039-2024-1-67-10

The study of the effect of heat treatment on the properties of the AMg2–10%TiC and AMg6–10%TiC composite materials produced by self-propagating high-temperature synthesis

Yuliya V. Sherina*[1], postgraduate student
of Chair "Metal Science, Powder Metallurgy, Nanomaterials"
Alfiya R. Luts[2], PhD (Engineering), Associate Professor,
assistant professor of Chair "Metal Science, Powder Metallurgy, Nanomaterials"
Samara State Technical University, Samara (Russia)

***E-mail: yulya.makhonina.97@inbox.ru**

[1]ORCID: https://orcid.org/0000-0002-5451-7107
[2]ORCID: https://orcid.org/0000-0001-7889-9931

Received 22.06.2023 *Accepted 21.08.2023*

Abstract: Dispersion-strengthened composite materials belong to the group of promising structural materials characterised by a diverse combination of properties. The paper considers examples of the creation and heat treatment of composite materials based on aluminium alloys strengthened by the titanium carbide dispersed phase characterised by high hardness, elastic modulus, and good melt wettability. At present, self-propagating high-temperature synthesis (SHS) is the most accessible, inexpensive and effective way to obtain them. The authors substantiate the expediency and show their successful experience of the formation in the composition of the AMg2 and AMg6 industrial alloys of a titanium carbide dispersed phase with a particle size of 130 nm in an amount of up to 10 wt. % using the SHS method, which makes it possible to increase the hardness of the alloys. Additional heating of the AMg2–10%TiC and AMg6–10%TiC samples after synthesis also contributes to the further increase in hardness. The complex of studies of physical, mechanical and operational characteristics presented in the paper was carried out to compare the properties of the work-hardened matrix alloys and the samples of composite materials before and after heating. The test results showed that heat treatment reduces the porosity of the composites and significantly increases their hardness and microhardness. A slight decrease in compressive strength at a significant increase in wear resistance is observed. It was found that composite materials are characterised by high corrosion resistance to carbon dioxide and hydrogen sulfide corrosion corresponding to the level of matrix alloys. The results obtained allow recommending the developed materials for the production of parts of the connecting rod and piston group, bearings and other wear-resistant parts of friction units.

Keywords: composite material; AMg2–10%TiC; AMg6–10%TiC; titanium carbide; heat treatment; self-propagating high-temperature synthesis.

Acknowledgments: The paper was written on the reports of the participants of the XI International School of Physical Materials Science (SPM-2023), Togliatti, September 11–15, 2023.

For citation: Sherina Yu.V., Luts A.R. The study of the effect of heat treatment on the properties of the AMg2–10%TiC and AMg6–10%TiC composite materials produced by self-propagating high-temperature synthesis. *Frontier Materials & Technologies*, 2024, no. 1, pp. 105–112. DOI: 10.18323/2782-4039-2024-1-67-10.

INTRODUCTION

One of the most promising ways to improve the mechanical characteristics of conventional aluminium alloys, is to introduce dispersed particles of an additional phase into their composition, for which ceramic compounds – oxides, carbides, nitrides, borides, etc. are most often used [1; 2]. However, in the case of an aluminium matrix, the most suitable phase for reinforcement is the titanium carbide phase, which has crystal lattice parameters as close as possible to aluminium, and possesses high hardness, elastic modulus, low density, and good wettability [3; 4]. The most common way to produce such composite materials is the method of mechanical mixing of particles into an aluminium melt, however, this approach excludes the possibility of obtaining a highly dispersed titanium carbide phase, since the introduced particles are prone to agglomeration, and often contain impurity adsorbed compounds, that prevent the complete assimilation of particles in the melt. In this regard, the most appropriate option is the formation of dispersed particles of titanium carbide directly in the melt from the initial elemental powders of titanium and carbon or their compounds [5–7].

This technology based on the method of self-propagating high-temperature synthesis (SHS) was developed and used at the Chair "Metal Science, Powder Metallurgy, Nanomaterials" of Samara State Technical University. According to the results of the studies, the possibility of successful synthesis of composite materials of the Al–10%TiC, Al–5%Cu–10%TiC, Al–5%Cu–2%Mn–10%TiC, etc. compositions characterised by increased mechanical characteristics has already been shown [8; 9].

A review of current publications showed a steady tendency towards reinforcement of industrial alloys, that have long been developed and actively used with the titanium carbide phase [10]. For example, in the study [11], the Al–10%TiC addition alloy was introduced into the composition of the 2014 aluminium matrix alloy, which allowed increasing the strength from 118 to 147 MPa, and the hardness from 61 to 94 HV. In [12],

based on the AA 6063 alloy (analogue of AD 31), hybrid-reinforced samples were produced using the SHS method, including 5 vol. % Al_2O_3 and 5 vol. % TiC. Then, since the matrix alloy is a thermally hardenable one, the resulting composite was subjected to T6 treatment in the form of quenching at 530 °C and artificial ageing at 175 °C. It was found that composite material samples demonstrated acceleration in aging kinetics. To achieve a maximum hardness of 78 HB after ageing, they required 2–4 h, whereas for an unreinforced alloy, this time was 6–8 h, and the material hardness did not exceed 65 HB. The authors explain the observed accelerated aging by an increase in the dislocation density near dispersed particles. This is associated with a large difference in the thermal expansion coefficient of these particles and the matrix alloy (Al_2O_3 and TiC particles have a TLEC of $8 \cdot 10^{-6}/K^{-1}$, Al – $23 \cdot 10^{-6}/K^{-1}$), as well as accelerated diffusion of dissolved atoms and modification of the base alloy. It is obvious that the presence of additional phase dispersed particles affects the order and intensity of structural transformations in the composition of conventional alloys. On the other hand, in addition to this, completely new effects may arise that are not typical for matrix alloys.

Thus, in the work [13], a composite material based on the AMg1 alloy containing 5 wt. % SiC was obtained by the mechanical mixing method, and then the possibility of its thermal hardening was shown for the first time. In particular, it was found that quenching at a temperature of 550 °C and subsequent ageing at a temperature of 160 °C leads to an increase in hardness from 770 to 1000 HB and strength to 152 MPa, and in combination with subsequent rolling, it leads to an increase in hardness to 1530 HB and strength up to 236 MPa.

Such an increase in the strength characteristics of aluminum-magnesium alloys is extremely important, since they are widespread due to their low cost, good deformability, corrosion resistance, and weldability; however, they are not good in strength [14]. The alloys under consideration contain microadditives of alloying elements (Fe, Si, Mn, Ti, etc.), which contribute to solid solution strengthening, but their quantity is too small to significantly increase the strength characteristics, so the alloys are additionally hardened by plastic deformation. However, the use of cold hardening leads to a decrease in ductility, so annealing is the final stage after plastic deformation, during which partial or complete removal of strain hardening occurs, which leads to a decrease in strength [15; 16].

Previously, studies on the production of AMg2–10%TiC and AMg6–10%TiC composite materials by SHS method were carried out, which showed that in both cases, an active and rapid SHS reaction was observed, and the fractures of the samples were characterised by a uniform grey colour without the remains of unreacted charging material [17]. After synthesis, according to X-ray microanalysis and X-ray phase analysis, the composition of the composites contained the target phase of titanium carbide (with a particle size of 130 nm), as well as magnesium, apparently in the precipitated β-phase (Al_3Mg_2), which was not detected due to its small amount. Hardness measurements showed an increase in the values for the AMg2 base from 59.4 to 64.4 HB, for the AMg6 base – from 83 to 90.9 HB. Then the samples were additionally heated with following cooling in air. It was found that heating at 150 °C and holding for 2 h leads to an increase in the hardness of AMg2–10%TiC to 67.6 HB, and heating at 230 °C and holding for 3 h of the AMg6–10%TiC sample leads to the hardness of 93 HB. Using phase analysis of the samples, the β-phase was detected in both cases, which indicates its additional precipitation after heating [17]. However, other properties than hardness of the obtained samples were not studied.

The purpose of the work is to study and compare the basic physical, mechanical and operational characteristics, of the AMg2–10%TiC and AMg6–10%TiC composite materials before and after heat treatment.

METHODS

To compare the results, all tests were carried out on matrix alloys in a cold-worked state (AMg2N and AMg6N) and composite materials based on them. AMg2 and AMg6 alloys were used as a matrix for creating melts with digital markings of these alloys as 1520 and 1560, respectively, according to GOST 4784-2019 (Table 1).

To obtain a charge mixture, titanium powders (grade TPP-7, TU1715-449-05785388) and carbon (P-701, GOST 7585-86), taken in a stoichiometric ratio, were mixed with 5 % by weight of the Na_2TiF_6 salt charge (GOST 10561-80). The resulting composition was divided into 3 equal portions, each of which was alternately introduced into AMg2 or AMg6 melts heated to a temperature of 900 °C in a graphite crucible of a PS-20/12 melting furnace, then synthesised and poured into a steel casting mold. Thermal treatment of the samples was carried out in a laboratory chamber furnace SNOL, with an operating temperature of up to 1300 °C. The experimental determination of the density of the samples was carried out using hydrostatic weighing in accordance with GOST 20018-74. The theoretical maximum possible density of a nonporous casting composite was calculated using the formula

$$\rho_т = \frac{\rho_1 \rho_2}{n\rho_1 + (1-n)\rho_2},$$

where ρ_T is theoretical density, kg/m^3;
ρ_1 is crystalline aluminium density, kg/m^3;
ρ_2 is second phase (titanium carbide) density, kg/m^3;
n is titanium carbide mass content in the composite.

The calculation of actual porosity was carried out using the formula

$$P = 1 - \frac{\rho_e}{\rho_т},$$

where ρ_e is experimentally measured density, kg/m^3;
P is porosity, %.

When calculating, the density of aluminium was taken to be 2700 kg/m^3, the density of the titanium carbide phase was 4920 kg/m^3, n=0.1.

The hardness of the obtained experimental samples was determined using a TSh-2M hardness tester according to GOST 9012-59. The microhardness of the samples was studied using a PTM-3 standard microhardness tester

according to GOST 9450-76 by indentation of a diamond pyramid with a square base and an interface angle at the apex of 136°. The weight on the indenter was 100 g. Compression tests were carried out on the III type samples, with a diameter of 20 mm according to GOST 25.503-97. The moment of appearance of the first cracks was determined visually. Corrosion resistance was tested according to GOST 13819–68 in the Coat Test 3.3.150.150 autoclave complex under the following conditions: aqueous solution of 5%NaCl; gas phase 1 MPa CO_2, 0.5 MPa H_2S, 3.5 MPa N_2 at a temperature of 80 °C; duration is 240 h; total pressure is 5 MPa. Corrosion resistance parameters were calculated, according to GOST 9.908-85. Tribological tests were carried out using the "Universal-1B" universal tribological complex, according to the ring–plane test scheme; counterbody material – steel 40X; normal contact load is 380 N; counterbody rotation speed – 600 rpm; test duration is 30 min or until complete setting occurs.

RESULTS

As a result of determining the physical properties (Table 2) of the AMg2N, AMg6N alloys, and the AMg2–10%TiC and AMg6–10%TiC composite materials, it was identified that the density of the composite materials is higher than the density of the matrix alloys, which is obviously related to the presence of a reinforcing ceramic phase of titanium carbide. Test results show, that additional heating leads to a decrease in the porosity of composite materials, due to an improvement in the adhesive bond between the matrix and the filler.

The study of mechanical characteristics (Table 3) showed that the ceramic phase reinforcement of matrix alloys leads to an increase in their hardness and microhardness. Additional heating of the AMg2–10%TiC and AMg6–10%TiC composite materials promotes an increase in hardness by 13 and 12 %, respectively, and microhardness by 22 and 7 %, respectively. Reinforcement, with a highly dispersed titanium carbide phase in combination with heat treatment does not have a strong negative effect on the yield strength and relative strain.

The results of determining the tribological characteristics (Table 4) of the AMg2N, AMg6N alloys and AMg2–10%TiC, AMg6–10%TiC composite materials before and after heat treatment, showed that reinforcement in combination with heat treatment leads to a significant decrease in the friction ratio and wear rate. The lowest tribological properties are observed in the original AMg2N and AMg6N alloys: they showed wear during setting and abrasive

Table 1. *Chemical composition of the AMg2 and AMg6 alloys*
Таблица 1. *Химический состав сплавов АМг2 и АМг6*

Alloy	Element content, %						
	Al	Mg	Fe	Si	Mn	Cu	Ti
AMg2	95.3–98.00	1.8–2.8	<0.4	<0.4	0.2–0.6	<0.1	<0.1
AMg6	91.1–93.68	5.6–6.8	<0.4	<0.4	0.5–0.8	<0.1	<0.1

Table 2. *Physical properties of the AMg2, AMg6 alloys and AMg2–10%TiC, AMg6–10%TiC composite materials before and after heat treatment*
Таблица 2. *Физические свойства сплавов АМг2, АМг6 и композиционных материалов АМг2–10%TiC, АМг6–10%TiC до и после термической обработки*

Alloys and composite materials on their base	Theoretical density, ρ_T, g/cm^3	Experimental density, ρ_e, g/cm^3	Porosity, P, %
AMg2N	2.690	–	–
AMg2–10%TiC, without HT	2.820	2.797±0.05	0.82
AMg2–10%TiC, after HT	2.820	2.820±0.03	0.00
AMg6N	2.640	–	–
AMg6–10%TiC, without HT	2.768	2.739±0.06	1.00
AMg6–10%TiC, after HT	2.768	2.768±0.04	0.00

Note. HT (heat treatment) is heating at T=150 °C for 3 h.
Примечание. НТ (термическая обработка) – нагрев при Т=150 °С в течение 3 ч.

wear, which led to rapid surface layer destruction; high values of the friction ratio and wear rate indicate unacceptable processes occurring in the friction zone. AMg2–10%TiC and AMg6–10%TiC samples showed significantly better tribological characteristics compared to the matrix alloy, however, they had scuff marks, on which friction was established with a ratio of about 0.1. The same samples, after additional heating according to the recommended conditions, showed the lowest values of the friction ratio, low wear rate and good conformability.

Table 5 shows that the titanium carbide ceramic phase reinforcement of the AMg2 and AMg6 alloys leads to a decrease in the corrosion resistance level.

DISCUSSION

Since composite materials, especially those obtained by the SHS method, are characterised by increased porosity, which has a significant impact on their properties, the density and porosity of the resulting materials were initially determined. The study of the porosity of the samples (Table 2) showed that after synthesis, the deviation from the calculated value does not exceed 1 %, and after heat treatment, it decreases to zero, which may be caused by a change in the composition and structure of the interphase boundaries and an improvement in the quality of the "matrix – filler" bond.

The titanium carbide phase is characterised by increased hardness, and, accordingly, low ductility, therefore, the main mechanical characteristic of composite materials containing it, as a rule, is compressive strength. However, since complete destruction of such samples does not occur, the yield strength value was used as an evaluation criterion, which corresponds to the temporary fracture resistance upon the occurrence of the first cracks. The obtained values of the strength, of the as-cast material (Table 3) comparable to the values after cold hardening, are obviously caused by the following factors. The first is the action of the Hall – Petch mechanism determined by the role of dispersed particles as the alloy crystallisation centres. The second is the Orowan mechanism, the essence of which is that the resistance to motion of dislocations, increases with decreasing distance between particles. The third is the emergence of difficulties for the motion of dislocations due to the formation of additional dislocations caused by the mismatch of the coefficients of thermal expansion and elastic modulus of the matrix material and the reinforcing phase particles. The study [18] showed that the introduction of reinforcing TiC particles with a size of 40–100 μm, into the AK12M2MgN aluminium alloy, using the mechanical mixing method, leads to a decrease in the compressive deformation degree from 17.01 to 12.65 %, and the ultimate compressive strength from 489 to 470 MPa, while the hardness increases by 30–50 HB. One can conclude that the presence of the carbide phase does not lead to an increase in the strength characteristics, but does contribute to an increase in hardness.

Since it was found that the presence of carbide phase particles contributes to an overall increase in the hardness of the resulting materials, it was assumed that this could have a positive effect on their wear resistance, so the tribological properties were further investigated. Low values of the friction ratio, low wear rate and good conformability of AMg2–10%TiC and AMg6–10%TiC composite materials after the optimal heat treatment mode, are obviously related to an increase in the quality of the interfacial bond, as well as additional precipitation of the solid intermetallic β-phase (Al_3Mg_2) [19].

One of the main advantages of aluminum-magnesium alloys is their high corrosion resistance. The study of this characteristic in an environment of CO_2 and H_2S gases at an elevated temperature of 80 °C, showed that the samples

Table 3. *Mechanical characteristics of the AMg2, AMg6 alloys and AMg2–10%TiC, AMg6–10%TiC composite materials before and after heat treatment*

Таблица 3. *Механические характеристики сплавов АМг2, АМг6 и композиционных материалов АМг2–10%TiC, АМг6–10%TiC до и после термической обработки*

Alloys and composite materials on their base	Uniaxial compressive strength test		Hardness HB	Microhardness HV, MPa
	$\sigma_т^c$, MPa	ε, %		
AMg2N	290±10	69.19	59.4±20	608±10
AMg2–10%TiC, without HT	271±13	59.70	59.4±20	736±15
AMg2–10%TiC, after HT	298±10	61.50	67.6±20	745±18
AMg6N	449±15	32.00	83.0±19	991±21
AMg6–10%TiC, without HT	403±18	19.00	90.9±19	1020±20
AMg6–10%TiC, after HT	395±19	14.00	93.0±19	1069±19

Note. HT (heat treatment) is heating at T=150 °C for 3 h.
Примечание. НТ (термическая обработка) – нагрев при Т=150 °С в течение 3 ч.

Table 4. *Tribotechnical properties of the AMg2, AMg6 alloys and AMg2–10%TiC, AMg6–10%TiC composite materials before and after heat treatment*
Таблица 4. *Триботехнические свойства сплавов АМг2, АМг6 и композиционных материалов АМг2–10%TiC, АМг6–10%TiC до и после термической обработки*

Alloys and composite materials on their base	Wear rate, μm/h	Friction ratio	Self-heating temperature, °C
AMg2N	37.6±5.2	<0.3	71
AMg2–10%TiC, without HT	6.4±1.6	0.11…0.12	65
AMg2–10%TiC, after HT	4.0±1.3	0.07…0.08	56
AMg6N	15.5±4.1	0.13...0.15	70
AMg6–10%TiC, without HT	3.5±0.6	0.07…0.09	59
AMg6–10%TiC, after HT	4.2±1.2	0.08…0.10	66

Note. HT (heat treatment) is heating at T=150 °C for 3 h.
Примечание. НТ (термическая обработка) – нагрев при Т=150 °С в течение 3 ч.

Table 5. *Corrosion resistance of the AMg2, AMg6 alloys and AMg2–10%TiC, AMg6–10%TiC composite materials before and after heat treatment*
Таблица 5. *Коррозионная стойкость сплавов АМг2, АМг6 и композиционных материалов АМг2–10%TiC, АМг6–10%TiC до и после термической обработки*

Alloys and composite materials on their base	Factor		
	Weight loss per unit area, Δm, kg/m^2	Corrosion rate, V, g/(m^2·h)	Corrosion depth index, π, mm/year
AMg2N	0.160	0.666±0.04	0.0021
AMg2–10%TiC, without HT	0.095	0.416±0.02	0.0014
AMg2–10%TiC, after HT	0.108	0.450±0.03	0.0014
AMg6N	0.231	0.962±0.06	0.0030
AMg6–10%TiC, without HT	0.151	0.627±0.04	0.0021
AMg6–10%TiC, after HT	0.208	0.868±0.02	0.0027

Note. HT (heat treatment) is heating at T=150 °C for 3 h.
Примечание. НТ (термическая обработка) – нагрев при Т=150 °С в течение 3 ч.

both of matrix alloys and of composite materials, before and after heating, have a depth corrosion rate at the level of 0.001–0.005 mm/year (Table 5). This indicates the high corrosion resistance of the AMg2–10%TiC and AMg6–10%TiC composite materials and allows classifying them as rather resistant metals [20].

CONCLUSIONS

According to the results of a set of studies of properties, the developed composite materials AMg2–10%TiC and AMg6–10%TiC produced by the SHS method and subjected to additional heating showed, a higher level of hardness, microhardness, wear and corrosion resistance compared to the matrix alloys AMg2 and AMg6 in the cold hardening state. Thus, reinforcement with a highly dispersed phase of titanium carbide in combination with heat treatment, is an appropriate way to increase mechanical and operational characteristics, as it helps to avoid the labour-intensive operation of cold strain hardening (cold hardening). Based on the data obtained, composite materials can be recommended to produce connecting rod and piston group parts, bearings, and other wear-resistant parts of friction units.

REFERENCES

1. Panfilov A.A., Prusov E.S., Kechin V.A. Problems and prospects of development of production and application

alyumomatrichnykh of composite alloys. *Trudy NGTU im. R.E. Alekseeva*, 2013, no. 2, pp. 210–217. EDN: QZLYCV.
2. Mikheev R.S., Chernyshova T.A. *Alyumomatrichnye kompozitsionnye materialy s karbidnym uprochneniem dlya resheniya zadach novoy tekhniki* [Aluminum-matrix composite materials with carbide hardening for solving problems of new technology]. Moscow, Maska Publ., 2013. 356 p.
3. Pandey U., Purohit R., Agarwal P., Dhakad S.K., Rana R.S. Effect of TiC particles on the mechanical properties of aluminium alloy metal matrix composites (MMCs). *Materials Today: Proceedings*, 2017, vol. 4, no. 4-D, pp. 5452–5460. DOI: 10.1016/j.matpr.2017.05.057.
4. Zhou D., Qiu F., Jiang Q. The nano-sized TiC particle reinforced Al–Cu matrix composite with superior tensile ductility. *Materials Science and Engineering: A*, 2015, vol. 622, pp. 189–193. DOI: 10.1016/j.msea.2014.11.006.
5. Nath H., Amosov A.P. SHS amidst other new processes for in-situ synthesis of Al-matrix composites: A review. *International Journal of Self-Propagating High-Temperature Synthesis*, 2016, vol. 25, pp. 50–58. DOI: 10.3103/S106138621601009X.
6. Pramod S.L., Bakshi S.R., Murty B.S. Aluminum-based cast in situ composites: A Review. *Journal of Materials Engineering and Performance*, 2015, vol. 24, no. 6, pp. 2185–2207. DOI: 10.1007/s11665-015-1424-2.
7. Chaubey A.K., Prashanth K.G., Ray N., Wang Z. Study on in-situ synthesis of Al-TiC composite by self – propagating high temperature synthesis process. *MSAIJ*, 2015, vol. 12, no. 12, pp. 454–461.
8. Amosov A.P., Luts A.R., Rybakov A.D., Latukhin E.I. Application of different powdered forms of carbon for reinforcement of aluminum matrix composite materials by carbon and titanium carbide. A review. *Izvestiya vysshikh uchebnykh zavedeniy. Tsvetnaya metallurgiya*, 2020, no. 4, pp. 44–64. DOI: 10.17073/0021-3438-2020-4-44-64.
9. Luts A.R., Amosov A.P., Latukhin E.I., Rybakov A.D., Novikov V.A., Shipilov S.I. Self-propagating high-temperature synthesis of (Al-2%Mn)-10%TiC and (Al-5%Cu-2%Mn)-10%TiC nanostructured composite alloys when doped with manganese powder. *Izvestiya vysshikh uchebnykh zavedeniy. Poroshkovaya metallurgiya i funktsionalnye pokrytiya*, 2018, no. 3, pp. 30–40. DOI: 10.17073/1997-308X-2018-3-30-40.
10. Wang L., Qiu F., Zhao Q., Wang H., Jiang Q. Simultaneously increasing the elevated-temperature tensile strength and plasticity of in situ nano-sized TiCx/Al-Cu-Mg composites. *Materials Characterization*, 2017, vol. 125, pp. 7–12. DOI: 10.1016/j.matchar.2017.01.013.
11. Kumar A., Mahapatra M.M., Jha P.K. Fabrication and Characterizations of Mechanical Properties of Al-4.5%Cu/10TiC Composite by In-Situ Method. *Journal of Minerals and Materials Characterization and Engineering*, 2012, vol. 11, no. 11, pp. 1075–1080. DOI: 10.4236/jmmce.2012.1111113.
12. Aziz M.A., Mahmoud T.S., Zaki Z.I., Gaafer A.M. Heat Treatment and Wear Characteristics of Al_2O_3 and TiC Particulate Reinforced AA6063 Al. *Journal of Tribology*, 2006, vol. 128, pp. 891–895. DOI: 10.1115/1.2345416.
13. Kurganova Yu.A., Kolmakov A.G., Chen I., Kurganov S.V. Study of mechanical characteristics of advanced aluminum-matrix composites reinforced with SiC and Al_2O_3. *Inorganic materials: applied research*, 2022, vol. 13, no. 1, pp. 157–160. DOI: 10.1134/S2075113322010245.
14. Bhoi N.K., Singh H., Pratap S. Developments in the aluminum metal matrix composites reinforced by micro/nano particles – a review. *Journal of Composite Materials*, 2020, vol. 54, no. 6, pp. 813–833. DOI: 10.1177/0021998319865307.
15. Belov N.A. *Fazovyy sostav alyuminievykh splavov* [Phase composition of aluminum alloys]. Moscow, MISIS Publ., 2009. 389 p.
16. Wang H., Geng H., Zhou D., Niitsu K., Muransky O., Zhang D. Multiple strengthening mechanisms in high strength ultrafine-grained Al–Mg alloys. *Materials Science and Engineering A*, 2020, vol. 771, article number 138613. DOI: 10.1016/j.msea.2019.138613.
17. Sherina Yu.V., Luts A.R., Kichaev P.E., Bogatov M.V., Amosov A.P. The effect of reinforcement with a titanium carbide high-dispersity phase and subsequent heat treatment on the structure and properties of the AMG6 alloy. *Naukoemkie tekhnologii v mashinostroenii*, 2023, no. 5, pp. 15–21. DOI: 10.30987/2223-4608-2023-15-21.
18. Mikheev R.S. Innovative ways to produce of antifriction composite coatings based on nonferrous alloys with enhanced properties. *Zagotovitelnye proizvodstva v mashinostroenii*, 2018, vol. 16, no. 5, pp. 204–210. EDN: UOVQQM.
19. Rao V.R., Ramanaiah N., Sarcar M.M. Mechanical and tribological properties of AA7075-TiC metal matrix composites under heat treatment (T6) and cast conditions. *Journal of Materials Research and Technology*, 2016, vol. 5, no. 4, pp. 377–383. DOI: 10.1016/j.jmrt.2016.03.011.
20. Alaneme K.K., Olubambi P. Corrosion and wear behaviour of rice husk ash–Alumina reinforced Al-Mg-Si alloy matrix hybrid composites. *Journal of Materials Research and Technology*, 2013, vol. 2, no. 2, pp. 188–194. DOI: 10.1016/j.jmrt.2013.02.005.

СПИСОК ЛИТЕРАТУРЫ

1. Панфилов А.А., Прусов Е.С., Кечин В.А. Проблемы и перспективы развития производства и применения алюмоматричных композиционных сплавов // Труды НГТУ им. Р.Е. Алексеева. 2013. № 2. С. 210–217. EDN: QZLYCV.
2. Михеев Р.С., Чернышова Т.А. Алюмоматричные композиционные материалы с карбидным упрочнением для решения задач новой техники. М.: Маска, 2013. 356 с.
3. Pandey U., Purohit R., Agarwal P., Dhakad S.K., Rana R.S. Effect of TiC particles on the mechanical properties of aluminium alloy metal matrix composites (MMCs) // Materials Today: Proceedings. 2017. Vol. 4. № 4-D. P. 5452–5460. DOI: 10.1016/j.matpr.2017.05.057.

4. Zhou D., Qiu F., Jiang Q. The nano-sized TiC particle reinforced Al–Cu matrix composite with superior tensile ductility // Materials Science and Engineering: A. 2015. Vol. 622. P. 189–193. DOI: 10.1016/j.msea.2014.11.006.
5. Nath H., Amosov A.P. SHS amidst other new processes for in-situ synthesis of Al-matrix composites: A review // International Journal of Self-Propagating High-Temperature Synthesis. 2016. Vol. 25. P. 50–58. DOI: 10.3103/S106138621601009X.
6. Pramod S.L., Bakshi S.R., Murty B.S. Aluminum-based cast in situ composites: A Review // Journal of Materials Engineering and Performance. 2015. Vol. 24. № 6. P. 2185–2207. DOI: 10.1007/s11665-015-1424-2.
7. Chaubey A.K., Prashanth K.G., Ray N., Wang Z. Study on in-situ synthesis of Al-TiC composite by self – propagating high temperature synthesis process // MSAIJ. 2015. Vol. 12. № 12. P. 454–461.
8. Амосов А.П., Луц А.Р., Рыбаков А.Д., Латухин Е.И. Применение различных порошковых форм углерода для армирования алюмоматричных композиционных материалов углеродом и карбидом титана (обзор) // Известия высших учебных заведений. Цветная металлургия. 2020. № 4. С. 44–64. DOI: 10.17073/0021-3438-2020-4-44-64.
9. Луц А.Р., Амосов А.П., Латухин Е.И., Рыбаков А.Д., Новиков В.А., Шипилов С.И. Самораспространяющийся высокотемпературный синтез наноструктурных композиционных сплавов (Al–2%Mn)–10%TiC и (Al–5%Cu–2%Mn)–10%TiC при легировании порошковым марганцем // Известия высших учебных заведений. Порошковая металлургия и функциональные покрытия. 2018. № 3. С. 30–40. DOI: 10.17073/1997-308X-2018-3-30-40.
10. Wang L., Qiu F., Zhao Q., Wang H., Jiang Q. Simultaneously increasing the elevated-temperature tensile strength and plasticity of in situ nano-sized TiCx/Al-Cu-Mg composites // Materials Characterization. 2017. Vol. 125. P. 7–12. DOI: 10.1016/j.matchar.2017.01.013.
11. Kumar A., Mahapatra M.M., Jha P.K. Fabrication and Characterizations of Mechanical Properties of Al-4.5%Cu/10TiC Composite by In-Situ Method // Journal of Minerals and Materials Characterization and Engineering. 2012. Vol. 11. № 11. P. 1075–1080. DOI: 10.4236/jmmce.2012.1111113.
12. Aziz M.A., Mahmoud T.S., Zaki Z.I., Gaafer A.M. Heat Treatment and Wear Characteristics of Al_2O_3 and TiC Particulate Reinforced AA6063 Al // Journal of Tribology. 2006. Vol. 128. P. 891–895. DOI: 10.1115/1.2345416.
13. Курганова Ю.А., Колмаков А.Г., Чэнь И., Курганов С.В. Исследование механических свойств перспективных алюмоматричных композиционных материалов, армированных SiC и Al_2O_3 // Материаловедение. 2021. № 6. С. 34–38. DOI: 10.31044/1684-579X-2021-0-6-34-38.
14. Bhoi N.K., Singh H., Pratap S. Developments in the aluminum metal matrix composites reinforced by micro/nano particles – a review // Journal of Composite Materials. 2020. Vol. 54. № 6. P. 813–833. DOI: 10.1177/0021998319865307.
15. Белов Н.А. Фазовый состав алюминиевых сплавов. М.: МИСИС, 2009. 389 с.
16. Wang H., Geng H., Zhou D., Niitsu K., Muransky O., Zhang D. Multiple strengthening mechanisms in high strength ultrafine-grained Al–Mg alloys // Materials Science and Engineering A. 2020. Vol. 771. Article number 138613. DOI: 10.1016/j.msea.2019.138613.
17. Шерина Ю.В., Луц А.Р., Кичаев П.Е., Богатов М.В., Амосов А.П. Влияние армирования высокодисперсной фазой карбида титана и последующей термической обработки на структуру и свойства сплава АМг6 // Наукоемкие технологии в машиностроении. 2023. № 5. С. 15–21. DOI: 10.30987/2223-4608-2023-15-21.
18. Михеев Р.С. Инновационные пути в создании антифрикционных композиционных покрытий на основе цветных сплавов с повышенными триботехническими свойствами // Заготовительные производства в машиностроении. 2018. Т. 16. № 5. С. 204–210. EDN: UOVQQM.
19. Rao V.R., Ramanaiah N., Sarcar M.M. Mechanical and tribological properties of AA7075-TiC metal matrix composites under heat treatment (T6) and cast conditions // Journal of Materials Research and Technology. 2016. Vol. 5. № 4. P. 377–383. DOI: 10.1016/j.jmrt.2016.03.011.
20. Alaneme K.K., Olubambi P. Corrosion and wear behaviour of rice husk ash–Alumina reinforced Al-Mg-Si alloy matrix hybrid composites // Journal of Materials Research and Technology. 2013. Vol. 2. № 2. P. 188–194. DOI: 10.1016/j.jmrt.2013.02.005.

Влияние термической обработки на свойства композиционных материалов АМг2–10%TiC и АМг6–10%TiC, полученных методом самораспространяющегося высокотемпературного синтеза

Шерина Юлия Владимировна*[1], аспирант
кафедры «Металловедение, порошковая металлургия, наноматериалы»
Луц Альфия Расимовна[2], кандидат технических наук, доцент,
доцент кафедры «Металловедение, порошковая металлургия, наноматериалы»
Самарский государственный технический университет, Самара (Россия)

***E-mail: yulya.makhonina.97@inbox.ru**

[1]ORCID: https://orcid.org/0000-0002-5451-7107
[2]ORCID: https://orcid.org/0000-0001-7889-9931

Поступила в редакцию 22.06.2023 *Принята к публикации 21.08.2023*

Аннотация: Дисперсно-упрочненные композиционные материалы относятся к группе перспективных конструкционных материалов, отличающихся разнообразным сочетанием свойств. В работе рассмотрены примеры создания и термической обработки композиционных материалов на основе алюминиевых сплавов, упрочненных дисперсной фазой карбида титана, для которой характерны высокая твердость, модуль упругости и хорошая смачиваемость расплавом. В настоящее время наиболее доступным, недорогим и эффективным способом получения этих материалов является самораспространяющийся высокотемпературный синтез (СВС). Обоснована целесообразность и показан собственный успешный опыт формирования в составе промышленных сплавов АМг2 и АМг6 дисперсной фазы карбида титана с размером частиц от 130 нм в количестве до 10 мас. % методом СВС, что позволяет увеличить твердость сплавов. Проведение после синтеза дополнительного нагрева образцов АМг2–10%TiC и АМг6–10%TiC также способствует последующему повышению твердости. Представленный в статье комплекс исследований физических, механических и эксплуатационных характеристик выполнен с целью сравнения свойств матричных сплавов в нагартованном состоянии и образцов композиционных материалов до и после нагрева. Результаты испытаний показали, что проведение термической обработки способствует снижению пористости композитов и значительному повышению их твердости и микротвердости. Наблюдается также незначительное снижение прочности на сжатие при существенном повышении износостойкости. Установлено, что композиционные материалы характеризуются высокой коррозионной стойкостью к углекислотной и сероводородной коррозии, соответствующей уровню матричных сплавов. Полученные результаты позволяют рекомендовать разработанные материалы для изготовления деталей шатунно-поршневой группы, подшипников и других износостойких деталей узлов трения.

Ключевые слова: композиционный материал; АМг2–10%TiC; АМг6–10%TiC; карбид титана; термическая обработка; самораспространяющийся высокотемпературный синтез.

Благодарности: Статья подготовлена по материалам докладов участников XI Международной школы «Физическое материаловедение» (ШФМ-2023), Тольятти, 11–15 сентября 2023 года.

Для цитирования: Шерина Ю.В., Луц А.Р. Влияние термической обработки на свойства композиционных материалов АМг2–10%TiC и АМг6–10%TiC, полученных методом самораспространяющегося высокотемпературного синтеза // Frontier Materials & Technologies. 2024. № 1. С. 105–112. DOI: 10.18323/2782-4039-2024-1-67-10.

OUR AUTHORS

Aksenov Denis Alekseevich, junior researcher.
Address 1: Institute of Physics of Molecules and Crystals
Ufa Federal Research Center of RAS,
450054, Russia, Ufa, Prospekt Oktyabrya, 71.
Address 2: Ufa University of Science and Technology,
450076, Russia, Ufa, Zaki Validi Street, 32.
E-mail: aksyonovda@mail.ru

Alekseev Valeriy Igorevich, postgraduate student.
Address: University of Science and Technology MISIS,
119049, Russia, Moscow, Leninsky Prospekt, 4, block 1.
E-mail: alval7@yandex.ru

Aryshenskiy Evgeny Vladimirovich, Doctor of Sciences (Engineering),
Associate Professor, senior researcher
of the Laboratory of Electron Microscopy and Image Processing.
Address: Siberian State Industrial University,
654007, Russia, Novokuznetsk, Kirov Street, 42.
E-mail: arishenskiy_ev@sibsiu.ru

Asfandiyarov Rashid Nailevich, PhD (Engineering), researcher.
Address 1: Institute of Physics of Molecules and Crystals
Ufa Federal Research Center of RAS,
450054, Russia, Ufa, Prospekt Oktyabrya, 71.
Address 2: Ufa University of Science and Technology,
450076, Russia, Ufa, Zaki Validi Street, 32.
E-mail: a.r.n@list.ru

Brilevskiy Aleksandr Igorevich, junior researcher
of the Research Institute of Advanced Technologies.
Address: Togliatti State University,
445020, Russia, Togliatti, Belorusskaya Street, 14.
E-mail: alexandrbril@yandex.ru

Danyuk Aleksey Valerievich, PhD (Physics and Mathematics),
senior researcher of the Research Institute of Advanced Technologies.
Address: Togliatti State University,
445020, Russia, Togliatti, Belorusskaya Street, 14.
E-mail: alexey.danyuk@gmail.com

Drits Aleksandr Mikhailovich, PhD (Engineering), leading researcher.
Address: Samara National Research University,
443086, Russia, Samara, Moskovskoye Shosse, 34.
E-mail: alexander.drits@samara-metallurg.ru

Dudarev Artemiy Aleksandrovich, graduate student.
Address: University of Science and Technology MISIS,
119049, Russia, Moscow, Leninsky Prospekt, 4, block 1.
E-mail: artemdudarev@mail.ru

Estemirova Svetlana Khusainovna, PhD (Chemistry), senior researcher.
Address: Institute of Metallurgy of the Ural Branch of RAS,
620016, Russia, Yekaterinburg, Amundsen Street, 101.
E-mail: esveta100@mail.ru

Fakhretdinova Elvira Ildarovna, PhD (Engineering), researcher.
Address 1: Institute of Physics of Molecules and Crystals
Ufa Federal Research Center of RAS,
450054, Russia, Ufa, Prospekt Oktyabrya, 71.
Address 2: Ufa University of Science and Technology,
450076, Russia, Ufa, Zaki Validi Street, 32.
E-mail: yelka89@mail.ru

Galieva Elvina Venerovna, PhD (Engineering), researcher.
Address: Institute for Metals Superplasticity Problems of RAS,
450001, Russia, Ufa, Stepan Khalturin Street, 39.
E-mail: galieva_elvina_v@mail.ru

Kharanzhevskiy Evgeny Viktorovich, Doctor of Sciences (Engineering), Professor,
Head of Laboratory of Physics and Chemistry of Materials.
Address: Udmurt State University,
426034, Russia, Izhevsk, Universitetskaya Street, 1.
E-mail: eh@udsu.ru

Klassman Ekaterina Yuryevna, postgraduate student, engineer.
Address: Institute for Metals Superplasticity Problems of RAS,
450001, Russia, Ufa, Stepan Khalturin Street, 39.
E-mail: klassman@mail.ru

Klevtsov Gennady Vsevolodovich, Doctor of Sciences (Engineering),
professor of Chair "Nanotechnologies, Materials Science and Mechanics".
Address: Togliatti State University,
445020, Russia, Togliatti, Belorusskaya Street, 14.
E-mail: klevtsov11948@mail.ru

Kodirov Davronjon Farkhodzhon ugli, postgraduate student.
Address: University of Science and Technology MISIS,
119049, Russia, Moscow, Leninsky Prospekt, 4, block 1.
E-mail: DFKodirov@yandex.ru

Konovalov Sergey Valerievich, Doctor of Sciences (Engineering), Professor,
Pro-rector for Research and Innovative Activities.
Address: Siberian State Industrial University,
654007, Russia, Novokuznetsk, Kirov Street, 42.
E-mail: konovalov@sibsiu.ru

Kudasheva Kristina Kamilievna, engineer
of the Research Institute of Advanced Technologies.
Address: Togliatti State University,
445020, Russia, Togliatti, Belorusskaya Street, 14.
E-mail: a.abdugaffarova@gmail.com

Kudrya Aleksandr Viktorovich, Doctor of Sciences (Engineering), Professor,
professor of Chair of Materials Science and Strength Physics.
Address: University of Science and Technology MISIS,
119049, Russia, Moscow, Leninsky Prospekt, 4, block 1.
E-mail: AVKudrya@misis.ru

Kudryavtsev Egor Alekseevich, PhD (Engineering), researcher
of the Common Use Center "Technologies and Materials of the National Research University BelSU".
Address: Belgorod State National Research University,
308015, Russia, Belgorod, Pobedy Street, 85.
E-mail: egoryoda@mail.ru

Levashov Evgeny Aleksandrovich, Doctor of Sciences (Engineering), Professor,
Head of Chair of Powder Metallurgy and Functional,
Head of Scientific-Educational Center of Self-Propagating High-Temperature Synthesis.
Address: National University of Science and Technology MISIS,
119049, Russia, Moscow, Leninsky Prospekt, 4, block 1.
E-mail: levashov@shs.misis.ru

Linderov Mikhail Leonidovich, PhD (Physics and Mathematics),
senior researcher of the Research Institute of Advanced Technologies.
Address: Togliatti State University,
445020, Russia, Togliatti, Belorusskaya Street, 14.
E-mail: dartvi@gmail.com

Loginov Pavel Aleksandrovich, PhD (Engineering),
senior researcher of Scientific-Educational Center of Self-Propagating High-Temperature Synthesis.
Address: National University of Science and Technology MISIS,
119049, Russia, Moscow, Leninsky Prospekt, 4, block 1.
E-mail: pavel.loginov.misis@list.ru

Luts Alfiya Rasimovna, PhD (Engineering), Associate Professor,
assistant professor of Chair "Metal Science, Powder Metallurgy, Nanomaterials".
Address: Samara State Technical University,
443100, Russia, Samara, Molodogvardeyskaya Street, 244.
E-mail: alya_luts@mail.ru

Makarov Aleksey Viktorovich, Doctor of Sciences (Engineering),
Corresponding member of RAS, Head of Department of Materials Science,
Head of Laboratory of Mechanical Properties.
Address: M.N. Mikheev Institute of Metal Physics of the Ural Branch of RAS,
620108, Russia, Yekaterinburg, Sofya Kovalevskaya Street, 18.
E-mail: avm@imp.uran.ru

Merson Dmitry Lvovich, Doctor of Sciences (Physics and Mathematics), Professor,
Director of the Research Institute of Advanced Technologies.
Address: Togliatti State University,
445020, Russia, Togliatti, Belorusskaya Street, 14.
E-mail: d.merson@tltsu.ru

Mukanov Samat Kuandykovich, PhD (Engineering), junior researcher
of Scientific-Educational Center of Self-Propagating High-Temperature Synthesis.
Address: National University of Science and Technology MISIS,
119049, Russia, Moscow, Leninsky Prospekt, 4, block 1.
E-mail: smukanov@misis.ru

Petrzhik Mikhail Ivanovich, Doctor of Sciences (Engineering),
professor of Chair of Powder Metallurgy and Functional Coatings,
leading researcher of Scientific-Educational Center
of Self-Propagating High-Temperature Synthesis.
Address: National University of Science and Technology MISIS,
119049, Russia, Moscow, Leninsky Prospekt, 4, block 1.
E-mail: petrzhik@shs.misis.ru

Pogorelov Egor Vasilyevich, postgraduate student.
Address: University of Science and Technology MISIS,
119049, Russia, Moscow, Leninsky Prospekt, 4, block 1.
E-mail: egor.pogorelov11@gmail.com

Raab Arseniy Georgievich, PhD (Engineering), researcher.
Address: Ufa University of Science and Technology,
450076, Russia, Ufa, Zaki Validi Street, 32.
E-mail: agraab@mail.ru

Rastorguev Dmitry Aleksandrovich, PhD (Engineering),
assistant professor of Chair "Equipment and Technologies of Machine Building Production".
Address: Togliatti State University,
445020, Russia, Togliatti, Belorusskaya Street, 14.
E-mail: rast_73@mail.ru

Rodionova Irina Gavrilovna, Doctor of Sciences (Engineering), Associate Professor,
Deputy Director of the Scientific Center for Physical
and Chemical Fundamentals and Technologies of Metallurgy.
Address: State Research Center FSUE I.P. Bardin Central Research Institute of Ferrous Metallurgy,
105005, Russia, Moscow, Radio Street, 23/9, block 1.
E-mail: igrodi@mail.ru

Sementeeva Yuliya Ramilevna, graduate student.
Address: Ufa University of Science and Technology,
450076, Russia, Ufa, Zaki Validi Street, 32.
E-mail: yu.nuriewa@yandex.ru

Sergeyev Maksim Ivanovich, postgraduate student.
Address: University of Science and Technology MISIS,
119049, Russia, Moscow, Leninsky Prospekt, 4, block 1.
E-mail: m1600219@edu.misis.ru

Sevastyanov Aleksandr Aleksandrovich, postgraduate student
of Chair "Equipment and Technologies of Machine Building Production".
Address: Togliatti State University,
445020, Russia, Togliatti, Belorusskaya Street, 14.
E-mail: alex-119977@yandex.ru

Sharipov Arseniy Eliseevich, graduate student.
Address: Ufa University of Science and Technology,
450076, Russia, Ufa, Zaki Validi Street, 32.
E-mail: arsenyarseny36728@gmail.com

Sherina Yuliya Vladimirovna, postgraduate student
of Chair "Metal Science, Powder Metallurgy, Nanomaterials".
Address: Samara State Technical University,
443100, Russia, Samara, Molodogvardeyskaya Street, 244.
E-mail: yulya.makhonina.97@inbox.ru

Shishkunova Mariya Andreevna, graduate student.
Address: Ufa University of Science and Technology,
450076, Russia, Ufa, Zaki Validi Street, 32.
E-mail: shishkunomashaa@gmail.com

Sokolovskaya Elina Aleksandrovna, PhD (Engineering), Associate Professor,
assistant professor of Chair of Metal Science and Physics of Strength.
Address: University of Science and Technology MISIS,
119049, Russia, Moscow, Leninsky Prospekt, 4, block 1.
E-mail: Sokolovskaya@misis.ru

Stepchenkov Aleksandr Konstantinovich, junior researcher.
Address: M.N. Mikheev Institute of Metal Physics of the Ural Branch of RAS,
620108, Russia, Yekaterinburg, Sofya Kovalevskaya Street, 18.
E-mail: stepchenkov@imp.uran.ru

Stukalova Natalia Anatolievna, postgraduate student.
Address: University of Science and Technology MISIS,
119049, Russia, Moscow, Leninsky Prospekt, 4, block 1.
E-mail: stukalova-n@mail.ru

Valitov Vener Anvarovich, Doctor of Sciences (Engineering), leading researcher.
Address: Institute for Metals Superplasticity Problems of RAS,
450001, Russia, Ufa, Stepan Khalturin Street, 39.
E-mail: valitov_va@mail.ru

Volkova Elena Georgievna, PhD (Physics and Mathematics), senior researcher.
Address: M.N. Mikheev Institute of Metal Physics of the Ural Branch of RAS,
620108, Russia, Yekaterinburg, Sofya Kovalevskaya Street, 18.
E-mail: volkova@imp.uran.ru

Yasnikov Igor Stanislavovich, Doctor of Sciences (Physics and Mathematics), Associate Professor,
professor of Chair "General and Theoretical Physics",
leading researcher of the Research Institute of Advanced Technologies.
Address: Togliatti State University,
445020, Russia, Togliatti, Belorusskaya Street, 14.
E-mail: yasnikov@phystech.edu

Zorin Igor Aleksandrovich, laboratory assistant-researcher,
student, II category electronic engineer
of the Laboratory of Mechanical Testing and Electron Microscopy.
Address 1: Samara National Research University,
443086, Russia, Samara, Moskovskoye Shosse, 34.
Address 2: Siberian State Industrial University,
654007, Russia, Novokuznetsk, Kirov Street, 42.
E-mail: zorin.ia@ssau.ru

НАШИ АВТОРЫ

Аксенов Денис Алексеевич, младший научный сотрудник.
Адрес 1: Институт физики молекул и кристаллов
Уфимского федерального исследовательского центра РАН,
450054, Россия, г. Уфа, пр-т Октября, 71.
Адрес 2: Уфимский университет науки и технологий,
450076, Россия, г. Уфа, ул. Заки Валиди, 32.
E-mail: aksyonovda@mail.ru

Алексеев Валерий Игоревич, аспирант.
Адрес: Университет науки и технологий МИСИС,
119049, Россия, г. Москва, Ленинский пр-т, 4, стр. 1.
E-mail: alval7@yandex.ru

Арышенский Евгений Владимирович, доктор технических наук, доцент,
старший научный сотрудник
лаборатории электронной микроскопии и обработки изображений.
Адрес: Сибирский государственный индустриальный университет,
654007, Россия, г. Новокузнецк, ул. Кирова, 42.
E-mail: arishenskiy_ev@sibsiu.ru

Асфандияров Рашид Наилевич, кандидат технических наук,
научный сотрудник.
Адрес 1: Институт физики молекул и кристаллов
Уфимского федерального исследовательского центра РАН,
450054, Россия, г. Уфа, пр-т Октября, 71.
Адрес 2: Уфимский университет науки и технологий,
450076, Россия, г. Уфа, ул. Заки Валиди, 32.
E-mail: a.r.n@list.ru

Брилевский Александр Игоревич, младший научный сотрудник
НИИ прогрессивных технологий.
Адрес: Тольяттинский государственный университет,
445020, Россия, г. Тольятти, ул. Белорусская, 14.
E-mail: alexandrbril@yandex.ru

Валитов Венер Анварович, доктор технических наук,
ведущий научный сотрудник.
Адрес: Институт проблем сверхпластичности металлов РАН,
450001, Россия, г. Уфа, ул. Степана Халтурина, 39.
E-mail: valitov_va@mail.ru

Волкова Елена Георгиевна, кандидат физико-математических наук,
старший научный сотрудник.
Адрес: Институт физики металлов имени М.Н. Михеева Уральского отделения РАН,
620108, Россия, г. Екатеринбург, ул. Софьи Ковалевской, 18.
E-mail: volkova@imp.uran.ru

Галиева Эльвина Венеровна, кандидат технических наук,
научный сотрудник.
Адрес: Институт проблем сверхпластичности металлов РАН,
450001, Россия, г. Уфа, ул. Степана Халтурина, 39.
E-mail: galieva_elvina_v@mail.ru

Данюк Алексей Валериевич, кандидат физико-математических наук,
старший научный сотрудник НИИ прогрессивных технологий.
Адрес: Тольяттинский государственный университет,
445020, Россия, г. Тольятти, ул. Белорусская, 14.
E-mail: alexey.danyuk@gmail.com

Дриц Александр Михайлович, кандидат технических наук,
ведущий научный сотрудник.
Адрес: Самарский национальный исследовательский университет
имени академика С.П. Королева,
443086, Россия, г. Самара, Московское шоссе, 34.
E-mail: alexander.drits@samara-metallurg.ru

Дударев Артемий Александрович, магистр.
Адрес: Университет науки и технологий МИСИС,
119049, Россия, г. Москва, Ленинский пр-т, 4, стр. 1.
E-mail: artemdudarev@mail.ru

Зорин Игорь Александрович, лаборант-исследователь,
студент, инженер-электроник II категории
лаборатории механических испытаний и электронной микроскопии.
Адрес 1: Самарский национальный исследовательский университет
имени академика С.П. Королева,
443086, Россия, г. Самара, Московское шоссе, 34.
Адрес 2: Сибирский государственный индустриальный университет,
654007, Россия, г. Новокузнецк, ул. Кирова, 42.
E-mail: zorin.ia@ssau.ru

Классман Екатерина Юрьевна, аспирант, инженер.
Адрес: Институт проблем сверхпластичности металлов РАН,
450001, Россия, г. Уфа, ул. Степана Халтурина, 39.
E-mail: klassman@mail.ru

Клевцов Геннадий Всеволодович, доктор технических наук,
профессор кафедры «Нанотехнологии, материаловедение и механика».
Адрес: Тольяттинский государственный университет,
445020, Россия, г. Тольятти, ул. Белорусская, 14.
E-mail: klevtsov11948@mail.ru

Кодиров Давронжон Фарходжон угли, аспирант.
Адрес: Университет науки и технологий МИСИС,
119049, Россия, г. Москва, Ленинский пр-т, 4, стр. 1.
E-mail: DFKodirov@yandex.ru

Коновалов Сергей Валерьевич, доктор технических наук, профессор,
проректор по научной и инновационной деятельности.
Адрес: Сибирский государственный индустриальный университет,
654007, Россия, г. Новокузнецк, ул. Кирова, 42.
E-mail: konovalov@sibsiu.ru

Кудашева Кристина Камильевна, инженер НИИ прогрессивных технологий.
Адрес: Тольяттинский государственный университет,
445020, Россия, г. Тольятти, ул. Белорусская, 14.
E-mail: a.abdugaffarova@gmail.com

Кудря Александр Викторович, доктор технических наук, профессор,
профессор кафедры металловедения и физики прочности.
Адрес: Университет науки и технологий МИСИС,
119049, Россия, г. Москва, Ленинский пр-т, 4, стр. 1.
E-mail: AVKudrya@misis.ru

Кудрявцев Егор Алексеевич, кандидат технических наук, научный сотрудник
Центра коллективного пользования «Технологии и Материалы НИУ "БелГУ"».
Адрес: Белгородский государственный национальный исследовательский университет,
308015, Россия, г. Белгород, ул. Победы, 85.
E-mail: egoryoda@mail.ru

Левашов Евгений Александрович, доктор технических наук, профессор,
заведующий кафедрой порошковой металлургии и функциональных покрытий,
директор научно-учебного центра самораспространяющегося высокотемпературного синтеза.
Адрес: Университет науки и технологий МИСИС,
119049, Россия, г. Москва, Ленинский пр-т, 4, стр. 1.
E-mail: levashov@shs.misis.ru

Линдеров Михаил Леонидович, кандидат физико-математических наук,
старший научный сотрудник НИИ прогрессивных технологий.
Адрес: Тольяттинский государственный университет,
445020, Россия, г. Тольятти, ул. Белорусская, 14.
E-mail: dartvi@gmail.com

Логинов Павел Александрович, кандидат технических наук,
старший научный сотрудник научно-учебного центра
самораспространяющегося высокотемпературного синтеза.
Адрес: Университет науки и технологий МИСИС,
119049, Россия, г. Москва, Ленинский пр-т, 4, стр. 1.
E-mail: pavel.loginov.misis@list.ru

Луц Альфия Расимовна, кандидат технических наук, доцент,
доцент кафедры «Металловедение, порошковая металлургия, наноматериалы».
Адрес: Самарский государственный технический университет,
443100, Россия, г. Самара, ул. Молодогвардейская, 244.
E-mail: alya_luts@mail.ru

Макаров Алексей Викторович, доктор технических наук, член-корреспондент РАН,
заведующий отделом материаловедения и лабораторией механических свойств.
Адрес: Институт физики металлов имени М.Н. Михеева Уральского отделения РАН,
620108, Россия, г. Екатеринбург, ул. Софьи Ковалевской, 18.
E-mail: avm@imp.uran.ru

Мерсон Дмитрий Львович, доктор физико-математических наук, профессор,
директор НИИ прогрессивных технологий.
Адрес: Тольяттинский государственный университет,
445020, Россия, г. Тольятти, ул. Белорусская, 14.
E-mail: d.merson@tltsu.ru

Муканов Самат Куандыкович, кандидат технических наук,
младший научный сотрудник научно-учебного центра
самораспространяющегося высокотемпературного синтеза.
Адрес: Университет науки и технологий МИСИС,
119049, Россия, г. Москва, Ленинский пр-т, 4, стр. 1.
E-mail: smukanov@misis.ru

Петржик Михаил Иванович, доктор технических наук,
профессор кафедры порошковой металлургии и функциональных покрытий,
ведущий научный сотрудник научно-учебного центра
самораспространяющегося высокотемпературного синтеза.
Адрес: Университет науки и технологий МИСИС,
119049, Россия, г. Москва, Ленинский пр-т, 4, стр. 1.
E-mail: petrzhik@shs.misis.ru

Погорелов Егор Васильевич, аспирант.
Адрес: Университет науки и технологий МИСИС,
119049, Россия, г. Москва, Ленинский пр-т, 4, стр. 1.
E-mail: egor.pogorelov11@gmail.com

Рааб Арсений Георгиевич, кандидат технических наук, научный сотрудник.
Адрес: Уфимский университет науки и технологий,
450076, Россия, г. Уфа, ул. Заки Валиди, 32.
E-mail: agraab@mail.ru

Расторгуев Дмитрий Александрович, кандидат технических наук,
доцент кафедры «Оборудование и технологии машиностроительного производства».
Адрес: Тольяттинский государственный университет,
445020, Россия, г. Тольятти, ул. Белорусская, 14.
E-mail: rast_73@mail.ru

Родионова Ирина Гавриловна, доктор технических наук, доцент,
заместитель директора научного центра физико-химических основ и технологий металлургии.
Адрес: ГНЦ ФГУП «ЦНИИчермет им. И.П. Бардина»,
105005, Россия, г. Москва, ул. Радио 23/9, стр. 1.
E-mail: igrodi@mail.ru

Севастьянов Александр Александрович, аспирант
кафедры «Оборудование и технологии машиностроительного производства».
Адрес: Тольяттинский государственный университет,
445020, Россия, г. Тольятти, ул. Белорусская, 14.
E-mail: alex-119977@yandex.ru

Сементеева Юлия Рамилевна, магистрант.
Адрес: Уфимский университет науки и технологий,
450076, Россия, г. Уфа, ул. Заки Валиди, 32.
E-mail: yu.nuriewa@yandex.ru

Сергеев Максим Иванович, аспирант.
Адрес: Университет науки и технологий МИСИС,
119049, Россия, г. Москва, Ленинский пр-т, 4, стр. 1.
E-mail: m1600219@edu.misis.ru

Соколовская Элина Александровна, кандидат технических наук, доцент,
доцент кафедры металловедения и физики прочности.
Адрес: Университет науки и технологий МИСИС,
119049, Россия, г. Москва, Ленинский пр-т, 4, стр. 1.
E-mail: Sokolovskaya@misis.ru

Степченков Александр Константинович, младший научный сотрудник.
Адрес: Институт физики металлов имени М.Н. Михеева Уральского отделения РАН,
620108, Россия, г. Екатеринбург, ул. Софьи Ковалевской, 18.
E-mail: stepchenkov@imp.uran.ru

Стукалова Наталья Анатольевна, аспирант.
Адрес: Университет науки и технологий МИСИС,
119049, Россия, г. Москва, Ленинский пр-т, 4, стр. 1.
E-mail: stukalova-n@mail.ru

Фахретдинова Эльвира Илдаровна, кандидат технических наук, научный сотрудник.
Адрес 1: Институт физики молекул и кристаллов
Уфимского федерального исследовательского центра РАН,
450054, Россия, г. Уфа, пр-т Октября, 71.
Адрес 2: Уфимский университет науки и технологий,
450076, Россия, г. Уфа, ул. Заки Валиди, 32.
E-mail: yelka89@mail.ru

Харанжевский Евгений Викторович, доктор технических наук, профессор,
заведующий лабораторией физики и химии материалов.
Адрес: Удмуртский государственный университет,
426034, Россия, г. Ижевск, ул. Университетская, 1.
E-mail: eh@udsu.ru

Шарипов Арсений Елисеевич, магистрант.
Адрес: Уфимский университет науки и технологий,
450076, Россия, г. Уфа, ул. Заки Валиди, 32.
E-mail: arsenyarseny36728@gmail.com

Шерина Юлия Владимировна, аспирант
кафедры «Металловедение, порошковая металлургия, наноматериалы».
Адрес: Самарский государственный технический университет,
443100, Россия, г. Самара, ул. Молодогвардейская, 244.
E-mail: yulya.makhonina.97@inbox.ru

Шишкунова Мария Андреевна, магистрант.
Адрес: Уфимский университет науки и технологий,
450076, Россия, г. Уфа, ул. Заки Валиди, 32.
E-mail: shishkunomashaa@gmail.com

Эстемирова Светлана Хусаиновна, кандидат химических наук,
старший научный сотрудник.
Адрес: Институт металлургии Уральского отделения РАН,
620016, Россия, г. Екатеринбург, ул. Амундсена, 101.
E-mail: esveta100@mail.ru

Ясников Игорь Станиславович, доктор физико-математических наук, доцент,
профессор кафедры «Общая и теоретическая физика»,
ведущий научный сотрудник НИИ прогрессивных технологий.
Адрес: Тольяттинский государственный университет,
445020, Россия, г. Тольятти, ул. Белорусская, 14.
E-mail: yasnikov@phystech.edu

On the cover: Image of the structure of the Mg–8.6Zn–1.2Zr alloy subjected to prolonged annealing in air at a temperature of 400 °C for 24 h. Light microscopy. Author of the photo: M.A. Shishkunova, postgraduate student (Ufa University of Science and Technology, Ufa, Russia).

На обложке: Изображение структуры сплава Mg–8,6Zn–1,2Zr, подвергнутого длительному отжигу в воздушной среде при температуре 400 °C в течение 24 ч. Световая микроскопия. Автор фото: Шишкунова М.А., аспирант (Уфимский университет науки и технологий, Уфа, Россия).